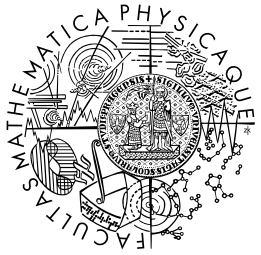

FACULTY
OF MATHEMATICS
AND PHYSICS
Charles University

DOCTORAL THESIS

Miroslav Hanzelka

Nonlinear processes in space plasmas and their effects on the generation and propagation of electromagnetic waves

Department of Surface and Plasma Science

Supervisor of the doctoral thesis: prof. RNDr. Ondřej Santolík, Dr.

Study programme: Physics

Study branch: Theoretical Physics, Astronomy and Astrophysics

Prague 2022

I declare that I carried out this doctoral thesis independently, and only with the cited sources, literature and other professional sources. It has not been used to obtain another or the same degree.

I understand that my work relates to the rights and obligations under the Act No. 121/2000 Sb., the Copyright Act, as amended, in particular the fact that the Charles University has the right to conclude a license agreement on the use of this work as a school work pursuant to Section 60 subsection 1 of the Copyright Act.

In ..... date ....

Author's signature

Here I want to express my gratitude to all my colleagues from the Department of Space Physics and from abroad, whose guidance was indispensable on my winding path through the field of space plasma physics, on which this thesis represents a major checkpoint. Namely, I would like to thank my supervisor Ondřej Santolík, for the numerous consultations, research assistance, and overall kindliness. I also want to express my gratitude to Prof. Omura from Kyoto University, who introduced me to the nonlinear growth theory during my visits to Japan. Another thanks goes to David Píša, who often served as my unofficial consultant and listened to my diverse questions and ideas. Concerning the more specialized topics of my research, discussions with Ulrich Taubenschuss often proved to be very inspiring. And I cannot forget Radek Lán, an expert on space technology who provided lecture-long descriptions of spacecraft instrumentation on demand.

Last but not least, I deeply appreciate the support from my family members, who have provided me with a pleasant working environment during the years of mandatory work from home.

This work was partly supported by the Charles University, project GA UK No. 64120.

Title: Nonlinear processes in space plasmas and their effects on the generation and propagation of electromagnetic waves

Author: Miroslav Hanzelka

Department: Department of Surface and Plasma Science

Supervisor: prof. RNDr. Ondřej Santolík, Dr., Department of Surface and Plasma Science

Abstract: Nonlinear interactions of charged particles and large-amplitude waves have a significant impact on magnetospheric dynamics. Here we focus on the cyclotron resonant interaction between energetic electrons and the discrete, whistler-mode chorus emissions in the Earth's outer radiation belt. The subject is introduced by an extensive review of whistler-mode dispersion properties, resonant electron trajectories and nonlinear wave-growth theories. We then present a new semi-empirical model of rising-tone chorus emissions with a fine subpacket structure. The model is then used in test-particle simulations to investigate nonlinear perturbations in hot electron distributions. Based on changes in electron fluxes, we estimate the resolution of spacecraft particle detectors required to detect the predicted perturbations. The test-particle method is further used to simulate atmospheric precipitation of electrons caused by interaction with a single chorus wavepacket, and the result is analysed connection with microbursts and pulsating auroras. We also detected a violation of the strong diffusion limit by the cyclotron resonant interaction, resulting in loss cone overfilling.

Keywords: radiation belt; whistler mode; nonlinear interaction; chorus emission; test-particle simulation

Contents

Introduction

In this thesis, we continue the decades-long line of research focused on nonlinear interactions between whistler-mode waves and energetic electrons in space plasmas. These interactions facilitate the formation of high amplitude coherent structures in the wave spectrum and have an important role in electron acceleration and transport in various plasma environments. While we will discuss these processes mainly within the frame of the Earth's magnetospheric dynamics, the underlying theory can be applied in the research of other planetary magnetospheres and solar wind, and it finds use even in the field of laboratory plasmas, with possible modifications for different wave modes and particle species.

It is sometimes said that the Earth's magnetosphere can be viewed as a large laboratory for experiments in a tenuous magnetized plasma. However, it is a very peculiar laboratory, where the scientists cannot control the environment and probing even a very tiny section of the system turns out to be difficult and costly. Apart from fundamental research, our interest in the magnetosphere is driven by the increasing number of man-made satellites orbiting in the near-Earth space, which can sustain damage due to radiation exposure, not to mention the effect on the passengers of manned missions. In this respect, the most attention is given to the outer radiation belt. This toroidal region, typically spanning between 3.0 and 6.5 Earth's radii near the magnetic equator (Baker et al., 2018), exhibits large and very variable fluxes of relativistic electrons. Understanding the fundamental physical processes behind the energization of radiation belt particles is essential for predicting high radiation hazard events.

The particle content in the outer radiation belt is in a dynamical equilibrium. Particles that become scattered and reach low altitudes during their bounce motion along magnetic field lines are lost to the atmosphere, and new populations of particles are injected during substorm events from the magnetotail. New electron populations have energies in the order of 10 keV, two orders below the MeV fluxes, which are considered a radiation hazard. The acceleration happens on various spatial and temporal scales, with the fastest energization being due to nonlinear interactions with coherent whistler-mode waves. Among the various electromagnetic emissions propagating in the right-hand polarized whistler mode, the chorus emission is of special interest. It consists of repeating rising-tone wave elements, which can reach very high intensities and exhibit fast amplitude modulations within each element. The growth mechanism of chorus and the energy exchange between resonant electrons and chorus is actively studied, and most of the new results presented here are focused in this direction.

The contents of this thesis are divided into two parts. In Chapters 1 to 3, we cover the essential theory of cold plasma waves and wave-particle interactions in space plasma, as well as the recent developments in observation and analysis of the chorus emissions and associated nonlinear effects. Chapter 1 deals with the dispersion of whistler-mode waves and the linearized theory of plasma wave growth and also describes selected electromagnetic emissions which can be detected by *in situ* measurements in the Earth's magnetosphere. In Chapter 2, the theory of resonant interaction of plasma waves and particles is summarized, with most space given to the second-order cyclotron resonance between whistler-mode waves and electrons and the related trapping effects. Although the bulk of the theory was developed in the 1960s and 1970s, we attempt to provide insights based on recent observational studies and numerical simulations. The Hamiltonian approach to wave-particle resonance is briefly mentioned to explain its limitations in the study of rising tone chorus elements. Chapter 3 is dedicated to the chorus emissions. Starting with a succinct account of recent observational findings,

we focus on the nonlinear growth theory of chorus emissions as presented in the works of Omura et al. (Omura, 2021). While our primary goal is to provide the theoretical framework for the new results presented in the second part of this work, we also review other theories dealing with the formation of chorus emissions and discuss some open research questions in this field.

The second part of the thesis is concerned with our new research on the structure of chorus emissions and their effect on hot electron populations. In Chapter 4 we present a new model of a rising tone chorus element propagating along magnetic field lines. We connect the nonlinear growth theory with older hypotheses about the resonant current in order to construct a wavefield with a subpacket structure comparable to observations provided by magnetic search coils on spacecraft which probe the outer radiation belt (Hanzelka et al., 2020). The model is used in test particle simulations in Chapter 5 to analyze the evolution of hot electron distribution during interaction with chorus. We reveal, in agreement with some previously published research, that multiple stripes of increased and decreased phase space density (PSD) are formed during the interaction, associated with the trapping and scattering effects of individual subpackets. The discovered perturbations in phase space density are analyzed in detail, and the measurability of these perturbations is assessed. Successful experimental confirmation of the perturbations would directly confirm the theories describing the nonlinear processes behind the chorus growth. It is shown that the particle instruments on currently or recently operating spacecraft lack the required pitch angle resolution to capture the small PSD structures, and the required parameters for a successful measurement are discussed (Hanzelka et al., 2021). In the last section, another example application of the model is given, in which we calculate the precipitating electron fluxes due to interaction with a single chorus element. Small, rapid fluctuations appear in the fluxes, related again to the subpackets, which might be reflected in the intensity modulation of pulsating auroras.

To keep the thesis focused and concise, we omit any general introduction to space plasmas or any deeper discussion of the broader connections between the chorus waves and various parts of the magnetosphere. For the same reasons, we mention the research on wave propagation and ray tracing, which was also done and published in the frame of this thesis work, only in passing and where it can support our assumptions about the behaviour of chorus waves. All authored or co-authored publications related to waves in space plasma (but not necessarily to chorus) can be found in the List of Publications at the end of the thesis.

1. Theory and observations of plasma waves in space

Plasma waves are ubiquitous throughout planetary magnetospheres, arising naturally due to the amplification of certain parts of the fluctuation spectrum through energy transfer between particles and electromagnetic fields. The tenuous magnetised plasma of the Earth's magnetosphere exhibits a rich wave mode structure, which must be understood in order to interpret data collected from electric and magnetic field receivers carried by scientific spacecraft. The dispersion and polarisation properties of plasma waves determine how they propagate through the medium and interact with charged particles, making detailed knowledge of dispersion relations essential for analysing linear and nonlinear wave-particle interactions.

In this chapter, we briefly review the hot plasma dispersion relation and its cold plasma approximation, limiting ourselves to small-amplitude waves and ignoring the possible trapping of particles in the wave potential. Focus is put on the propagation properties of the whistler mode and the linear instabilities of this mode. The ray tracing method of propagation analysis is described with examples. We then give an overview of spacecraft instrumentation relevant to the research on whistler-mode waves, followed by a short description of numerical methods used to process raw data from electric antennas and magnetic search coils to obtain wave propagation properties. In the last section, we list some of the most common and most important electromagnetic emissions which can occur in planetary magnetospheres, again with particular attention to the whistler-mode emissions.

1.1 Dispersion of small-amplitude plasma waves

1.1.1 The Vlasov–Maxwell equations

Most space plasmas can be described by the Vlasov-Maxwell system of equations (Ichimaru, 2004; Gurnett and Bhattacharjee, 2017)

$$\frac{\partial f_s}{\partial t} + \boldsymbol{v}_s \cdot \frac{\partial f_s}{\partial \boldsymbol{r}} + Z_s e \left(\boldsymbol{E} + \boldsymbol{v}_s \times \boldsymbol{B}\right) \cdot \frac{\partial f_s}{\partial \boldsymbol{u}} = 0 \quad \forall s \tag{1.1}$$

$$\nabla \cdot \boldsymbol{E} = \frac{\rho}{\varepsilon_0}\,, \tag{1.2}$$

$$\nabla \cdot \boldsymbol{B} = 0\,, \tag{1.3}$$

$$\nabla \times \boldsymbol{E} = -\frac{\partial \boldsymbol{B}}{\partial t}\,, \tag{1.4}$$

$$\nabla \times \boldsymbol{B} = \mu_0 \boldsymbol{J}_{\mathrm{tot}} + \mu_0 \varepsilon_0 \frac{\partial \boldsymbol{E}}{\partial t}\,. \tag{1.5}$$

The electromagnetic fields $\boldsymbol{E}(\boldsymbol{r}, t)$ and $\boldsymbol{B}(\boldsymbol{r}, t)$ are sums of internal fields induced the through particle distribution and of external fields, e.g. the planetary magnetic field. The charge density $\rho(\boldsymbol{r}, t)$ and the current density $\boldsymbol{J}_{\mathrm{tot}}(\boldsymbol{r}, t)$ are calculated self-consistently from the single-particle phase space distributions $f_s(\boldsymbol{r}, \boldsymbol{u}, t)$,

$$\rho = e \int \sum_s Z_s f_s \mathrm{d}^3 u\ , \tag{1.6}$$

$$\boldsymbol{J}_{\mathrm{tot}} = \boldsymbol{J} + \boldsymbol{J}_{\mathrm{ext}} = e \int \sum_s Z_s f_s \boldsymbol{v}_s \mathrm{d}^3 u + \boldsymbol{J}_{\mathrm{ext}}\,, \tag{1.7}$$

where we allow for an external source of current that was not implicitly included in the plasma description. Subscript s represents a particle species or population, with Z_s carrying the sign and magnitude of the particle charge in units of the elementary charge e. A complete List of Symbols can be found at the end of this thesis.

The particle velocity $\boldsymbol{v}_s$ is defined through the relativistic momentum $\boldsymbol{u}$ as

$$\boldsymbol{v}_s = \frac{\boldsymbol{u}}{\gamma m_\mathrm{s}} \tag{1.8}$$

$$\gamma_s = \left(1 + \frac{\boldsymbol{u}\cdot\boldsymbol{u}}{m_s^2 c^2}\right)^{1/2} . \tag{1.9}$$

Since a typical velocity of dominant particle populations in the Earth's magnetosphere and the solar wind is much smaller than the speed of light (Russell et al., 2016), time dilation and length contraction effects have negligible impact on the plasma dispersive properties described in the rest of the chapter. However, when discussing the resonance curves in Chapter 2, the importance of relativistic Doppler shift becomes apparent.

By using the Vlasov equation, we reduce the plasma description to a continuous fluid. In other words, the distributions f_s are coarse-grained and do not retain the fluctuations due to the discreteness of the particles. The fluid limit is achieved when the number of electrons per Debye sphere

$$N_\mathrm{De} = \frac{4\pi n_\mathrm{e}}{3}\lambda_\mathrm{De}^3 \tag{1.10}$$

is much larger than one. The Debye length

$$\lambda_\mathrm{De} = \sqrt{\frac{\varepsilon_0 k_\mathrm{B} T_\mathrm{e}}{n_\mathrm{e} e^2}} , \tag{1.11}$$

along with the plasma oscillation frequency

$$\omega_\mathrm{pe} = \sqrt{\frac{n_\mathrm{e} e^2}{\varepsilon_0 m_\mathrm{e}}} , \tag{1.12}$$

are invariant scales of a plasma fluid. The product $\lambda_\mathrm{De}\omega_\mathrm{pe}$ gives the electron thermal speed

$$C_\mathrm{e} = \sqrt{\frac{k_\mathrm{B} T_\mathrm{e}}{m_\mathrm{e}}} . \tag{1.13}$$

In the definition of the Debye length and the thermal speed, it is assumed for simplicity that the plasma is in thermal equilibrium, so that the temperature can be treated as a scalar quantity. When the energy $k_\mathrm{B}T_\mathrm{e}$ is equal to 1 eV, the electron component of the plasma is said to have a temperature of 1 eV, which corresponds to approximately 11600 K.

Because the fluid limit effectively removes particle collisions that are not captured by the collective behaviour of the averaged (macroscopic) electromagnetic field, the Vlasov equation is sometimes called the collisionless Boltzmann equation. As a consequence, it cannot be used to derive the wave dispersion in lower layers of the ionosphere, where the collision frequency becomes significant (Schunk and Nagy, 2004).

1.1.2 General form of the dispersion relation

The Maxwell equations, a set of coupled linear partial differential equations, can be transformed into a set of algebraic equations using the Fourier transform. A function

$f(\boldsymbol{r},t)$ of position and time can be represented by its Fourier transform $f(\boldsymbol{k},\omega)$ through the expression

$$f(\boldsymbol{r},t) = \frac{1}{(2\pi)^2}\int_{-\infty}^{\infty} f(\boldsymbol{k},\omega)\mathrm{e}^{\mathrm{i}(\omega t-\boldsymbol{k}\cdot\boldsymbol{r})}\mathrm{d}\omega\,\mathrm{d}^3k\,; \tag{1.14}$$

the normalization factor and sign convention given here are used throughout the text. The vector $\boldsymbol{k}$ is the wave vector, and ω represents the angular wave frequency. The explicit dependence on $(\boldsymbol{r},t)$ or $(\boldsymbol{k},\omega)$ will be given only when not clear from the context.

The dispersion of small amplitude waves in a plasma is controlled by the linear response of the medium to an electromagnetic disturbance. The induced current $\boldsymbol{J}(\boldsymbol{k},\omega)$ is connected to the electric field $\boldsymbol{E}(\boldsymbol{k},\omega)$ through Ohm's law

$$\boldsymbol{J}(\boldsymbol{k},\omega) = \boldsymbol{\sigma}(\boldsymbol{k},\omega)\cdot\boldsymbol{E}(\boldsymbol{k},\omega)\,, \tag{1.15}$$

which serves as the definition of the conductivity tensor $\boldsymbol{\sigma}$. The relative permittivity of an anisotropic dielectric is described by the dielectric tensor, $\boldsymbol{\varepsilon}$, which is related to the conductivity by the formula

$$\boldsymbol{\varepsilon} = \boldsymbol{I} - \frac{\boldsymbol{\sigma}}{\mathrm{i}\omega\varepsilon_0} \tag{1.16}$$

where $\boldsymbol{I}$ is a unit 3×3 matrix. The permeability is assumed to be scalar and close to the vacuum value, as the magnetic moment of particles in a space plasma is usually very small (Baumjohann and et al., 2012). Using the continuity equation for the induced current

$$\frac{\partial\rho}{\partial t} + \nabla\cdot\boldsymbol{J} = 0\,, \tag{1.17}$$

the Fourier transformed Maxwell equations can be cast in the form

$$\boldsymbol{k}\cdot\boldsymbol{\varepsilon}\cdot\boldsymbol{E} = 0\,, \tag{1.18}$$

$$\boldsymbol{k}\cdot\boldsymbol{B} = 0\,, \tag{1.19}$$

$$\boldsymbol{k}\times\boldsymbol{E} - \omega\boldsymbol{B} = 0\,, \tag{1.20}$$

$$\boldsymbol{k}\times\boldsymbol{B} + \frac{\omega}{c^2}\boldsymbol{\varepsilon}\cdot\boldsymbol{E} = -\mathrm{i}\mu_0\boldsymbol{J}_{\mathrm{ext}}\,. \tag{1.21}$$

By eliminating the magnetic field from Ampère's law and Faraday's law, we obtain

$$\left(\boldsymbol{\varepsilon} - \frac{k^2c^2}{\omega^2}\left(\boldsymbol{I} - \frac{\boldsymbol{kk}}{k^2}\right)\right)\cdot\boldsymbol{E} = \frac{-\mathrm{i}\boldsymbol{J}_{\mathrm{ext}}}{\omega\varepsilon_0}\,. \tag{1.22}$$

We can now define the dispersion tensor

$$\mathcal{D}(\boldsymbol{k},\omega) = \boldsymbol{\varepsilon}(\boldsymbol{k},\omega) - \frac{k^2c^2}{\omega^2}\left(\boldsymbol{I} - \frac{\boldsymbol{kk}}{k^2}\right)\,, \tag{1.23}$$

and in the case of a plasma without external sources ($\boldsymbol{J}_{\mathrm{ext}} = 0$), we get the homogeneous equation

$$\mathcal{D}\cdot\boldsymbol{E} = 0\,. \tag{1.24}$$

Nontrivial solutions are found by setting the determinant of the dispersion tensor to zero,

$$|\mathcal{D}(\boldsymbol{k},\omega)| \equiv \bar{D}(\boldsymbol{k},\omega) = 0\,. \tag{1.25}$$

The last equation determines the dispersion relations $\boldsymbol{k}(\omega)$ for electromagnetic wave modes in a magnetized plasma.

We will often express the dispersion properties through a dimensionless quantity, the refractive index

$$\boldsymbol{\mu} = \frac{\boldsymbol{k}c}{\omega}\,. \tag{1.26}$$

The phase velocity $\boldsymbol{V}_\mathrm{p}$ of a wave is directed along the wave vector (or the vector refractive index), and its magnitude is given by

$$V_\mathrm{p} = \frac{\omega}{k} = \frac{c}{\mu}\,. \tag{1.27}$$

For a pulse with a slowly varying amplitude, the inverted dispersion relation $\omega(\boldsymbol{k})$ can be well approximated by the first-order Taylor expansion about the mean wave vector $\boldsymbol{k}_0$,

$$\omega(\boldsymbol{k}) \approx \omega(\boldsymbol{k}_0) + \frac{\partial\omega}{\partial\boldsymbol{k}}(\boldsymbol{k} - \boldsymbol{k}_0)\,. \tag{1.28}$$

The coefficient of the linear term is called the group velocity,

$$\boldsymbol{V}_\mathrm{g} = \frac{\partial\omega}{\partial\boldsymbol{k}}\,, \tag{1.29}$$

and describes the propagation of the envelope of the packet. In the case of shorter pulses, higher-order terms start to play a role, and the wave packet experiences spread and decrease in amplitude, accompanied by a frequency chirp (Orfanidis, 2016).

The group velocity also represents the flow of energy carried by a wave packet. For a loss-free plasma medium, we can write (Stix, 1992)

$$\boldsymbol{V_g} = \frac{\boldsymbol{S} + \boldsymbol{T}}{W}\,, \tag{1.30}$$

where

$$\boldsymbol{S} = \frac{1}{2\mu_0}(\boldsymbol{E}^* \times \boldsymbol{B} + \boldsymbol{E} \times \boldsymbol{B}^*) \tag{1.31}$$

is the flux of electromagnetic energy (the Poynting vector) with $*$-notation for the complex conjugates;

$$\boldsymbol{T} = -\frac{\omega\varepsilon_0}{2}\boldsymbol{E}^* \cdot \frac{\partial\boldsymbol{\varepsilon}}{\partial\boldsymbol{k}} \cdot \boldsymbol{E} \tag{1.32}$$

is the flux of acoustic energy, and

$$W = \frac{1}{2}\left(\frac{1}{\mu_0}\boldsymbol{B}^* \cdot \boldsymbol{B} + \varepsilon_0\boldsymbol{E}^* \cdot \frac{\partial}{\partial\omega}(\omega\boldsymbol{\varepsilon}) \cdot \boldsymbol{E}\right) \tag{1.33}$$

denotes the energy density. As we show below in Section 1.1.3, a hot magnetoplasma is not loss-free. Nevertheless, for wave modes that are not heavily damped, the energy flow formulation of group velocity gives very accurate results.

1.1.3 Hot plasma dispersion relation

The derivation of dispersion modes of small amplitude waves in a hot magnetized plasma starts with the linearization of the Vlasov-Maxwell system, Eqs. 1.1–1.5. Since this thesis focuses on large amplitude waves and nonlinear effects, we present only those parts of the linear theory that are relevant for theoretical discussion in later sections.

Assuming that the distribution function can be split into a homogeneous, time-independent zero-order term $f_{s0}(\boldsymbol{u})$ and a first-order perturbation $f_s(t, \boldsymbol{r}, \boldsymbol{u})$, the linear expansion of the Vlasov equation is given by (Gurnett and Bhattacharjee, 2017; Ichimaru, 2004)

$$(\boldsymbol{v_s} \times \boldsymbol{B}_0) \cdot \frac{\partial f_{s0}}{\partial\boldsymbol{u}} = 0\,, \tag{1.34}$$

$$\frac{\partial f_s}{\partial t} + \boldsymbol{v_s} \cdot \frac{\partial f_s}{\partial \boldsymbol{r}} + Z_s e(\boldsymbol{v_s} \times \boldsymbol{B}_0) \cdot \frac{\partial f_s}{\partial \boldsymbol{u}} + Z_s e(\boldsymbol{E} + \boldsymbol{v_s} \times \boldsymbol{B}) \cdot \frac{\partial f_{s0}}{\partial \boldsymbol{u}} = 0\,. \tag{1.35}$$

Fields $\boldsymbol{E}$ and $\boldsymbol{B}$ represent perturbations associated with the plasma waves, $\boldsymbol{B}_0$ is a constant ambient magnetic field (e.g. the geomagnetic field), and $\boldsymbol{E}_0 = 0$. In cylindrical momentum space coordinates

$$u_x = u_\perp \cos\varphi\,, \tag{1.36}$$
$$u_y = u_\perp \sin\varphi\,, \tag{1.37}$$
$$u_z = u_\parallel\,, \tag{1.38}$$

the zero-order equation reads

$$-B_0 \frac{\partial f_{s0}}{\partial \varphi} = 0\,. \tag{1.39}$$

We will call this formula the gyrotropic condition. Under the action of large amplitude waves, the azimuthal symmetry can be broken, and vortex structures will emerge in the $(\varphi, u_\parallel)$ space. This type of nongyrotropy will be reintroduced later in Chapter 3 through external currents.

The first order Vlasov equation for the perturbation f_s is most easily solved through Fourier transform in space and time. Using the cylindrical coordinates and Faraday's law, we arrive at

$$\frac{\partial f_s}{\partial \varphi} - \mathrm{i}(\alpha_s + \beta_s \cos\varphi) f_s = \frac{\mathrm{sgn}(Z_s) e}{\Omega_s/\gamma_s} \left(\boldsymbol{E} + \boldsymbol{v_s} \times \left(\frac{\boldsymbol{k} \times \boldsymbol{E}}{\omega} \right) \right) \cdot \frac{\partial f_{s0}}{\partial \boldsymbol{u}}\,. \tag{1.40}$$

Here, $\boldsymbol{E}$ and f_s depend on $(\omega, \boldsymbol{k})$ instead of $(t, \boldsymbol{r})$. We have introduced the unsigned cyclotron frequency

$$\Omega_s = \frac{B_0 |Z_s e|}{m_s} \tag{1.41}$$

and the substitutions

$$\alpha_s = \mathrm{sgn}(Z_s) \frac{k_\parallel \gamma_s v_{s\parallel} - \gamma_s \omega}{\Omega_s}\,, \tag{1.42}$$
$$\beta_s = \mathrm{sgn}(Z_s) \frac{k_\perp \gamma_s v_{s\perp}}{\Omega_s}\,. \tag{1.43}$$

The formal solution $f_s(\boldsymbol{k}, \omega)$ enters into the calculation of current density $\boldsymbol{J}$ in Equation 1.7, which is then plugged into Ohm's law and allows us to express the conductivity tensor and the dielectric tensor.

The hot plasma dielectric tensor for a general normalized distribution $F_s = f_s/n_s$ takes the form (Stix, 1992; Ichimaru, 2004)

$$\begin{aligned} \boldsymbol{\varepsilon} = \boldsymbol{I} + \sum_s \frac{\omega_{\mathrm{p}s}^2}{\omega \Omega_s} \int_0^\infty 2\pi u_\perp \mathrm{d}u_\perp \int_{-\infty}^\infty \mathrm{d}u_\parallel \Bigg[\hat{\boldsymbol{e}}_\parallel \hat{\boldsymbol{e}}_\parallel \frac{\Omega_s}{\gamma_s \omega} \left(\frac{1}{u_\parallel} \frac{\partial F_{s0}}{\partial u_\parallel} - \frac{1}{u_\perp} \frac{\partial F_{s0}}{\partial u_\perp} \right) u_\parallel^2 - \\ - \sum_{n=-\infty}^{\infty} \mathrm{sgn}(Z_s) \frac{u_\perp}{\alpha_s + n} \left(\frac{\partial F_{s0}}{\partial u_\perp} + \frac{k_\parallel}{\omega} \left(v_{s\perp} \frac{\partial F_{s0}}{\partial u_\parallel} - v_{s\parallel} \frac{\partial F_{s0}}{\partial u_\perp} \right) \right) \boldsymbol{T_n} \Bigg]\,, \end{aligned} \tag{1.44}$$

where

$$\boldsymbol{T_n} = \begin{pmatrix} \frac{n^2 J_n^2}{\beta_s^2} & \frac{\mathrm{i} n J_n J_n'}{\beta_s} & \frac{n J_n^2 u_\parallel}{\beta_s u_\perp} \\ -\frac{\mathrm{i} n J_n J_n'}{\beta_s} & (J_n')^2 & -\frac{\mathrm{i} J_n J_n' u_\parallel}{u_\perp} \\ \frac{n J_n^2 u_\parallel}{\beta_s u_\perp} & \frac{\mathrm{i} J_n J_n' u_\parallel}{u_\perp} & \frac{J_n^2 u_\parallel^2}{u_\perp^2} \end{pmatrix}\,. \tag{1.45}$$

To make the formula as compact as possible, we introduced the unit vector $\hat{\boldsymbol{e}}_{\parallel} = (1, 0, 0)$ in cylindrical coordinates $(u_{\parallel}, u_{\perp}, \varphi)$ and the argument β_s of the Bessel functions of the first kind J_n and their derivatives J_n' was omitted. The denominator $\alpha_s + n$ reveals divergences encountered at cyclotron harmonics,

$$\omega - k_{\parallel} v_{\parallel} - \mathrm{sgn}(Z_s) \frac{n\Omega_s}{\gamma_s} = 0\,. \tag{1.46}$$

The integral over parallel momenta in Eq. 1.44 is to be taken along a deformed Landau contour that encircles the poles (Stix, 1992). To convert the integrands to the form which would be obtained through the Laplace transform, we can simply make the substitution $\omega_{\mathrm{r}} + \mathrm{i}\gamma_{\mathrm{L}} \to \mathrm{i}p$, where p represents a complex frequency and ω_{r} is the real frequency. The imaginary part of the frequency, γ_{L}, represents the growth or damping of the given wave mode. In later sections, the subscript r is dropped and the real frequency is denoted simply by ω.

Going back to the general form of the dispersion tensor from Eq. 1.23, we can write the linear dispersion relation (Eq. 1.25) as

$$\begin{vmatrix} \varepsilon_{xx} - \mu^2 \cos^2\theta_{\mathrm{k}} & \varepsilon_{xy} & \varepsilon_{xz} + \mu^2 \sin\theta_{\mathrm{k}} \cos\theta_{\mathrm{k}} \\ \varepsilon_{yx} & \varepsilon_{yy} - \mu^2 & \varepsilon_{yz} \\ \varepsilon_{zx} + \mu^2 \sin\theta_{\mathrm{k}} \cos\theta_{\mathrm{k}} & \varepsilon_{zy} & \varepsilon_{zz} - \mu^2 \sin\theta_{\mathrm{k}} \end{vmatrix} = 0\,. \tag{1.47}$$

Here we introduced the polar angle θ_{k} between the wave vector $\boldsymbol{k}$ and the ambient magnetic field $\boldsymbol{B}_0$. Due to the complicated form of the hot plasma dielectric tensor, the dispersion curves are usually obtained numerically or through analytical solutions of approximated forms of the dispersion relation.

1.1.4 Cold plasma approximation

In a typical magnetospheric plasma, the wave-particle resonances associated with thermal motion appear at velocities higher than the thermal velocity. The number of particles entering the resonance can be thus considered as relatively small, and the growth rate becomes negligible compared to the frequency, $|\gamma_{\mathrm{L}}| \ll |\omega|$ (here, ω represents the real part of frequency from Eq. 1.44). Taylor series expansion of the dispersion relation $\bar{D}(\boldsymbol{k}, \omega)$ to the first order can be broken down into real and imaginary parts (Gurnett and Bhattacharjee, 2017)

$$\bar{D}_{\mathrm{r}} = 0 \tag{1.48}$$

and

$$\gamma_{\mathrm{L}} = \frac{-\bar{D}_{\mathrm{i}}}{\partial \bar{D}_{\mathrm{r}} / \partial \omega}\,. \tag{1.49}$$

We will return to the imaginary part when discussing instabilities of specific wave modes in Section 1.1.6. The real part of the dispersion relation can be further simplified if we completely neglect the impact of resonant particles and replace the normalized distribution F_{s0} with a Dirac delta function,

$$F_{s0} = \frac{1}{2\pi u_{\perp}} \delta(u_{\perp}) \delta(u_{\parallel})\,. \tag{1.50}$$

This is called the cold plasma approximation. As a consequence of setting the temperature to zero, we cannot obtain any acoustic dispersion branches in this approximation (e.g. the ion-acoustic waves, abundant in solar wind plasma, Píša et al. (2021)), and wave modes associated with Doppler-shifted resonances also disappear. Any relativistic effects are naturally absent.

While it is in principle possible to insert the delta function into Eq. 1.44, a more direct approach starts from the equation of motion for particles experiencing the Lorentz force exerted by the perturbation fields $\boldsymbol{E}$, $\boldsymbol{B}$ and the background magnetic field $\boldsymbol{B}_0$. Treating the particle velocity $\boldsymbol{v_s}$ as a first-order perturbation, we may express the current as $\boldsymbol{J} = \sum_s n_{s0} Z_s e \boldsymbol{v_s}$ and use it to obtain the conductivity tensor. Following the treatment in Section 1.1.2, we arrive at the cold plasma dispersion relation

$$\bar{D}(\boldsymbol{\mu}, \omega) = \begin{vmatrix} S - \mu^2 \cos^2\theta_\mathrm{k} & -\mathrm{i}D & \mu^2 \sin\theta_\mathrm{k} \cos\theta_\mathrm{k} \\ \mathrm{i}D & S - \mu^2 & 0 \\ \mu^2 \sin\theta_\mathrm{k} \cos\theta_\mathrm{k} & 0 & P - \mu^2 \sin^2\theta_\mathrm{k} \end{vmatrix} = 0\,. \tag{1.51}$$

The terms S, D and P are called the Stix coefficients (Stix, 1992; Gurnett and Bhattacharjee, 2017), with definitions

$$S = \frac{1}{2}(R + L) = 1 - \sum_s \frac{\omega_{\mathrm{p}s}^2}{\omega^2 - \Omega_s^2}\,, \tag{1.52}$$

$$D = \frac{1}{2}(R - L) = \sum_s \frac{\mathrm{sgn}(Z_s)\Omega_s \omega_{\mathrm{p}s}^2}{\omega(\omega^2 - \Omega_s^2)}\,, \tag{1.53}$$

$$P = 1 - \sum_s \frac{\omega_{\mathrm{p}s}^2}{\omega^2}\,, \tag{1.54}$$

$$R = 1 - \sum_s \frac{\omega_{\mathrm{p}s}^2}{\omega(\omega + \mathrm{sgn}(Z_s)\Omega_s)}\,, \tag{1.55}$$

$$L = 1 - \sum_s \frac{\omega_{\mathrm{p}s}^2}{\omega(\omega - \mathrm{sgn}(Z_s)\Omega_s)}\,. \tag{1.56}$$

The dispersion relation can be reduced to a biquadratic equation in μ with solutions

$$\mu^2 = \frac{RL \sin^2\theta_\mathrm{k} + PS(1 + \cos^2\theta_\mathrm{k}) \pm \sqrt{(RL - PS)^2 \sin^4\theta_\mathrm{k} + 4P^2 D^2 \cos^2\theta_\mathrm{k}}}{2\left(S \sin^2\theta_\mathrm{k} + P\cos^2\theta_\mathrm{k}\right)}\,. \tag{1.57}$$

For each frequency and a given wave normal angle θ_k, there can be at most two cold plasma wave modes. In Figure 1.1, we show dispersion branches in a cold plasma with three ion species, protons, He^+ and O^+, with density ratios $n_\mathrm{O}/n_\mathrm{e} = 0.05$ and $n_\mathrm{He}/n_\mathrm{e} = 0.1$.

In the two sections below, we will summarize the properties of the two modes that play a prominent role in nonlinear wave-particle interactions in the Earth's outer radiation belt: the whistler-mode waves and the electromagnetic ion cyclotron (EMIC) waves.

Whistler mode waves

In the case of propagation parallel to the background magnetic field ($\theta_\mathrm{k} = 0$), the cold plasma dispersion relation for $P \neq 0$ has two roots, $\mu^2 = R$ and $\mu^2 = L$. These solutions correspond to right-hand and left-hand circularly polarized electromagnetic wave modes, respectively. The polarization, tied to the direction of $\boldsymbol{B}_0$, can be obtained by solving the homogeneous equation 1.24, converting $\boldsymbol{E}$ to $\boldsymbol{B}$ through Faraday's law, and looking at the ratio of the magnetic field components B_y/B_x. Magnetic field polarization is preferred because $\boldsymbol{B}$ rotates in the plane perpendicular to $\boldsymbol{k}$ (a direct consequence of Eq. 1.20). We will postpone the discussion of the left-handed mode to the next section and focus on the R-mode.

Looking at the definition of Stix coefficient R, or at the Figure 1.1a, we can see that the R-mode is evanescent between the electron resonance frequency Ω_e and the cutoff

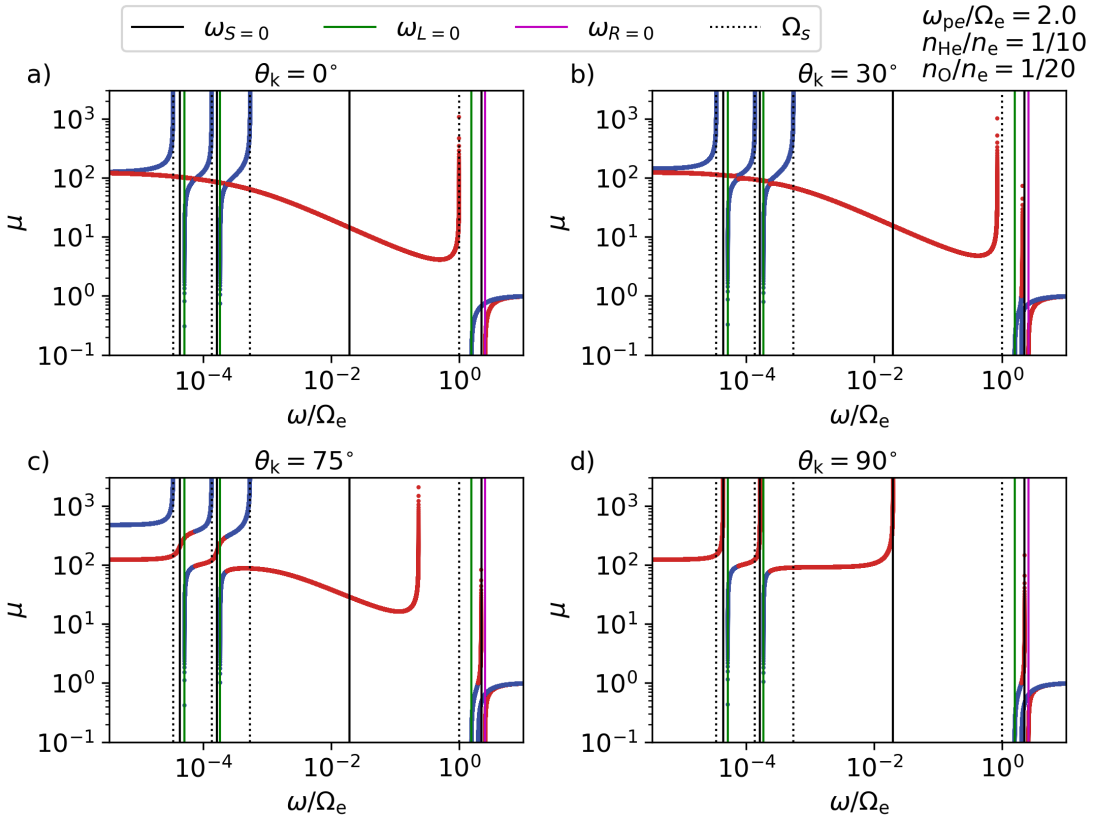

Figure 1.1: Dispersion branches of the cold plasma dispersion relation. Values of refractive index are plotted in red when the corresponding mode is left hand polarized, and in blue for left-handed waves. The hybrid resonance frequencies $\omega_{S=0}$ (upper hybrid, lower hybrid and ion hybrid, $\omega_{\rm uh} > \omega_{\rm lh} > \omega_{\rm ih}$) are represented by solid black vertical lines, and the cutoff frequencies $\omega_{L=0}$ and $\omega_{R=0}$ are plotted in green and magenta, respectively. Gyrofrequencies Ω_s of electrons and the three ions, H^+, He^+ and O^+, are shown as dotted lines. The wave normal angle used in refractive index calculations is printed at the top of each panel.

frequency $\omega_{R=0}$. The high-frequency branch represents the free space mode (also called the X-mode), and the lower frequency branch is called the whistler mode. Notice that when we follow the whistler branch to low frequencies, it crosses the L-mode branches, but it does not encounter any resonance or cutoff and converges to the fast Alfvén mode $\mu_{\rm A}^2 = 1 + \sum_s \omega_{{\rm p}s}^2/\Omega_s^2$ for $\omega \to 0$. However, most of the whistler-mode emissions important for the dynamics of radiation belts occur at frequencies $\omega \gg \Omega_{\rm p}$. Under such conditions, we can neglect the motion of ions and obtain the simplified refractive index formula

$$\mu^2 = 1 + \frac{\omega_{\rm pe}^2}{\omega(\Omega_{\rm e} - \omega)}\,. \tag{1.58}$$

In studies of the inner magnetosphere, we can often apply the high density approximation $(\Omega_{\rm e}/\omega_{\rm pe})^2 \to 0$ and erase the 1 at the right-hand side of Eq. 1.58. A quick calculation reveals that μ has its minimum at $\omega = 0.5\Omega_{\rm e}$, which corresponds to the maximum of the phase velocity. The group velocity

$$\frac{V_{\rm g}}{c} = \frac{2(\Omega_{\rm e} - \omega)^{3/2}(\omega^2(\Omega_{\rm e} - \omega) + \omega\omega_{\rm pe}^2)^{1/2}}{2\omega(\Omega_{\rm e} - \omega)^2 + \Omega_{\rm e}\omega_{\rm pe}^2} \overset{\omega_{\rm pe}^2 \gg \Omega_{\rm e}^2}{\approx} \frac{2(\Omega_{\rm e} - \omega)^{3/2}\omega^{1/2}}{\Omega_{\rm e}\omega_{\rm pe}} \tag{1.59}$$

attains its maximum at $\omega = 0.25\Omega_{\rm e}$ in the high-density approximation. The approximate formulas also reveal that $V_{\rm p} = V_{\rm g}$ at $\omega = 0.5\Omega_{\rm e}$.

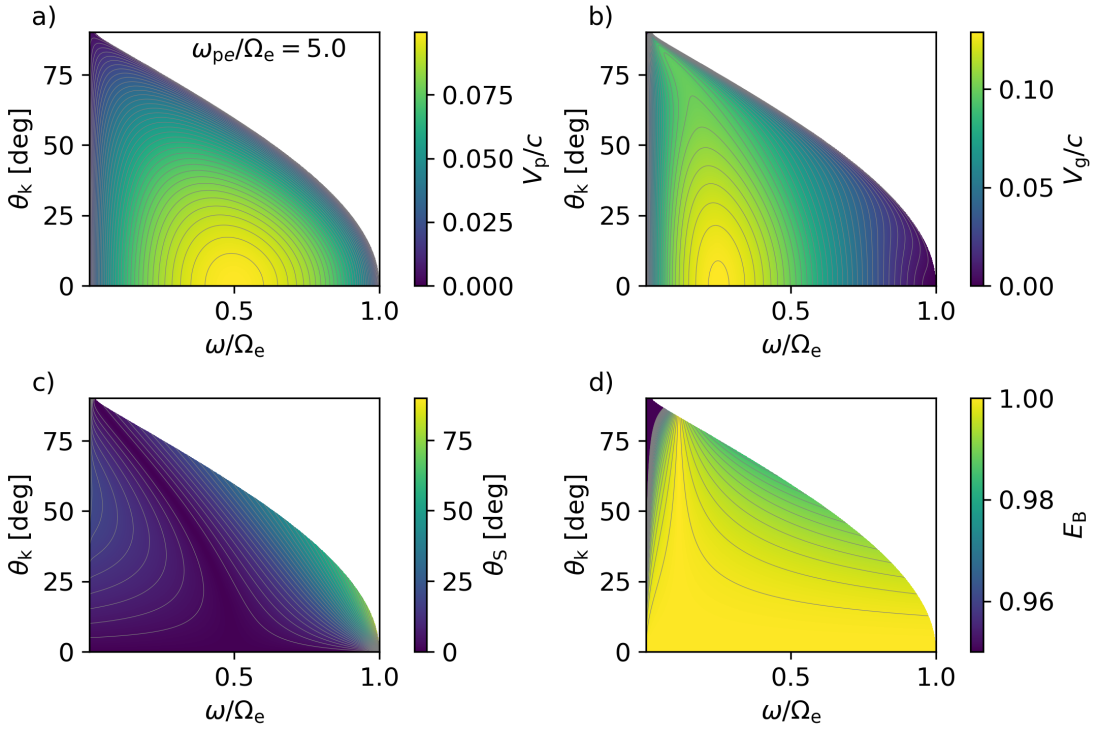

Figure 1.2: Propagation properties of whistler-mode waves in the frequency range $\Omega_p < \omega < \Omega_e$. The plasma-to-cyclotron frequency ratio is set to $\omega_{pe}/\Omega_e = 5.0$, and the effect of heavier ions is negligible.

Dispersive properties of oblique whistler-mode waves are harder to analyze in full generality because the whistler branch connects to the L-mode below Ω_p and stops at the $\omega_{L=0}$ cutoff (see Fig. 1.1b,c). For simplicity, we will apply the immobile ion assumption and high-density approximation directly to the full dispersion relation in Equation 1.51. Only the whistler mode can exist in the range of frequencies $\Omega_p^2 < \omega^2 < \Omega_e^2$, and its refractive index is

$$\mu^2 \approx \frac{\omega_{pe}^2}{\omega(\Omega_e \cos\theta_k - \omega)} \,. \tag{1.60}$$

We can see that the waves cannot exist at wave normal angles larger than the resonance cone angle $\theta_{res} = \arccos(\omega/\Omega_e)$. However, as shown in Figure 1.1d, a perpendicular whistler-mode branch exists below the lower hybrid frequency ω_{lh} when ion motions are included. This means that as the waves propagate from higher to lower altitudes and ω/Ω_e decreases, the wave normal angle can go through $\theta_k = 90°$. This results in reflection of the wave packet, because the parallel component of the group velocity always has the same sign as the parallel component of the wave vector (a consequence of Equations 1.20 and 1.30 for $\boldsymbol{T} = 0$).

Starting from Equation 1.60, it can be shown that the group velocity of oblique whistler waves points along the field line as long as

$$\theta_k = \theta_G \equiv \arccos\left(\frac{2\omega}{\Omega_e}\right) \,. \tag{1.61}$$

Here, θ_G is the Gendrin angle (Gendrin, 1961), which will appear again when discussing the detailed properties of the chorus emission in Section 3.1. The angle θ_G is defined as a nonzero wave normal angle for which the waves satisfy the condition $\boldsymbol{V}_g \parallel \boldsymbol{B}_0$. Another intriguing property of the Gendrin angle is that the phase velocity as a function of frequency maximizes at $\theta_k = \theta_G$.

A numerical solution of the cold plasma dispersion in the frequency range $\Omega_\mathrm{p} < \omega < \Omega_\mathrm{e}$ reveals additional interesting properties of the oblique whistler mode. In Figure 1.2, we plot the $(\omega, \theta_\mathrm{k})$ dependence of the phase velocity V_p, group velocity V_g, polar angle $\theta_\mathrm{S} = \angle(\boldsymbol{V}_\mathrm{g}, \boldsymbol{B}_0)$ and magnetic field ellipticity E_B (see Section 1.2.2 for the definition of ellipticity). Small deviations from parallel direction have a negligible effect on the phase velocity and the group velocity, but both quantities start to quickly decrease as θ_k approaches the resonance cone. The $\theta_\mathrm{S} = 0$ valley in Figure 1.2c represents the Gendrin angle, which very closely follows the approximate formula 1.61. The ellipticity plot shows that oblique whistler modes are nearly circularly polarized for all wave normal angles, except near the lower hybrid frequency. However, this is not true for the electric field ellipticity (not shown), which converges to zero as θ_k approaches the resonance cone.

EMIC waves

Other modes of cold plasma waves that take part in the acceleration of radiation belt particles are the electromagnetic ion cyclotron modes, often abbreviated as EMIC. In the parallel approximation, they are represented by the $\mu^2 = L$ dispersion branches located between ion gyrofrequencies. Their dispersive properties are strongly dependent on the ion composition and ion density ratios. In Figure 1.1c we can see that the proton cyclotron mode has a left-handed polarization near the $\omega = \Omega_\mathrm{p}$ resonance, then experiences a polarization reversal at the crossover frequency $\omega_{D=0}$ and continues to lower frequencies as a right-handed mode. With multiple heavier ions, additional $\omega_{L=0}$ cutoffs appear, and the proton branch stops at an ion-ion cutoff located between the gyrofrequencies of the second and the third lightest ion (we always assume once-ionized atoms). The EMIC wave associated with the heaviest ion, i.e. oxygen O^+ in Figure 1.1, is always left-hand polarized.

Due to the presence of multiple cyclotron resonances, finding a suitable approximation for the refractive index of EMIC waves is more complicated than in the case of whistler mode waves. We can always safely assume $\omega \ll \Omega_\mathrm{e}$, and then we get

$$\mu^2 = 1 + \sum_i \frac{\omega_{\mathrm{p}i}^2}{\omega(\Omega_i - \omega)} - \frac{\omega_\mathrm{pe}^2}{\omega\Omega_\mathrm{e}} \tag{1.62}$$

for the parallel L-mode; the index i now runs only over the ion species. The refractive index converges to the shear Alfvén mode at low frequencies (Gurnett and Bhattacharjee (2017), chapter 6.5). The group velocity is expressed as

$$\frac{V_\mathrm{g}}{c} = \frac{\left(1 - \dfrac{\omega_\mathrm{pe}^2}{\omega\Omega_\mathrm{e}} + \sum\limits_i \dfrac{\omega_{\mathrm{p}i}^2}{\omega(\Omega_i - \omega)}\right)^2}{1 - \dfrac{\omega_\mathrm{pe}^2}{2\omega\Omega_\mathrm{e}} + \sum\limits_i \dfrac{\Omega_i \omega_{\mathrm{p}i}^2}{2(\Omega_i - \omega)^2}}, \tag{1.63}$$

which reduces to a more straightforward form in a high-density proton-electron plasma:

$$\frac{V_\mathrm{g}}{c} \approx \frac{(\Omega_\mathrm{p} - \omega)^{3/2}}{\mathcal{M}\Omega_\mathrm{p}^{1/2}\omega_\mathrm{pe}\left(1 - \dfrac{\omega}{2\Omega_\mathrm{p}}\right)}, \tag{1.64}$$

where $\mathcal{M} = (m_\mathrm{e}/m_\mathrm{p})^{1/2}$. The phase velocity can be written as

$$\frac{V_\mathrm{p}}{c} \approx \frac{\Omega_\mathrm{p}^{1/2}(\Omega_\mathrm{p} - \omega)^{1/2}}{\mathcal{M}\omega_\mathrm{pe}} \tag{1.65}$$

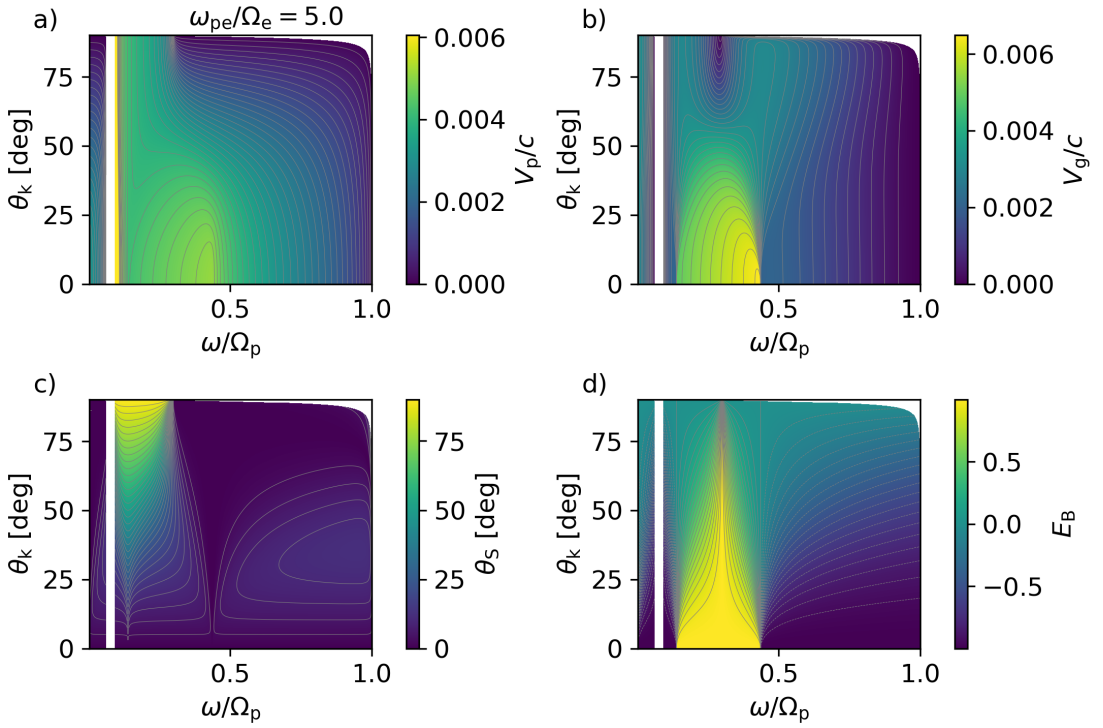

Figure 1.3: Propagation properties of two EMIC modes with dispersion branches starting at Ω_p and Ω_O. Relative ion densities are the same as in Figure 1.1, and $\omega_{pe}/\Omega_e = 5.0$. Panels copy the format of Figure 1.2.

under the same approximation and is strictly smaller than V_g for all nonzero frequencies. Unlike in the whistler-mode case, there is no simple formula for the resonance cone. Moreover, the results obtained for a one-component plasma have very little use in magnetospheric physics due to the ubiquitous presence of helium ions (Lee and Angelopoulos, 2014). The dispersive properties of EMIC change drastically at the crossover frequency $\omega_{D=0} > \Omega_{He}$ and the waves are strongly damped near Ω_p, leaving a relatively narrow range of frequencies where the approximate formulas can be used.

Wave propagation properties of two EMIC modes are plotted in Figure 1.3 as a function of ω and θ_k. The oblique proton cyclotron wave is coupled to the whistler (fast magnetosonic) wave and then to the helium wave, creating one branch with two polarization reversals, as shown in Figure 1.3d. The second plotted branch is the oxygen cyclotron wave, visible near the left boundary of each panel. The mode which exhibits helium-magnetosonic coupling is not shown due to the frequency overlap. Both plotted modes have very large resonance cone angles, allowing the EMIC wave to become highly oblique at all frequencies. The group velocity of the right-handed wave is much larger than that of the left-handed wave, as long as we assume a quasiparallel propagation. However, at very high θ_k, the right-handed wave experiences a major decrease in V_g at the proton-helium hybrid frequency $\omega_{S=0}$ ($\sim 0.3\Omega_p$ with our parameter choice). As with the whistler mode, the hybrid frequency marks the point where the resonance cone reaches 90°. At the same frequency, the direction of the Poynting vector of highly oblique waves switches from parallel to nearly perpendicular; above $\omega_{S=0}$, the wave packet propagates parallel to the local field line across all θ_k (Fig. 1.3c). Exactly at the hybrid frequency, the magnetic field ellipticity stays near +1 across all wave normal angles up to the resonance cone (Fig. 1.3d). There is no Gendrin angle analogy for the coupled proton branch or any other EMIC modes.

The striking difference between the multi-ion dispersion branches and the whistler

branch causes difficulties in the modelling of EMIC propagation and wave-particle resonances. These dispersive properties reflect on theories that attempt to explain the growth of discrete elements in EMIC spectra through nonlinear interaction, finding less success than in the case of whistler-mode chorus. See Section 3.4 for additional discussion.

1.1.5 Ray approximation of wave propagation

In many magnetospheric applications of the plasma wave theory, the wavelength stays much smaller than the characteristic spatial scale of irregularities of the plasma medium, and the wave period is typically much smaller than characteristic timescales of variations in the plasma. In such cases, wave propagation can be studied within the ray approximation of geometric optics (Bernstein, 1975; Suchy, 1981). Specifically, for a plane wave propagating through an inhomogeneous, nonstationary medium, we require that

$$\left|\frac{\partial E_0}{\partial r_i}\right| \ll \left|\frac{\partial S}{\partial r_i}\right| , \tag{1.66}$$

$$\left|\frac{\partial E_0}{\partial t}\right| \ll \left|\frac{\partial S}{\partial t}\right| . \tag{1.67}$$

For electromagnetic waves, the same conditions must hold for the amplitude of the magnetic field. The amplitudes are taken as real functions here, and the eikonal function S captures the fast variation of the phase,

$$\boldsymbol{E}(\boldsymbol{r},t) = \boldsymbol{E}_0(\boldsymbol{k},\omega;\boldsymbol{r},t)\mathrm{e}^{\mathrm{i}(\boldsymbol{k}\cdot\boldsymbol{r}-\omega t)} \equiv \boldsymbol{E}_0(\boldsymbol{k},\omega;\boldsymbol{r},t)\mathrm{e}^{\mathrm{i}S(\boldsymbol{r},t)} . \tag{1.68}$$

$\boldsymbol{E}_0$ is a complex amplitude function in $\boldsymbol{k}$-space that expresses the dependence of field components on $\boldsymbol{k}$ and ω (i.e. it carries the dispersive properties). The wave vector and frequency, which are related to the eikonal through

$$\frac{\partial S}{\partial \boldsymbol{r}} = \mathrm{i}\boldsymbol{k} , \tag{1.69}$$

$$\frac{\partial S}{\partial t} = -\mathrm{i}\omega , \tag{1.70}$$

are assumed to be slowly varying in space and time.

The dispersion equation (Eq. 1.24), which was stated for a homogeneous, stationary medium, can now be written as

$$\mathcal{D}\left(\frac{\partial S}{\partial \boldsymbol{r}}, \frac{\partial S}{\partial t}; \boldsymbol{r}, t\right) \cdot \boldsymbol{E} = 0 . \tag{1.71}$$

The dispersion relation represents the solvability condition for the dispersion equation, and it can be restated in the form

$$-\frac{\partial S}{\partial t} = H\left(\frac{\partial S}{\partial \boldsymbol{r}}, \boldsymbol{r}, t\right) . \tag{1.72}$$

This is the Hamilton-Jacobi equation of geometric optics, with H in units of frequency. It has been shown (Horne, 1989; Maxworth and Gołkowski, 2017) that for the purpose of wave propagation studies in the magnetosphere, it is sufficient to use the real form of the dispersion relation with the cold plasma approximation. The Hamilton canonical equations for a stationary medium, also called the ray tracing equations in this context, can be written as (see Budden (1985) for the relationship between H and $\bar{D}$)

$$\frac{\mathrm{d}\boldsymbol{r}}{\mathrm{d}t} = -\frac{\partial \bar{D}}{\partial \boldsymbol{k}}\left(\frac{\partial \bar{D}}{\partial \omega}\right)^{-1} = \boldsymbol{V}_\mathrm{g} , \tag{1.73}$$

$$\frac{\mathrm{d}\boldsymbol{k}}{\mathrm{d}t} = \frac{\partial \bar{D}}{\partial \boldsymbol{r}} \left(\frac{\partial \bar{D}}{\partial \omega} \right)^{-1} = -\frac{\partial \omega}{\partial \boldsymbol{r}} \,. \tag{1.74}$$

Hanzelka and Santolík (2019) kept the full hot plasma dispersion relation in their ray-tracing code (using the real Hamilton equations for media with moderate absorption as derived by Suchy (1981)) but did not observe any significant changes to whistler-mode wave trajectories compared to the ideal cold plasma dispersion. Maxworth and Gołkowski (2017) used finite temperatures to describe the cold plasma distribution and discussed the effect of temperature on the reflection points of whistler waves near the lower hybrid frequency, confirming that the impact of warm or hot plasma on the ray tracing results is negligible. The variation of amplitude can be obtained by applying the linear growth factor (Eq. 1.49) along precalculated trajectories. In the case of field-aligned propagation, the convergence of field lines will increase the wave energy density; to capture this effect, multiple rays starting near the field line must be traced.

An important mode of whistler wave propagation is ducting inside density enhancements. It is hypothesized that the cold plasma in the inner magnetosphere is filamented (Bell et al., 2009) and thus can guide the waves from the equatorial plane to higher latitudes without significant attenuation. To analyze two-dimensional ducted propagation in a dipole magnetic field, the equations 1.73 and 1.74 must be solved for functions of density $n_\mathrm{e}(x, z)$ and magnetic field $\boldsymbol{B}_0(x, z)$. However, with suitable approximations, the basic principles can be explained in a homogeneous field case. Let us assume the simplified dispersion 1.60, $\boldsymbol{B}_0$ directed along the z-axis and electron density n_e dependent on the x-coordinate only. The nonzero derivatives of the dispersion relation

$$\bar{D}(k, \omega) = 1 - \frac{c^2 k^2}{\omega^2} + \frac{\omega_\mathrm{pe}^2}{\omega(\Omega_\mathrm{e} - \omega)} \tag{1.75}$$

are found to be

$$\frac{\partial \bar{D}}{\partial c k_z} = -\frac{\omega_\mathrm{pe}(\Omega_\mathrm{e} + (\Omega_\mathrm{e} \cos\theta_\mathrm{k} - 2\omega)\cos\theta_\mathrm{k})}{\omega^{3/2}(\Omega_\mathrm{e}\cos\theta_\mathrm{k} - \omega)^{3/2}} \,, \tag{1.76}$$

$$\frac{\partial \bar{D}}{\partial c k_x} = -\frac{\omega_\mathrm{pe}(\Omega_\mathrm{e} \cos\theta_\mathrm{k} - 2\omega)\sin\theta_\mathrm{k}}{\omega^{3/2}(\Omega_\mathrm{e}\cos\theta_\mathrm{k} - \omega)^{3/2}} \,, \tag{1.77}$$

$$\frac{\partial \bar{D}}{\partial x} = \frac{1}{n_\mathrm{e}} \frac{\partial n_\mathrm{e}}{\partial x} \frac{\omega_\mathrm{pe}^2}{\omega(\Omega_\mathrm{e}\cos\theta_\mathrm{k} - \omega)} \,, \tag{1.78}$$

$$\frac{\partial \bar{D}}{\partial \omega} = \frac{\omega_\mathrm{pe}^2 \Omega_\mathrm{e} \cos\theta_k}{\omega^2(\Omega_\mathrm{e}\cos\theta_\mathrm{k} - \omega)^2} \,. \tag{1.79}$$

By introducing the small-angle approximation $\sin\theta_\mathrm{k} \approx \theta_\mathrm{k}$, $\cos\theta_\mathrm{k} \approx 1$, we get $k_z \approx$ const., $V_{\mathrm{g}z} \approx$ const., reducing the system to one dimension. The problem can be further simplified by using a parabolic density profile

$$n_\mathrm{e}(x) = n_\mathrm{e0} \left(1 + s_\mathrm{duct} \frac{x^2}{w^2} \right) \,, \tag{1.80}$$

where $s_\mathrm{duct} = -1$ stands for a density enhancement, $s_\mathrm{duct} = 1$ models a density depletion, and w represents a characteristic width of the duct. Finally, the ray evolution in the (x, k_x) space reduces to an elliptical/hyperbolic motion,

$$\frac{\mathrm{d}(ck_x)}{\mathrm{d}(x/w)} = -s_\mathrm{duct} R_\mathrm{yx}^2 \frac{x/w}{ck_x} \,, \quad R_\mathrm{yx}^2 = \frac{2\omega\omega_\mathrm{p0}^2}{2\omega - \Omega_\mathrm{e}} \,, \tag{1.81}$$

where we used an additional simplification $(x/w)^2 \ll 1$ and denoted the plasma frequency at $x = 0$ as ω_p0. Whether the ray will be guided depends on the sign of $2\omega - \Omega_\mathrm{e}$ and s_duct. Table 1.1 summarizes the four possible combinations.

Table 1.1: Classification of whistler mode ducting in field-aligned density inhomogeneities.

	Upper band $\omega > \Omega_e/2$	Lower band $\omega < \Omega_e/2$
Density depletion	ducting	no ducting
Density enhancement	no ducting	ducting

Recalling the group velocity definition from Eq. 1.73 and combining it with the ducted propagation described by Eq. 1.81 above, we can show that $x(t)$ behaves like a harmonic oscillator. The oscillation frequency is found to be

$$\frac{\Omega_{HO}}{\omega} = \frac{c\Omega_e^{-1}}{w} \frac{\left(1 - \frac{\omega}{\Omega_e}\right)\left(2s_{duct}\left(\frac{2\omega}{\Omega_e} - 1\right)\right)^{1/2}}{\left(\frac{\omega^2}{\Omega_e^2}\left(1 - \frac{\omega}{\Omega_e}\right) + \frac{\omega\omega_{pe}^2}{\Omega_e^3}\right)^{1/2}}. \tag{1.82}$$

For example, a whistler-wave ray with frequency $\omega = 0.25\Omega_e$ in a plasma with $\omega_{p0} = 5\Omega_{e0}$ and a magnetic field $B_0 = 300\,\mathrm{nT}$ will oscillate in a 100 km wide duct ($w = 50\,\mathrm{km}$) with frequency $\Omega_{HO} = 1.1 \cdot 10^{-2}\,\omega$. In this case, approximately 50 wavelengths will fit between two crossing of $x = 0$.

In a typical magnetospheric environment, the wave is also affected by the radial gradient of the magnetic field, which can be approximated as $-3/(R_E L_0)$ near the magnetic equatorial plane (L_0 is the L-shell at $x = 0$). For the small oscillations discussed above, the gradient force shifts the centre of the harmonic motion from $x_0/w = 0$ to

$$\frac{x_0}{w} = -\frac{3\Omega_e w}{2s_{duct}(\Omega_e - \omega)R_E L_0}. \tag{1.83}$$

For larger angles, the division between lower and upper frequency band is determined by $2\omega - \Omega_e \cos\theta_k$ and the oscillations become anharmonic. The curvature of the magnetic field further enhances the amplitude of oscillations and increases the probability of rays escaping from the duct. See Figure 1.4 or the ray-tracing study of Hanzelka and Santolík (2019) for more on this topic.

In cases where the density gradient $\partial n_e/\partial x$ becomes large, the approximation of geometric optics fails, and full-wave simulations must be employed to faithfully capture the flux of wave energy. For more information on the limitations of ray tracing, see the discussion of ray tracing applications in Hanzelka et al. (2017) and Chen et al. (2017), and the full-wave simulations of Streltsov et al. (2012) and Shklyar and Prokhorenko (2020).

1.1.6 Instabilities and linear wave growth

Bump-on-tail instability and Landau damping

One of the most studied linear instabilities of plasma waves is arguably the bump-on-tail instability, which is associated with the collisionless Landau damping (Landau, 1946; Dawson, 1961; Sazhin, 1991). While our primary focus is on parallel whistler waves, which do not experience this type of instability, the Landau damping acts as the main source of attenuation of oblique whistler-mode waves, which is the effect that allows us to limit our theoretical investigations to parallel propagation.

As mentioned in the paragraph after Equation 1.45, the rigorous approach to hot plasma dispersion starts with the (one-sided) Laplace transform of the Vlasov equation in time, changing the task to an initial value problem with a disturbance imposed at

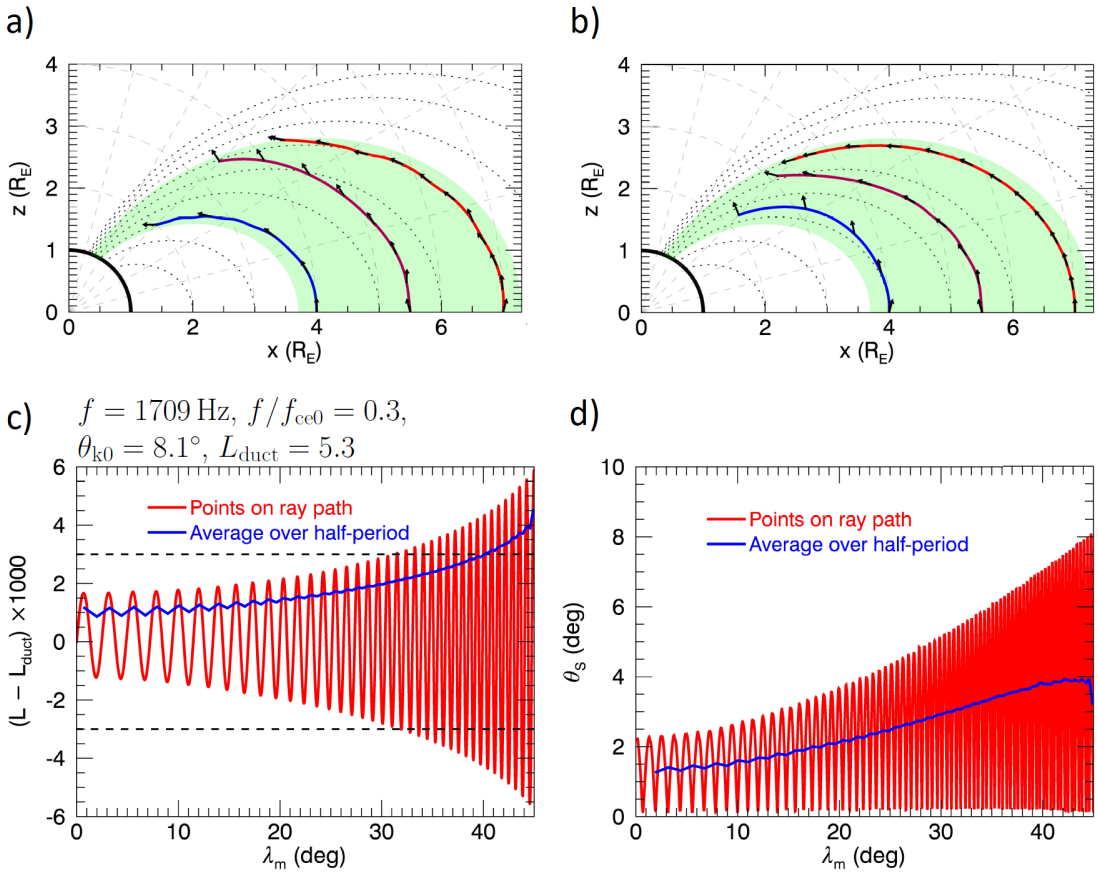

Figure 1.4: Examples of ray propagation in the inner magnetosphere. a) Guided propagation in a duct modelled by a Gaussian with standard deviation $\sigma = 96\,\mathrm{km}$ and peak density 6 % above the background. Black arrows represent the wave vectors. L-shells are denoted by dotted black lines; limiting L-shells of the density model enclose the light-green area. Initial parameters of the color-coded ray trajectories are $L = 4.0$, $\theta_\mathrm{k} = 0°$ (blue); $L = 5.5$, $\theta_\mathrm{k} = -15°$ (purple); $L = 7.0$, $\theta_\mathrm{k} = 15°$ (red). Wave frequency is always $f = 0.3 f_\mathrm{ce0}$. b) Same as plot a), but with $\sigma = 48\,\mathrm{km}$, $\delta n = 0.05$, and the initial ray parameters are $L = 4.0$, $\theta_\mathrm{k} = 15°$ (blue); $L = 5.5$, $\theta_\mathrm{k} = -15°$ (purple); $L = 7.0$, $\theta_\mathrm{k} = 0°$ (red). c) Oscillation about the ray path. Duct parameters: $\sigma = 20\,\mathrm{km}$, $\delta n = 0.06$. d) Oscillations of the Poynting vector. Panels a) and b) are adapted from Hanzelka and Santolík (2019), where more details about the models can be found.

$t = 0$. The evolution of electromagnetic perturbations is obtained through an inverse transform of the Laplace-transformed fields, in which the integrand features one or multiple poles associated with wave-particle resonances. For the simple case of an electrostatic wave in a one-component unmagnetized plasma, the electric potential is given as (Gurnett and Bhattacharjee (2017); note that in space physics, the term *electrostatic* commonly refers to waves whose magnetic field can be removed by Lorentz transform)

$$\Phi(k,t) = \frac{1}{2\pi\mathrm{i}} \int_{\sigma-\mathrm{i}\infty}^{\sigma+\mathrm{i}\infty} \Phi(k,p)\mathrm{e}^{pt}\mathrm{d}p\,, \tag{1.84}$$

$$\Phi(k,p) = \frac{\mathrm{i}\dfrac{en_\mathrm{e}}{\varepsilon_0 k^3}\displaystyle\int_{-\infty}^{\infty} \frac{F_0(0)}{v_z - \mathrm{i}p/k}\mathrm{d}v_z}{1 - \dfrac{\omega_\mathrm{p}^2}{k^2}\displaystyle\int_{-\infty}^{\infty} \frac{\partial F_0/\partial v_z}{v_z - \mathrm{i}p/k}\mathrm{d}v_z}\,, \tag{1.85}$$

where $p = \gamma_\mathrm{L} - \mathrm{i}\omega$ is the complex frequency, and σ is a real number. In order to use the residue theorem in the calculation of the inverse, $\Phi(k,p)$ must be holomorphic

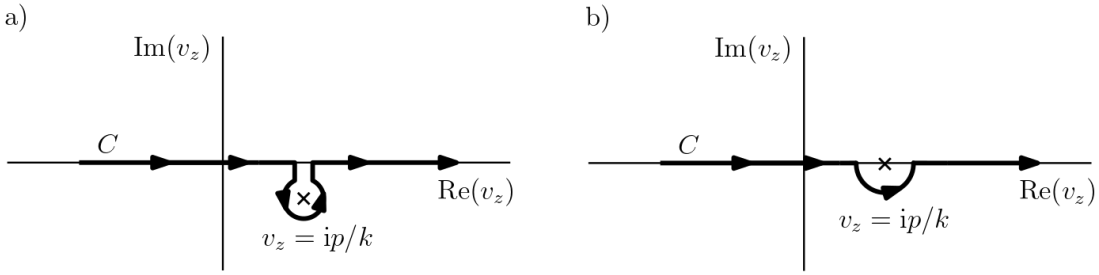

Figure 1.5: a) Integration contour used to obtain the residue from Equation 1.86. The contour is closed by a large half-circle with radius $R \to \infty$. b) Integration contour employed in the weak-growth approximation.

everywhere except for a finite number of points. Discontinuities in the numerator and denominator at $\mathrm{Re}(p) = 0$, which pose a problem for the analytic continuation of $\Phi(k,p)$ to the left half-plane, are resolved by distorting the integration contour around the $v_z = \mathrm{i}p/k$ poles. For $k > 0$, $\mathrm{Re}(p) < 0$, the denominator, which represents the dispersion relation, takes the form

$$\bar{D}(k,p) = 1 - \frac{\omega_\mathrm{p}^2}{k^2}\int_{-\infty}^{\infty}\frac{\partial F_0/\partial v_z}{v_z - \mathrm{i}p/k}\mathrm{d}v_z - 2\pi\mathrm{i}\frac{k}{|k|}\frac{\omega_\mathrm{p}^2}{k^2}\left.\frac{\partial F_0}{\partial v_z}\right|_{v_z=\mathrm{i}p/k} \tag{1.86}$$

The integration contour for this case is depicted in Figure 1.5a.

Under the weak growth rate approximation (Equations 1.48 and 1.49), we take the $\gamma_\mathrm{L} \to 0$ limit of $\bar{D}(k,p)$, which effectively leads to taking only half of the residue of the $v_z = \omega/k$ pole, see Figure 1.5b. The real and imaginary parts of the dispersion relation now read (p.v. stands for *principal value*)

$$\bar{D}_\mathrm{r}(\omega,k) = 1 - \frac{\omega_\mathrm{p}^2}{k^2}\mathrm{p.v.}\int_{-\infty}^{\infty}\frac{\partial F_0/\partial v_z}{v_z - \omega/k}\mathrm{d}v_z\,, \tag{1.87}$$

$$\bar{D}_\mathrm{i}(\omega,k) = -\pi\frac{k}{|k|}\frac{\omega_\mathrm{p}^2}{k^2}\left.\frac{\partial F_0}{\partial v_z}\right|_{v_z=\omega/k}\,, \tag{1.88}$$

leading us to the linear growth coefficient

$$\gamma_\mathrm{L} = \pi\frac{k}{|k|}\frac{\omega_\mathrm{p}^2}{k^2}\left(\frac{\partial\bar{D}}{\partial\omega}\right)^{-1}\left.\frac{\partial F_0}{\partial v_z}\right|_{v_z=\omega/k}\,. \tag{1.89}$$

The expressions in Equations 1.87 and 1.88 are a manifestations of Kramers-Kronig relations for the susceptibility of hot unmagnetized plasmas (Ichimaru, 2004).

We must note here that while the derivation of Landau damping from electrostatic potential gives a correct formula for the damping rate, it also leads to an erroneous belief that the damping comes from the transfer of electrostatic wave energy to particle kinetic energy. A careful analysis based on the law of energy conservation reveals that both electrostatic and compressional components must contribute to the energy balance (Swanson, 2003). Landau damping can also arise in neutral gas, where it becomes clear that the true physical picture of Landau damping does not include charges or electrostatic energy Stubbe and Sukhorukov (1999). We keep the electrostatic picture here because it is the most common approach in plasma wave literature and because it bears a close connection to the concept of *nonlinear* Landau damping in plasmas – see Section 2.1 for additional details.

As an example, the dispersion relation of the Langmuir wave in a high-velocity approximation takes the form (see also Section 2.1)

$$\bar{D}_\mathrm{r}(\omega,k) = 1 - \frac{\omega_\mathrm{p}^2}{\omega^2}\left(1 + 3\frac{k^2}{\omega^2}\langle v_z^2\rangle\right)\,. \tag{1.90}$$

To calculate the frequency derivative, we can ignore the temperature dependence introduced through $\langle v_z^2 \rangle$, and obtain the linear growth rate

$$\gamma_{\mathrm{L}} = \frac{\pi}{2} \frac{k}{|k|} \frac{\omega_{\mathrm{p}}^3}{k^2} \left. \frac{\partial F_0}{\partial v_z} \right|_{v_z = \omega/k} . \tag{1.91}$$

Notice that the sign of γ_{L} is connected with the gradient of F_0. A symmetric distribution that decreases monotonically for $v_z > 0$ will thus always cause damping of electrostatic waves in an unmagnetized plasma. On the other hand, a bump near the phase velocity changes the sign of the gradient and becomes a source for wave growth.

Landau damping affects oblique whistler waves, but it is not possible to derive a simple algebraic formula for the growth rate without resorting to substantial approximations. The refractive index is taken in the high-density approximation, Eq. 1.60, and the dielectric tensor (Eq. 1.44) is simplified by assuming a bi-Maxwellian distribution

$$F_0(v_\parallel, v_\perp) = \frac{1}{(2\pi)^{3/2} \sigma_\perp^2 \sigma_\parallel} \exp\left(\frac{-v_\parallel^2}{2\sigma_\parallel^2}\right) \exp\left(\frac{-v_\perp^2}{2\sigma_\perp^2}\right) \tag{1.92}$$

within a low-temperature limit $c^2 \gg (\omega/k)^2 \gg \sigma_\parallel^2$. The characteristic velocities $\sigma_\parallel$, $\sigma_\perp$ are an anisotropic generalization of the thermal speed from Equation 1.13. Following Sazhin (1993), we can show that the Landau resonant particles cause attenuation of oblique whistlers with a growth factor

$$\gamma_{\mathrm{L0}} = -\frac{\sqrt{\pi} c^3 \Omega_{\mathrm{e}} \sin^2\theta_{\mathrm{k}} \exp\left(-c^2/(2\mu^2\sigma_\parallel^2)\right)}{2^{3/2} \mu^3 \sigma_\parallel^3 \cos^4\theta_{\mathrm{k}}} . \tag{1.93}$$

In the $\cos\theta_{\mathrm{k}} \approx 1$ approximation used to derive the oscillations of ducted whistler waves (see Eq. 1.82), this damping effect can be neglected.

At higher wave normal angles, γ_{L0} starts to compete with the cyclotron damping and anisotropy-driven instability (γ_{L1}) described in the next section. For a distribution with arbitrary temperature, the oscillatory properties of Bessel functions must be considered, and the damping becomes dependent on perpendicular velocities of the resonant particle population (Stix, 1992).

Cyclotron damping and anisotropy-driven instability

The hot plasma dispersion relation from Equation 1.47 simplifies considerably when we restrict our analysis to the parallel propagation of circularly polarized electromagnetic modes. In the Fourier transform notation, we get (Gurnett and Bhattacharjee, 2017)

$$\begin{aligned} \bar{D}(k,\omega) = 1 - \frac{c^2 k_\parallel^2}{\omega^2} - \sum_s \frac{\omega_{\mathrm{p}s}}{\omega} \times \\ \times \int_{-\infty}^{\infty} \int_0^{\infty} \frac{\dfrac{\partial F_{s0}}{\partial u_\perp} + \dfrac{k_\parallel}{\gamma\omega}\left(u_\perp \dfrac{\partial F_{s0}}{\partial u_\parallel} - u_\parallel \dfrac{\partial F_{s0}}{\partial u_\perp}\right)}{k_\parallel u_\parallel - \omega \pm \mathrm{sgn}(Z_s)\Omega_s} \pi u_\perp^2 \,\mathrm{d}u_\perp \mathrm{d}u_\parallel = 0 . \end{aligned} \tag{1.94}$$

Let us now focus on the whistler mode (+ sign in the denominator) in the weak growth approximation. In most magnetospheric applications, we may assume that the electron distribution comprises a cold core f_{c} with density n_{e} and a hot population f_{h} with density $n_{\mathrm{he}} \ll n_{\mathrm{e}}$. Under such conditions, the real part of the dispersion relation is

well-approximated by the cold plasma theory. The linear growth rate is then given by the formula (Xiao et al., 1998)

$$\gamma_{\mathrm{L}} = \frac{\pi\omega_{\mathrm{pe}}^2\mathcal{R}}{2\omega + \dfrac{\omega_{\mathrm{pe}}^2\Omega_{\mathrm{e}}}{(\omega-\Omega_{\mathrm{e}})^2}}(A - A_{\mathrm{m}})\,, \tag{1.95}$$

where we have introduced the fraction of resonant electrons

$$\mathcal{R} = \pi\frac{n_{\mathrm{he}}}{n_{\mathrm{e}}}\frac{\omega-\Omega_{\mathrm{e}}}{k_\parallel}\int_0^\infty \frac{u_\perp^2\,\mathrm{d}u_\perp}{1-\dfrac{\omega U_{\mathrm{R}}}{c^2k_\parallel\gamma_{\mathrm{R}}}}\left.\frac{\partial F_{\mathrm{h}}}{\partial u_\perp}\right|_{u_\parallel=U_{\mathrm{R}}} \tag{1.96}$$

and the relativistic pitch angle anisotropy

$$A = \frac{\dfrac{k_\parallel}{\omega-\Omega_{\mathrm{e}}}\int_0^\infty \dfrac{\mathrm{d}u_\perp}{1-\dfrac{\omega U_{\mathrm{R}}}{c^2k_\parallel\gamma_{\mathrm{R}}}}\dfrac{u_\perp^2}{\gamma_{\mathrm{R}}}\left(u_\perp\dfrac{\partial F_{\mathrm{h}}}{\partial u_\parallel} - u_\parallel\dfrac{\partial F_{\mathrm{h}}}{\partial u_\perp}\right)_{u_\parallel=U_{\mathrm{R}}}}{\displaystyle\int_0^\infty \frac{\mathrm{d}u_\perp}{1-\dfrac{\omega U_{\mathrm{R}}}{c^2k_\parallel\gamma_{\mathrm{R}}}}u_\perp^2\left.\frac{\partial F_{\mathrm{h}}}{\partial u_\perp}\right|_{u_\parallel=U_{\mathrm{R}}}}\,. \tag{1.97}$$

For the definition of resonance momentum U_{R} (or resonance velocity V_{R}), see Equations 2.3, 2.18 and 2.19.

In a nonrelativistic limit, the integral over $u_\perp$ can be simplified by per partes (derivatives going to 0 at integral limits), reducing the growth rate formula to (Kennel and Petschek, 1966)

$$\gamma_{\mathrm{L}} = \pi\Omega_{\mathrm{e}}\left(1-\frac{\omega}{\Omega_{\mathrm{e}}}\right)^2|V_{\mathrm{R}}|\left(A-\frac{\omega}{\Omega_{\mathrm{e}}-\omega}\right)\left.\int_0^\infty F_{\mathrm{h}}2\pi v_\perp\mathrm{d}v_\perp\right|_{v_\parallel=V_{\mathrm{R}}}\,. \tag{1.98}$$

Furthermore, for a bi-Maxwellian distribution (Equation 1.92), A reduces to the temperature anisotropy

$$A = \frac{\sigma_\perp^2}{\sigma_\parallel^2} - 1\,. \tag{1.99}$$

The critical value of anisotropy

$$A_{\mathrm{m}} = \frac{\omega}{\Omega_{\mathrm{e}}-\omega} \tag{1.100}$$

corresponds to the marginal instability $\gamma_{\mathrm{L}} = 0$. For $A \equiv 0$, the growth rate reduces to a pure cyclotron damping. A typical damping profile prescribed by $\gamma_{\mathrm{L}}(\omega; A=0)$ is plotted in Figure 1.6a. When $A(\omega) > A_{\mathrm{m}}$, whistler-mode fluctuations at frequency ω become unstable, as shown in Figure 1.6a. Quasilinear theory predicts that during the anisotropy-driven wave growth process, the hot electron distribution relaxes towards an isotropic state (Ossakow et al., 1972).

Derivation of whistler-mode instabilities for $\theta_{\mathrm{k}} > 0$ is much more formidable than the parallel case (Liu and Chen, 2019) and will not be pursued here. Under the simplifications introduced in the formulation of oblique Landau damping (Equation 1.93), the growth rate due to cyclotron resonance can be expressed as (Sazhin, 1993)

$$\gamma_{\mathrm{L1}} = \frac{\sqrt{\pi}\dfrac{n_{\mathrm{he}}}{n_{\mathrm{e}}}\Omega_{\mathrm{e}}\left(1-\dfrac{\omega}{\Omega_{\mathrm{e}}}\right)^2|V_{\mathrm{R}}|\left(A-\dfrac{\omega}{\Omega_{\mathrm{e}}-\omega}\right)((\omega+\Omega_{\mathrm{e}})\cos\theta_{\mathrm{k}}-\Omega_{\mathrm{e}})^2\exp\left(\dfrac{-V_{\mathrm{R}}^2}{2\sigma_\parallel^2}\right)}{2^{5/2}\omega^2\sigma_\parallel\cos^4\theta_{\mathrm{k}}\,(1+\cos\theta_{\mathrm{k}})^{-2}}\,, \tag{1.101}$$

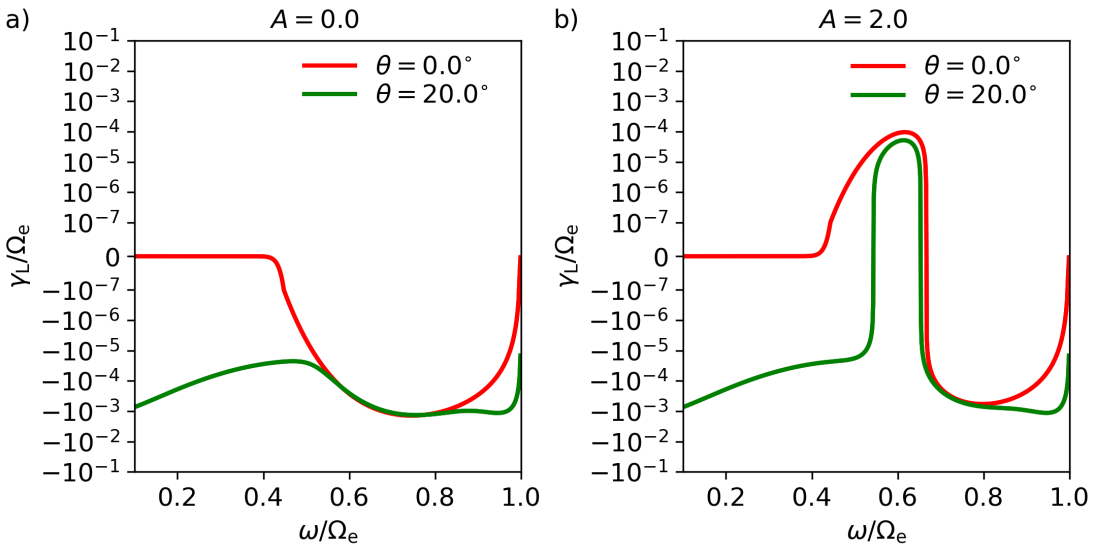

Figure 1.6: Linear growth rate of parallel and quasiparallel whistler-mode waves based on the approximate, nonrelativistic equations 1.93 and 1.101. a) Isotropic hot electron distribution. b) Anisotropic hot electron distribution with $A = 2$. Wave and plasma parameters used for these plots were: $\omega_{\mathrm{pe}}/\Omega_{\mathrm{e}} = 5.0$, $n_{\mathrm{he}}/n_{\mathrm{e}} = 0.01$, $\sigma_{\parallel}/c = 0.025$.

where we have added the density ratio $n_{\mathrm{he}}/n_{\mathrm{e}}$ to reflect the splitting of the electron population into cold and hot components. This formula was used in combination with Equation 1.93 to calculate the quasiparallel growth rate curves in Figure 1.6. In practice, the growth rates of plasma waves in a general setting are calculated by numerical software (e.g. WHAMP (Rönnmark, 1983) or KUPDAP (Sugiyama et al., 2015)) directly from the hot plasma dispersion relation.

We note here that the pitch angle anisotropy is obtained through integration along the resonance velocity curve and is thus very sensitive to changes of PSD gradients in the resonance region. Any sharp edges that could form due to loss cone formation, wave-particle interactions, or beam injections are highly unstable. See Section 2.2 for more information on resonance velocity curves, and Section 5.3 for an example of gradient formation due to nonlinear wave-particle interactions.

Ion instabilities

Because the velocities of gyroresonant protons and heavier ions are typically much lower than electron velocities, relativistic effects on the growth rate can be neglected. Under the approximations leading to the simplified formula for proton EMIC wave phase velocity (Equation 1.65), we can derive the weak growth rate factor (Gurnett and Bhattacharjee, 2017)

$$\gamma_{\mathrm{L}} = \pi \frac{(\Omega_{\mathrm{p}} - \omega)^2}{(2\Omega_{\mathrm{p}} - \omega)} \frac{\Omega_{\mathrm{p}}}{\omega} |V_{\mathrm{R}}| \left(A - \frac{\omega}{\Omega_{\mathrm{p}} - \omega} \right) \int_0^{\infty} F_{\mathrm{h}} 2\pi v_{\perp} \mathrm{d}v_{\perp} \Big|_{v_{\parallel} = V_{\mathrm{R}}} . \tag{1.102}$$

The velocity distribution F_{h} with anisotropy A now represents the hot proton population, and

$$\frac{V_{\mathrm{R}}}{c} = -\frac{\Omega_{\mathrm{p}}^{1/2} (\Omega_{\mathrm{p}} - \omega)^{3/2}}{\omega \omega_{\mathrm{pp}}} . \tag{1.103}$$

Apart from the initial factors pertaining to the derivative $\partial \bar{D}_{\mathrm{r}}/\partial\omega$, this result is equivalent to the nonrelativistic whistler growth rate from Equation 1.98. However, in most

magnetospheric applications, the presence of heavier ions cannot be neglected (cf. Section 1.1.4), and they can have a significant impact on the linear growth rate of EMIC waves (Summers and Thorne, 2003).

1.2 Observations of electromagnetic emissions in the Earth's inner magnetosphere

As anticipated in the introduction, *in situ* observations of magnetospheric plasma waves are much harder to perform than in the case of a laboratory plasma. While it became possible to predict the existence of ionospheric layers already in the early twentieth century based on radio wave propagation, the true advent of space plasma science started in 1958 when Explorer I and III discovered the existence of the inner radiation belt (van Allen et al., 1958). The first spacecraft observation of the chorus emission, which is the central subject of later chapters, followed soon after in 1963 (Gurnett and O'Brien, 1964).

In this section, we briefly review the instrumentation essential to the detection and study of the whistler-mode chorus emission: electric antennas, search coil magnetometers and fluxgate magnetometers. Description of those instruments is based mainly on the wave analysis suites from the Cluster spacecraft (Pedersen et al., 1997) and Van Allen Probes spacecraft (Kletzing et al., 2013; Wygant et al., 2013). We follow with a summary of signal analysis methods used to construct spectrograms and instantaneous frequency plots in Chapters 4 and 5. The section concludes with an overview of some of the most abundant types of electromagnetic emissions observed in the Earth's magnetosphere.

1.2.1 Spacecraft and instrumentation

Electric antennas

One of the most crucial components of an instrument suite for plasma wave measurements are electric antennas. The Cluster spacecraft uses four 50m wire booms with Langmuir probes attached to their tips to measure the fluctuating electric field (Gustafsson et al., 1997). The antennas are orthogonal to each other and rotate with the spacecraft, utilizing the centrifugal force to remain taut. An average of probe-to-spacecraft potential differences from the current-biased probes is used to determine the spacecraft floating potential and estimate the local plasma density.

The Van Allen Probes have an additional, shorter rigid antenna that is aligned with the spin axis and provides the third field component (Wygant et al., 2013). The plasma density is determined from electrostatic fluctuations near the upper hybrid frequency (ω_{uh}), which are naturally triggered by electron anisotropic instability. Unlike the potential method, the ω_{uh} approach works even in the higher density environment of the plasmasphere (Kurth et al., 2015), but it fails in regions of very diluted plasma, where $\lambda_{\mathrm{De}} \gtrsim \ell$ (ℓ is the dimension of the antenna system) and where upper-hybrid emissions thus become invisible. The knowledge of plasma frequency, which is determined from the plasma density, is essential for comparing measured wave properties with theoretical calculations based on the cold plasma dispersion relation.

Search coil magnetometers

The search coil magnetometer provides a time series of magnetic fluctuations derived from the induced voltage measurements. It typically consists of three orthogonal coils

attached to a several metre long boom to prevent interference from the spacecraft circuitry. Various implementations exist, depending on the desired sensitivity, frequency range and noise levels (Hospodarsky, 2016). The search coils of the Cluster STAFF instrument (Cornilleau-Wehrlin et al., 1997) provide measurements of magnetic fluctuations from 10 Hz to 4 kHz, with a noise floor below $10^{-9}\,\mathrm{nT\,Hz^{-1}}$ at frequencies above 100 Hz (which is the range relevant for chorus emissions). The triaxial magnetic search coil magnetometer on the Van Allen Probes (part of the EMFISIS instrument) measures in a frequency range from 10 Hz up to 12 kHz, with noise levels in the kilohertz range even slightly lower than on the STAFF magnetometers. Whistler emissions in the outer radiation belt with spectral power below about $10^{-8}\,\mathrm{nT\,Hz^{-1}}$ are not relevant for nonlinear processes, making the search coil sensor sensitivity levels perfectly suitable for our purposes.

However, at frequencies below approx 100 Hz the noise level quickly increases. At low frequencies below 1 – 10 Hz the search coil sensors therefore loose sensitivity, and the slowly varying magnetic field is measured using another type of sensors (fluxgate magnetometers). The fluxgate cadence can be large enough to detect EMIC waves with frequencies up to tens of hertz (Kletzing et al., 2013).

1.2.2 Signal analysis

The time series of electric and magnetic field measurements are often not provided continuously due to limitations on storage capacity and downlink speed. Between the short, high-resolution "burst mode" periods, the data is processed onboard and stored in the form of averaged spectral matrices. The spectrum is obtained with short-time Fourier transform (STFT) with predetermined sample length, window overlap, time averaging and frequency averaging. The resulting product is usually not well suited for chorus studies due to low resolution. Therefore, we must rely on burst mode snapshots.

Waves in space plasmas are usually analyzed and classified based on a time-frequency spectrogram. The power spectral density is obtained directly from the STFT spectral matrices of individual electromagnetic field components. An example of electric and magnetic wave power spectrum can be seen in the first two panels of Figure 1.7.

Apart from the wave power and amplitude, we are also interested in various wave propagation properties: wave vector $\boldsymbol{k}$, Poynting vector $\boldsymbol{S}$, sense of polarization, and the shape of the polarization ellipse. These can be obtained from the complex power-spectral matrices $\hat{M}^{\mathrm{B}}_{ij} = \hat{B}_i\hat{B}_j$, $\hat{M}^{\mathrm{B}}_{ij} = \hat{E}_i\hat{E}_j$, and the cross-spectral matrix $\hat{M}^{\mathrm{EB}}_{ij} = \hat{E}_i\hat{B}_j$, where each frequency bin retains the necessary phase information. The wave vector direction, up to a sign, can be obtained from the magnetic field components, while the Poynting vector requires all six electromagnetic components – the third electric component, if missing, can be obtained from Faraday's law. In practice, the presence of noise introduces an uncertainty into the resulting quantities, and the amount of uncertainty depends on the signal-to-noise ratio and the chosen spectral method. In this thesis, both natural and artificial (noiseless) spectra were processed with the singular value decomposition method (Santolík et al., 2003b). This method uses an overdetermined system defined by the 6×3 real spectral matrix to find the least square estimate of $\boldsymbol{k}$-vector components through the solution of the normal equation. The ellipticity of the wave magnetic field, shown e.g. in Figures 1.2d and 1.3d, is then defined as the ratio of the largest and the second-largest singular value,

$$E_{\mathrm{B}} = \frac{w_2^{\mathrm{B}}}{w_3^{\mathrm{B}}}\,. \tag{1.104}$$

For natural, noisy signals, the planarity of polarization is defined as Santolík et al. (2003b)

$$F_{\mathrm{B}} = 1 - \sqrt{\frac{w_1^{\mathrm{B}}}{w_3^{\mathrm{B}}}}\,, \tag{1.105}$$

which is equal to 1 for an ideal plane wave. Isotropic noise contributes to all three singular values equally, and thus reduces F_B to a value below 1. The analysis of the magnetic spectrum is preferred not only because of its direct relation to the $\boldsymbol{k}$-vector but also because the search-coil data is typically less noisy than the electric fields measured by antennas. For a detailed review of the SVD methods and the effects of signal-to-noise ratio on the resulting wave propagation properties, see Taubenschuss and Santolík (2018).

In the case of narrowband emissions, the Hilbert transform of signal $B(t)$ allows us to obtain the analytic representation

$$B_{\mathrm{a}}(t) = B(t) + \mathrm{i}H(B)(t) = B_{\mathrm{m}}(t)\mathrm{e}^{\omega t + \psi_{\mathrm{B}}}\,, \tag{1.106}$$

where B_{m} is the amplitude modulation, and $\omega = \partial\psi_{\mathrm{B}}/\partial t$ is the instantaneous frequency. This phase and frequency analysis is important in studies of the frequency of rising-tone, narrowband emissions, see e.g. Figures 4.8 and 4.9. The wave vector, Poynting vector and ellipticity can be obtained directly in the time domain, but in practice, they are derived from the spectral matrices even when the bandwidth is narrow.

1.2.3 Classification of electromagnetic emissions

Electromagnetic emissions in magnetospheres are classified based on their propagation properties, spectral features, location of occurrence, and origin (natural or anthropogenic). We will avoid using the VLF, ELF and ULF terminology (Very, Extremely, Ultra Low Frequency) because the definition of these bands is not consistent across radio science and space science, and the division bears no connection to characteristic frequencies of a magnetized plasma environment.

As in Section 1.1.4, we will focus mostly on waves occurring below the local cyclotron frequency. An overview of various emissions in this frequency range is presented in Figure 1.7, which shows electric and magnetic spectra obtained from the EMFISIS survey mode over one 9-hour orbital period of the Van Allen Probe A spacecraft. The emission types relevant to the theoretical and numerical results presented in this thesis are briefly described below. For the description of the other emissions appearing in the exemplary spectrogram, see Hospodarsky et al. (2016).

Whistler-mode chorus

The two bands of intense emissions ranging from about $0.1\Omega_{\mathrm{e0}}$ to $0.8\Omega_{\mathrm{e0}}$ represent the chorus emission. A 6-second burst mode snapshot of magnetic wave power is presented in the form of a spectrogram in Figure 1.8. These emissions are characterized by narrowband spectral elements with chirping frequency (rising or falling), whose presence needs to be confirmed in the high-cadence burst mode data to avoid confusing chorus with the exohiss emission (see below). The emission is generated near the magnetic equator by nonlinear resonant interactions with energetic electrons. These interactions and the origin of the lower-band chorus ($0.1\Omega_{\mathrm{e0}}$ to $0.5\Omega_{\mathrm{e0}}$) are analyzed in detail in Chapters 2 to 5.

Statistical results from the THEMIS, Cluster and Polar spacecraft have shown that chorus occurs predominantly in the night and morning sectors at L-shells ranging from the plasmapause to the magnetopause, with average wave power steeply decreasing

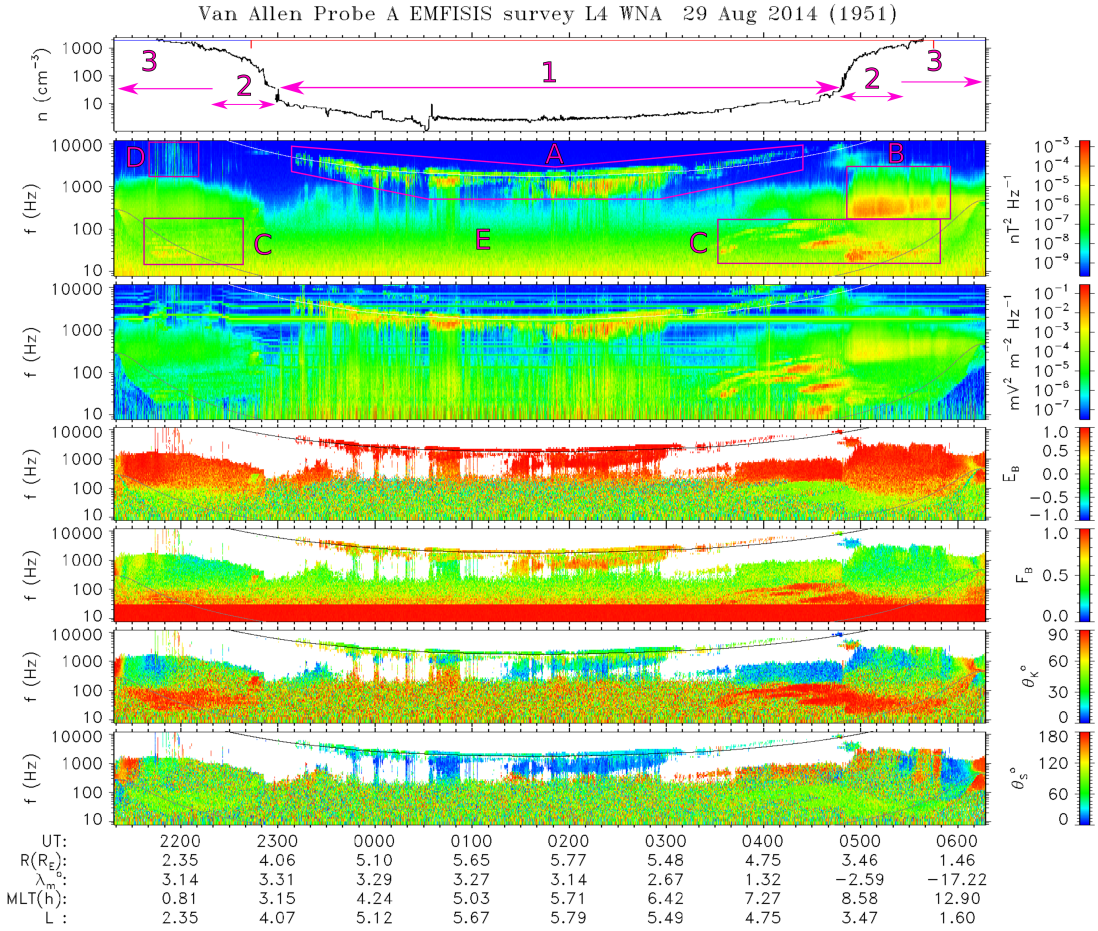

Figure 1.7: Electron density and wave spectrograms from a full orbit of Van Allen Probe A recorded on 29-30 August 2014, processed by the methods of Santolík et al. (2003b, 2010). The panels show, in order: electron density from ω_{uh} measurements, magnetic power spectral density, electric power spectral density, ellipticity of the magnetic field, planarity of the magnetic field, wave normal angle and polar Poynting angle. The upper line in the spectrogram marks half of the electron gyrofrequency; the lower line follows the proton gyrofrequency, which rises into the EMFISIS frequency range only at low altitudes. (1) Plasmatrough: region of tenuous plasma outside the plasmasphere (2) Plasmapause: outer boundary of the plasmasphere. (3) Plasmasphere: cold, dense plasma co-rotating with the Earth. (A) Whistler-mode chorus/exohiss. (B) Plasmaspheric hiss. (C) Equatorial noise, coupling of electron whistler mode and proton whistler mode. (D) Lightning generated whistlers, kHz radiation emitted from lightning strokes. (E) Instrument noise.

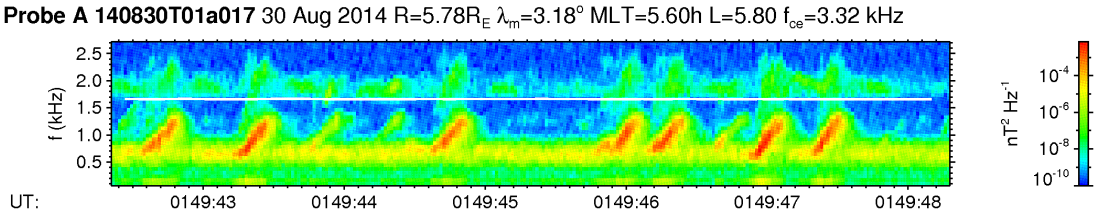

Figure 1.8: Magnetic power spectral density from a 6-second burst mode snapshot taken during the orbit in Figure 1.7, starting at 01:49:43.35 UT. It reveals narrow-band, rising-tone chorus elements in the lower frequency band, with weaker coherent emissions in the upper band. The emission band centred around 700 Hz is assumed to be the result of linear growth, while the discrete elements are a product of nonlinear interaction between electrons and whistler waves.

above 40° of latitude (Li et al., 2009; Bunch et al., 2012; Santolík et al., 2014b). However, these studies did not use high-resolution data to confirm the presence of discrete, chirping structure in the spectrograms. Details on the fine spectral structure and propagation properties of chorus are usually based on case studies – these are discussed in Section 3.1.

Whistler-mode hiss

The incoherent broadband emission found in the plasmasphere at frequencies around $0.1\Omega_e$ and below is called *plasmaspheric hiss*. The name comes from the hissing, noise-like sounds produced by the audio-converted signal of the emission. Bortnik et al. (2009) proposed that the hiss might originate from chorus waves propagating to higher latitudes where they penetrate the plasmapause and lose their coherent structure, but other sources of these waves cannot be excluded Santolík and Chum (2009). Omura et al. (2015) and Nakamura et al. (2018) hinted at the possible relation between chorus and plasmaspheric hiss, showing that the hiss structure might consist of short, coherent tones generated by the same type of nonlinear interaction as the chorus.

Hiss emissions may also occur outside the plasmapause, where they are called *exohiss*. The relatively narrow band of unstructured whistler-mode emission below the lower-band chorus (Figure 1.8) can also be called exohiss. It originates from anisotropy-driven linear instability, and it was conjectured by Trakhtengerts et al. (1996) that rising-tone chorus emissions grow from this exohiss emission. However, the hiss band is not always present alongside chorus.

Like chorus, hiss can cause scattering of resonant electrons, but the lack of clear, coherent structure results in slower, diffusive processes, which can be analyzed within the quasilinear theory.

EMIC emissions

As discussed in the paragraphs dealing with cold plasma dispersion (Section 1.1.4) and ion instabilities (Section 1.1.6), the EMIC waves can be generated only below the proton gyrofrequency and grow from anisotropy-driven instability of hot protons and other, heavier ions. Their source region is in the vicinity of the magnetic equator, or the B_0-minimum of the local field-line, with radial distances ranging from the plasmapause up to the magnetopause (Saikin et al., 2015; Grison et al., 2021).

As shown, e.g., in Grison et al. (2018) (see also Figure 1.9), the EMIC waves can form coherent, chirping structures, with spectral and propagation features similar to the whistler-mode chorus. However, unlike chorus, the ion waves can nonlinearly trap and scatter both electrons and ions. The similarities in the formation process of those two types of emissions are discussed in greater detail in Section 3.4.

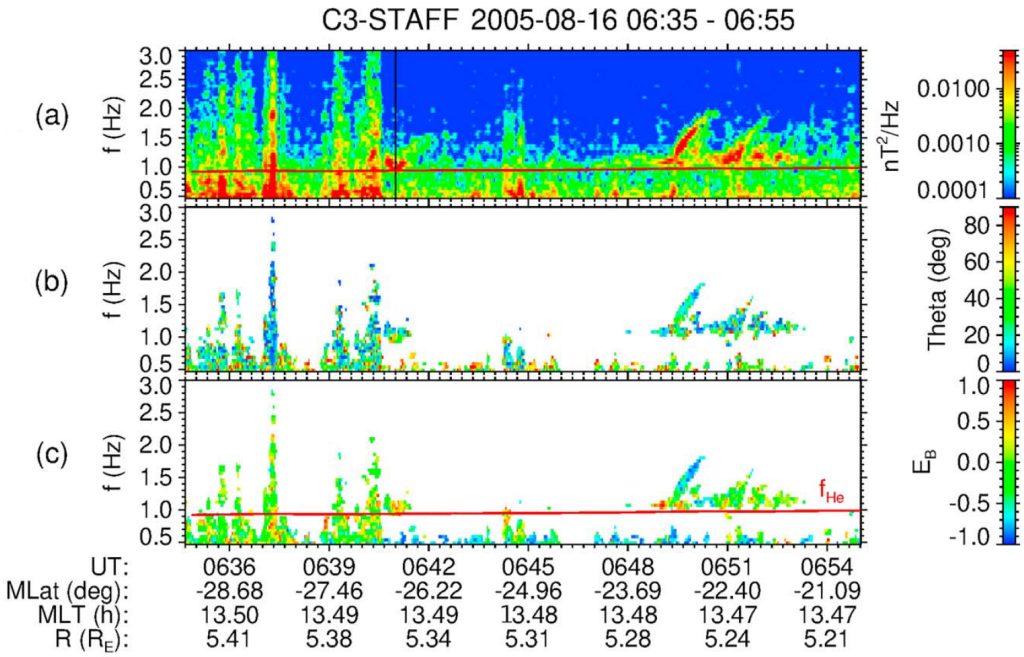

Figure 1.9: Spectrograms of EMIC emissions computed from STAFF search coil data. A discrete, rising-tone element appears above the helium gyrofrequency (red line) after 06:49 UT, followed by less structured emissions with ambiguous frequency drift. a) Magnetic power spectral density, with a black vertical line denoting the time at which the Cluster C3 spacecraft left a high-density region; b) wave normal angle; c) ellipticity of magnetic field. Adapted from Grison et al. (2018).

2. Nonlinear wave-particle interactions

In Section 1.1.6, we mentioned some important wave instabilities that result from the linearized Vlasov equation. In the linear approach, the current density calculated from phase space density perturbations determined the propagation properties of waves that can exist in the plasma medium, but these waves did not act back on the particle distribution. In other words, the amplitude of plasma waves in a linear theory is assumed to be negligibly small, and the trajectories of particles passing through these waves are considered to be unperturbed.

This chapter reviews the particle motion in large-amplitude waves, focusing chiefly on cyclotron resonance with parallel-propagating waves. The general resonance condition has the form

$$\omega - k_\parallel v_\parallel - \mathrm{sgn}(Z_s)\frac{n\Omega_s}{\gamma_s} = 0\,, \tag{2.1}$$

where $\omega - k_\parallel v_\parallel$ is the Doppler-shifted frequency, Ω_s/γ_s is the unsigned cyclotron frequency of a relativistic particle of species s, and n is an integer.

For $n = 0$, we get the Landau resonance condition

$$v_\parallel = \frac{\omega}{k_\parallel} \equiv V_{\mathrm{R}0}\,, \tag{2.2}$$

showing us that a particle is in exact Landau resonance if it travels on a surface of constant wave phase.

For $n = \pm 1$, we get the first (fundamental) cyclotron resonance condition

$$v_\parallel = \frac{1}{k_\parallel}\left(\omega \mp \mathrm{sgn}(Z_s)\frac{\Omega_s}{\gamma_{s\mathrm{R}}}\right) \equiv V_{s\mathrm{R}1}\,, \tag{2.3}$$

with $\gamma_{s\mathrm{R}} = 1/\sqrt{1 - V_{s\mathrm{R}}^2/c^2 - v_{s\perp}^2/c^2}$. In this case, the particle is in exact resonance when the particle gyrophase along its trajectory follows the phase of the perpendicular components of the wavefield.

Higher order harmonics are not considered here, since they become important only when the perpendicular component $k_\perp$ of the wave vector becomes large (Swanson (2003), Section 4.3.7.2).

2.1 Landau resonance

The effect of Landau resonance is most easily shown on an electrostatic wave in an unmagnetized plasma. The total electromagnetic field can then be expressed as

$$\boldsymbol{E} = E_{\mathrm{w}}(0, 0, \sin(\omega t - kz))\,. \tag{2.4}$$

A typical example of an electrostatic plasma wave would be the Langmuir wave with $\omega^2 \approx \omega_{\mathrm{pe}}^2 + 3C_{\mathrm{e}}^2 k^2$, where C_{e} is the electron thermal speed.

The equation of motion of an electron propagating in the z-direction is then simply

$$\frac{\mathrm{d}v_z}{\mathrm{d}t} = -\frac{eE_{\mathrm{w}}}{m_{\mathrm{e}}}\sin(\omega t - kz)\,. \tag{2.5}$$

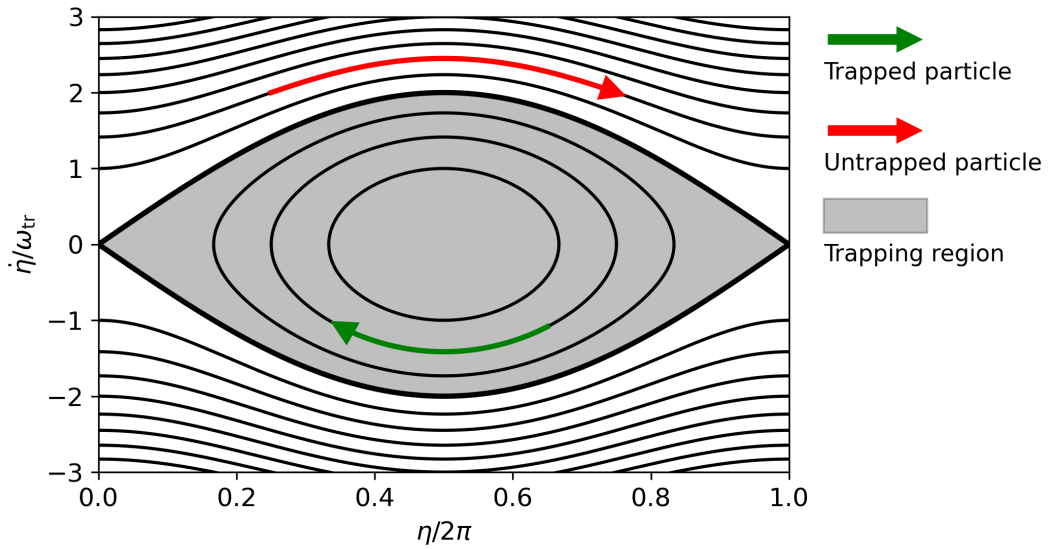

Figure 2.1: Phase space diagram showing the behaviour of electrons near Landau resonance as described by Equation 2.6. The velocity of particles in the trapping region oscillates around a plane of constant wave phase $\eta = \pi$ (green arrow). Untrapped particles (red arrow) also 'feel' the potential but are not phase-locked.

It is more convenient to work in the phase velocity frame and with dimensionless coordinates of angle $\eta = k(z - V_{\rm p}t)$ and its time derivative $\dot{\eta} = k(v_z - V_{\rm p})$. These substitutions lead to a pendulum equation for η,

$$\frac{{\rm d}^2\eta}{{\rm d}t^2} - \omega_{\rm tr}^2 \sin\eta = 0\,, \tag{2.6}$$

with oscillation frequency

$$\omega_{\rm tr} = \sqrt{\frac{ekE_{\rm w}}{m_{\rm e}}}\,. \tag{2.7}$$

Particle trajectories in $(\eta, \dot{\eta})$ space are shown in Figure 2.1. Particles within the region delimited by separatrices (thicker lines) are called trapped particles since they are bound to a local minimum of the electrostatic wave potential.

To examine the energy exchange between particles and the wave, we set up a periodic system $\eta \in (0, 2\pi)$ with an initial velocity distribution which decreases linearly with $\dot{\eta}$ and is homogeneous in η. It is assumed here that the loss of wave energy

$$\left(\frac{E_{\rm w}(t)}{E_{\rm w}(0)}\right)^2 - 1 = \int_0^t 2\gamma_{\rm NL}(t'){\rm d}t'\,, \tag{2.8}$$

where $\gamma_{\rm NL}$ stands for a nonlinear growth rate, is small enough so that we can neglect it in the calculation of the width of the resonance region

$$V_{\rm tr} = \frac{4\omega_{\rm tr}}{k} = 4\sqrt{\frac{eE_{\rm w}}{km_{\rm e}}}\,. \tag{2.9}$$

In Figure 2.2, we capture the state of the distribution at times $T_{\rm tr}/4$, $T_{\rm tr}/2$, $T_{\rm tr}$, and $5T_{\rm tr}$, where $T_{\rm tr} = 2\pi/\omega_{\rm tr}$. The last panel in Figure 2.2 shows the changes in particle kinetic energy over time. After a sufficiently long time, the energy source is depleted, and a plateau is formed in the velocity distribution, with a net increase in particle energy.

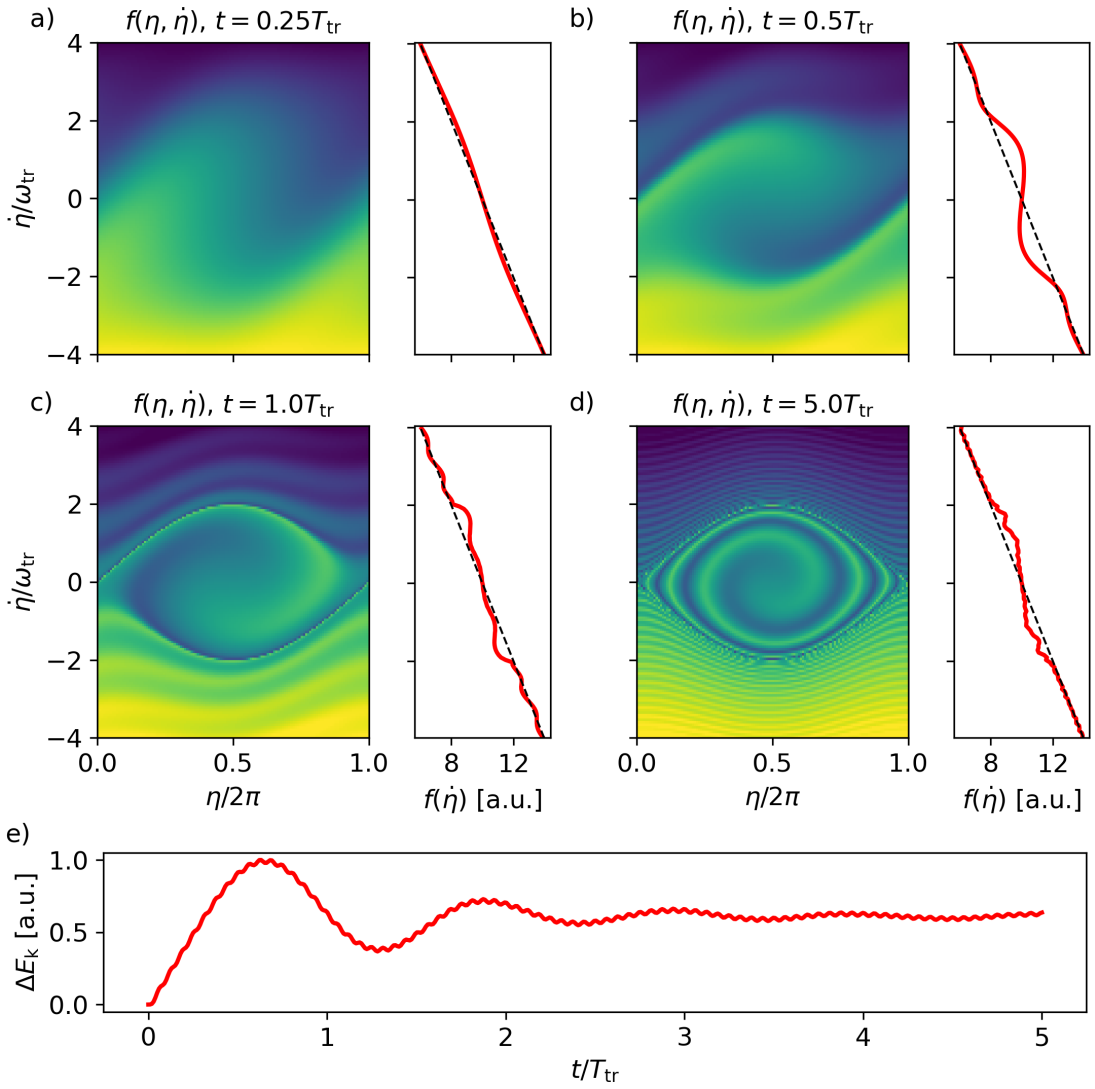

Figure 2.2: Evolution of velocity distribution of electrons interacting with an electrostatic wave at the $n = 0$ (Landau) resonance. The initial distribution has a linear slope in velocities and is uniform in phases. Panels a-d) show 2D distributions $f(\eta, \dot{\eta})$ – with density increasing from darker (blue) to brighter (yellow) colors – and reduced 1D distributions $f(\dot{\eta})$ at four different times: $T_{\rm tr}/4$, $T_{\rm tr}/2$, $T_{\rm tr}$ and $5T_{\rm tr}$. Initial 1D distribution is plotted by a dashed line. See Section 5.2 for the simulation method used to produce the plots. Panel e) shows the evolution of total particle kinetic energy in the resonance region. The high-frequency oscillations are related to the simulation box size $\pm 16\omega_{\rm tr}$ and the choice of velocity distribution. Note that due to $E_{\rm w} = \text{const.}$, these plots serve only as an illustration of phase mixing and cannot be used to make any definite statements about the nonlinear damping rate.

In the linear theory, the small amplitude assumption leads to large trapping periods; therefore, the linear Landau damping coefficient relates only to a very short initial part of the plot in Figure 2.2e where the particle energy grows exponentially (waves are exponentially damped). The energy conservation law of the wave-particle system at the initial stage can be cast into the form (Dawson, 1961; Gurnett and Bhattacharjee, 2017)

$$\frac{\mathrm{d}}{\mathrm{d}t}\left\langle \frac{1}{2} n_\mathrm{e} m_\mathrm{e} \left(V_\mathrm{p} + \frac{\dot{\eta}}{k} \right) \right\rangle = -\pi \left(\frac{\varepsilon_0 E_\mathrm{w}^2}{2} \right) \frac{\omega_\mathrm{pe}^3}{k} \left. \frac{\mathrm{d}f_0(\dot{\eta})}{\mathrm{d}\dot{\eta}} \right|_{\dot{\eta}=0} , \tag{2.10}$$

where $f_0(\dot{\eta})$ is the reduced initial velocity distribution expressed in the normalized velocities $\dot{\eta}$, and $\langle \bullet \rangle$ denotes averaging over resonance region. Solving for E_w recovers the weak-growth approximation of the growth coefficient as presented in Equation 1.91. Comments about the issues of electrostatic description of Landau damping still apply (see the paragraph after Equation 1.89).

During later stages of the resonance interaction where $0 < t \ll T_\mathrm{tr}$ does not hold anymore, the nonlinear growth rate can be found by inserting the resonance particle trajectories, expressed in terms of elliptic functions, into the Vlasov equation. This calculation was carried out by O'Neil (1965) and is again based on the energy conservation law. However, O'Neil assumed (as we did in Figure 2.2) a constant wave amplitude, or in other words, a constant width of the resonance region V_tr. Furthermore, there is no consideration of the impact of the perturbed electron velocity distribution on the dispersive properties of present wave modes.

A different approach was used by Al'tshul' and Karpman (1966) who expanded the integral solution of the Fourier-transformed Vlasov equation in powers of the wavefield. Isolation of principal secular terms in the formal expansion leads to a formula for the electrostatic wave potential similar to the Dyson equation from quantum field theory. While the resulting nonlinear growth coefficient provided a consistent description of the wave amplitude evolution, they still needed to assume slow changes in amplitude to find a closed-form expression. Al'tshul' and Karpman also predicted the existence of amplitude oscillations in the $t \to \infty$ limit, meaning that the phase mixing does not force the growth rate to zero. This unexpected asymptotic behaviour was pointed out to be due to the assumption of negligible wave generation at higher harmonics (O'Neil, 1965; Chen and Zonca, 2016). A novel application of the Dyson equation approach in the analysis of chorus emission growth is reviewed in Section 3.3.3.

2.2 Cyclotron resonance

In contrast to the Landau resonance, the condition for cyclotron resonance in Eq. 2.3 includes a dependence on the Lorentz factor through time dilation of the gyroperiod. Therefore, it will be more convenient to work with momenta $u = \gamma m v$ and set $c = 1$ for the speed of light and $m_\mathrm{e} = 1$ for electron mass. A constant ambient magnetic field $\boldsymbol{B}_0$ pointing along the z-axis is first assumed, with effects of nonuniformity being addressed later in Section 2.2.1.

To further simplify the analysis, we will write the equations of motion for an electron interacting with the electromagnetic field of a right-hand polarized parallel whistler wave

$$\boldsymbol{B}_\mathrm{w} = B_\mathrm{w} \left(\cos\psi_\mathrm{B}, \sin\psi_\mathrm{B}, 0 \right) , \tag{2.11}$$

$$\boldsymbol{E}_\mathrm{w} = V_\mathrm{p} B_\mathrm{w} \left(\sin\psi_\mathrm{B}, -\cos\psi_\mathrm{B}, 0 \right) , \tag{2.12}$$

and we introduce a tilde notation for normalization to the electron gyrofrequency, i.e. $\tilde{\omega} \equiv \omega/\Omega_\mathrm{e}$ etc. The equations would take a similar form for positive ions and a left-hand

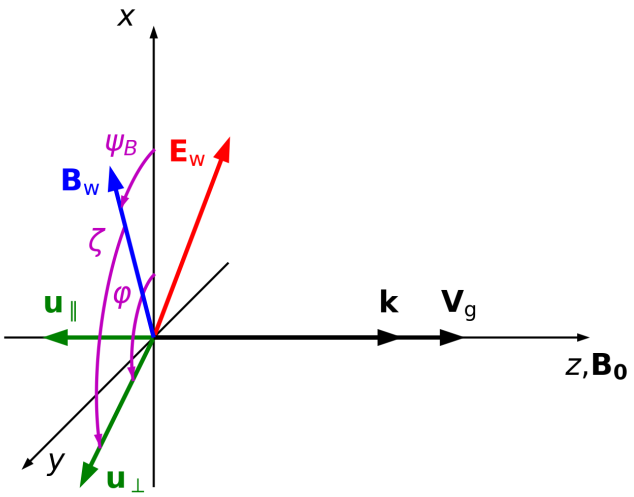

Figure 2.3: Schematic depiction of the configuration of the studied system of the parallel whistler wave and a gyrating electron. The transverse wavefield propagates in the direction of the ambient magnetic field $\boldsymbol{B}_0$, opposite to the direction of propagation of the particle.

polarized wave, e.g. protons and EMIC waves. Further, we introduce the relative phase difference

$$\zeta = \varphi - \psi_\mathrm{B}\,, \tag{2.13}$$

where ψ_B is the phase of the perpendicular wave magnetic field, and φ is the phase of the perpendicular component of the particle momentum $\boldsymbol{u}_\perp$. The configuration of the system is depicted in Figure 2.3. The equations of motion then take the form

$$\frac{\mathrm{d}u_\parallel}{\mathrm{d}t} = \frac{\Omega_\mathrm{w} u_\perp \sin\zeta}{\gamma} \tag{2.14}$$

$$\frac{\mathrm{d}u_\perp}{\mathrm{d}t} = -\left(\frac{u_\parallel}{\gamma} - V_\mathrm{p}\right)\Omega_\mathrm{w}\sin\zeta \tag{2.15}$$

$$\frac{\mathrm{d}\zeta}{\mathrm{d}t} = \frac{\Omega_\mathrm{e}}{\gamma} - \frac{1}{u_\perp}\left(\frac{u_\parallel}{\gamma} - V_\mathrm{p}\right)\Omega_\mathrm{w}\cos\zeta - \omega + \frac{k u_\parallel}{\gamma}\,, \tag{2.16}$$

where we have introduced the normalized amplitude $\Omega_\mathrm{w} = B_\mathrm{w} e/m_\mathrm{e}$.

For typical amplitudes of whistler waves in the Earth's radiation belt, $\tilde{\Omega}_\mathrm{w} \lesssim 0.01$, the second term in Eq. 2.16 can be neglected unless $u_\perp \ll 1$. With this term removed, the equation reads as

$$\frac{\mathrm{d}\zeta}{\mathrm{d}t} = \frac{\Omega_\mathrm{e}}{\gamma} - \omega + \frac{k u_\parallel}{\gamma}\,, \tag{2.17}$$

and setting $\mathrm{d}\zeta/\mathrm{d}t = 0$ recovers the resonance condition from Eq. 2.3. Since γ_R in that equation is a function of V_R, we can derive the resonance curve formula

$$U_\mathrm{R}(u_\perp) = \frac{-k\Omega_\mathrm{e} + \omega\sqrt{(k^2-\omega^2)(1+u_\perp^2) + \Omega_\mathrm{e}^2}}{k^2-\omega^2}\,, \tag{2.18}$$

or equivalently,

$$V_\mathrm{R}(v_\perp) = \frac{k\omega - \Omega_\mathrm{e}\sqrt{(\Omega_\mathrm{e}^2+k^2)(1-v_\perp^2) - \omega^2}}{\Omega_\mathrm{e}^2 + k^2}\,. \tag{2.19}$$

The curve $V_\mathrm{R}(v_\perp)$ is plotted in Fig. 2.4a for $\tilde{\omega} = 0.25$, $\tilde{\omega}_\mathrm{pe} = 5.0$, and has the shape of an elliptical arc which touches the $v_\parallel^2 + v_\perp^2 = 1$ circle at $V_\mathrm{R} = V_\mathrm{p}$. A simple algebraic manipulation shows that the ratio of the major (perpendicular) axis to the minor

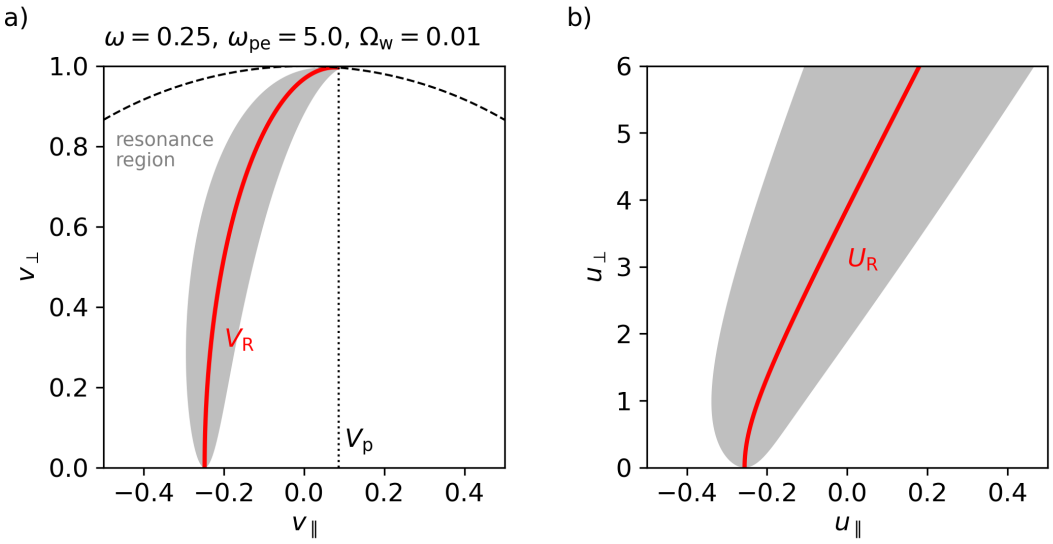

Figure 2.4: a) Resonance curve $V_R(v_\perp)$ based on Equation 2.19. Properties of the whistler wave are determined by wave frequency $\tilde{\omega} = 0.25$ and plasma frequency $\tilde{\omega}_{pe} = 5.0$. The grey region $\pm V_{tr}/2$ shows the extent of the trapping potential and is based on Equation 2.32 with $\tilde{\Omega}_w = 0.01$. The dashed curve represents the speed of light limit, and the dotted vertical line connects to the point at which the resonance velocity reaches the speed of light. b) Resonance curve in the momentum space.

(parallel) axis is $\sqrt{1 + k^2/\Omega_e^2}$. In the $(u_\parallel, u_\perp)$ space (Fig. 2.4b), the curve takes on a hyperbolic shape.

To better understand the electron's three-dimensional motion in the momentum space, we first examine trajectories in the $(u_\parallel, u_\perp)$ space. Dividing Eq. 2.15 by Eq. 2.14 results in

$$\frac{\mathrm{d}u_\perp}{\mathrm{d}u_\parallel} = \frac{-u_\parallel + \gamma V_p}{u_\perp}\,, \tag{2.20}$$

This differential equation has a closed-form solution

$$u_\perp = \left(u_\parallel^2\left(V_p^2 - 1\right) + u_{\parallel 0}^2\left(V_p^2 + 1\right) + 2u_\parallel\left(\gamma_0 V_p - u_{\parallel 0}V_p^2\right) - 2u_{\parallel 0}\gamma_0 V_p\right)^{\frac{1}{2}}\,, \tag{2.21}$$

where $\gamma_0 = \sqrt{1 + u_{\parallel 0}^2}$ and $u_{\parallel 0}$ denotes the $u_\parallel$-intercept. Curves from this family are ellipses with a minor (perpendicular) to major (parallel) axis ratio $\sqrt{1 - V_p^2}$ and with their centre shifted towards positive parallel momenta by

$$\frac{\gamma_0 V_p - u_{\parallel 0}V_p^2}{1 - V_p^2}\,; \tag{2.22}$$

a representative plot is shown in Fig. 2.5. Notice that there is no Ω_w- or ζ-dependence, meaning that when an electron passes through a whistler wave packet, it will stay on one of these curves as long as the wave frequency and background magnetic field remain constant. Changes in frequency are, however, a fundamental property of chorus emissions, and will be properly discussed in Chapter 3. For adiabatic changes of frequency (more specifically, when $\partial V_R/\partial t \ll V_{tr}\omega_{tr}$ – see Equations 2.31 and 2.32 for definitions of the trapping frequency and velocity, respectively), we may write $\gamma V_p = u_\parallel + \Omega_e/k$ and show that the centre of the phase space oscillations moves along the resonant diffusion curves for a broadband wave spectrum; the exact form of these curves was derived by Summers et al. (1998). However, as a consequence of Equation 3.46, the adiabatic approximation does not apply to chorus waves.

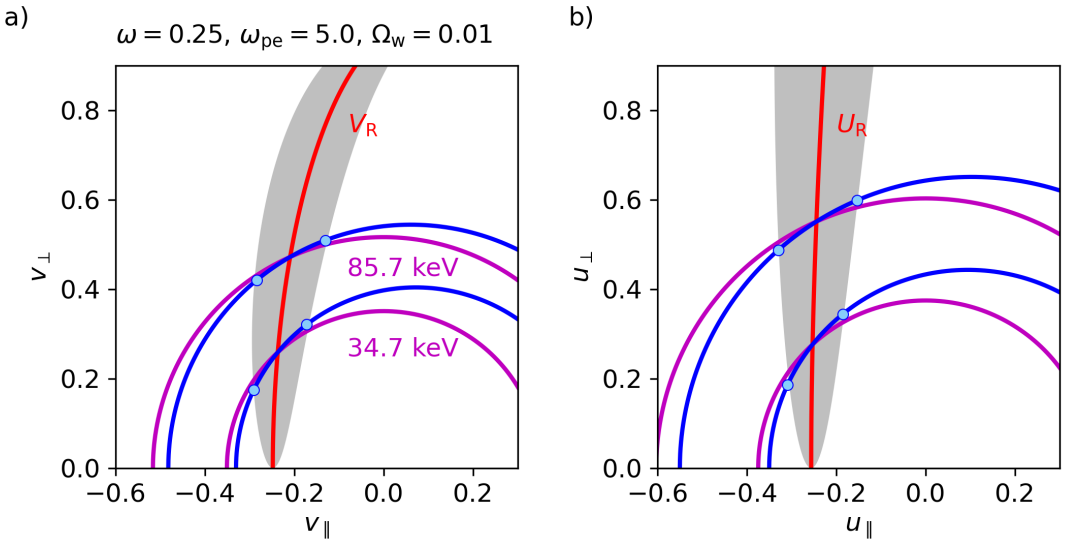

Figure 2.5: The motion of resonant particles is restricted to curves given by Equation 2.21, plotted in blue colour for exact-resonance energies 34.6 keV and 85.7 keV. The grey patch represents the approximate extent of the trapping potential based on Equation 2.32, while the light blue circles show the more exact trapping boundaries derived from the numerical solution of Equations 2.14, 2.17 and 2.21. Magenta circles show the constant energy surface, and the red line represents the resonance curve. b) Same plots as in panel a), but in the $(u_\parallel, u_\perp)$ space.

Since the motion in $(u_\parallel, u_\perp)$ space does not depend on the amplitude, it comes as no surprise that there exists a relation to the linear growth formula shown in Section 1.1.6, Eq. 1.98. Let us take the low-speed approximation of the electron motion,

$$\frac{\mathrm{d}v_\perp}{\mathrm{d}v_\parallel} = \frac{-v_\parallel + V_\mathrm{p}}{v_\perp}\,, \tag{2.23}$$

and compare it to isolines of a bi-Maxwellian distribution with anisotropy A, described by a differential equation

$$\frac{\mathrm{d}v_\perp}{\mathrm{d}v_\parallel} = -(1+A)\frac{v_\parallel}{v_\perp}\,. \tag{2.24}$$

Recall that for a bi-Maxwellian distribution, temperature anisotropy and pitch-angle anisotropy are identical, i.e. $A = T_\perp/T_\parallel - 1$ (Eqs. 1.97 and 1.99). Equating the above two differential expressions gives

$$Av_\parallel = -V_\mathrm{p}\,. \tag{2.25}$$

Putting $v_\parallel$ at the exact resonance defined in Eq. 2.3 (with $\gamma = 1$), we arrive at

$$\frac{\omega}{\Omega_\mathrm{e}} = \frac{A}{1+A}\,, \tag{2.26}$$

which is the marginal instability condition for anisotropy-driven whistler wave growth (Equation 1.100). This has a clear physical meaning: electrons which oscillate on the isolines of the bi-Maxwellian do not change the velocity space distribution, the net change in particle energy is zero, and thus the waves cannot grow or be damped. The equivalent formula for a relativistic case cannot be found so simply because the pitch angle anisotropy defined in Equation 1.97 is not constant in the $(u_\parallel, u_\perp)$ space. A constant frequency whistler wave can thus take energy from particles in one region of the momentum space and accelerate particles in another region at the same time.

To analyze the evolution of the ζ angle near resonance, we start with the simplified time evolution of ζ as given by Eq. 2.17 and define

$$\nu \equiv \frac{\mathrm{d}\zeta}{\mathrm{d}t} = \frac{k}{\gamma}(u_\parallel - \gamma V_\mathrm{R})\,. \tag{2.27}$$

The quantity ν represents a parallel velocity shift with respect to the resonance velocity, similar to the quantity $\dot{\eta}$ which appeared in the discussion of Landau resonance in Section 2.1. As a next step, we take the time derivative of ν, using

$$\frac{\mathrm{d}\gamma}{\mathrm{d}t} = \frac{u_\parallel \dfrac{\mathrm{d}u_\parallel}{\mathrm{d}t} + u_\perp \dfrac{\mathrm{d}u_\perp}{\mathrm{d}t}}{\gamma} = \frac{u_\perp V_\mathrm{p} \Omega_\mathrm{w} \sin\zeta}{\gamma}\,, \tag{2.28}$$

and obtain a pendulum-like equation with a harmonic driving force

$$\frac{\mathrm{d}^2\zeta}{\mathrm{d}t^2} = \frac{k u_\perp \Omega_\mathrm{w}}{\gamma^2} \sin\zeta \left(1 - V_\mathrm{p}^2 - \frac{\omega}{k^2}\frac{\mathrm{d}\zeta}{\mathrm{d}t}\right)\,. \tag{2.29}$$

Here, it is a common approach to replace $u_\perp$ by some constant mean value $\langle u_\perp \rangle$, with γ being calculated for this mean perpendicular momentum at the exact resonance (Omura et al., 2008). We then proceed to make the expansion around the resonance by setting $\nu = 0$, which leads to

$$\frac{\mathrm{d}\nu}{\mathrm{d}t} = \frac{\mathrm{d}^2\zeta}{\mathrm{d}t^2} = \omega_\mathrm{tr}^2 \sin\zeta\,, \tag{2.30}$$

where

$$\omega_\mathrm{tr} = \frac{\sqrt{1 - V_\mathrm{p}^2}}{\gamma_\mathrm{R}} \sqrt{k \langle u_\perp \rangle \Omega_\mathrm{w}} \tag{2.31}$$

is the trapping frequency (frequency of oscillations in the trapping potential). This result is sometimes called the second-order resonance equation and was first derived by Sudan and Ott (1971). As in the case of Landau resonance, we have arrived at a pendulum equation, but the meaning is slightly different. The resonant electron is now phase-locked in the gyrating frame, and its perpendicular velocity vector oscillates around $-\boldsymbol{B}_\mathrm{w}$. Also, as predicted by the resonance velocity formula (Eq. 2.19, Fig. 2.4a), the electrons propagate in the direction opposite to the whistler wave unless there is a substantial gyroperiod dilation ($\gamma \gg 1$). With plasma and wave parameters typical for the Earth's outer radiation belt, we get $\omega_\mathrm{tr} \ll \omega$, which is an important scaling relation for chorus theories discussed in Chapter 3.

The relation between ω_tr and the width of the resonance region V_tr can be treated in the same way as in Equation 2.9, resulting in

$$V_\mathrm{tr} = \frac{4\omega_\mathrm{tr}}{k} = 4\frac{\sqrt{1 - V_\mathrm{p}^2}}{\gamma_\mathrm{R}} \sqrt{\frac{\langle u_\perp \rangle \Omega_\mathrm{w}}{k}}\,. \tag{2.32}$$

The $\pm V_\mathrm{tr}/2$ region is plotted in grey in Figures 2.4 and 2.5. However, since we are using a fixed perpendicular momentum and calculating the Lorentz factor as $\gamma_\mathrm{R} = \sqrt{1 + U_\mathrm{R}^2 + \langle u_\perp \rangle^2}$, it is not immediately clear if the grey areas well approximate the full width of the trapping region. With the $u_\perp(u_\parallel)$-dependence from Equation 2.21, we can get a differential equation for $\mathrm{d}u_\parallel/\mathrm{d}\zeta$ with a separable right-hand side, but the solutions cannot be expressed in terms of elementary functions. However, the problem can be solved numerically, and the boundaries of the trapping region at $\zeta = \pi$ are shown along with example trajectories in Figure 2.5 as blue circles. We can see that both approaches to calculating the resonance width give nearly identical results.

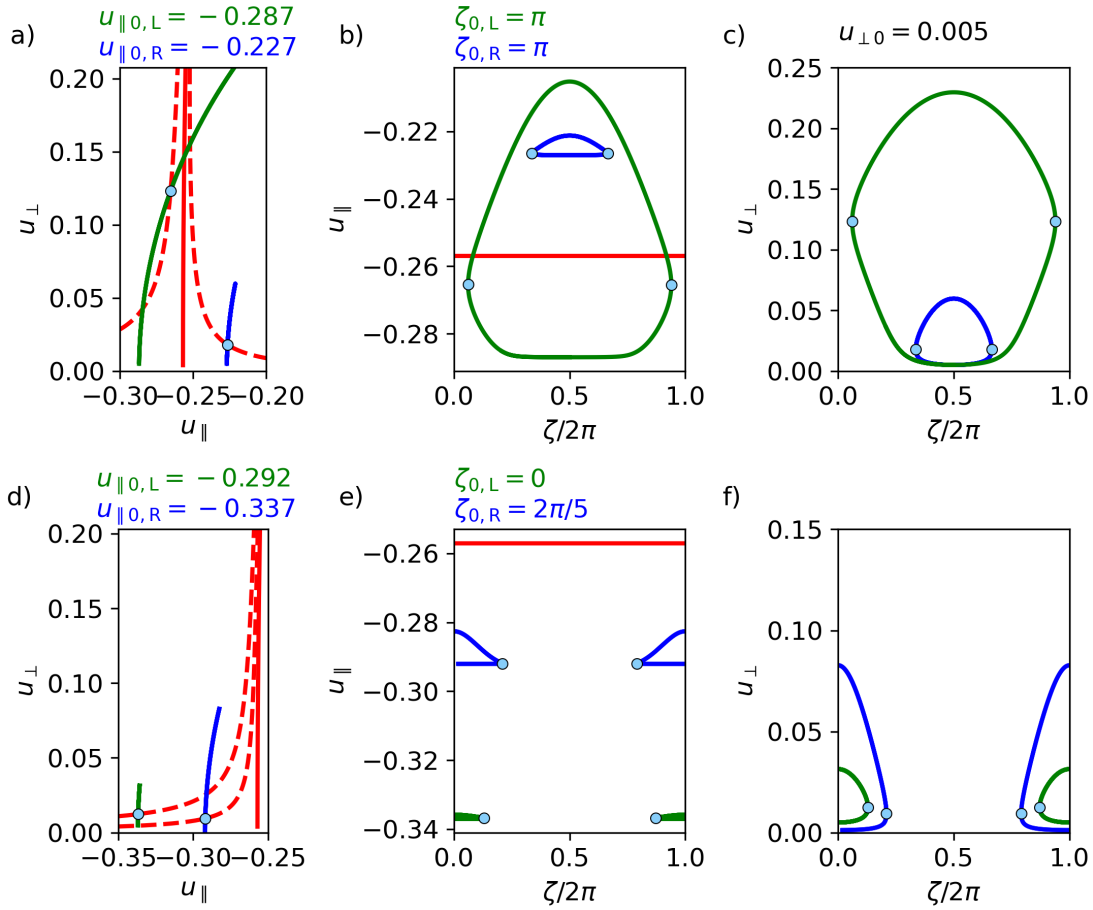

Figure 2.6: Behaviour of resonant particles with a low initial perpendicular momentum $u_{\perp 0} = 0.005$. Initial parallel momenta and phase angles of each particle are specified in the figure, wave properties are as in Figure 2.4. a,d) Particle trajectories in $(u_\parallel, u_\perp)$ space. Red curve represents the standard resonance momentum (Equation 2.18), dashed curves are resonance momenta computed from Equation 2.33 for ζ at which the trapped particles experience reflection. b,e) Trajectories in the $(\zeta, u_\parallel)$ space. The red resonance curve is calculated at the initial point, without ζ-dependence. c,f) Trajectories in the $(\zeta, u_\perp)$ space. Note: All modified resonance curves must start at $u_\perp = 0$, $u_\parallel = \gamma V_\mathrm{p}$, the return path of curves arcing to the left is not plotted.

For $\langle u_\perp \rangle \ll 1$, changes in $u_\perp$ during resonance dominate over changes in $u_\parallel$, so the simplified evolution of ζ, as given in Equations 2.30 and 2.31, is not valid. If we numerically solve the two equations of motion for parallel and perpendicular momentum (Eq. 2.14 and Eq. 2.15) together with the pendulum equation, $u_\perp(t)$ will go to negative values during the oscillatory motion. Using time-dependent perpendicular momentum in the definition of trapping frequency will result in deformation of the phase space trajectories, but the pathological behaviour remains. To get rid of it, we need to use the full equation of motion for ζ as given by Eq. 2.16. The second term is proportional to $u_\perp^{-1}$ and becomes dominant when $v_\parallel B_\mathrm{w} \gtrsim v_\perp B_0$. Due to its $\cos\zeta$ dependence, this term can shift the resonance momentum (as derived from the first-order resonance condition $\nu = 0$) to lower or higher values, depending on the particle's position in the trapping potential.

Figure 2.6 shows some examples of how the resonant particle behaviour changes at low perpendicular momenta. Some particles can now be trapped even though they do not cross the resonance momentum curve calculated from Equation 2.18. However,

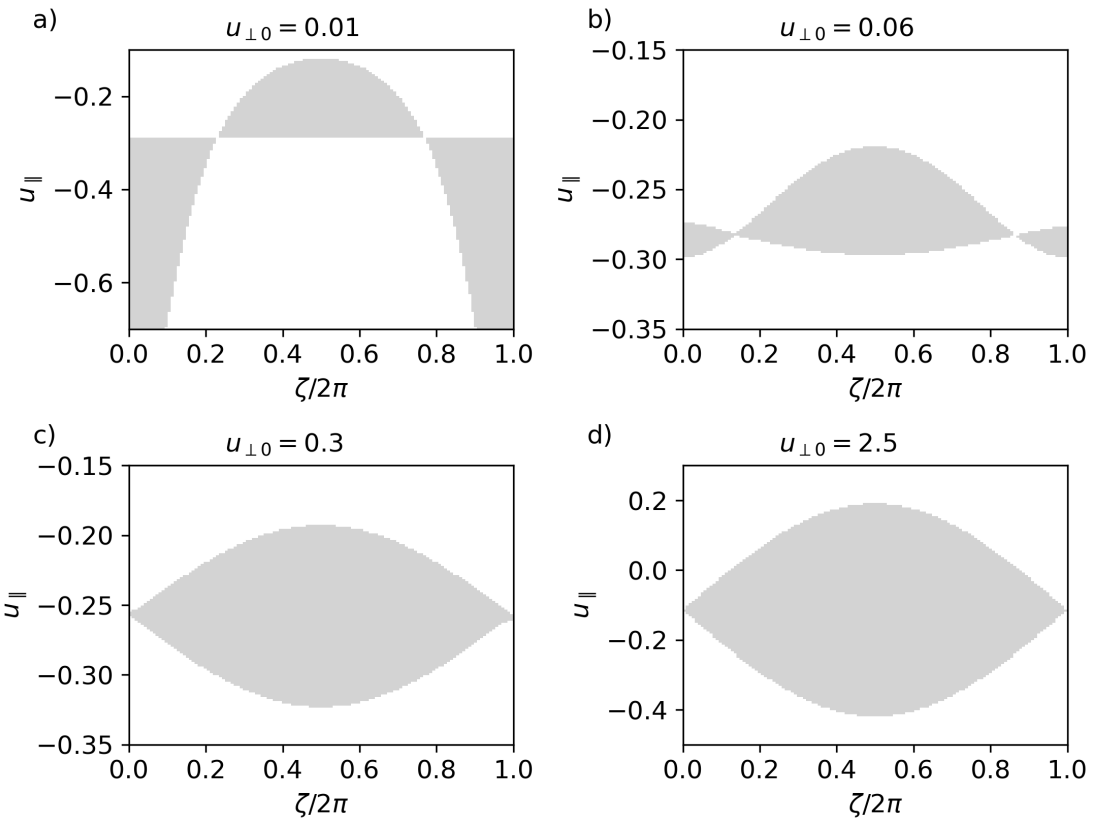

Figure 2.7: Phase space trapping regions for different initial values of perpendicular momentum. Particles which start their motion in the grey regions of the $(\zeta, u_\parallel)$ space are phase locked to the whistler wave.

trapped particles always cross the modified resonance curve

$$U_{\mathrm{R}}^{\zeta} = \frac{-k\Omega_{\mathrm{e}} + \omega\sqrt{\Omega_{\mathrm{e}}^2 + (k^2-\omega^2)(1+u_\perp^2)(1-\tilde{\Omega}_\zeta)^2}}{(k^2-\omega^2)(1-\tilde{\Omega}_\zeta)}\,, \tag{2.33}$$

$$\tilde{\Omega}_\zeta \equiv \Omega_{\mathrm{w}} \cos\zeta/(ku_\perp)\,, \tag{2.34}$$

where the ζ-dependence is included. The curves calculated for ζ values at which the trapped particles experience reflection are plotted in Figures 2.6a and 2.6d as red dashed lines, and blue circles represent the crossing points. The equilibrium points $\zeta = \{0, \pi\}$ which lay on the resonance curve U_{R} now lie on the curves U_{R}^0 and U_{R}^π. Also, the saddle point at $\zeta = 0$ can become a stable point for particles with $u_{\parallel 0} < U_{\mathrm{R}}$ and low perpendicular momenta. Examples of particles oscillating around $\zeta = 0$ are in Figures 2.6d-f.

Another view on the trapping regions is presented in Figure 2.7. Here we uniformly sampled the $(\zeta, u_\parallel)$ space for four different values of initial perpendicular momentum (panels a-d) and calculated particle trajectories over the time period of $4T_{\mathrm{tr}}$, where the trapping period was calculated from Equation 2.31 using the initial perpendicular momentum. The grey regions represent sets of initial states of particles that remained trapped – the crossing of $\zeta = -\pi$ or $\zeta = 3\pi$ was treated as an escape. We can see that at low $u_\perp$, there are two trapping regions divided by both ζ and $u_\parallel$. As the perpendicular momentum increases, the region of stability around $\zeta = 0$ diminishes until the central trapping region becomes nearly identical to the pendulum approximation results from Equation 2.30. At relativistic velocities, the central region becomes wider, but there are no apparent changes to the shape of the region.

A rigorous analysis of charged particle motion trapped in a circularly polarized wave was given by Bellan (2013) and Yoon and Bellan (2020) (see also Section 2.3 for the Hamiltonian approach). They introduced a resonance mismatch

$$\xi \equiv \gamma \frac{\nu}{\Omega_\mathrm{e}} = 1 + k u_\parallel - \gamma \frac{\omega}{\Omega_\mathrm{e}} \tag{2.35}$$

and rewrote the equations of motion for this mismatch in the form

$$\frac{\mathrm{d}^2 \xi}{\mathrm{d}t_\mathrm{p}^2} = -\frac{1}{\gamma_\mathrm{p}} \frac{\partial \Xi}{\partial \xi}\,, \tag{2.36}$$

where

$$\Xi(\xi) = \frac{1}{8}\xi^4 + \left(\frac{\Omega_\mathrm{w}^2}{\Omega_\mathrm{e}^2} - \frac{\xi_0^2}{2} - \frac{k u_{\perp 0}}{\gamma_\mathrm{p} \Omega_\mathrm{e}^2} \Omega_\mathrm{w} \cos\zeta_0 \right) \frac{\xi^2}{2} - \frac{\Omega_\mathrm{w}^2}{\Omega_\mathrm{e}^2} \xi \tag{2.37}$$

is a pseudo-potential, and subscript p denotes a quantity calculated in the frame propagating with phase velocity (a.k.a. the wave frame). They further show that depending on the values of ζ_0, $u_{\perp 0}$ and ξ_0, the potential can have a single-valley shape or a two-valley shape. The two valleys correspond to the trapping regions centred at $\zeta = 0$ and $\zeta = \pi$, as shown in Figures 2.7a and 2.7b.

Two comments are in place. Firstly, while the change in resonant particle behaviour seems dramatic, it has little impact on the energy flow between waves and particles. In Figure 2.6, only particles that cross the standard resonance curve can reach higher perpendicular momenta. Particles that are trapped but stay at low $u_\perp$ have a negligible contribution to net energy variation because, as shown by Equation 2.28, the time derivative of kinetic energy is proportional to $u_\perp$. Secondly, the low-$u_\perp$ resonant particles may be in the loss cone where the phase space density of electrons remains very low, which makes their impact on the energy flow even smaller.

To conclude the analysis of electron motion in a constant frequency, constant amplitude whistler wave, we show examples of the evolution of phase space density near the trapping region. Unlike in Figure 2.2, we have to define a model of a hot electron velocity distribution in both parallel and perpendicular directions. We choose a bi-Maxwellian distribution in momenta (without normalization)

$$f(u_\parallel, u_\perp) = \exp\left(\frac{-u_\parallel^2}{2U_{\mathrm{t}\parallel}^2}\right) \exp\left(\frac{-u_\perp^2}{2U_{\mathrm{t}\perp}^2}\right) \tag{2.38}$$

with perpendicular thermal momentum $U_{\mathrm{t}\perp} = 0.3$ and anisotropy $A = U_{\mathrm{t}\perp}^2 / U_{\mathrm{t}\parallel}^2 - 1 = 3$, which is much larger than the non-relativistic estimate on marginal instability $A = 1/3$ for $\tilde{\omega} = 0.25$ resulting from Equation 2.26. The resulting plots in Figure 2.8 show that hole formation proceeds at very different rates at different momenta, as predicted by the pendulum approximation in Eq. 2.30. The trapping frequency T_tr appearing in the labels is calculated at $u_\perp = 0.3$. The eye-shaped trapping region observed at $u_\perp = 0.05$ is less apparent at $u_\perp = 0.29$ and distorted near the boundaries of the periodic ζ-domain. The distribution integrated over perpendicular momenta is impacted by the curvature of the U_R curve, resulting in a less distinct plateau in the 1D distribution than in the case of Landau resonance. Finally, panel g) shows that the particles are losing kinetic energy, which signifies wave growth. The rapid saturation suggests that most of the energy comes from high-$u_\perp$ particles, which have short bounce periods in the trapping potential, and the approach to saturation is faster than in the case of Landau resonance.

The illustration of the evolution of phase space density near resonance provided in Figure 2.8 agrees with the analytical results of Palmadesso and Schmidt (1971). They

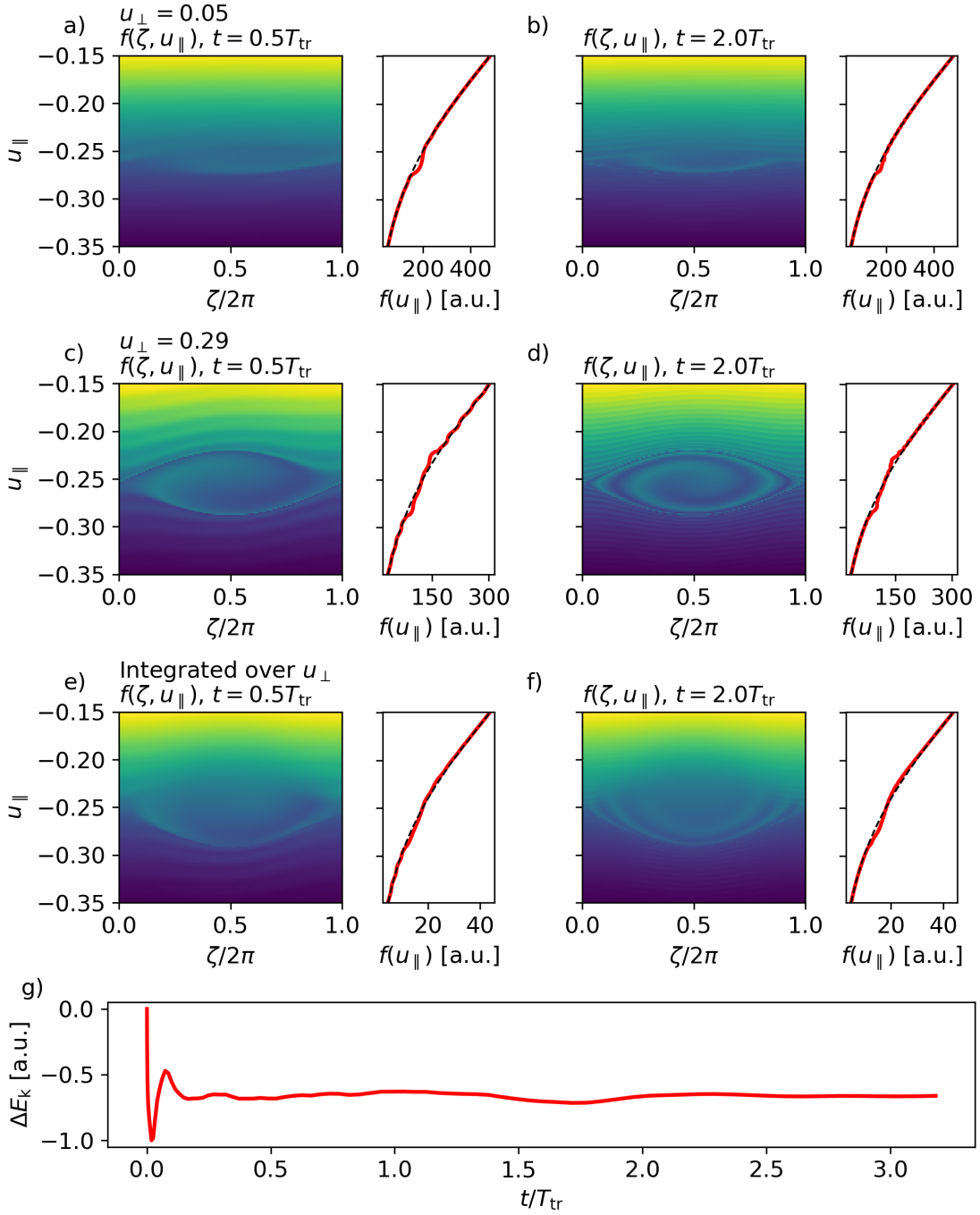

Figure 2.8: Evolution of an highly anisotropic ($A = 3$) bi-Maxwellian momentum distribution of electrons interacting with a whistler wave at the $n = -1$ cyclotron resonance. The plasma frequency is set to $\tilde{\omega}_{pe} = 5$, wave frequency and amplitude are $\tilde{\omega} = 0.25$ and $\tilde{\Omega}_w = 0.003$, respectively. Panels a,b) show 2D distributions $f(\zeta, u_\parallel)$, obtained as a cut of the full 3D distribution at $u_\perp = 0.06$, and the integrated 1D distributions $f(u_\parallel)$ at two different times $T_{tr}/2$, $2T_{tr}$. The trapping period is calculated for the thermal momentum $u_\perp = U_{t\perp} = 0.3$. Initial 1D distribution is plotted by a dashed line. Panels c,d) capture the cut at $u_\perp = 0.29$, and in panels e,f), the distributions integrated over perpendicular momenta are presented. See Section 5.2 for the simulation method used to produce the plots. Panel g) shows the change of total particle kinetic energy over time in the resonance region.

followed the approach of O'Neil (1965) used to analyze nonlinear Landau damping (see also Section 2.1) and applied it to the interaction of a Maxwellian velocity distribution of electrons with a constant amplitude whistler wave. Unfortunately, this approach does no apply to chorus emissions. The effects of the perturbed electron distribution on the whistler wave dispersion properties are essential for explaining the growth of chorus elements. Furthermore, the constant amplitude approximation $\gamma_{\mathrm{NL}} T_{\mathrm{tr}}/2\pi \ll 1$ goes against the observations of steep amplitude gradients in chorus subpackets mentioned in Section 1.2.3. In Chapter 3, we review theories that attempt to deal with the shortcomings of classical computations.

2.2.1 Inhomogeneous background

In the previous section, we have assumed a homogeneous background which allowed us to treat the system as 2π periodic in ζ. In a more realistic scenario, both magnetic field strength and plasma density change with distance h along the field line. The existence of a gradient $\partial B_0/\partial h$ is connected to field line convergence, and in the first-order expansion around the guiding centre motion, we can represent its effects by an additional radial component (Gurnett and Bhattacharjee (2017), Sec. 3.4)

$$\boldsymbol{B}_{0\perp} = -\frac{1}{2}\frac{\partial B_0}{\partial h}\boldsymbol{r}_{\mathrm{L}}\,, \tag{2.39}$$

where

$$r_{\mathrm{L}} = \frac{u_\perp}{\Omega_{\mathrm{e}}} \tag{2.40}$$

is the Larmor radius. The equations of motion for $u_\parallel$ and $u_\perp$ become

$$\frac{\mathrm{d}u_\parallel}{\mathrm{d}t} = \frac{\Omega_{\mathrm{w}} u_\perp \sin\zeta}{\gamma} - \frac{u_\perp^2}{2\gamma\Omega_{\mathrm{e}}}\frac{\partial\Omega_{\mathrm{e}}}{\partial h}\,, \tag{2.41}$$

$$\frac{\mathrm{d}u_\perp}{\mathrm{d}t} = -\left(\frac{u_\parallel}{\gamma} - V_{\mathrm{p}}\right)\Omega_{\mathrm{w}}\sin\zeta + \frac{u_\parallel u_\perp}{2\gamma\Omega_{\mathrm{e}}}\frac{\partial\Omega_{\mathrm{e}}}{\partial h}\,. \tag{2.42}$$

The curvature drift, perpendicular to the curvature radius vector and $\boldsymbol{B}_0$, is neglected. Since $\Omega_{\mathrm{e}}(h)$ is now h-dependent, we normalize to $\Omega_{\mathrm{e}0} = \Omega_{\mathrm{e}}(0)$. The second terms in Equations 2.41 and 2.42 represent adiabatic motion in a magnetic trap. The inhomogeneity in plasma density n_{e} is introduced through h-dependent ω_{pe}, which appears in V_{p} and k (see Equation 1.58).

Now we can repeat the approximate calculation leading to the pendulum equation for resonance motion (Equation 2.30). The extra terms coming from $\partial k/\partial h$ and $\partial\Omega_{\mathrm{e}}/\partial h$ are not ζ-dependent, so we arrive at a pendulum equation with a torque

$$\frac{\mathrm{d}^2\zeta}{\mathrm{d}t^2} = \omega_{\mathrm{tr}}^2(\sin\zeta + S)\,, \tag{2.43}$$

where we introduced the inhomogeneity factor

$$S = \frac{1}{\omega_{\mathrm{tr}}^2\gamma_{\mathrm{R}}^2}\left(s_n\frac{\partial n_{\mathrm{e}}}{\partial h}\frac{1}{n_{\mathrm{e}}} + s_\Omega\frac{\partial\Omega_{\mathrm{e}}}{\partial h}\frac{1}{\Omega_{\mathrm{e}}}\right) \tag{2.44}$$

with

$$s_n = \frac{kU_{\mathrm{R}}^2}{2}(1 - V_{\mathrm{p}}^2)\,, \tag{2.45}$$

$$s_\Omega = U_{\mathrm{R}}\Omega_{\mathrm{e}}\left(1 + \frac{1 - V_{\mathrm{p}}^2}{2}\frac{\Omega_{\mathrm{e}} - \gamma_{\mathrm{R}}\omega}{\Omega_{\mathrm{e}} - \omega}\right) - \frac{k\langle u_\perp\rangle^2}{2}\,. \tag{2.46}$$

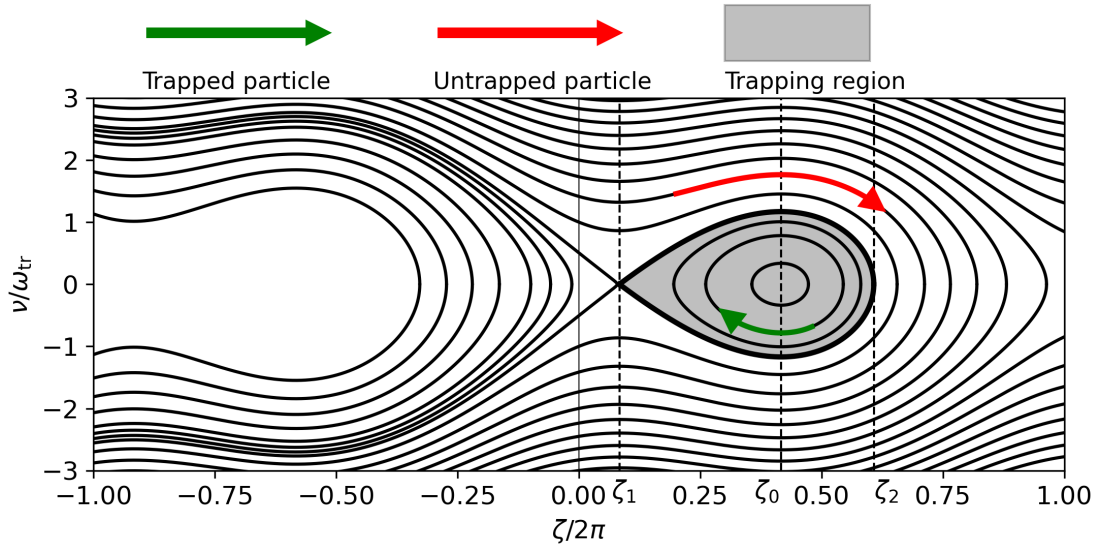

Figure 2.9: Phase space diagram showing the behaviour of electrons near cyclotron resonance as described by Equation 2.43. The plotted black lines represent streamlines at a given distance h along the magnetic field line, not particle trajectories. Particles in the trapping region (green arrow) oscillate around a constant phase ζ_0. Untrapped particles (red arrow) are not phase-locked. The 2π-periodic ζ dimension is duplicated to provide a better picture of the trajectory shape.

A detailed derivation of the inhomogeneity factor can be found in Vomvoridis and Denavit (1979) and Omura et al. (2008), with the additional inclusion of the wave frequency drift rate $\partial\omega/\partial t$. We will return to this in Chapter 3.

Let us examine the particle trajectories in (ζ, ν) space. Notice that unlike in the homogeneous case, ν is now h-dependent through k, so the particle trajectories will have a different shape in the $(\zeta, u_\parallel)$ space than in the (ζ, ν) space. We must therefore normalize ν to the trapping frequency and use a fixed value of S. If we assume that the electron is travelling from $h > 0$ towards $h = 0$, where the magnetic field strength has a global minimum, and that density is also growing away from $h = 0$, then S must be negative for U_R negative. In Figure 2.9, we plot the trajectories and trapping region for $S = -0.5$. The trajectories can be expressed as a family of curves

$$\nu^2 + 2\omega_\mathrm{tr}^2(\cos\zeta - S\zeta) = C\,, \tag{2.47}$$

where C is a real constant. The separatrix, which represents the boundary of the trapping region, has a function form

$$\nu_\mathrm{s} = \pm\omega_\mathrm{tr}\sqrt{2(\cos\zeta_1 - \cos\zeta + S(\zeta - \zeta_1))}\,, \quad \zeta_1 < \zeta < \zeta_2\,, \tag{2.48}$$

where $\zeta_0 = \pi - \arcsin(-S)$ is at the stable point, $\zeta_1 = \arcsin(-S)$ is at the saddle point, and ζ_2 is at the right boundary of the separatrix. For $|S| > 1$, the resonance mismatch $\nu(t)$ never changes sign, and thus the particles would never become phase-locked.

For $u_\perp \ll 1$, the trajectories are more difficult to analyze. The numerical solution of the full equations of motion (Eqs. 2.41, 2.42, 2.16) for some representative initial values is shown in Figure 2.10. We choose $\tilde{\omega} = 0.25$, $\tilde{\omega}_\mathrm{pe} = 5$ and $\tilde{\Omega}_\mathrm{w} = 0.01$ (all constant values), and a magnetic field with a constant gradient $\tilde{\Omega}_\mathrm{e} = 1 + ah$. All particles start at $h = 0$ and a is chosen so that $S(h = 0) = -0.5$ for $u_\perp(h = 0) = 0.3$. Similar to the analysis in Figure 2.6, we can identify two stable points at lower perpendicular momenta, but the trajectories feature a distortion similar to the 'fish-like' streamlines in Figure 2.9. It is important to notice that the inhomogeneity factor becomes very large

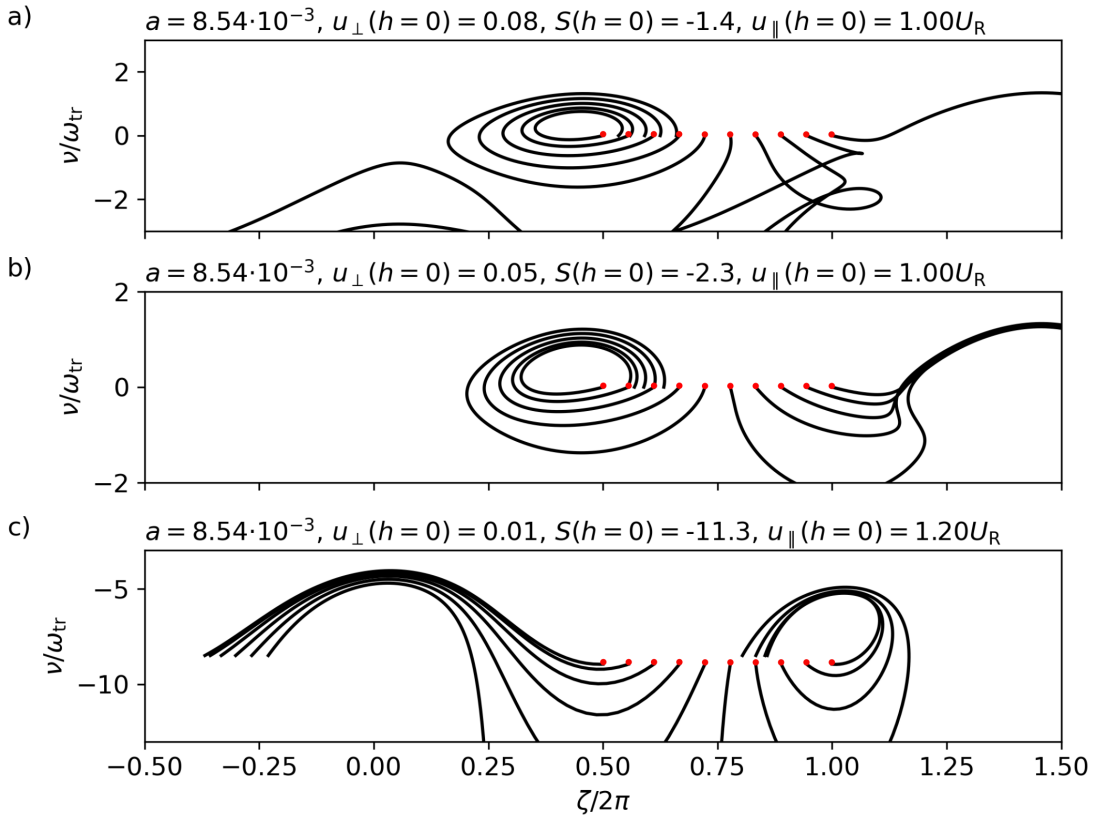

Figure 2.10: Motion of low-$u_\perp$ particles resonating with a whistler wave in an inhomogeneous magnetic field. Particles start at angles $\zeta \in [\pi, 2\pi]$ in exact resonance (red circles) and are stopped when they return to their initial ν/ω_tr, or when they escape from the depicted range of ζ. Particles in panel c) start away from the approximate resonance $u_\parallel = U_\mathrm{R}$ to show the stable trajectories around $\zeta = 2\pi$.

at low $u_\perp$ due to its proportionality to ω_tr^{-2}; for $S = -0.5$ at $u_\perp = 0.01$, there would be no apparent distortion. Since S is not constant along h (result of not fixing $u_\perp$) and we are not using the first-order expansion near resonance, the variables ζ and ν do not form a conjugate pair of position and momentum, so trajectory crossings become possible.

2.2.2 Quasiparallel waves

The assumption of parallel propagation of whistler waves along magnetic field lines is never fully satisfied in planetary magnetospheres. Even with strong field-aligned density enhancements, the wave normal angle can reach up to about 30° (Katoh, 2014; Hanzelka and Santolík, 2019). We will now briefly look at the motion of electrons resonating with a whistler wave in the quasiparallel approximation $\sin\theta_\mathrm{k} = \theta_\mathrm{k}$, $\cos\theta_\mathrm{k} = 1$, which is satisfactory in most cases of ducted propagation.

The quasiparallel approximation of cold dispersion relation has a whistler-mode solution with a small perpendicular wave vector component $k_\perp \approx \theta_\mathrm{k} k_\parallel$, where $k_\parallel$ is the same as in the ideal parallel propagation case. The electric and magnetic field components are then simply

$$\boldsymbol{B}_\mathrm{w} = B_\mathrm{w}\left(\cos\psi_\mathrm{B}, \sin\psi_\mathrm{B}, -\theta_\mathrm{k}\cos\psi_\mathrm{B}\right) \tag{2.49}$$

$$\boldsymbol{E}_\mathrm{w} = V_\mathrm{p} B_\mathrm{w}\left(\sin\psi_\mathrm{B}, -\cos\psi_\mathrm{B}, \theta_\mathrm{k}\sin\psi_\mathrm{B}\right) . \tag{2.50}$$

The additional parallel component in $\boldsymbol{B}_\mathrm{w}$ is negligible, $\theta_\mathrm{k} B_\mathrm{w} \ll B_0$, so we can focus

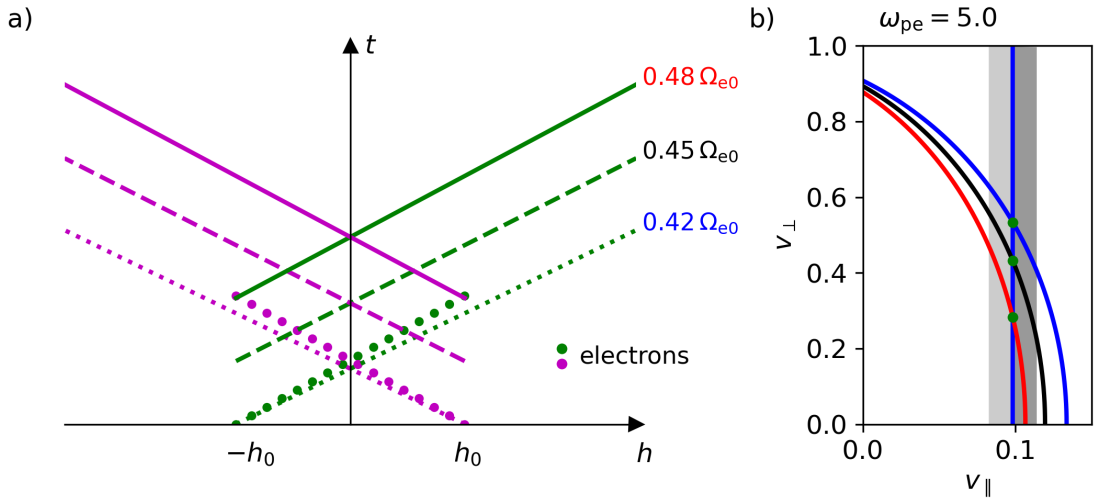

Figure 2.11: Schematic illustration of Landau resonance influencing the cyclotron resonant electrons of counter-streaming waves. a) Electron travelling along the field line (large dots) resonates with a co-streaming quasiparallel whistler wave at frequency $0.42\,\Omega_{e0}$ (dotted line). The parallel velocity of the electron is only slightly lower than group velocity of the wave, resulting into a long interaction time and a large perturbation in the velocity distribution function (grey areas in panel b: darker color represents increased PSD). The same electron will also experience cyclotron-resonant scattering and trapping from counter-streaming waves at slightly higher frequencies, depending on the perpendicular velocity. However, the cyclotron interaction will not result into formation of the electron hole depicted in Figure 2.8 because of the previous formation of a plateau in the parallel velocity distribution. The off-equatorial position of the wave sources and the growth in frequency are inspired by the chorus studies of Demekhov et al. (2020), Hanzelka et al. (2020) and Nogi and Omura (2022). b) $n = 0$ resonant velocity for a $\tilde{\omega} = 0.42$ whistler wave with positive group velocity, and $n = -1$ resonant velocities for three different frequencies distinguished by color. Green dots show the crossing points at which the electron from panel a) lies in exact Landau resonance with the co-streaming wave and in exact cyclotron resonance with the counter-streaming wave.

only on the electric component. The parallel motion of an electron is now described by

$$\frac{\mathrm{d}u_\parallel}{\mathrm{d}t} = \frac{\Omega_\mathrm{w} u_\perp \sin\zeta}{\gamma} - V_\mathrm{p}\Omega_\mathrm{w}\theta_\mathrm{k}\sin\psi_\mathrm{B}\,. \tag{2.51}$$

Except for ultrarelativistic particles, the $n = 0$ resonance represented by the second term is always far away from the $n = -1$ resonance represented by the first term. Thus when an electron is experiencing a strong resonant cyclotron interaction, the Landau resonance will result in high-frequency, low-amplitude oscillation in $u_\parallel$ with little impact on the overall particle acceleration.

However, the Landau resonance can have a substantial impact on the whistler mode, even in the case of short wave packets where a correspondingly short interaction time would be expected. Using the approximate group velocity formula from Equation 1.59 (with quasiparallel corrections based on Equation 1.60), we get that $V_\mathrm{g} = V_\mathrm{R0}$ for

$$\omega = \frac{\Omega_\mathrm{e}\cos\theta_\mathrm{k}}{2} \approx \frac{\Omega_\mathrm{e}}{2}\,. \tag{2.52}$$

Therefore, a particle in Landau resonance with a whistler wave packet at half of the local gyrofrequency will not leave the packet until ω/Ω_e changes. The long-term Landau resonance activity at $v_\parallel = V_\mathrm{g}$ is recognized as one of the reasons for the observed decrease in wave power of whistler emissions near $\Omega_\mathrm{e}/2$ (Omura et al., 2009; Li et al., 2019).

Another interesting relation between the characteristic velocities near $\omega = \Omega_e/2$ is

$$V_{R1} = \frac{\Omega_e}{k}\left(\frac{1}{\gamma} - \frac{1}{2}\right) \approx -V_{R0}\,, \tag{2.53}$$

where we have used $\gamma \approx 1$ and the quasiparallel approximation. Conversely, the equation $V_{R1} = -V_{R0}$ can be solved for ω with an arbitrary $\gamma > 1$, and we arrive at

$$\omega = \frac{\Omega_e}{2\gamma}\,. \tag{2.54}$$

This means that when a whistler wave with frequency just below Ω_e propagates in both direction along field line, a plateau will be formed in parallel velocity distribution of weakly relativistic electrons due to Landau resonance, which will disturb the wave-particle power transfer during cyclotron resonance. This connection between Landau and cyclotron resonance may be another reason for the aforementioned power gap in whistler-mode chorus spectrum, and is expected to play a major role in future 2D generalizations of chorus emission models (see Hanzelka et al. (2020) or Chapter 4 for a 1D model). The time-space configuration of this process is further illustrated in Figure 2.11.

For increasing values of θ_k, the $n = 0$ resonance motion will become strongly dependent on the transverse wavefield through a term $\sim B_{w\perp} J_1(\beta)$, where J is the Bessel function of the first kind and $\beta = u_\perp k_\perp/\Omega_e$. Even in the quasiparallel approximation, β can become large in a high-density plasma environment. For $\tilde{\Omega}_e = 1$, $u_\perp = 0.3$, $\tilde{\omega} = 0.25$ and $\theta_k = 30°$, we get $\beta = 0.96$ with $\tilde{\omega}_{pe} = 10$. Since J_1 has its first maximum at $\beta = 1.84$, we conclude that whistler-mode emissions which are characterized by larger θ_k, e.g. the plasmaspheric hiss (see Section 1.2.3), always require a full two-dimensional treatment. The equations of motion and second-order cyclotron resonance condition in an inhomogeneous magnetic field for general θ_k can be found in Omura et al. (2019).

2.3 Hamiltonian approach to wave-particle resonance

The Hamiltonian of a charged, relativistic particle moving through the field of an electromagnetic wave in the magnetosphere can be written in natural units as (Artemyev et al., 2018)

$$\mathcal{H} = \sqrt{1 + (\boldsymbol{U} - q\boldsymbol{A})^2} = \gamma\,, \tag{2.55}$$

where $\boldsymbol{U} = \boldsymbol{u} + \boldsymbol{A}$ is the canonical momentum and $\boldsymbol{A} = \boldsymbol{A}_w + \boldsymbol{A}_0$ is the vector potential of the wave and the background magnetic field. For a purely electromagnetic wave like the parallel-propagating whistler wave, there is no scalar potential. The whistler-wave potential has two components

$$A_{wx} = A_w \cos\psi_B\,, \quad A_{wy} = A_w \sin\psi_B \tag{2.56}$$

with

$$\psi_B(t,h) = \omega t - \int_0^h k(h')\mathrm{d}h'\,, \tag{2.57}$$

and the dipole field has one component

$$A_{0x} = -yB_0(h)\,. \tag{2.58}$$

With a carefully chosen canonical transformation, the gyro-averaged electron Hamiltonian for the $n = -1$ resonance, expanded to the lowest order of the relativistic first adiabatic invariant, can be expressed as (Albert et al., 2021; Albert, 1993)

$$\mathcal{H}(I,\zeta;h) = \mathcal{H}_0(I,h) + \mathcal{H}_1(I,h)\sin\zeta\,, \tag{2.59}$$

where

$$I = \frac{u_\perp^2}{2}\frac{\omega}{\Omega_\mathrm{e}} \tag{2.60}$$

is proportional to the approximate first adiabatic invariant and the distance h is an autonomous variable which replaces time as a curve parameter (but changes sign at reflection points). The function

$$\mathcal{H}_1(I,h) = -\frac{B_\mathrm{w}}{B_0}\sqrt{\frac{\Omega_\mathrm{e}^3}{\omega k^2}}\frac{\sqrt{2I}}{p_\parallel} \tag{2.61}$$

represents a wave-induced perturbation to the adiabatic gyromotion and bounce motion described by

$$\mathcal{H}_0(I,h) = \frac{k}{\omega}(I - C_\mathrm{m}) - p_\parallel\,. \tag{2.62}$$

Here, $C_\mathrm{m} = I - \gamma$ is a constant of motion and

$$p_\parallel = \sqrt{(I - C_\mathrm{m})^2 - 1 - 2\frac{\Omega_\mathrm{e}}{\omega}I} \tag{2.63}$$

is a momentum-like variable, reducing to the parallel momentum $u_\parallel$ in an unperturbed system.

The resonance is defined by

$$\frac{\mathrm{d}\zeta}{\mathrm{d}t} = \frac{\partial\mathcal{H}}{\partial I} = 0\,, \tag{2.64}$$

and solutions of this equation give the resonance values

$$I_\mathrm{R} = \frac{u_\parallel^2}{2\omega\Omega_\mathrm{e}}(k^2 - \omega^2) + \frac{k}{\omega}u_\parallel + \frac{\Omega_\mathrm{e} - \omega}{2\omega}\,, \tag{2.65}$$

and

$$p_{\parallel\mathrm{R}} \approx u_{\parallel\mathrm{R}} = \frac{1}{k}(\omega\gamma - \Omega_\mathrm{e}) = U_\mathrm{R}\,, \tag{2.66}$$

where the approximation $\partial\mathcal{H}_1/\partial I = 0$ has been used. The Hamiltonian $\mathcal{H}(I,\zeta;h)$ can be then expanded around the resonance to the second order,

$$\mathcal{H}(I,\zeta;h) = \mathcal{H}_0(I_\mathrm{R},h) + \frac{1}{2}\frac{\partial^2\mathcal{H}_0}{\partial I^2}(I - I_\mathrm{R})^2 + \mathcal{H}_1(I,h)\sin\zeta\,, \tag{2.67}$$

providing a very close approximation to the phase space motion described in Figures 2.5 or 2.6. Replacing I and $u_\parallel$ by I_R and U_R in $\mathcal{H}_1$ results in electrons reaching velocities $v_\perp < 0$, similar to the description provided by Equation 2.17. The nonrelativistic form of the resonance Hamiltonian in an inhomogeneous field was already guessed by Vomvoridis and Denavit (1979) in the form of the total energy of a mathematical pendulum with a torque.

The advantage of the Hamiltonian approach comes from the easy identification of conserved variables and from the reduction of the second-order equations of motion to the first-order Hamilton's equations, which are easily integrated by the Störmer-Verlet algorithm or any other symplectic integrator (Press et al., 1992). Other formulations of the resonant Hamiltonian exist that yield directly solvable quadratics (Albert et al., 2021). Furthermore, the vector potential can be straightforwardly expanded to include oblique whistler waves, making use of the identity

$$\sin\left(\psi_\mathrm{B} - \frac{u_\perp k_\perp}{\Omega_\mathrm{e}}\sin\varphi\right) = -\sum_{n=-\infty}^{\infty} J_n\left(\frac{u_\perp k_\perp}{\Omega_\mathrm{e}}\right)\sin\zeta_n\,, \tag{2.68}$$

where $\zeta_n = n\varphi - \psi_B$. The resulting Hamilton's equations are much more formidable than the parallel case discussed above but can be treated in a similar way, performing expansions around the nearest resonance (Albert, 1993; Albert et al., 2012).

The disadvantage of the Hamiltonian method becomes apparent when analysing waves with variable frequency, as is the case of chorus discussed in Chapter 3. Notice that the wave frequency in the definition of ψ_{B} in Equation 2.57 is considered to be constant. A chirping wave with $\partial\omega/\partial t \neq 0$ would introduce a time dependence into the Hamiltonian that cannot be transformed away by a clever choice of coordinates, making $\partial H/\partial I$ explicitly dependent on time. The Hamiltonian formalism then loses the advantage stemming from the simple and efficient numerical solvers for time-independent Hamilton equations.

3. Growth and propagation of chorus emissions

The electron motions in a whistler-wave potential analyzed in Chapter 2 form the basis for theories of chorus wave growth. In the following paragraphs, we provide a brief overview of the chorus spectral features and wave propagation properties, followed by a review of the nonlinear growth theory of Omura et al. (NGTO) for parallel propagating waves. Some other possible explanations of natural chorus generation are summarized towards the end of the chapter. For more reviews on the history and current state of research on chorus emissions, see Omura et al. (1991), Gołkowski and Gibby (2017) and Tao et al. (2020).

In this chapter, we retain the normalization $m_\mathrm{e} = 1$, $e = 1$ form previous sections, but the speed of light c is written explicitly. The usage of normalized quantities is summarized in the List of Symbols at the end of the thesis.

3.1 Spacecraft observations

In the short overview of plasma wave emissions in the inner magnetosphere given in Section 1.2.3, we established the typical spectral features of the chorus emission and its distribution throughout the magnetosphere. Taubenschuss et al. (2014) analyzed over 500 burst-mode snapshots gathered by the THEMIS satellite and found that the lower band is split into two populations based on the wave normal angle: quasiparallel waves below the Gendrin angle and oblique waves near the resonance cone. The upper band shows no clear division, and is sometimes connected to the lower band, i.e. the spectral gap at $0.5\Omega_\mathrm{e}$ is not always present (Kurita et al., 2012; Teng et al., 2019; Gao et al., 2019). As mentioned in Section 2.2.2 when discussing the effect of Landau damping on quasiparallel whistler waves, this gap is associated with obliquity and thus will not appear in the theory of parallel chorus wave growth described in Section 3.2. As established by many observational studies (Taubenschuss et al., 2014; Santolík et al., 2014b; Agapitov et al., 2018), the very oblique chorus waves are much less common than the parallel ones and their origin is likely associated with Landau resonant interaction near the resonance cone (Soto-Chavez et al., 2014; Mourenas et al., 2015) rather than with the cyclotron resonance. Furthermore, the oblique, lower-band chorus consists mainly of falling tones, while risers dominate the quasiparallel propagation (Taubenschuss et al., 2014).

Research focusing on lower-band waves reveals a very narrow average bandwidth of $0.01\Omega_\mathrm{e}$ (Gao et al., 2014) and the frequency sweep rates ranging from about $5 \cdot 10^{-6}\Omega_\mathrm{e}^2$ to $10^{-4}\Omega_\mathrm{e}^2$ (Macúšová et al., 2010; Teng et al., 2017). The typical RMS magnetic field amplitudes range from 0.01 nT to 0.3 nT (Li et al., 2011), with some elements occasionally reaching peak amplitudes $B_\mathrm{w} > 1\,\mathrm{nT}$ and $B_\mathrm{w}/B_0 > 0.01$ (Santolík et al., 2014a; Gao et al., 2014). Examples of a series of very intense chorus elements detected by the Van Allen Probes are shown in Figure 3.1.

A unique feature of the lower-band chorus is the amplitude modulations of the elements, often described as subpackets (Santolík et al., 2003a, 2014a). Figures 3.2a-b,e-f show the time series of magnetic field components corresponding to elements highlighted by magenta rectangles in Figure 3.1. Statistical analysis of Santolík et al. (2014a) shows that the length of subpackets exhibits a large variance, with an average near 15 ms. The rapid changes in instantaneous frequency near amplitude minima (Figure 3.2c,g) hint at jumps in the wave phase. However, a smooth evolution of phase

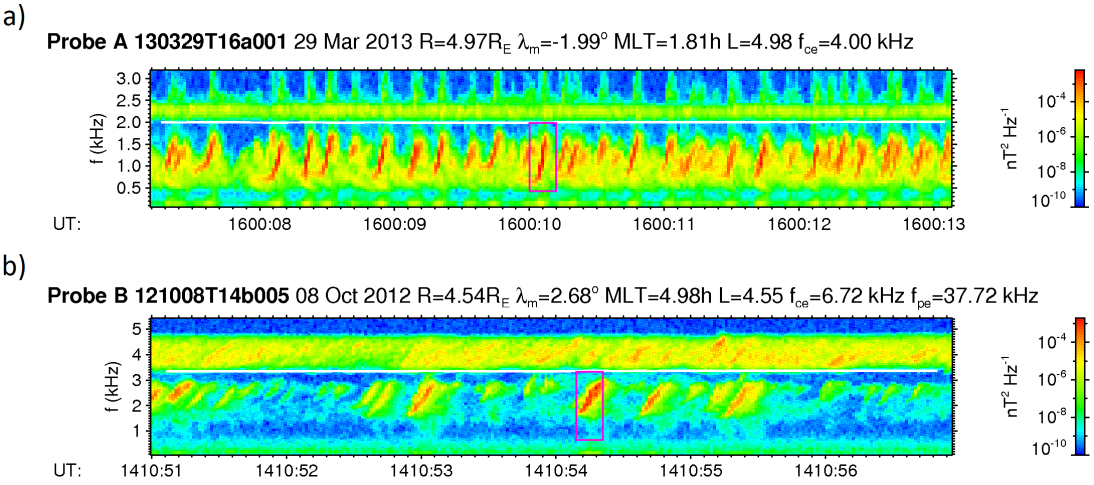

Figure 3.1: Two examples of what we consider "typical" chorus elements, taken from the dataset assembled by Santolik et al. (2015). Magnetic power spectral density was obtained from a 6-second waveform snapshot recorded by the Van Allen Probes EMFISIS instrument. Magenta boxes highlight the parts of the spectrum that were processed by Hilbert transform in Figure 3.2.

might be more likely at the beginning of an element, as demonstrated by Crabtree et al. (2017) and Foster et al. (2021). Based on simulations of Nogi and Omura (2022), the character of subpackets might be strongly related to their distance from the source region. However, the source region has a field-aligned width of thousands of kilometres (Santolík et al., 2004), complicating the definition of distance travelled from the source. An extended discussion is provided in Section 4.4 (see also the phenomenological model of Tao et al. (2021), briefly reviewed in Section 3.3.4), but the origin of the subpacket structure is currently still unclear.

Another interesting property of the high-amplitude chorus subpackets is the variations in wave normal angle. Since we are near the source, Landau damping at large θ_k values has not acted long enough to suppress such features (Omura et al., 2009; Hsieh and Omura, 2018). The spikes in obliquity apparently arise from a mismatch in amplitude modulations of the perpendicular and the parallel magnetic field component, as seen in the right half of Figure 3.2d. This suggests that a complete description of chorus formation requires a two-dimensional treatment, possibly with the inclusion of transverse density irregularities that modulate the field-aligned power distribution (see Katoh (2014) and the comments about ducting below Equation 1.82). Such theories are currently not available, and a detailed analysis of the two-dimensional behaviour goes beyond the scope of this thesis.

Finally, it should be mentioned that the well-behaved chorus elements, with a very narrow bandwidth and nearly constant chirping rate, are not the only form of chorus. An example of chorus elements with more diffuse features is shown in Figure 3.3a. Similarly, the subpacket structure is not always present, as demonstrated by the waveform presented in Figure 3.4. The evolution of such emissions cannot be described with the plane wave approximation employed in the nonlinear growth theory (Section 3.2); therefore, the results of Chapters 4 and 5, which are based on the NGTO, do not apply to these more broadband types of chorus.

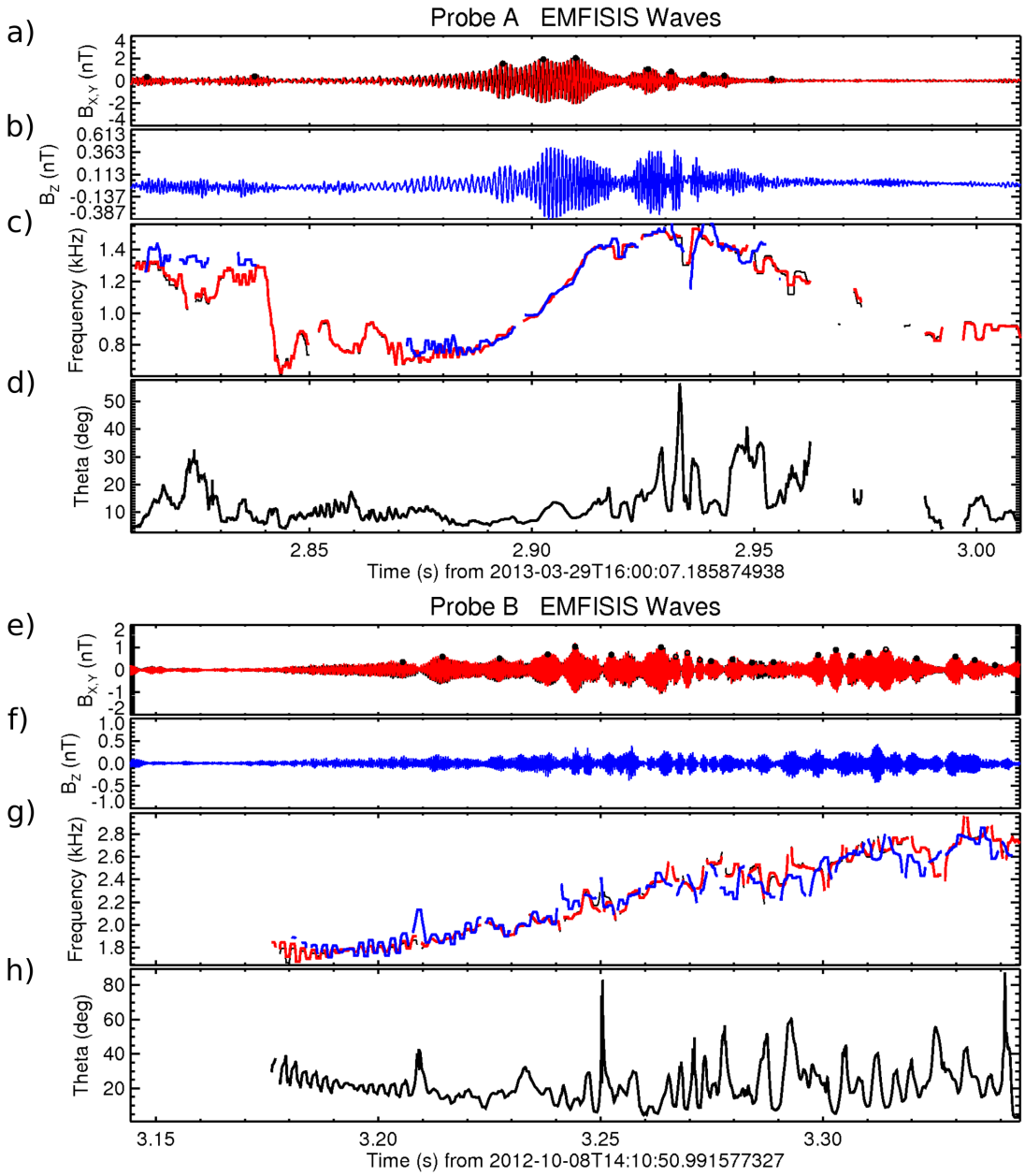

Figure 3.2: a,b) Perpendicular ($B_{x,y}$) and parallel (B_z) magnetic field components of the highlighted chorus element from Figure 3.1. Black dots mark amplitude peaks with prominence of at least 50 pT. The black line in the background is the total magnetic field of the fluctuations. c) Instantaneous frequency obtained from the analytic signal. d) Wave normal angle calculated by SVD methods from the instantaneous spectral matrices. e-g) The same plots as previous panels, but for the element from Figure 3.1b.

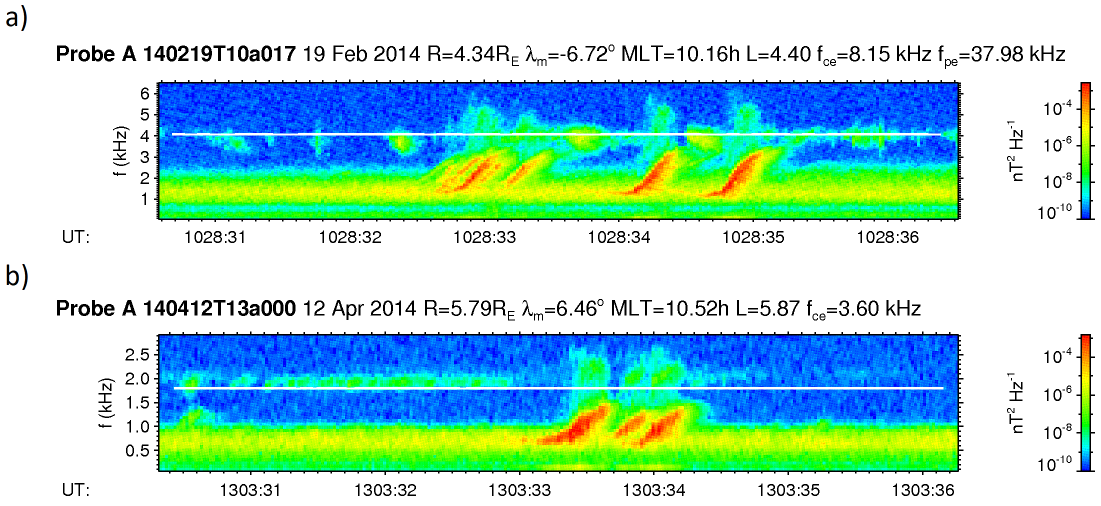

Figure 3.3: Two spectrograms constructed from EMFISIS waveform snapshots showing intense chorus elements with a broader frequency spectrum.

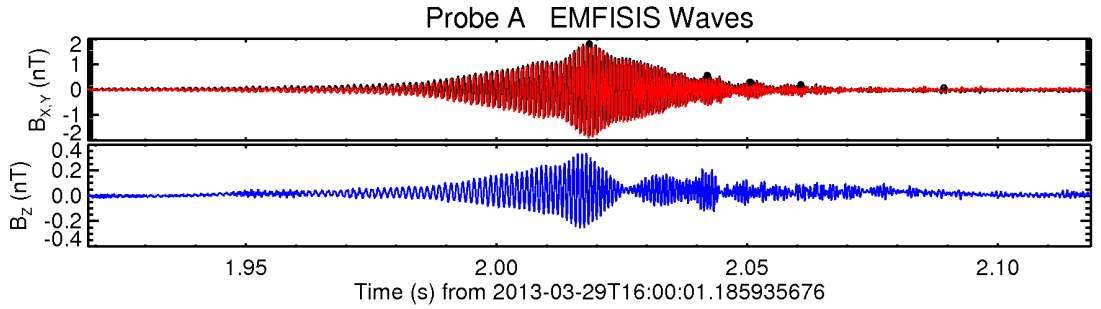

Figure 3.4: Waveform of a chorus element without a clear subpacket structure. The plots have the same format as Figures 3.2a,b.

3.2 Nonlinear growth theory of Omura et al.

In a series of papers starting with Omura et al. (2008), a theory was developed that attempts to describe the frequency drift and amplitude growth of chorus emissions as observed by spacecraft and in kinetic simulations. This theory is the basis for the chorus wavefield model described in Chapter 4. The summary of the theory presented below is largely based on the recent review paper Omura (2021). Details concerning the oblique propagation of chorus are left out.

3.2.1 Wave equations

The parallel-propagating monochromatic whistler wave defined in Equations 2.11–2.12 can be rewritten in a complex form as

$$\tilde{B}_\mathrm{w} = B_\mathrm{w} \exp(\mathrm{i}\psi_\mathrm{B})\,, \tag{3.1}$$

$$\tilde{E}_\mathrm{w} = E_\mathrm{w} \exp(\mathrm{i}\psi_\mathrm{E})\,, \tag{3.2}$$

where $\psi_\mathrm{E} = \psi_\mathrm{B} - \pi/2$. The Maxwell curl equations for this wavefield are

$$\mathrm{i}\frac{\partial \tilde{E}_\mathrm{w}}{\partial h} = -\frac{\partial \tilde{B}_\mathrm{w}}{\partial t}\,, \tag{3.3}$$

$$\mathrm{i}\frac{\partial \tilde{B}_\mathrm{w}}{\partial h} = \mu_0(\tilde{J}_\mathrm{c} + \tilde{J}_\mathrm{R}) + \frac{1}{c^2}\frac{\partial \tilde{E}_\mathrm{w}}{\partial t}\,. \tag{3.4}$$

The current density is decomposed into two components: the cold current $\tilde{J}_\mathrm{c}$, which captures the flow of cold electron fluid and gives rise to the cold dispersion relation for whistler waves, and the transverse resonant current J_R that arises from the nongyrotropy of hot electron distribution, which forms due to cyclotron resonant interaction of electrons with large amplitude waves. The resonant current can be decomposed into components parallel to the wave electric and magnetic fields,

$$\tilde{J}_\mathrm{R} = (J_\mathrm{B} - \mathrm{i}J_\mathrm{E})\exp(\mathrm{i}\psi_\mathrm{B})\,. \tag{3.5}$$

Following Omura et al. (2008), we use the Lorentz force acting on electrons to eliminate J_c and rewrite the Maxwell equations 3.3–3.4 without E_w. Dropping all higher-order derivatives of B_w and ψ_B and all derivatives of $\tilde{J}_\mathrm{R}$, we decompose the resulting equation into the real and imaginary part and obtain

$$\frac{\partial B_\mathrm{w}}{\partial t} + V_\mathrm{g}\frac{\partial B_\mathrm{w}}{\partial h} = -\frac{\mu_0 V_\mathrm{g}}{2}J_\mathrm{E} \tag{3.6}$$

and

$$c^2k^2 - \omega^2 - \frac{\omega\omega_\mathrm{pe}^2}{\Omega_\mathrm{e} - \omega} = \mu_0 c^2 k\frac{J_\mathrm{B}}{B_\mathrm{w}}\,, \tag{3.7}$$

where we have used the whistler-mode group velocity from the left side of Equation 1.59. These equations have been first derived in a slightly different form by Nunn (1971).

We observe that the resonant current component J_E modifies the wave amplitude, and the $J_\mathrm{B}/B_\mathrm{w}$ quantity modifies the dispersion relation. While Equation 3.6 could be in principle solved numerically, given suitable initial conditions and knowledge of J_E, Equation 3.7 is more difficult to interpret. First, it breaks for $B_\mathrm{w} \to 0$, unless J_B goes to 0 as B_w or faster (which will be later shown not to be the case in the NGTO). Second, the changes in frequency indicated by the modified dispersion contradict the initial assumption of a monochromatic wave. Omura and Nunn (2011) view the growth of chorus elements as a triggering process, where a strong initial wave of frequency ω_0 forms the resonant current and preserves its spatial structure given by a fixed wavenumber k_0. Under this assumption, we can write in Equation 3.7 $k = k_0$, $\omega = \omega_0 + \delta\omega$, where $\delta\omega \ll \omega_0$ is a small perturbation in frequency. Solving for $\delta\omega$, we get

$$\delta\omega = \frac{-\mu_0 V_\mathrm{g}}{2}\frac{J_\mathrm{B}}{B_\mathrm{w}}\,. \tag{3.8}$$

Nunn (1974) suggests that ω_0 must be changed periodically to reflect that a triggered wave has replaced the initial triggering wave at a higher frequency. Unfortunately, it is unclear how to implement this stepping up in frequency. We will tackle this issue in Chapter 4, using a modified version of the chorus equations from Section 3.2.3.

3.2.2 Resonant current

To evaluate the resonant current appearing in Equations 3.6 and 3.7, we need to find the perturbed distribution function of hot electrons. Following Omura et al. (2009), we choose the initial equatorial distribution to be bi-Maxwellian in momenta,

$$f_\mathrm{eq}(u_\parallel, u_\perp) = \frac{n_\mathrm{eq}}{(2\pi)^{3/2}U_{\mathrm{t}\parallel 0}U_{\mathrm{t}\perp 0}^2}\exp\left(-\frac{u_\parallel^2}{2U_{\mathrm{t}\parallel 0}^2}\right)\exp\left(-\frac{u_\perp^2}{2U_{\mathrm{t}\perp 0}^2}\right)\,, \tag{3.9}$$

where

$$n_\mathrm{eq} = \int_{-\infty}^{\infty}\int_0^{\infty}\int_0^{2\pi} u_\perp f_\mathrm{eq}(u_\parallel, u_\perp)\mathrm{d}\zeta\mathrm{d}u_\perp\mathrm{d}u_\parallel \tag{3.10}$$

is the number density of the hot population. We point out that this distribution is chosen mostly for convenient integration and works well in a weakly relativistic setting, but for higher values of γ, a two-temperature generalization of the Jüttner distribution should be used, as proposed, e.g., by Kuzichev et al. (2019). However, it should also be mentioned that we need to model the electron distribution only in the range where the interaction happens. Therefore we do not need to use a sum of Maxwellians or kappa distributions to represent both tail and core of the electron momentum distribution.

We further assume that a bi-Maxwellian can model the electron distribution along a magnetic field line at any distance h. From Liouville's theorem, we have

$$\begin{aligned} f(u_{\parallel 0}, u_{\perp 0}, 0) = f(u_\parallel(u_{\parallel 0}, u_{\perp 0}, h), u_\perp(u_{\parallel 0}, u_{\perp 0}, h), h) = \\ = \frac{n(h)}{(2\pi)^{3/2} U_{\mathrm{t}\parallel}(h) U_{\mathrm{t}\perp}(h)^2} \exp\left(-\frac{u_\parallel^2}{2U_{\mathrm{t}\parallel}(h)^2}\right) \exp\left(-\frac{u_\perp^2}{2U_{\mathrm{t}\perp}(h)^2}\right) \end{aligned} \tag{3.11}$$

During adiabatic motion, kinetic energy and first adiabatic invariant are preserved and give

$$u_\perp^2 = \frac{B(h)}{B_0} u_{\perp 0}^2 \,, \tag{3.12}$$

$$u_\parallel^2 = u_{\parallel 0}^2 + u_{\perp 0}^2 \left(1 - \frac{B(h)}{B_0}\right) . \tag{3.13}$$

By substituting into Equation 3.11 and comparing the result with Equation 3.9, we obtain the off-equatorial thermal momenta and density

$$U_{\mathrm{t}\parallel}(h) = U_{\mathrm{t}\parallel 0} \,, \tag{3.14}$$

$$U_{\mathrm{t}\perp}(h) = W(h) U_{\mathrm{t}\perp 0} \tag{3.15}$$

and

$$n(h) = W(h)^2 n_{\mathrm{eq}} \,, \tag{3.16}$$

where

$$W(h) = \left(1 + \left(1 - \frac{B_0}{B(h)}\right) A_0\right)^{-1/2} \tag{3.17}$$

and

$$A_0 = \frac{U_{\mathrm{t}\perp 0}^2}{U_{\mathrm{t}\parallel 0}^2} - 1 \tag{3.18}$$

is the equatorial temperature anisotropy.

Another simplification in the NGTO comes from reducing the distribution $f(u_\parallel, u_\perp, h)$ to

$$f_\delta(u_\parallel, u_\perp, h) = K \exp\left(-\frac{u_\parallel^2}{2U_{\mathrm{t}\parallel}^2(h)}\right) \delta(u_\perp - U_\perp(h)) \,, \tag{3.19}$$

where K is a normalization constant. By requiring that $f_\delta(u_\parallel, u_\perp, h)$ and $f(u_\parallel, u_\perp, h)$ both integrate to the same density, $n(h)$, and that they have the same average perpendicular momentum, $U_\perp(h)$, we finally get

$$f_\delta(u_\parallel, u_\perp, h) = \frac{n(h)}{(2\pi)^{3/2} U_{\mathrm{t}\parallel}(h) U_{\mathrm{t}\perp}(h)} \exp\left(-\frac{u_\parallel^2}{2U_{\mathrm{t}\parallel}^2(h)}\right) \delta(u_\perp - U_\perp(h)) \tag{3.20}$$

with

$$U_\perp(h) = \left(\frac{\pi}{2}\right)^{1/2} U_{\mathrm{t}\perp}(h)\,. \tag{3.21}$$

We can now evaluate the components of resonant current J_E, J_B. In general, they are expressed as ($m_\mathrm{e} = 1$, $e = 1$)

$$J_\mathrm{E} = \int_{-\infty}^{\infty}\int_0^{\infty}\int_0^{2\pi} (v_\perp \sin\zeta) u_\perp f(\zeta, u_\parallel, u_\perp) \mathrm{d}\zeta \mathrm{d}u_\perp \mathrm{d}u_\parallel\,, \tag{3.22}$$

$$J_\mathrm{B} = \int_{-\infty}^{\infty}\int_0^{\infty}\int_0^{2\pi} (-v_\perp \cos\zeta) u_\perp f(\zeta, u_\parallel, u_\perp) \mathrm{d}\zeta \mathrm{d}u_\perp \mathrm{d}u_\parallel\,, \tag{3.23}$$

where we have dropped the h-dependence for brevity. In the case of gyrotropic distributions, the current density will be zero due to the dependence on $\sin\zeta$ and $\cos\zeta$. We proceed by factorization

$$f(\zeta, u_\parallel, u_\perp) = (g_0(u_\parallel) - Q g_\mathrm{tr}(\zeta, u_\parallel))\delta(u_\perp - U_\perp)\,, \tag{3.24}$$

where the simplified perpendicular distribution from Eq. 3.20 is used. Factor $Q \in [0, 1]$ represents the depth of the depletion in the trapping region, g_tr is the trapped particle distribution and g_0 is the unperturbed distribution. We now assume that g_tr can be replaced by a constant $G = f_\delta(U_\mathrm{R}, U_\perp)$, that is, the phase space density inside the trapping region is assumed to be perfectly mixed (a waterbag model). Recalling the shape of the boundaries of the inhomogeneous electron trap from Equation 2.48, the components of the resonant current can now be expressed as

$$J_\mathrm{E} = -J_0 \int_{\zeta_1}^{\zeta_2} (\cos\zeta_1 - \cos\zeta + S(\zeta - \zeta_1))^{1/2} \sin\zeta\,, \tag{3.25}$$

$$J_\mathrm{B} = J_0 \int_{\zeta_1}^{\zeta_2} (\cos\zeta_1 - \cos\zeta + S(\zeta - \zeta_1))^{1/2} \cos\zeta \tag{3.26}$$

with

$$J_0 = (2)^{3/2}(k)^{-1/2}\gamma_\mathrm{R}^{-1}(1 - V_\mathrm{p}^2/c^2)^{1/2} Q G U_\perp^{5/2} B_\mathrm{w}^{1/2}\,. \tag{3.27}$$

In Figure 3.5, we show the plots of $-J_\mathrm{E}(S)$ and $-J_\mathrm{B}(S)$ as obtained from numerical integration of Equations 3.25 and 3.26. The quantity $-J_\mathrm{E}/J_0$ has a peak $J_\mathrm{E,max} \doteq 0.98$ at $S \doteq -0.41 \equiv S_\mathrm{max}$, and $-J_\mathrm{B}/J_0$ attains value $J_\mathrm{B,max} \doteq 1.29$ at S_max. Note that $-J_\mathrm{B}$ has a maximum at $S \doteq -0.07$, which is however not relevant for maximization of wave power transfer.

Unlike in Omura (2021), we allow for G to be h-dependent, making it a constant in velocity space, but not in the positional space. This decision has impact on the boundary conditions presented in the next section.

3.2.3 Chorus equations

In the NGTO, we assume that the frequency growth of each chorus element (or each subpacket of the element, see Chapter 4) happens locally at a single point along the chosen field line at $h = h_0$. We call this point the source, and we assume that the transfer of energy from particles to waves maximizes in the source, and thus $J_\mathrm{E} = J_\mathrm{E,max}$, $S = S_\mathrm{max}$. It is usually assumed that the strength of the ambient magnetic field minimizes at $h = 0$; in that case, the linear growth rate for parallel whistler waves reaches its maximum at the equator and serves as the energy source for the naturally generated, narrowband triggering wave (Omura et al., 2008).

With no convective growth, the evolution equation for the wave frequency is simply

$$\frac{\partial\omega}{\partial t} + V_\mathrm{g}\frac{\partial\omega}{\partial h} = 0\,. \tag{3.28}$$

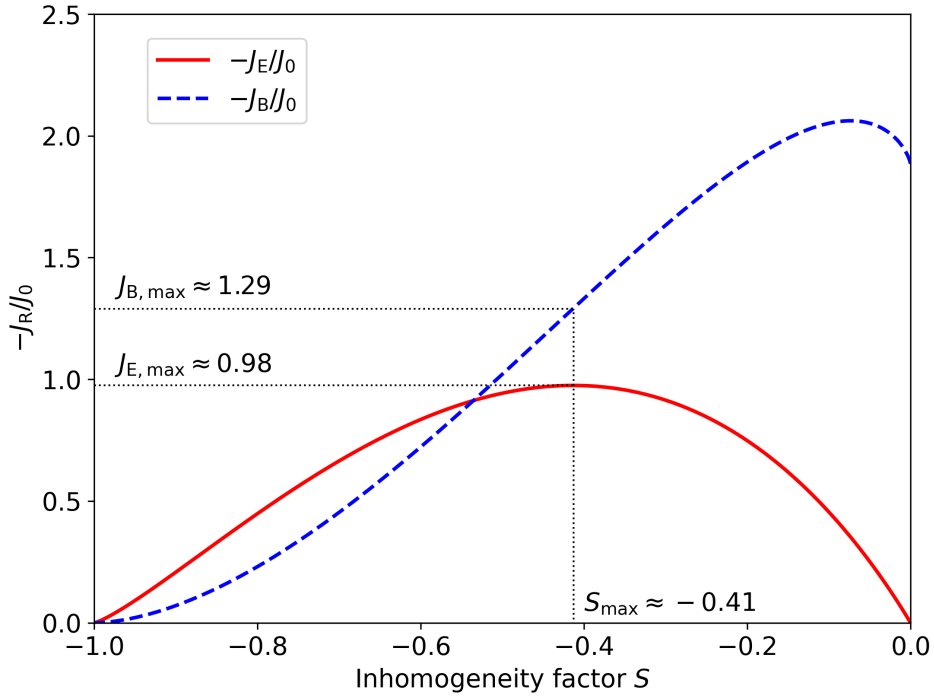

Figure 3.5: Normalized value of the components of resonant current plotted in dependence on the inhomogeneity factor S. The dotted lines show the point where $-J_\mathrm{E}$ maximizes and the values of the currents at this point.

Since the frequency is now assumed to be time-dependent, the resonance frequency V_R in the source also changes with time, and the pendulum equation 2.43 needs to be rederived. The additional term containing $\partial\omega/\partial t$ can be pulled into the inhomogeneity factor S, which now takes the form

$$S = \frac{1}{\omega_\mathrm{tr}^2 \gamma_\mathrm{R}^2}\left(cs_\Omega \frac{\partial \Omega_\mathrm{e}}{\partial h} + s_\omega \frac{\partial \omega}{\partial t}\right) \tag{3.29}$$

with

$$s_\omega = -\gamma_\mathrm{R}^2 \left(1 - \frac{V_\mathrm{R}}{V_\mathrm{g}}\right)^2, \tag{3.30}$$

$$s_\Omega = \frac{U_\mathrm{R}}{c}\left(1 + \frac{(1 - V_\mathrm{p}^2/c^2)}{2}\frac{\Omega_\mathrm{e} - \gamma_\mathrm{R}\omega}{\Omega_\mathrm{e} - \omega}\right) - \frac{k\langle u_\perp\rangle^2}{2c\Omega_\mathrm{e}}. \tag{3.31}$$

The density gradient $\partial n_\mathrm{e}/\partial h$ has been set to zero, as under the conditions found in the Earth's outer radiation belt, it is negligible compared to the other two terms. The partial time derivative of wave frequency, also called the frequency drift rate or the chirp can be expressed in the source point as

$$\left.\frac{\partial \omega}{\partial t}\right|_{h_0} = \frac{S_\mathrm{max} k\langle u_\perp\rangle (1 - V_\mathrm{p}^2)}{s_\omega}\Omega_\mathrm{w} - \frac{cs_\Omega}{s_\omega}\left.\frac{\partial \Omega_\mathrm{e}}{\partial h}\right|_{h_0}. \tag{3.32}$$

The trapping frequency has been written out explicitly to highlight the dependence of frequency on amplitude. Let us remark that the wavenumber k depends not only on frequency but also on the position h through the gyrofrequency $\Omega_\mathrm{e}(h)$. Equation 3.32 is the first of two chorus equations and serves as an initial boundary condition for the transport equation 3.28.

To obtain the growth factor for the absolute nonlinear instability in the source, we first rewrite the inhomogeneous transport equation for amplitude, Eq. 3.6, as

$$\frac{\partial \Omega_\mathrm{w}}{\partial t} + V_\mathrm{g}\frac{\partial \Omega_\mathrm{w}}{\partial h} = \Gamma_\mathrm{N}\Omega_\mathrm{w}\,. \tag{3.33}$$

Γ_N is the convective nonlinear growth rate. To proceed further, we need to estimate the spatial gradient of the amplitude of a growing chorus subpacket. For simplicity, we are going to assume that the ambient magnetic field strength along the field line can be approximated by a parabolic function, and so the gyrofrequency

$$\Omega_\mathrm{e} = \Omega_\mathrm{e0}(1 + ah^2)\,, \tag{3.34}$$

$$a = \frac{9}{2}\frac{1}{(LR_\mathrm{E})^2}\,, \tag{3.35}$$

with a derived from the Taylor expansion of dipole field strength at $h = 0$. Omura et al. (2009) propose that to achieve a self-sustaining nonlinear growth in the near-equatorial region, the spatial gradient of the wave amplitude should be approximately constant in space. Assuming that the chirp does not change much over distance (which is true because the whistler wave group velocity remains almost constant near the equator and in the frequency interval corresponding to the chorus lower band), we can neglect its contribution to S at larger distances and make an estimate

$$\frac{\partial \Omega_\mathrm{w}}{\partial h} = \frac{cs_\Omega V_\mathrm{p}}{(1 - V_\mathrm{p}^2/c^2)S_\mathrm{max}\omega\langle u_\perp\rangle}\frac{\partial^2\Omega_\mathrm{e}}{\partial h^2} = \frac{2acs_\Omega\Omega_\mathrm{e0}V_\mathrm{p}}{(1 - V_\mathrm{p}^2/c^2)S_\mathrm{max}\omega\langle u_\perp\rangle}\,. \tag{3.36}$$

Here we must note that, in general, $S = S_\mathrm{max}$ does not have to hold away from the source, which limits the precision of quantitative predictions of the nonlinear growth theory. Finally, the second chorus equation, i.e. the initial boundary value condition for amplitude growth, can be stated as

$$\left.\frac{\partial \Omega_\mathrm{w}}{\partial t}\right|_{h_0} = \Gamma_\mathrm{N}(h_0)\Omega_\mathrm{w} - \frac{2acs_\Omega V_\mathrm{p}V_\mathrm{g}}{(1 - V_\mathrm{p}^2/c^2)S_\mathrm{max}\omega\langle u_\perp\rangle}\frac{\Omega_\mathrm{e0}}{\omega} \tag{3.37}$$

with

$$\Gamma_\mathrm{N}(h_0) = \left(2\gamma_\mathrm{R}^3\frac{V_\mathrm{p}}{c}\left(1 - \frac{V_\mathrm{p}^2}{c^2}\right)\right)^{\frac{1}{2}} QJ_\mathrm{E,max}\frac{\Omega_\mathrm{e0}^2}{(\Omega_\mathrm{w}\omega)^{1/2}}\left(\frac{\omega_\mathrm{phe}}{\Omega_\mathrm{e0}}\right)^2\frac{V_\mathrm{g}}{c}\left(\frac{V_{\perp 0}}{c}\right)^{\frac{5}{2}}\frac{c^2G(h_0)}{n_\mathrm{he}}\,. \tag{3.38}$$

Here we substituted $\langle u_\perp\rangle$ with $\gamma_\mathrm{R}V_{\perp 0}$, which is a common simplification in the treatment of the inhomogeneity factor under the NGTO.

Equations 3.6, 3.28, 3.37 and 3.32 can be solved numerically to obtain the wavefield of a parallel propagating chorus element.

3.2.4 Threshold amplitude and optimum amplitude

To complete the description of the nonlinear growth theory, we need two additional parameters: the threshold amplitude at which the growth rate becomes positive and the so-called optimum amplitude at which the growth saturates. The condition on absolute instability is

$$\frac{\Gamma_\mathrm{N}}{V_\mathrm{g}}\Omega_\mathrm{w} > \frac{\partial \Omega_\mathrm{w}}{\partial h}\,, \tag{3.39}$$

and by inserting the expression from Equation 3.36 on the right-hand side, the amplitude for which the marginal instability is encountered becomes

$$\Omega_\mathrm{thr} = \frac{s_\Omega^2}{2(S_\mathrm{max}QJ_\mathrm{E,max})^2(\gamma_\mathrm{R}(1 - V_\mathrm{p}^2/c^2))^3}\frac{c^3V_\mathrm{p}}{\omega\Omega_\mathrm{e0}^4}\left(\frac{\partial^2\Omega_\mathrm{e}}{\partial h^2}\right)^2\left(\frac{\Omega_\mathrm{e0}}{\omega_\mathrm{phe}}\right)^2\left(\frac{c}{V_{\perp 0}}\right)^7\left(\frac{n_\mathrm{he}}{c^2G}\right)^2\,. \tag{3.40}$$

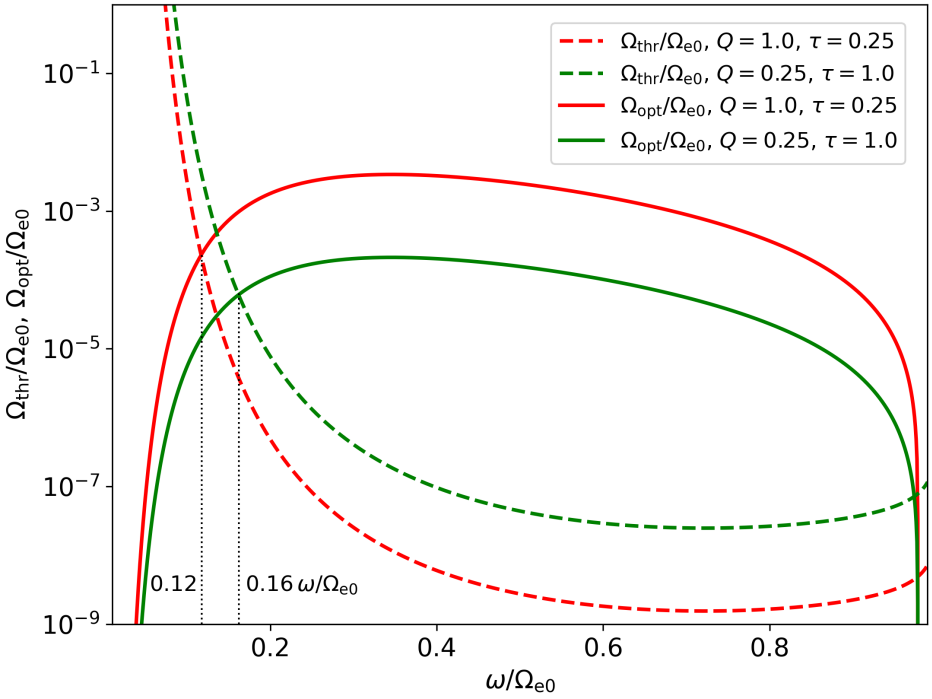

Figure 3.6: Threshold amplitude and optimum amplitude in dependence on wave frequency for two pairs of values of the free parameters τ, Q. The dotted black lines show at which frequency does the nonlinear growth of chorus waves become theoretically possible.

The threshold amplitude is meaningful only in the source, so all variables are assumed to be evaluated at $h = h_0$.

Let us now return to the frequency perturbation related to $-J_B/B_w$ stated in Equation 3.8, and let us further assume that the actual frequency change within a single subpacket proceeds gradually. We now define a nonlinear transition time T_N by equating

$$\frac{\partial \omega}{\partial t} = \frac{\delta \omega}{T_N} \,. \tag{3.41}$$

Next, we introduce a new parameter

$$\tau = \frac{T_N}{T_{tr}} \,, \tag{3.42}$$

where T_{tr} is the trapping period. In the source, the left-hand side of Equation 3.41 can be replaced with the chorus equation 3.32, and the B-component of the resonant current can be calculated from Equations 3.25 and 3.26 with $S = S_{max}$. After these substitutions, we can express the amplitude

$$\Omega_{opt} = \frac{J_{B,max} Q s_\omega}{2^{1/2} \pi S_{max} \tau} \frac{\Omega_{e0}^2}{\omega} \left(\frac{\omega_{phe}}{\Omega_{e0}} \right)^2 \frac{V_p V_g}{c^2} \left(\frac{V_{\perp 0}}{c} \right)^4 \frac{c^2 G}{n_{he}} + \frac{c s_\Omega V_p}{(1 - V_p^2/c^2) S_{max} \omega \gamma_R V_{\perp 0}} \frac{\partial \Omega_e}{\partial h} \,. \tag{3.43}$$

Vlasov hybrid simulations have shown (Omura and Nunn, 2011) that the optimum amplitude is close to the maximum amplitude at which the wave growth breaks down.

Together, he threshold amplitude and the optimum amplitude define a range of wave frequencies $\omega : \Omega_{thr}(\omega) < \Omega_{opt}(\omega)$, in which the nonlinear growth of chorus emissions becomes possible. In Figure 3.6, we plot $\Omega_{thr}(\omega)$ and $\Omega_{opt}(\omega)$ for two pairs of the free parameters τ and Q. For $(\tau, Q) = (0.25, 1.0)$, the lowest frequency at which the growth is possible is $\omega = 0.12\Omega_{e0}$, while for $(\tau, Q) = (1.0, 0.25)$, the limiting frequency increases to $\omega = 0.16\Omega_{e0}$. The characteristic amplitudes themselves can change by more than

an order of magnitude in dependence on the two free parameters. In general, these parameters have to be estimated from simulations.

3.2.5 Summary

In essence, the nonlinear growth theory of Omura et al. provides an approximate formula for the calculation of resonant currents arising from the nongyrotropy near the trapping region, and it assigns meaning to the nonlinear dispersion relation by postulating that the wavenumber remains constant within a single subpacket. Using further simplifications based on self-consistent simulations of the triggering process, three new features are introduced:

1. Relativistic form of the inhomogeneity ratio S, improving on the previous results of Vomvoridis and Denavit (1979).
2. Threshold amplitude for the onset of the nonlinear growth.
3. Optimum amplitude at which the resonant current saturates.

With these tools, a plane-wave model can be constructed that predicts the growth of amplitude and frequency of a triggered rising-tone chorus element.

Description of oblique propagation and falling tones is so far outside of the scope of the theory; however, the relativistic inhomogeneity ratio can be generalized to Landau and cyclotron resonance with oblique whistler waves, as shown by Omura et al. (2019). A calculation by Omura et al. (2009) tells us how the Landau damping can contribute to creating the spectral gap at $0.5\Omega_e$ during propagation away from the magnetic equator, but it cannot explain existence of the gap inside the source (Li et al., 2019). Nevertheless, the theory cannot be used in its current state to model wavefields of chorus elements with higher wave normal angles, and therefore we omitted the discussion of oblique propagation.

Overall, the NGTO brings more clarity to the discussion of the chorus triggering process, and it enables us to estimate the chirp and wave amplitudes based on the properties of cold and hot plasma in the generation region. However, it has several shortcomings. First of all, the emission source is reduced to a single point at the equator, while observations (see the discussion of chorus properties in Section 3.1) show that the source region extends thousands of kilometres away from the B_0-minimum. The homogeneous density distribution in the electron hole contradicts test-particle simulations and PIC simulations of the trapped particle population during the initial stage. The applicability of the plane wave approximation has been challenged by subpacket studies, e.g. Crabtree et al. (2017), and the examples in Figure 3.1 suggest that the spectral width of a subpacket can easily reach half of the full element spectral width. The reduction of the perpendicular momentum distribution of electrons to a delta function and the use of averaged $\langle u_\perp \rangle$ in the second-order resonance complicates comparison with particle simulations and decreases the credibility of quantitative predictions. Furthermore, the theory provides no description of the deformation/breakdown of the electron hole, which is expected to happen between subpackets (Tao et al., 2017). The derivation of threshold amplitude is based on the assumption of constant field-aligned amplitude gradient $\partial B/\partial h$, for which there is no clear support in self-consistent simulations. And finally, the NGTO does not provide any mechanism that would explain the repetition of elements, which is one of the most defining features of the whistler-mode chorus.

In conclusion, it is evident that the theoretical description of the chorus emission is still incomplete, and while the NGTO provides us with mathematical tools for analysis of this emission type, we need to overcome the above-mentioned shortcomings to gain a deeper understanding of the nonlinear wave-particle interactions.

3.3 Other chorus growth theories

The nonlinear growth theory of Omura et al. is the most widely used approach in analytical and numerical studies of chorus in recent years (see e.g. Kurita et al. (2012), Foster et al. (2017), Juhász et al. (2019) and the references in Omura (2021)). However, other theories have been proposed over the last decades, with some of them being able to describe processes omitted in the NGTO. Below, we briefly review four theories we consider to be the most developed, most successful, or most general in their approach. The focus of this section is on parallel propagation. Theories of very oblique whistler wave generation on the resonance cone are left out as they cannot be compared to the NGTO – for more about the current research on this topic, see Mourenas et al. (2015), Fu et al. (2017) or Roytershteyn and Delzanno (2021).

3.3.1 Backward wave oscillator regime of cyclotron masers

In the inner magnetosphere, where field lines are closed, separate magnetic flux tubes can be viewed as resonant cavities, with the conjugate ionospheres acting as mirrors for electromagnetic waves. Whistler wave packets bouncing between the mirrors experience amplification through interaction with trapped populations of energetic electrons. This concept is called the magnetospheric cyclotron maser and can explain the origin of certain types of electromagnetic emissions, e.g. the quasiperiodic hiss emissions (Trakhtengerts and Rycroft, 2008). However, the predicted amplification is not fast enough to explain the growth of chorus emissions. To achieve large wave growth, the maser must operate in a backward wave oscillator (BWO) regime where the EM wave packets interacts with a well-organized electron beam propagating in the opposite direction. As shown by Trakhtengerts (1995), the BWO regime can also be achieved when a step-like deformation is present in the $f(v_\parallel)$ distribution of hot electrons, situated close to the cyclotron resonance velocity. Their calculations demonstrated that the presence of a hiss band could lead to the formation of coherent wavelets near the upper frequency bound of the noise.

The basic equations of the BWO theory of chorus generation are the same as in the NGTO: the equations of motion for electrons in a whistler wavefield (Equations 2.41, 2.42, and 2.16) and the amplitude equation 3.6 in its complex form

$$\left(\frac{\partial}{\partial t} + V_\mathrm{g}\frac{\partial}{\partial h}\right)\tilde{B}_\mathrm{w} = -\mathrm{i}\frac{\mu_0 V_\mathrm{g}\tilde{J}_\mathrm{R}}{2}\,, \tag{3.44}$$

complemented with the conservation of phase space density of electrons (Liouville's theorem). Assuming that the resonant current is carried mainly by particles near V_R and that the magnetic field inhomogeneity is small, the perturbation δf to the initial hot electron distribution can be expressed in simple terms. The final set of equations of the step-BWO system are four inhomogeneous transport equations for B_w, δf, the phase mismatch ζ and the velocity of the step (Demekhov and Trakhtengerts , 2008). Because the evolution of the phase space density perturbations is included in the system, we have a self-consistent system of equations. The parameters Q and τ from the NGTO are not needed, but we must have an estimate on the length of the resonant cavity.

The set of PDE for chorus generation through the step-BWO maser is, unfortunately, a stiff numerical problem, and unlike the NGTO, it does not provide simple analytical estimates on the amplitudes and frequencies of chorus elements. The nonlinear growth rate to which the numerical results are often compared (Demekhov and Trakhtengerts, 2005; Demekhov, 2017) is based on exact calculations of the trapped particle motion (monochromatic plane wave, homogeneous field) carried out by Bud'ko

et al. (1972), resulting in

$$\frac{\gamma_{\mathrm{BWO}}}{\omega_{\mathrm{tr}}} = \frac{3\pi}{32}\,. \tag{3.45}$$

This relationship between growth rate and trapping frequency can be plugged into the formula for inhomogeneity ratio S to express the chirp rate, resulting in the qualitative relation

$$\frac{\partial\omega}{\partial t} \propto \omega_{\mathrm{tr}}^2\,. \tag{3.46}$$

However, as discussed in more detail in Section 3.3.2 when dealing with the sideband instability, the above growth rate formula does not include the distortion of particle trajectories caused by secondary waves. Nonetheless, the simulation results from the numerical solution of the PDE system can be successfully compared with direct satellite observations, as shown most recently by Demekhov et al. (2020).

The step-BWO theory and associated simulations successfully explained the repetition of chorus elements, which is a prediction outside of the scope of the NGTO, and Demekhov (2011) also demonstrated the possibility of falling-tone chorus formation in off-equatorial sources. A major shortcoming of the BWO theory comes from the assumption of a step-like feature in $f(v_\parallel)$, which is supposed to be formed due to cyclotron interaction of hot electrons with a hiss emission. As shown in Figure 3.1b, the presence of low-frequency whistler-mode hiss does not always correlate with observations of chorus elements. Furthermore, the simulation results on step formation from the hiss emission by Trakhtengerts et al. (1996) have never been experimentally confirmed. However, as noted by Demekhov et al. (2017) and Hanzelka et al. (2021) (see also Chapter 5), phase space density depletions caused by interaction with a chorus subpacket form a step-like feature in the direction perpendicular to $V_{\mathrm{R}}(v_\perp)$, which relates the electron hole formation described in the NGTO to the BWO approach. Unfortunately, this observation can be applied only to later stages of the chorus growth when a strong wave packet has already been formed, leaving the processes of PSD perturbation taking place in the initial stage of chorus growth unexplained.

3.3.2 Sideband instability

During the 1960s, it was observed that dashes in Morse code signals sent by military VLF stations trigger rising-tone whistler-mode emissions in the plasmasphere (Helliwell et al., 1964). The first complete dynamical theory of this phenomenon was provided by Sudan and Ott (1971). They assumed that a sufficiently long triggering signal at a constant frequency creates a population of strongly phase-correlated resonant electrons, emitting a secondary whistler wave. Under a simplified model of the correlated population, they found instability in sidebands with frequency shifts $\delta\omega$ in the order of ω_{tr}. These shifts are significantly larger than the adiabatic frequency drift caused by the gradual change of resonance velocity due to inhomogeneity of the geomagnetic field, as considered by Helliwell (1967). However, Sudan and Ott (1971) noted that the inhomogeneity of B_0 is essential because as long as the correlated particles stay in resonance with the triggering wave, the radiated power will support amplitude growth of this primary wave instead of the sidebands. The approximate formula for the sideband growth rate was found to be

$$\frac{\gamma}{\omega} = \left(\frac{n_{\mathrm{R}}}{n_{\mathrm{c}}}\frac{\langle v_\perp\rangle}{c}\frac{\omega_{\mathrm{pe}}}{\Omega_{\mathrm{e}}}\right)^{\frac{2}{5}}\,. \tag{3.47}$$

Following the choice of parameters presented later in Section 4.3, we set $\langle v_\perp\rangle/c = 0.4$, $\omega_{\mathrm{pe}}/\Omega_{\mathrm{e}} = 4.2$, and estimate the fraction of phase-correlated particles as $n_{\mathrm{R}}/n_{\mathrm{c}} \in [5\cdot$

$10^{-6}, 5 \cdot 10^{-5}]$. With $\omega = 10^4\,\mathrm{s}^{-1}$, we get a wave growth estimate in the approximate range from $10^2\,\mathrm{s}^{-1}$ to $2 \cdot 10^2\,\mathrm{s}^{-1}$. This matches the average growth of $2 \cdot 10^2\,\mathrm{s}^{-1}$ of the first model subpacket from Figure 4.6. Similarly, Sudan and Ott (1971) conclude that the numerical results obtained from Equation 3.47 agree with the observations of Helliwell et al. (1964).

On the other hand, Karpman (1974) criticised the above-reviewed results on the sideband growth rate, pointing out that the perfect phase correlation assumed by Sudan and Ott (1971) (δ-function in parallel velocities at V_R and a cosine distribution in phases) is unrealistic, and claimed that the sideband growth rate should be much closer to the linear growth rate γ_L. They based their arguments on the analytical computations of Bud'ko et al. (1972), who in turn were inspired by the exact nonlinear Landau damping theory of O'Neil (1965) and assumed that the distribution of resonant particles reaches an ergodic state. Here, the term "ergodic" refers to the mixing property of the trapped particle evolution operator: for $t/T_\mathrm{tr} \to \infty$, a coarse-grained distribution is asymptotically constant along phase space trajectories for any mesh size, and its value at any point can be obtained by averaging of the initial distribution. Based on energy conservation and the ergodic theorem, Bud'ko et al. (1972) conclude that the maximum growth rate of the sideband is about $1.4\gamma_\mathrm{L}$, which is typically much less than the predictions based on Equation 3.47. Karpman (1974) also notes that the inhomogeneity of the background magnetic field introduces an asymmetry between the upper and lower sidebands, explaining the dominance of rising tone elements.

Denavit and Sudan (1975) proposed a more general distribution of resonant electrons, which was still assumed to be strongly concentrated near $\zeta \approx \pi$. Unlike Bud'ko et al. (1972), they worked with a set of secondary waves coupled to the primary wave. The shift between the mean velocity of the resonant particles and the resonance velocity of the primary wave, which is responsible for the frequency shift of sidebands, comes from the slope of the initial velocity distribution along $v_\parallel$. The dispersion relation derived by Denavit and Sudan (1975) shows a splitting of the whistler mode determined by the amplitude of the primary wave. Depending on the inhomogeneity of B_0 and the shape of the initial velocity distribution, the excitation coefficient of one of the sidebands can increase, leading to a preferential rising-tone or falling tone structure. The resulting peak growth rate formula is

$$\frac{\gamma}{\omega} = \left(\left(\frac{\omega_{\mathrm{pR2}}}{\omega} \right)^2 \left(1 - \frac{\omega}{\Omega_\mathrm{e}} \right) \frac{\langle v_\perp^2 \rangle}{2c^2} \right)^{\frac{1}{3}} , \tag{3.48}$$

where the density of resonant particles $n_\mathrm{R2} \propto \omega_\mathrm{pR2}^2$ corresponds only to the component of resonant current J_R that contributes to the instability of magnetic field perturbations; Denavit and Sudan (1975) estimate $n_\mathrm{R2}/n_\mathrm{c} = 10^{-7}$. With this estimate and the values of frequencies and velocities defined below Equation 3.47, we get a growth rate of $1.4 \cdot 10^2\,\mathrm{s}^{-1}$. Despite the different power-law coefficients, there is little quantitative change for the chosen representative values of input parameters.

Nunn (1986) sidestepped the difficulties of finding the analytical expression for the resonant particle distribution by performing a backward numerical integration of electron trajectories. However, as in all of the above-discussed approaches, the amplitude of the primary wave was slowly changing, and the amplitude of the secondary wave was supposed to be much smaller so as not to perturb the particle trajectories.

In a realistic scenario, the triggering wave (either artificial or naturally generated from anisotropy-driven instabilities) will experience fast growth, increasing ω_tr and widening the spectral gap between the primary wave and the sidebands. Therefore, the power radiated by the phase-correlated electron should create a rising-frequency fluctuation spectrum, similar to the continuous frequency drift assumption (Equation 3.41)

made by Omura and Nunn (2011). Furthermore, the overlapping of trapping potentials of the triggered wave and the primary wave will result in loss of phase correlation before the ergodic state sets in, making the application of Bud'ko's results to chorus growth questionable. Unfortunately, a self-consistent description of the frequency drift poses serious mathematical challenges which have yet to be fully resolved. One promising path towards a complete analytical description of the nonlinear chorus growth is reviewed in the following paragraphs.

3.3.3 General framework of chorus excitation

A new theoretical framework developed by Zonca et al. (2022) aims to provide a self-consistent analytical description of the interaction between a whistler-mode fluctuation spectrum and resonant electrons. As a first step, Zonca et al. split the current density into cold and hot components, deriving a nonlinear dispersion relation equivalent to Equation 3.7. Next, they formulate a complex wave equation analogous to Equation 3.44. However, instead of the amplitude and phase of the wave magnetic field, they use the wave intensity and arrive at

$$W(h,t,\omega)+i\Gamma(h,t,\omega)\equiv\left.\frac{\mu c}{\omega\dfrac{\partial\bar{D}_{\mathrm{w}}}{\partial k}}\frac{\mu_0 V_{\mathrm{g}}(\widetilde{\boldsymbol{J}}_{\mathrm{R}k}\cdot\widetilde{\boldsymbol{B}}^{*}_{\mathrm{w}k})}{|\widetilde{\boldsymbol{B}}_{\mathrm{w}k}|^2}\right|_{k=\omega\mu/c}, \tag{3.49}$$

where W is the temporal phase shift, Γ is the growth rate, and μ represents the refractive index solution to the whistler-mode dispersion relation $\bar{D}_{\mathrm{w}}$ (see Equation 1.58). This form is more similar to the energy density formulation of Karpman et al. (1975).

Unlike in the sideband theory or the NGTO, Zonca et al. (2022) do not assume a test wave at $\omega+\delta\omega$ or a continuous shift in the frequency of a plane wave. Instead, they write the perturbation of the hot electron density δf as a response to a dense fluctuation spectrum, summing over all possible wavenumbers k. The spectral components are always assumed to approximately fulfil the whistler dispersion relation. Further, they use the Vlasov equation to derive an evolution equation of the background distribution (zeroth summation component) f_0 in dependence on $B_{\mathrm{w}k}$ and δf_k, and another evolution equation for δf_k in dependence on f_0. By formal inversion of the evolution operators, $(\partial_t+v_\parallel\partial_z)f_0$ can be cast in a form similar to the Dyson equation, describing the emission and absorption of whistler-mode electromagnetic oscillators. The resulting Dyson-like equation captures the self-consistent evolution of the phase space structures and the chirping chorus element, accounting for self-interactions in the fluctuation spectrum. We do not call this equation Schinger-Dyson because it has been derived perturbatively by summing interaction diagrams (Al'tshul' and Karpman, 1966), as opposed to the variational approach (Schwinger, 1951).

Due to the complexity of the general framework presented by Zonca et al. (2022), we will not review the resulting equations in further detail, and we will rather focus on the new concepts and their relation to older theories. The growth and chirping of chorus emissions are shown to be associated with the maximization of wave power transfer, in agreement with Omura et al. (2008). However, instead of excitation of discrete whistler seeds, the chirping comes from excitation of a noise fluctuation spectrum, with the frequency of the dominant wavenumber continuously sliding towards higher values. Furthermore, the nonlinear phase shift is found to be associated with wave intensity modulations (subpackets) rather than with the frequency drift. This suggests that the connection between $\partial\omega/\partial t$ and $\delta\omega$ postulated in Equation 3.41 stems from misidentifying the cause of chirping. Zonca et al. (2022) show that the peak phase shift in the frequency space is locked to the peak of wave intensity, thus explaining why

the results based on Equation 3.41 (definition of optimum amplitude, simulations in Chapter 4) provide reasonable agreement with observations and PIC simulations.

The new theoretical framework also reveals the connection between the nonlinear growth rate, trapping period, and chirping: $\gamma_{\mathrm{NL}} \propto \omega_{\mathrm{tr}}$, $\partial\omega/\partial t \propto \gamma_{\mathrm{NL}}^2$. These proportionalities can be found in the earlier sideband and BWO theories (Bud'ko et al., 1972; Trakhtengerts, 1999), but now, they have been placed on a rigorous mathematical foundation. A reduced (velocity-space averaged) version of the Dyson-like equation can be treated analytically to retrieve

$$\frac{\partial\omega}{\partial t} = \pm\frac{1}{2}\frac{\omega_{\mathrm{tr}}^2}{(1 - V_{\mathrm{R}}/V_{\mathrm{g}})^2}\,, \tag{3.50}$$

where the constant $1/2$ defines the optimum value of the nonrelativistic version of the inhomogeneity factor S as derived by Vomvoridis et al. (1982). The theory of Zonca et al. (2022) provides the first fully analytical derivation of chirping in both rising and falling elements, as indicated by the $\pm$ sign.

Another interesting feature of the new approach is the treatment of the magnetic field nonuniformity. It is shown that the nonuniform initial hot electron distribution provides the energy source for the nonlinear excitation and that the B_0 field can be treated as homogeneous. However, a nonuniform ambient magnetic field might contribute to the symmetry breaking between fallers and risers, as suggested by the simulations of Wu et al. (2020).

In summary, the new theoretical framework developed by Zonca et al. (2022) provides a rigorous rederivation of previous major results on the chorus growth mechanism and rejects the nonlinear phase shift as a source of frequency chirping. On top of that, it shows a one-to-one correspondence of chorus chirping with superradiance in free-electron lasers and indicates the possible application of the new description in the BWO mechanism (Chen and Zonca, 2016). Nevertheless, at this point, wavefield calculations rely on a reduction of the Dyson-like equation and its numerical solution, which requires Savitzky-Golay filtering to prevent the loss of regularity in ∂_ω. Furthermore, the current description is nonrelativistic, assumes parallel propagation in a parabolic magnetic field, and it cannot handle discrete steps in the frequency spectrum due to the continuous limit introduced in the reduced model. Therefore, the explanation of the origin of subpackets, defined in the sense of Santolík et al. (2003a), is currently beyond the reach of the reduced model.

3.3.4 Trap-Release-Amplify

The Trap-Release-Amplify phenomenological model of chorus waves (TARA for short) presented by Tao et al. (2021) describes the growth of chorus elements based on the qualitative results of the theoretical framework from Section 3.3.3 and PIC simulations. It also utilizes the antenna effect introduced by Helliwell (1967), which was considered in the NGTO-based numerical model of Hanzelka et al. (2020); see Chapter 4. The frequency drift in the TARA model does not come from the J_{B} component of the resonant current but instead from the selective amplification of new emissions from the broadband whistler-wave spectrum due to the phase-locking condition ($\mathrm{d}^2\zeta/\mathrm{d}t^2 \approx 0$), which is connected with the maximization of wave power transfer. The chirp is thus partially explained due to inhomogeneity of the ambient magnetic field in the upstream, as originally suggested by Helliwell (1967). This description differs from the analytical results of Zonca et al. (2022), who neglected $\partial B_0/\partial h$ and recovered the frequency growth from the nonuniformity of the hot electron distribution.

Unlike in the theory of Helliwell (1967), the TARA model also acknowledges the relation of frequency shift to the particle trapping and wave amplitude as prescribed by

Equation 3.50, thus taking into account the case when the s_ω component of Equation 3.29 dominates the s_Ω component (note that the TARA model is presented in a non-relativistic form, but the concepts easily translate to the equations of Section 3.2 based on relativistic particle motion). This allows for the formation of rising-tone elements in a uniform magnetic field, but the origin of the chirp for this case is not captured by the TARA model.

The explanation of the origin of subpackets differs significantly from the NGTO. Instead of considering each subpacket as the basic unit of wave excitation (which later becomes the new triggering wave), in TARA, modes at all frequencies contribute to the generation of new emissions, and the subpackets form in the downstream due to conservation of momentum and energy between waves and phase-trapped electrons. Oscillations of resonant particles in the order of $\omega_{\mathrm{tr}}^{-1}$ modulate the wave power transfer (Tao et al., 2017), and this translates to amplitude modulations, which are further accentuated due to convective growth downstream (cf. Nogi and Omura (2022)). This poses difficulty for the spacecraft analysis of subpackets (Santolík et al., 2014a; Foster et al., 2017) by suggesting that multipoint measurements are required to capture the important convective evolution of the subpacket structure. Furthermore, wave superposition needs to be taken into account when analyzing the fine structure of chorus (Santolík et al., 2004; Zhang et al., 2020; Nunn et al., 2021).

We may conclude that while the TARA model provides an interesting novel description of the chorus generation mechanism, there are still many contentious points (e.g. the role of J_{B}, $\partial B_0/\partial h$, and wave superposition) that need to be resolved by further theoretical and experimental investigations.

3.4 Similarity of chorus emissions and EMIC

The equations of motion of electrons in a right-hand polarized whistler wave (Eqs. 2.14–2.16) can be easily translated to the motion of protons in a left-hand polarized EMIC wave. Similarly, the calculation of resonant current within the nonlinear growth theory of chorus emissions (Section 3.2.2) can be modified to describe the currents which drive the growth of EMIC discrete elements. The proton trajectories will have the same shape as in Figure 2.9, but instead of a hole, a so-called proton hill will form in the trapping region that moves towards higher parallel velocities, supporting the growth of a falling-tone emission (Figure 3.7a). A proton hole, with $S \approx +0.4$, is associated with rising tones (Pickett et al., 2010; Omura et al., 2010; Shoji et al., 2021). EMICs can also interact with co-streaming electrons, with the resonance velocity curve

$$V_{\mathrm{R}}(v_\perp) = \frac{1}{k}\left(\omega + \frac{\Omega_{\mathrm{e}}}{\gamma}\right) = \frac{\dfrac{ck\omega}{\Omega_{\mathrm{e}}^2} + \sqrt{\left(1 + \dfrac{c^2k^2}{\Omega_{\mathrm{e}}^2}\right)\left(1 - \dfrac{v_\perp^2}{c^2}\right) - \dfrac{\omega^2}{\Omega_{\mathrm{e}}^2}}}{1 + \dfrac{c^2k^2}{\Omega_{\mathrm{e}}^2}} \tag{3.51}$$

forming a near-circular arc in the $(v_\parallel, v_\perp)$ space at relativistic energies, as shown in Figure 3.7b. Notice that this is the same formula as for the whistler-electron interaction in Equation 2.19, but the other root of the quadratic equation is chosen. Due to the shape of $V_{\mathrm{R}}(v_\perp)$, the EMIC-electron interaction results in pitch angle scattering with negligible changes to the electron energy (Omura et al., 2013).

Unlike in the case of chorus, spacecraft observations have not detected any signs of a spectral gap in discrete EMIC emissions, not counting the gaps between different ion cyclotron branches (Nakamura et al., 2015). Therefore, as the wave element reaches frequencies $\omega > \Omega_{\mathrm{p}}/2$, the downstream chirping rate will decrease due to the downward trend of V_{g}; see Figure 1.3 for a visual overview of the EMIC wave propagation

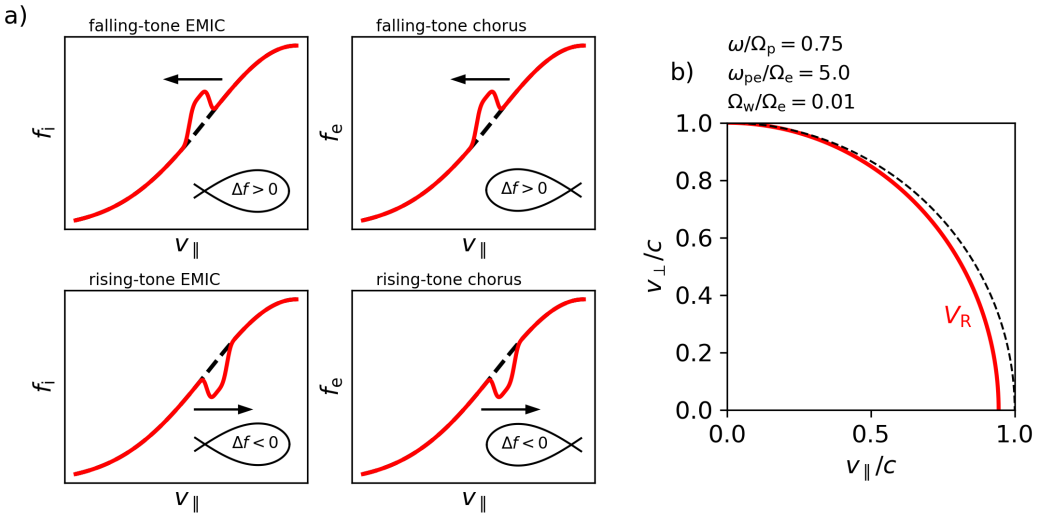

Figure 3.7: a) Schematic explanation of the connection between proton (electron) hill and hole formation and the chirping of discrete EMIC (chorus) elements. The plot in the bottom right corners of each panel shows the shape of the separatrix in the $(\zeta, v_\parallel)$ space. Black arrows point to the direction of motion of the phase space perturbation. b) Resonance velocity curve of EMIC-electron interaction. Even at a high wave frequency of $0.75\Omega_p$, we have $\gamma \gg 1$, showing that only relativistic electrons can experience resonance scattering by proton EMICs. Compare with the results on electron-chorus interaction, Figure 2.5.

properties. Because the source location of the EMIC is not always known, estimation of this dispersion effect is not straightforward, complicating the comparison of $\partial\omega/\partial t$ with the theory.

A more serious complication arises at lower frequencies. Wave vectors of EMIC waves tend to be more oblique than the lower-band rising-tone chorus (Allen et al., 2015; Taubenschuss et al., 2014), and even with a small amount of obliquity, a proton EMIC can transition from L-mode to R-mode as it propagates towards higher $\boldsymbol{B}_0$. Therefore, the NGTO can be used only at very low latitudes unless we focus on the oxygen frequency band – or more generally, on the band of the heaviest ion, e.g. the water group ions in the magnetosphere of Saturn (Leisner et al., 2006). However, even if the crossover frequency is absent, the waves will quickly become oblique because the EMIC ducting mechanism requires large-scale field-aligned density enhancement (de Soria-Santacruz et al., 2013). Under these considerations, the frequency range and latitudinal range where the NGTO and the EMIC-chorus equations (Omura et al., 2010) are applicable is severely limited.

Furthermore, the EMIC spectrum tends to be less structured than the chorus spectrum, and the separation of individual elements and subpackets is often impossible (Omura et al., 2010; Grison et al., 2013; Ojha et al., 2021). For this and the above reasons, the NGTO-based wavefield modelling in Chapter 4 will be applied only to the rising-tone, parallel-propagating, lower-band whistler-mode chorus.

4. Semi-empirical model of chorus wavefield

The nonlinear growth theory of chorus emissions (NGTO), which we described in Chapter 3, can be used to model the wavefield of a parallel-propagating rising-tone chorus element near the magnetic equator. However, additional assumptions about the resonant current and the triggering process must be made to reproduce the subpacket structure. These modelling efforts serve two main purposes. First, they help us understand the parametric dependence of various chorus properties, as shown in this chapter. Second, they provide a reasonable approximation of the real wavefield, which can be used as an input for test-particle studies of electron acceleration and scattering of resonant electrons. The latter application is the subject of Chapter 5.

The contents of this chapter are based on the publication Hanzelka et al. (2020), which can be found in Attachment A.2. It must be noted here that the nonlinear growth theory included a small inconsistency in the use of weakly relativistic electron distributions and the calculation of resonant currents, and this inconsistency was first corrected in Omura (2021). Because these corrections have a negligible effect on the simulated chorus wavefield described in Hanzelka et al. (2020), we do not reflect them in Sections 4.1 and 4.2. For discussion of the corrections, see Attachment A.1.

4.1 Basic principles and model equations

Our chorus wavefield model is based on the advection equations 3.6 and 3.28 for amplitude and frequency, with the chorus equations 3.37 and 3.32 serving as the initial boundary value conditions. The quantity $G(h)$, which carries the information about the electron distribution, is based on the momentum distribution from Equation 3.11 and the parabolic approximation of magnetic field 3.34. The resulting formula for $G(h)$ is

$$G(h) = \left(\frac{1 + ah^2}{1 + ah^2(1 + A_0)} \right)^{\frac{1}{2}} \frac{n_{\mathrm{he}}}{2\pi^2 U_{\mathrm{t}\perp 0} U_{\mathrm{t}\parallel 0}} \exp\left(-\frac{U_{\mathrm{R}}^2}{2U_{\mathrm{t}\parallel 0}^2} \right) . \tag{4.1}$$

As shown by the numerical solution of the system of advection and chorus equations provided by Summers et al. (2012), the wave amplitude in the source grows without any sign of oscillations and thus does not predict the formation of subpacket structure. This is the expected behaviour stemming from the fact that the nonlinear growth theory does not describe the breakdown or distortion of the vortex structure in the trapping region (see Section 3.2.5). Following Kubota and Omura (2018), we switch the sign of the nonlinear growth rate Γ_{N} when the optimum amplitude is reached and let the wave damp until the threshold amplitude is encountered. This heuristic approach ensures that we obtain highly symmetric packet envelopes, which is in agreement with self-consistent simulations and observations (see Section 3.1).

The NGTO assumes that the absolute instability is localized at a single point along the field line. However, it is known that the resonant current causes instability over a larger region of latitudes, and it has also been suggested that the source location is shifting as the chorus element grows. Demekhov et al. (2020) used the motion of the source to explain variations of the lowest frequency of individual chorus elements in THEMIS spacecraft observations, and Nogi and Omura (2022) discussed the upstream shift of the source based on particle-in-cell simulations. To include this behaviour into our model, we assume the following scheme (see also Figure 4.1): During the growth

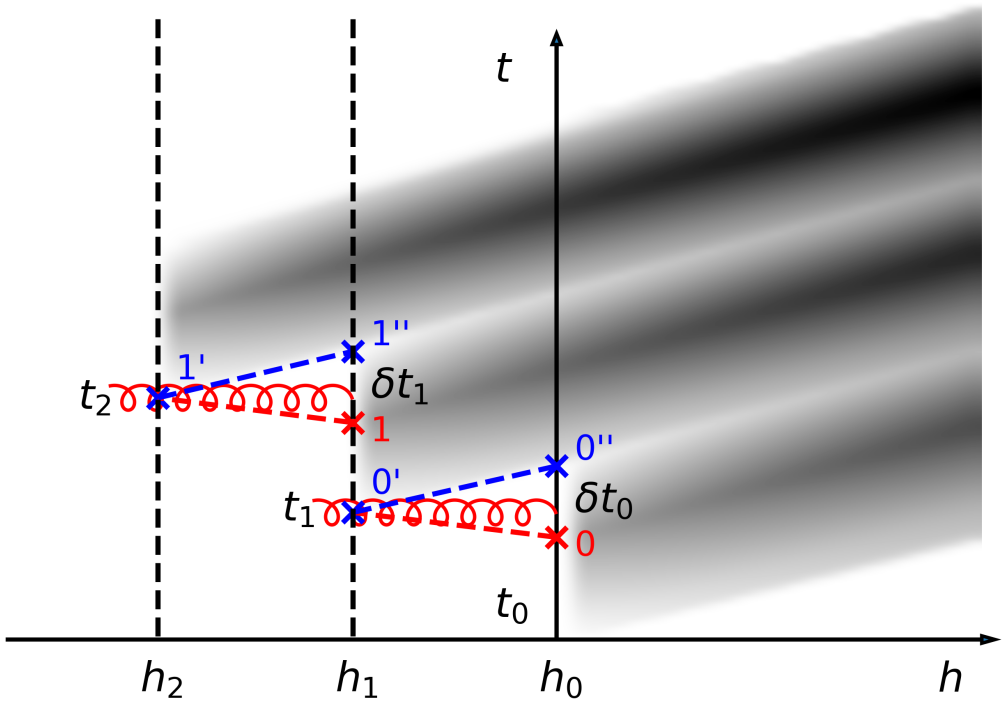

Figure 4.1: Schematic representation of the sequential subpacket formation model. After the wave amplitude reaches the optimum amplitude $\Omega_{\rm opt}$ at $(t_{\rm max,0}, h_0) \sim$ Point 0, it starts decreasing until it reaches the threshold amplitude $\Omega_{\rm thr}$ at $(t_{\rm end,0}, h_0) \sim$ Point $0''$ within a time period δt_0. At this point the radiation emitted from $(t_1, h_1) \sim$ Point $0'$ arrives, where $0'$ corresponds with the peak resonant current which was released from Point 0. The new subpacket starts growing from Point $0'$. This generation process is then repeated with each subpacket (Points 1, $1'$, and $1''$, etc.). Adapted from Hanzelka et al. (2020).

of a subpacket, the maximum amplitude is reached at one point, which also marks the peak of the resonant current $J_{\rm E}$. The 3D spatial distribution of the current has a helical shape, making the resonant electrons act as an antenna radiating whistler-mode waves at a frequency determined by the pitch of the helix and the cold plasma dispersion relation. We postulate that the continuous radiation from the antenna cannot replace the previous subpacket until its normalized amplitude drops below $\Omega_{\rm thr}$. This uniquely defines the source location (t_{i+1}, h_{i+1}) of the new subpacket in time and space,

$$h_{i+1} = h_i + \frac{V_{{\rm g}i} V_{{\rm R}i}}{V_{{\rm g}i} - V_{{\rm R}i}} \delta t_i \,, \tag{4.2}$$

$$t_{i+1} = \frac{V_{{\rm g}i} t_{{\rm end},i} - V_{{\rm R}i} t_{{\rm max},i}}{V_{{\rm g}i} - V_{{\rm R}i}} \tag{4.3}$$

The interval between Points $(i+1)$ and $(i+1)''$ in Figure 4.1 was denoted $\delta t_i = t_{{\rm end},i} - t_{{\rm max},i}$; the times where the previous subpacket reaches its maximum and where it ends are called $t_{{\rm max},i}$ and $t_{{\rm end},i}$, respectively. Because the dispersive properties between source points of two adjacent subpackets do not change much, we use the resonance velocity and group velocity at $(t_{{\rm max},i}, h_i)$ in the calculation of the new source location. The whole computation is repeated for each subpacket until an upper frequency limit is reached.

Hanzelka et al. (2020) have shown that the whistler wave radiated from a perfect helix of length $h_{i+1} - h_i$ could easily reach normalized amplitudes larger than $\Omega_{\rm opt}$ at the end of the helix. In the model, we simply assume that the amplitude in the new

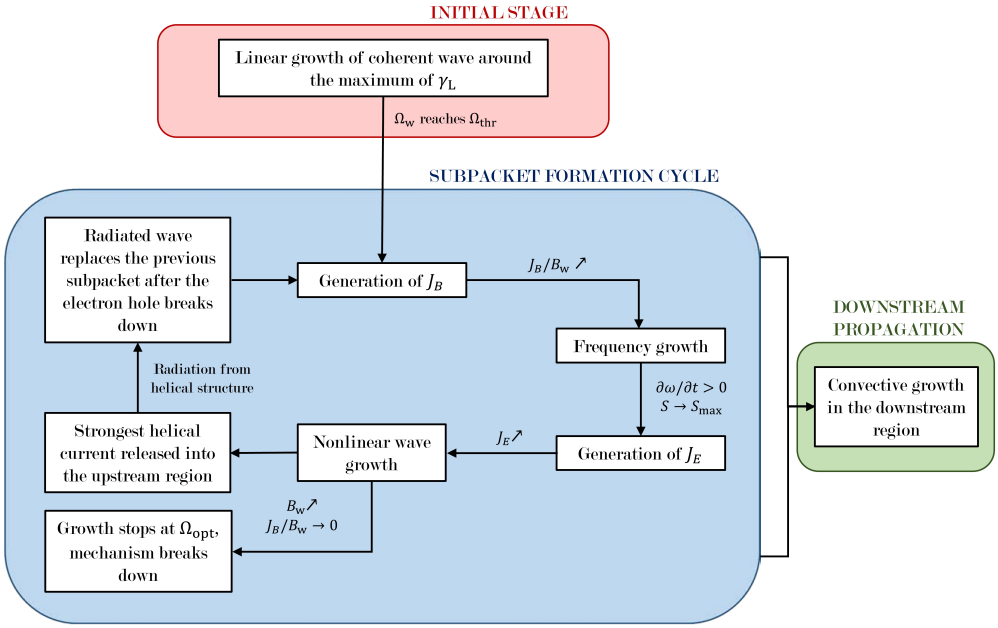

Figure 4.2: Flowchart of the generation mechanism of the subpacket structure of a whistler-mode chorus element. The initial stage is skipped in our model. Reprinted from Hanzelka et al. (2020).

source is near the threshold amplitude, which is the necessary condition for nonlinear growth. A more rigorous treatment of the antenna effect was presented by Trakhtengerts et al. (2003), who studied the spectral and amplitude characteristics of the secondary wave. They concluded that due to a phase mismatch along the antenna and further acceleration and scattering of electrons by the primary wave, the energy transferred into the new subpacket significantly decreases. They found that the amplitude of the secondary wave is of the same order of magnitude as the threshold amplitude used in the simulation presented below.

The individual steps in our sequential model of chorus generation are summarized in the flowchart in Figure 4.2.

4.2 Numerical simulation and results

We solved the advection equations for amplitude and frequency with an upwind integration scheme, with a spatial step $h_{\mathrm{step}} = 1\, c\Omega_{\mathrm{e0}}^{-1}$ and the largest possible time step which ensures the validity of the Courant-Friedrichs-Lewy (CFL) condition for all V_{g}, i.e.

$$t_{\mathrm{step}} \approx h_{\mathrm{step}} / \max_{\omega,h}(V_{\mathrm{g}})\,. \tag{4.4}$$

The starting frequency was set to $\omega_0 = 0.2\Omega_{\mathrm{e0}}$, and the initial amplitude of each subpacket was chosen as $\Omega_{\mathrm{w}}(t_i, h_i) = 2\Omega_{\mathrm{thr}}(\omega_i, h_i)$. The choice of initial amplitude has negligible effect on the result as long as $\Omega_{\mathrm{opt}}(\omega_i, h_i) \gg \Omega_{\mathrm{thr}}(\omega_i, h_i)$ and $\Omega_{\mathrm{w}}(t_i, h_i) \approx \Omega_{\mathrm{thr}}(\omega_i, h_i)$. If $\Omega_{\mathrm{w}}(t_i, h_i) > \Omega_{\mathrm{opt}}(\omega_i, h_i)$, the calculation is terminated. Another termination condition, $\omega(t_i, h_i) \geq \omega_{\mathrm{f}} = 0.5\,\Omega_{\mathrm{e0}}$, ensures that the growth of wave frequency ends near the spectral gap appearing in spacecraft observations – see Sections 3.1 and 3.2.5 for the experimental and theoretical description of the gap.

	Q	τ	$\frac{\omega_{pe}}{\Omega_{e0}}$	$\frac{\omega_{phe}}{\Omega_{e0}}$	$\frac{V_{\perp 0}}{c}$	$\frac{U_{t\parallel 0}}{c}$	$\frac{a \cdot 10^7}{c^{-2}\Omega_{e0}^2}$
Set 0	0.5	0.5	5.0	0.3	0.4	0.15	1.36
Set 1	0.25	0.25	5.0	0.3	0.4	0.15	1.36
Set 2	0.5	1.0	6.0	0.4	0.4	0.20	0.86

Table 4.1: Three sets of input parameters used to produce Figures 4.3, 4.4 and 4.5.

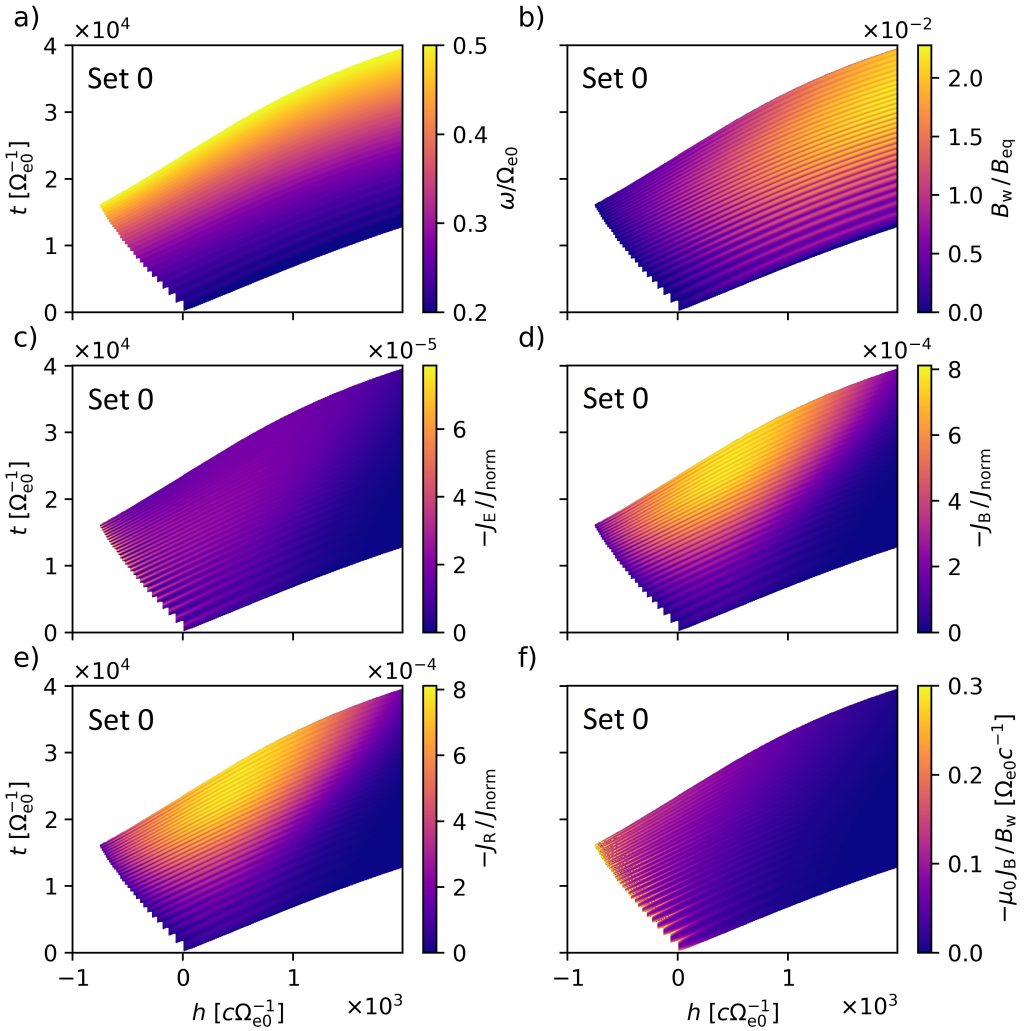

Figure 4.3: Evolution of a chorus element in time and space obtained with input parameters from Set 0 in table 4.1. The axes ranges can be converted to SI units to get $t \approx (0, 670)$ ms and $h \approx (-5000, 10000)$ km. The components of the resonant current and its magnitude in panels c), d), and e) are normalized by $J_{norm} = m_e \Omega_{e0}^2 \mu_0^{-1} c^{-1} e^{-1} \approx 5.4 \cdot 10^{-5}$ A $\cdot$ m^{-2}. Reprinted from Hanzelka et al. (2020).

In Figure 4.3, we show the time-space plots of frequency, amplitude and resonant currents in a simulated wavefield. The input parameters for this case can be found in Table 4.1 under the label "Set 0". The coefficient a of parabolic approximation of the dipole field strength corresponds to field line $L = 4.5$, and the gyrofrequency $\Omega_{e0} = 6.0 \cdot 10^4\,\mathrm{s}^{-1}$ is based on equatorial magnetic field $B_{surf} = 3.1 \cdot 10^{-5}$ T at the surface of the Earth. Looking at Figure 4.3a, we notice that a large number of subpackets has been produced ($N_S = 28$) and that their source is moving upstream, with $h_{27} = -750\, c\Omega_{e0}^{-1} \sim \lambda_m = -7.5°$ being the furthest distance from the equator. The length of individual

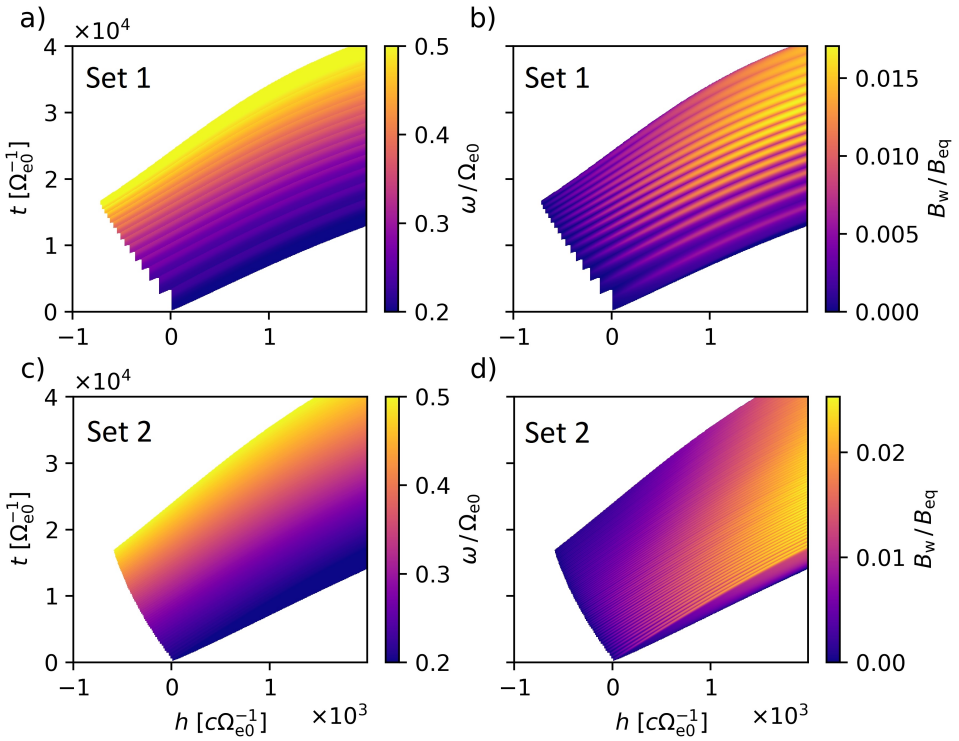

Figure 4.4: Plots of wave frequency and amplitude as in 4.3, but for input parameters sets 1 and 2 from Table 4.1. The choice $L = 5 \sim a = 0.86 \cdot 10^{-7}\, c^{-2}\Omega_{e0}^2$ in Set 2 changes the SI range of axes to $t \approx (0, 530)$ ms and $h \approx (-3500, 7000)$ km. Reprinted from Hanzelka et al. (2020).

subpackets in the source decreases from $1600\,\Omega_{e0}^{-1} \sim 27$ ms to $240\,\Omega_{e0}^{-1} \sim 4$ ms. This is in agreement with Santolík et al. (2014a) who analyzed large number of high-amplitude chorus elements detected by the Van Allen Probes and found that the majority of the subpackets has length between 5 ms and tens of ms. The highest amplitudes reached in observations were limited by instrumental capabilities at 3 nT, which is less than the maximum amplitude of $\Omega_w/\Omega_{e0} = 0.023 \sim B_w = 7.8$ nT predicted by our simulation. This peak amplitude can be decreased by treating the overlap of resonance regions, which we show in Section 4.3. The wave growth should be further limited by the Landau damping, which however does not appear in our 1D model. Moreover, the parabolic approximation of magnetic field starts deviating from the dipole field at larger latitudes, making the simulation unreliable in these regions even when strong ducting is assumed.

The resonance current plots in Figures 4.3c–e show that the J_E component, which is associated with amplitude growth, attains its largest value in the source (starting position and time) of each subpacket and then slowly decreases as the wave propagates downstream. An exception is the subpackets near the upper-frequency limit, where J_E quickly drops down even before reaching the equator and then slowly picks up before decreasing again at larger latitudes ($\lambda_m > 15°$). The B-component grows with distance from the subpacket sources and reaches its peak a few degrees of latitude downstream from the equator. However, the relevant quantity for frequency growth is J_B/B_w, as dictated by Equations 3.7 and 3.8. Figure 4.3f reveals that $\mu_0 J_B$ maximizes in the subpacket source, which is consistent with the approximation of localized frequency growth made in the construction of the NGTO.

Another way to look at our results is to plot the time evolution of the wave frequency and amplitude at fixed points in space, as shown in Figure 4.5. Such visualization resembles the results provided by spacecraft observations more closely because the ratio

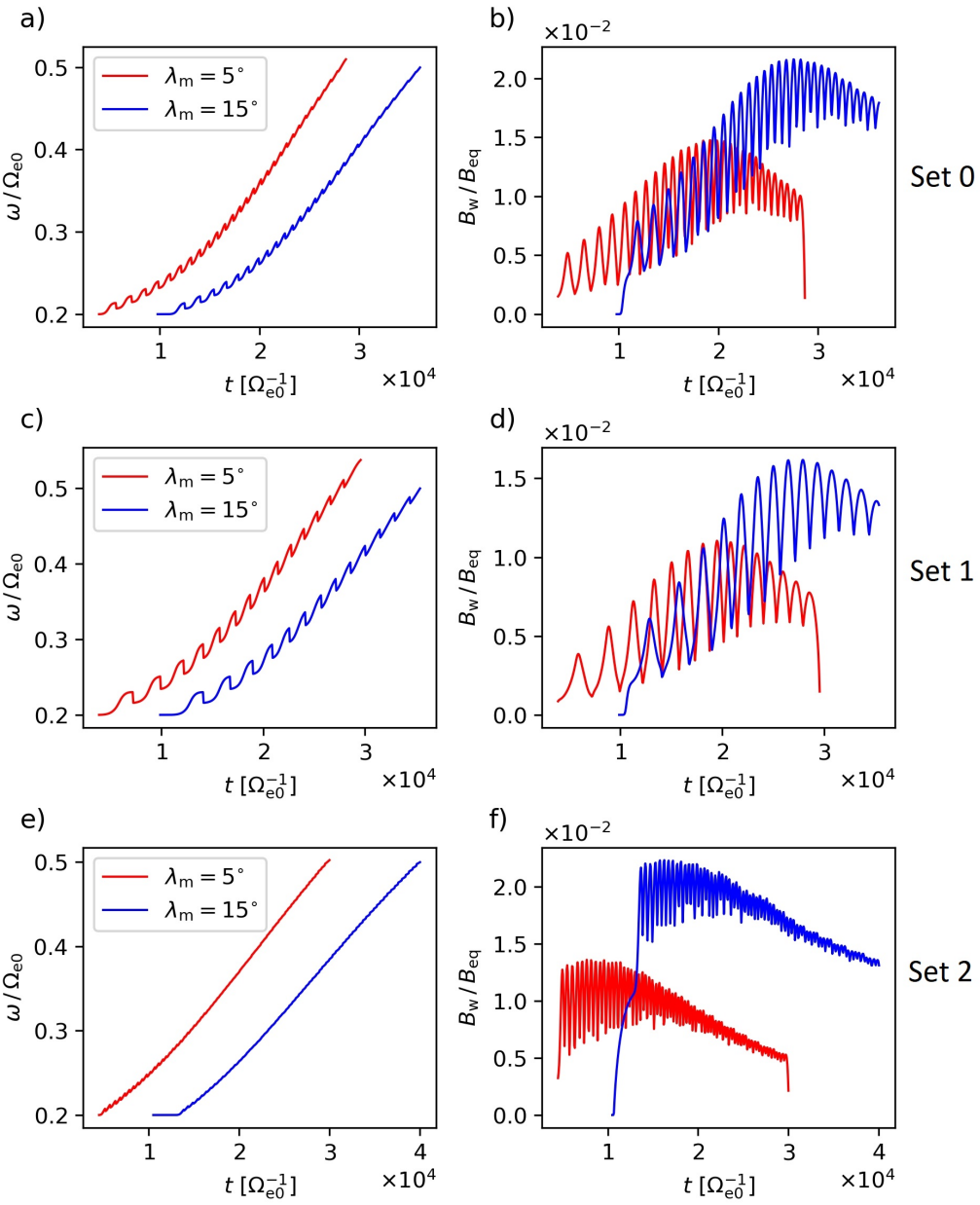

Figure 4.5: Time evolution of wave frequency and amplitude for all three simulations, plotted as spatial sections at $\lambda_m = 5°$ and $\lambda_m \approx 15°$. Reprinted from Hanzelka et al. (2020).

of chorus group velocity and spacecraft orbital velocity is typically around 10^4, allowing us to assume that the electromagnetic field detectors are not moving with respect to the plasma. Frequency plots in panels a), c), and e) show an almost linear trend, but we can also clearly notice the small sharp drops in between adjacent subpackets, which come from the choice of determining frequency ω_i from the shape of resonant current at the peak of subpacket $i-1$. The amplitude of subpackets has a sharp peak in their source that smoothens downstream due to dispersion and partly also due to numerical diffusion. Another effect of dispersion is the convergence of amplitude peaks and dips at higher frequencies and latitudes, which becomes especially visible in Figure 4.5f.

4.3 Improved treatment of the resonance region

To improve the above-described model, Hanzelka et al. (2021) have taken into account the width of the resonance island associated with each subpacket and considered its effects on the magnitude of the resonant current. Omura et al. (2015) derived a frequency separability criterion to determine whether the resonance islands of two subpackets are overlapping. For subpackets with frequencies ω_0 and ω_1 at a point (t, h), we require that

$$|\omega_1 - \omega_0| > \Delta\omega\,, \tag{4.5}$$

where

$$\Delta\omega = \left\langle \left(\frac{\partial V_\mathrm{R}}{\partial \omega}\right)^{-1} V_\mathrm{tr} \right\rangle_\omega . \tag{4.6}$$

Unlike Omura et al. (2015), we include the frequency averaging $\langle\bullet\rangle_\omega$ to account for the different frequencies of the two subpackets in the calculation of the resonance velocity and trapping frequency. The width V_tr is defined by Equation 2.9. Evaluation of the partial derivative results into

$$\Delta\omega = \left\langle 4\omega_\mathrm{tr}(1 - V_\mathrm{R} V_\mathrm{g}^{-1}) \right\rangle_\omega \tag{4.7}$$

In our simulation, each subpacket starts at a higher upstream position, so their sources never overlap. However, two waves with the same or similar frequency can meet later during propagation. In such a case, the resonance islands will collide, and the resonant current will be modified. Because the NGTO does not describe the dynamics of the resonance region in detail, we simply introduce a monotonic suppression factor

$$\begin{aligned} s_\mathrm{J}^{i+1}(t,h) &= \cos^2\left(\frac{\pi}{2}\delta_\omega(t,h)\right) && \text{for} \quad \delta_\omega \in [0,1]\,, \\ &= 0 && \text{for} \quad \delta_\omega > 1\,, \\ &= 1 && \text{for} \quad \delta_\omega < 0\,, \end{aligned} \tag{4.8}$$

by which we multiply the resonant current in the $(i+1)$-th subpacket. We also introduce the normalized frequency difference

$$\delta_\omega = \frac{\Delta\omega - (\omega^{i+1} - \omega^i)}{\Delta\omega}\,. \tag{4.9}$$

Furthermore, we drop the parabolic approximation and use the perfect dipole model to calculate the gradient of magnetic field strength.

Figure 4.6 shows simulation results obtained with the improved model under the following initial conditions and parameters: $\omega_0 = 0.21\,\Omega_\mathrm{e0}$, $\omega_\mathrm{f} = 0.46\,\Omega_\mathrm{e0}$, $B_\mathrm{surf} = 2.52 \cdot 10^{-5}\,\mathrm{T}$, $Q = 0.5$, $\tau = 0.35$, $\omega_\mathrm{pe} = 4.2\,\Omega_\mathrm{e0}$, $\omega_\mathrm{phe} = 0.3\,\Omega_\mathrm{e0}$, $V_{\perp 0} = 0.4\,c$, $U_{\mathrm{t}\parallel 0} = 0.16\,c$, $L = 4.58$. Looking at the wave amplitudes in panels a) and b), we immediately

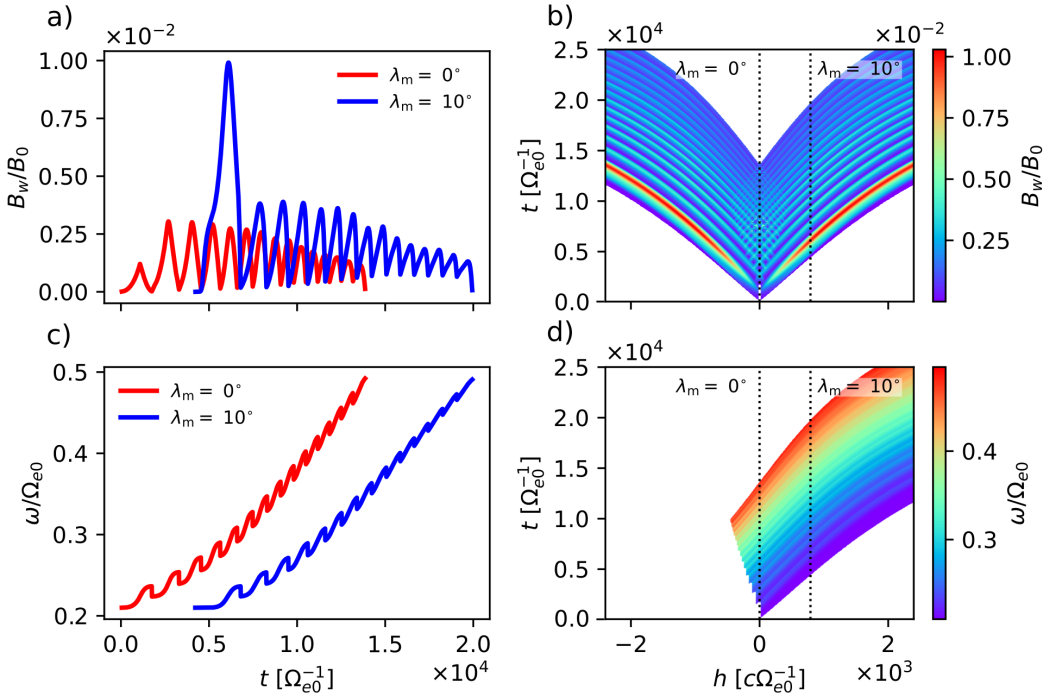

Figure 4.6: Chorus wavefield calculated from an improved model with resonant current suppression. Time evolution of the wave magnetic field amplitude B_w of a chorus element propagating along the magnetic field line towards positive h. Plotted for two values of latitude, $\lambda_\mathrm{m} = 0°$ (red line) and $\lambda_\mathrm{m} = 10°$ (blue line). b) Evolution of amplitude in time and space. Dotted lines show the spatial cuts at 0° and 10° of latitude. The total wavefield was obtained as a superposition of the left- and right-propagating waves. Panels c) and d) show the wave frequency ω and follow the format of panels a) and b), with only the right-propagating element being plotted. Reprinted from Hanzelka et al. (2021).

notice that the first subpacket still reaches large amplitudes of about 2.6 nT, which is a consequence of the sequential generation – the suppression factor does not apply here. However, the rest of the wavefield features realistic amplitudes < 1 nT. Another improvement is the increased difference between minima and maxima of each subpacket, resulting in well defined peaks.

To analyze the effect of changes in the input parameters, we ran multiple simulations and looked for correlations with the following output parameters: number of subpackets N_S, latitudinal shift of the source λ_drift, frequency drift rate (chirp) $\partial\omega/\partial t$, total length of the element ΔT, and maximum amplitude B_w/B_0. The last three parameters were determined at the equator. In Figure 4.7 we present the Pearson correlation coefficients obtained from data of type $O_k(I_i; \{I_{j\neq i}\})$, where O_k is the k-th output parameter, I_i is the i-th input parameter and $\{I_{j\neq i}\}$ is the rest of inputs whose values are fixed. Values of the input parameters are chosen from a range where strong nonlinear growth was ensured across the whole range of frequencies. Apart from the correlation coefficients, we also plot the dependencies to demonstrate their nonlinear character and the magnitude of their effect.

While our model is completely deterministic, it would be challenging to derive some of the dependencies analytically due to its complexity. For example, $U_{\mathrm{t}\|0}$ appears in the argument of an exponential in the variable $G(h)$, but it has minimal effect on any of the output parameters and shows some of the lowest correlations in the table. On the other hand, the influence of Q and τ on the input parameters can be easily traced back to the definition of the optimum and threshold amplitudes. Both of these input parameters show strong correlations with output variables (> 0.97 for all output parameters). In

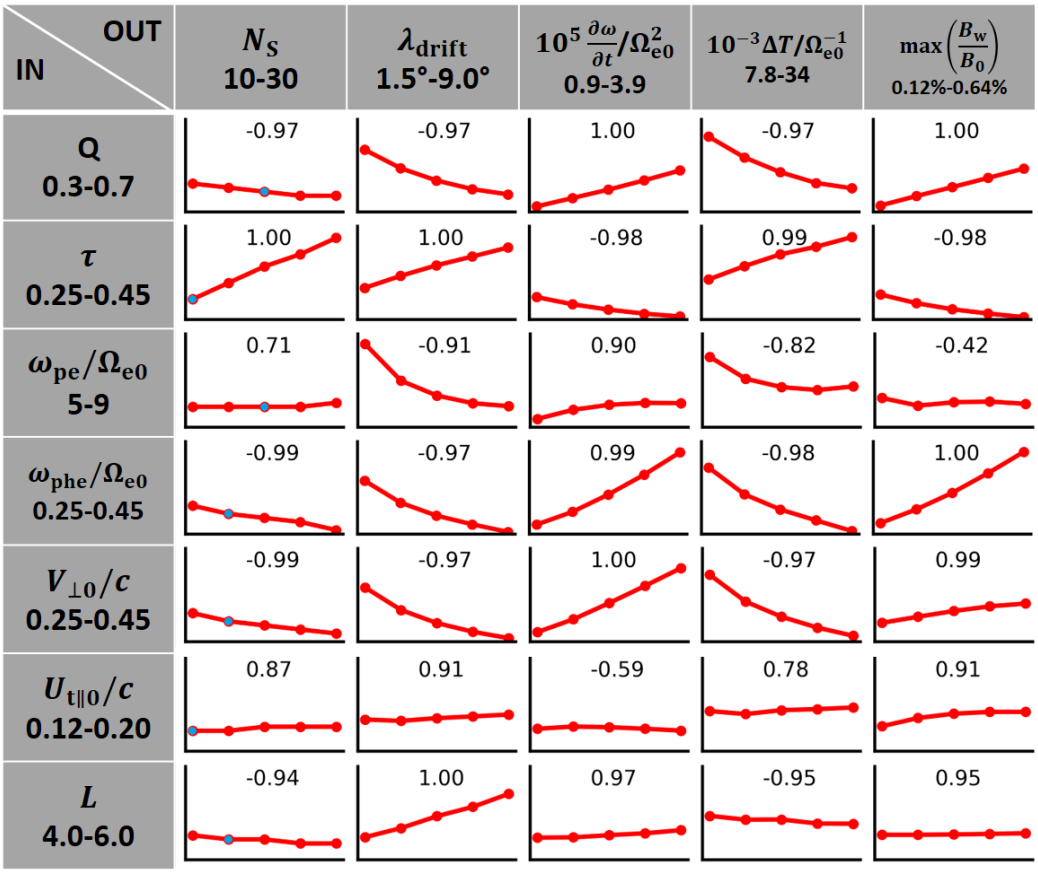

Figure 4.7: Table of correlation coefficients and plotted dependencies between output and input parameters of our wave model. The full horizontal and vertical axes ranges are given in the first column and the top row, respectively. In the first column of plots, the blue dots in each cell denote the value of the input parameter used in the computation of the other rows.

general, correlation analyses can assist us in the construction of a wavefield that fits closely to observational data.

4.4 Comparison with spacecraft observations

In Figure 4.8a, we show an example spectrogram of a chorus emission with a very regular subpacket structure as detected by Van Allen Probe B on 08 Oct 2012 in the outer radiation belt near the magnetic equator. Instantaneous amplitude and frequency of the parallel and perpendicular components of the magnetic field are plotted in panels b) and c). We can compare this observation with the simulation from Figure 4.6 which was based on input parameters chosen specifically to replicate this measurement (L-shell, electron gyrofrequency, plasma frequency and wave frequency range are identical). The simulated duration of the element 320 ms and the equatorial maximum amplitude 0.7 nT (off-equatorial 2.7 nT) match reasonably well with the observed values of 340 ms and 1.4 nT. On the other hand, the length of individual subpackets decreases from 38 ms to 15 ms in the simulation, while the experimental results give average subpacket length < 10 ms.

It follows from the discussion in Section 3.3 that analysing subpackets with analytical and semi-empirical models proves to be difficult because the exact origin of the amplitude modulations is still disputed. This lack of theoretical understanding becomes critical when comparing the instantaneous frequencies from Figure 4.8c with

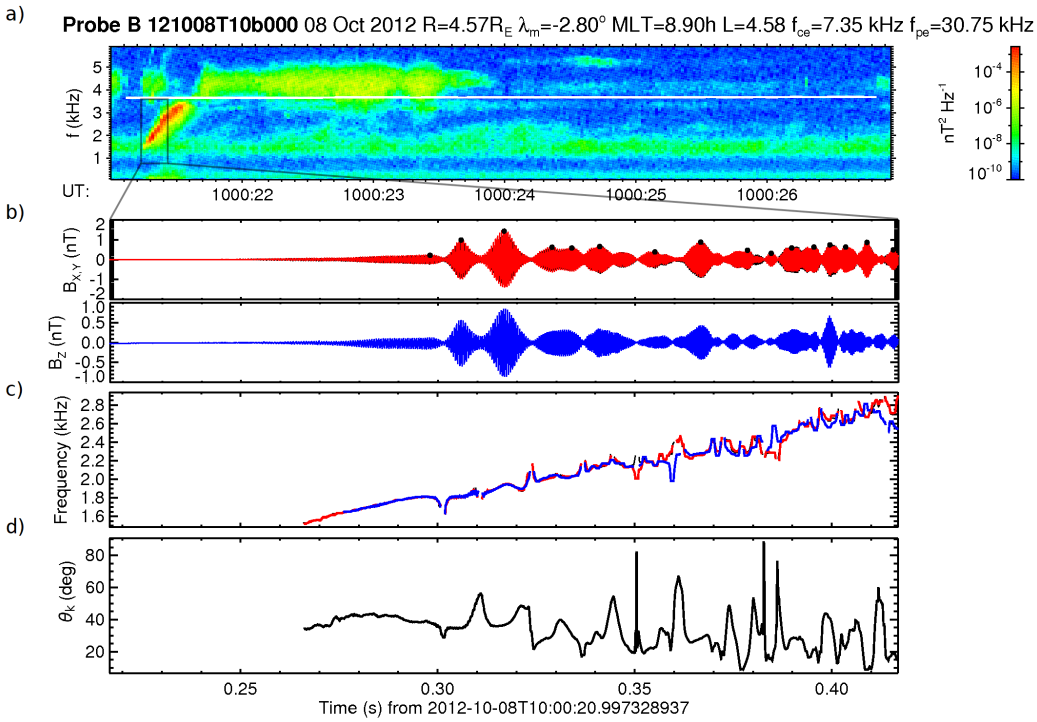

Figure 4.8: A chorus element observed by the Van Allen Probe B on October 8, 2012. a) A power spectrogram constructed from magnetic field waveforms. The white line denotes $\Omega_e/2$. b) Perpendicular and parallel magnetic field components from the first 200 milliseconds of the element. Black dots denote the peaks of individual subpackets. c) Instantaneous frequency obtained from the Hilbert transform of the time series $B_{x,y}$ and B_z. Data from time intervals corresponding to amplitudes smaller than 50 pT are omitted. d) Wave normal angles. Adapted from Hanzelka et al. (2021).

our model. The drops in frequency found between the first two pairs of subpackets resemble the irregular chirp rate from simulation; however, it is not apparent if these features come from the breakdown of the resonance island, as assumed in the sequential triggering model, or if they are a simple result of wave beating with a phase mismatch. It was discovered with Bayesian spectral analysis (Crabtree et al., 2017) that the initial subpackets correspond to a single chirping plane wave, but the later amplitude modulations are better explained by summation of multiple plane waves. Wavelet analysis of several RBSP observations (Tsurutani et al., 2020) even suggests that the subpackets have constant frequency and that the chirping comes from discrete jumps.

To investigate the effects of wave beating of dephased, constant-frequency packets, we used the statistical study of the subpacket structure by Santolík et al. (2014a) as a reference and constructed an artificial waveform, presented in Figure 4.9a. A total of 25 packets of various widths and amplitudes is summed, with each packet having a slightly higher frequency than the previous. The phase jumps between individual packets come from a uniform random distribution. Figure 4.9c shows the instantaneous frequency obtained from the Hilbert transform, and we can see frequency jumps near the amplitude minima, similar to the observational results in Figure 4.8c. Also, the amplitude seems to be growing in certain packets purely due to wave superposition. This observation suggests that the irregular growth of frequency towards the right half of Figure 4.8c might come from wave beating of constant-frequency waves rather than from a continuous chirp – compare this conclusion with the sideband theory from Section 3.3.2. However, the frequency change within the first, long subpacket cannot be explained this way. For the sake of completeness, we also constructed the power

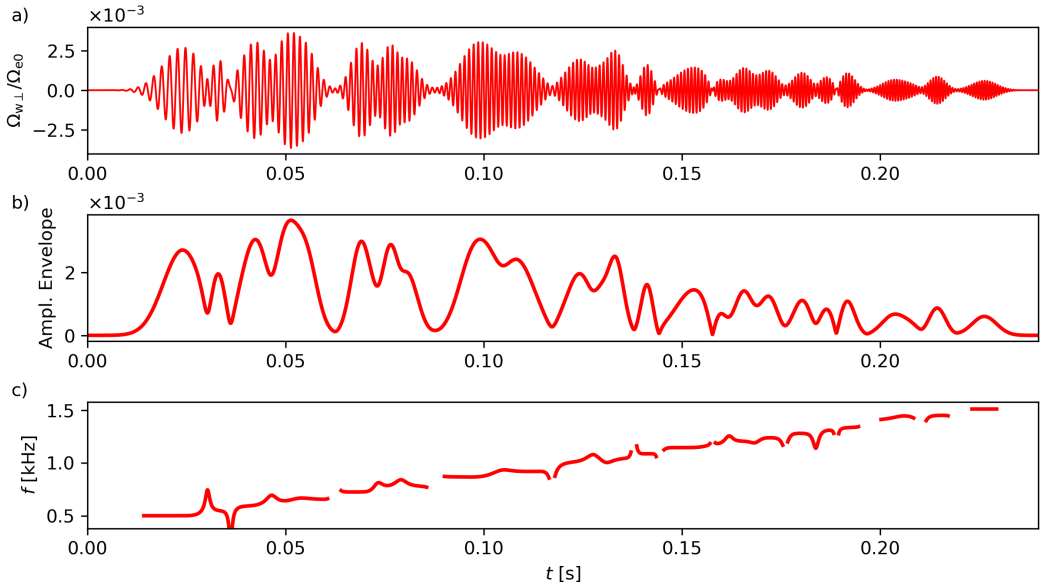

Figure 4.9: a) Normalized waveform of perpendicular magnetic field (parallel component is 0) constructed from constant-frequency subpackets to resemble a spacecraft measurement of a chorus element. b) Amplitude envelope obtained from the Hilbert transform of the time series in the above panel. c) Instantaneous frequency obtained as the time derivative of the wave phase. Data corresponding to amplitudes below 10 % of the maximum are omitted.

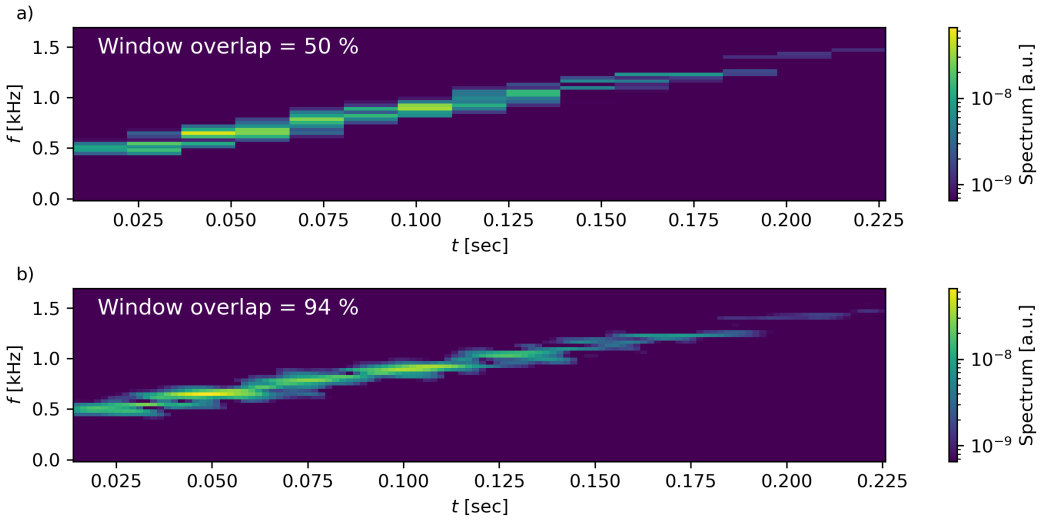

Figure 4.10: Time-frequency spectrogram of magnetic wave power constructed from the artificial time series in 4.9. a) 256-point FFT with a 94% window overlap. b) 256-point FFT with a 50% window overlap.

spectra of the artificial chorus element, one with a 50% overlap of 256-point Cooley-Tukey windows (Figure 4.10a) and another with a 94% overlap (Figure 4.10b). While the second spectrum exhibits certain step-like features, it is clear that the chirp of individual subpackets cannot be easily derived from STFT spectrograms.

The motion of the source can be compared to multipoint measurements from the Cluster spacecraft fleet (Santolík et al., 2004). It was shown that the source position fluctuates within 1000 km to 2000 km of the geomagnetic equator, and the extent of the source ranges from 3000 km to 5000 km. The λ_{drift} values from Figure 4.7 can be recalculated to distances ranging from 900 km to 4600 km. However, the analysis of Santolík et al. (2004) does not determine whether the source is in motion. The motion

of the source was indirectly proven by Demekhov et al. (2020), who observed frequency differences in THEMIS observation of chorus elements near the equator and linked them to the bidirectional motion of the source. The velocity of the upstream motion has been determined to be $V_\mathrm{g} + V_\mathrm{R}$ based on PIC simulations Nogi and Omura (2022). This result does not agree with our model, where the velocity is found to be (derived from Equations 4.2 and 4.3)

$$\frac{V_\mathrm{R} V_\mathrm{g}}{V_\mathrm{g} t_\mathrm{end} - V_\mathrm{R} t_\mathrm{max}} (t_\mathrm{end} - t_\mathrm{max}) \,, \tag{4.10}$$

which is a strictly positive value. So far, there is no rigorous theoretical support for the conclusion of Nogi and Omura (2022).

The chirping rates can be compared to the results of Teng et al. (2017), who studied the relation between ΔT (element duration) and $\partial\omega/\partial t$ in Van Allen Probes chorus data. They found a dependence

$$\Omega_\mathrm{e0} \Delta T = 0.04 \left(\frac{1}{\Omega_\mathrm{e0}^2} \frac{\partial \omega}{\partial t} \right)^{-1.1} \,, \tag{4.11}$$

while the simulation dataset from Figure 4.7 gives

$$\Omega_\mathrm{e0} \Delta T = (0.37 \pm 0.06) \cdot \left(\frac{1}{\Omega_\mathrm{e0}^2} \frac{\partial \omega}{\partial t} \right)^{-0.98 \pm 0.02} \,. \tag{4.12}$$

Unfortunately, Teng et al. (2017) do not provide standard deviation of the fitted multiplicative factor, but we can conclude that the sweep rates in our model are higher than average. The exponent must be approximately equal to -1 in the simulated data because the frequency range $\omega_\mathrm{f} - \omega_0$ was fixed in all runs.

When comparing wavefield models and observations, we must remember that the NGTO describes parallel propagation, while experimental data always show a certain degree of obliquity. Figure 4.8d shows large variation in wave normal angle, which is a consequence of misalignment between the subpacket structure of the perpendicular and the parallel magnetic field. The origin of the difference in wave amplitude modulation of the two components is unknown; it might be related to propagation effects and ducting. Nevertheless, even without the prominent peaks in θ_k, the average values range between 20° and 40°, suggesting that a quasiparallel approximation would be more appropriate.

4.5 Conclusion

Summarizing the results of Hanzelka et al. (2020), we have shown that the nonlinear growth theory, together with the theory of helical antenna radiation, can be used to construct a numerical model of a parallel-propagating, rising-tone chorus element with a subpacket structure. The simulated chorus elements' amplitude, duration, and chirping rate match well with spacecraft observations. The motion of the source and irregularities in the chirping rate are a natural result of our sequential generation scheme, which is an improvement over earlier models (Kubota and Omura, 2018).

Unfortunately, an in-depth comparison between model and observations is not possible, mostly due to two reasons. First, certain input parameters cannot be observed with sufficient precision. As we discuss in Chapter 5, reliable measurements of phase space density in the resonance region on scales of T_tr are currently not feasible, and thus we cannot determine Q. The measurements of the hot electron distribution are also plagued with large uncertainties, limiting our knowledge of ω_phe, $V_\perp$ and $U_{\mathrm{t},\parallel}$. Parameter τ is related to the nonlinear transition time for the formation of the resonant

current J_R, and J_R can be directly determined only by precise measurements of phase space density near the electron hole. And second, the model has seven input parameters (nine when counting ω_0 and ω_f), which makes the sampling of the full configuration space unfeasible.

We suggest that future modelling efforts should focus on removing the free parameters τ and Q, and the parallel theory should be updated to a quasiparallel version which could explain the frequency gap near $\Omega_e/2$ and allow to expand the model to higher latitudes. However, even such improvements might not resolve the questions about subpackets, which may originate not only from the nonlinear generation process, but also from convective growth, superposition of multiple plane waves, and possibly also from propagation effects in an inhomogeneous plasma (ducting). Furthermore, a thorough statistical analysis of the subpacket structure is missing in current literature, limiting thus our ability to validate theoretical and numerical results.

5. Test-particle simulations of electron distribution interacting with chorus emissions

Calculations of particle trajectories in Chapter 2 show that electrons interacting with a counter-streaming, large-amplitude whistler wave can be either scattered or become trapped in the wave potential. In the case of a rising-tone chorus emission, the resonance velocity gradually decreases, and the low-density trapped particles move to higher density regions of the phase space. According to the nonlinear growth theory (Section 3.2), this depression in the electron distribution, sometimes called the electromagnetic electron hole, forms the resonant current, which transfers energy to the chirping wave and supports its further growth. However, because the transition between two neighbouring chorus subpackets and the associated electron holes happens on a millisecond scale, observations of the velocity space perturbations have proven to be quite challenging. Shoji et al. (2021) investigated an analogous phase space feature, the proton hill associated with falling-tone EMIC emissions, and observed a distinct nongyrotropy of the hot proton distribution during the time interval in which the EMIC was detected. Nonetheless, no experimental study has successfully observed these nonlinear features of the phase space evolution on subpacket timescales.

Here we use test-particle simulations to assess the resolution needed to observe electron holes in velocity space without superposition or composition of multiple measurements. Unlike particle-in-cell methods or similar self-consistent approaches, backwards-in time test-particle simulations (Section 5.2) can provide high-resolution data and allow us to study the hole structure while keeping the requirements on computer resources reasonably low. Results on the evolution of the hot electron distribution and the measurability of the phase space hole can be found in Sections 5.3, 5.4 and 5.5. The contents of Sections 5.1 through 5.5 are based on the publication Hanzelka et al. (2021), which can be found in Attachment A.3.

The test-particle motion can also be adiabatically extended beyond the range of the wavefield model to investigate the precipitation of energetic electrons into the atmosphere, related to the microbursts (Lampton, 1967; Lorentzen et al., 2001). These results are presented in Section 5.6.

5.1 Wavefield model

Since test-particle simulations by definition cannot solve the Maxwell-Vlasov equations, the chorus wavefield must be prescribed across the whole time-space range of each simulation run. We use the semi-empirical model developed in Chapter 4; specifically, the amplitudes and frequencies are prescribed by the results presented in Figure 4.6. To obtain the phase of the magnetic field vector ψ_B, we use the eikonal approximation from Section 1.1.5, which defines the wave frequency and wave number as

$$\omega = \frac{\partial \psi_B}{\partial t}\,, \tag{5.1}$$

$$k = -\frac{\partial \psi_B}{\partial h}\,, \tag{5.2}$$

and we integrate these in time and space. Each subpacket is integrated separately, first in time in the source point, then in space away from the source. Values of k

are derived from the cold plasma dispersion for parallel whistler waves, Equations 1.58 and 1.26. During particle simulation, phase angles from adjacent grid points are bilinearly interpolated to the position of the traced particle. The initial phase in the source is always set to zero, and because the position of the source is a variable with complicated dependence on input parameters, we can consider the phase difference between adjacent subpackets as random. The electric field components are obtained by multiplication of $\boldsymbol{B}_\mathrm{w}$ by V_p and a subsequent 90° phase shift in accordance with Equation 2.12.

As an alternative to the model wavefield, we could use electromagnetic measurements from spacecraft. However, the provided electric and magnetic fields follow a single worldline, and even with multipoint measurements, we have no reliable methods that would extrapolate the observation to the whole simulation box. Therefore, the theoretical model is preferred, but we must keep in mind that the amplitude and frequency variations in the model element are less irregular than in situ observations, which will impact the evolution of the electromagnetic electron hole.

5.2 Backward-in-time simulation method

The purpose of the test-particle simulations described in this chapter is to study the evolution of velocity distributions in the 4D phase space $(h, v_\parallel, v_\perp, \varphi)$. If we were to uniformly sample this space at $t = 0$ and then wanted to determine the phase space density in the vicinity of an arbitrary point at $t > 0$, performance-related limitations on the number of particles would force us to either use large grid cells or to accept high levels of noise. Therefore, we instead sample the velocity space at a final point $(t_\mathrm{f}, h_\mathrm{f})$ and propagate the particles back in time until they reach a region of spacetime where the distribution was unperturbed and known. This method relies on Liouville's theorem, which states that the phase space density is constant along any trajectory in a Hamiltonian system. The bi-Maxwellian distribution function from Equation 3.11, which serves as the initial distribution in our particle simulations, was derived so that the phase space density is preserved along paths traced by the adiabatic motion of particles (see the Attachment A.1 for the Jacobian of the $\mathrm{d}u^3 \to \mathrm{d}v^3$ transformation). A schematic illustration of the method is presented in Figure 5.1. Note that we can sample an arbitrarily small section of the phase space to increase resolution in the resonance region, and we can also change the initial distribution *a posteriori* without the need to repeat the simulation. On the other hand, the resulting perturbed distribution is known only at one point in the spacetime, and the whole simulation has to be repeated for each new point.

The equations of motion are solved in their Cartesian form

$$m_\mathrm{e} \frac{\mathrm{d}\gamma \boldsymbol{v}}{\mathrm{d}t} = -e\left(\boldsymbol{E}_\mathrm{w} + \boldsymbol{v} \times (\boldsymbol{B}_0 + \boldsymbol{B}_\mathrm{w})\right) , \tag{5.3}$$

$$\frac{\mathrm{d}\boldsymbol{r}}{\mathrm{d}t} = \boldsymbol{v} , \tag{5.4}$$

with the magnetic field curvature incorporated into $\boldsymbol{B}_0$ through the perpendicular components defined by 2.39, that is,

$$\frac{e\boldsymbol{B}_0}{m_\mathrm{e}} = \left(\frac{-\gamma v_y}{2\Omega_\mathrm{e}} \frac{\partial \Omega_\mathrm{e}}{\partial h}, \frac{\gamma v_x}{2\Omega_\mathrm{e}} \frac{\partial \Omega_\mathrm{e}}{\partial h}, \Omega_\mathrm{e} \right) . \tag{5.5}$$

The velocity of the particles is advanced in time by the relativistic Boris push in the form presented by Higuera and Cary (2017), which was shown to preserve both the phase space volume and the $v_{\boldsymbol{E}\times\boldsymbol{B}}$ drift velocity. Additionally, we keep the gyrophase

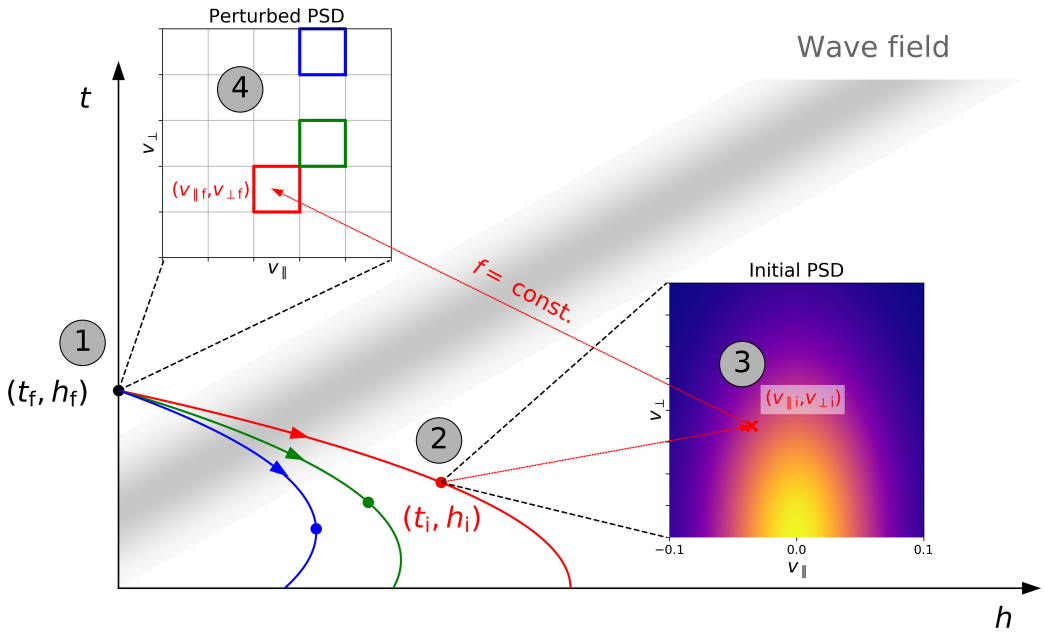

Figure 5.1: A schematic illustration explaining the idea behind backwards-in-time test particle simulations. (1) The particles start from the final point $(t_\mathrm{f}, h_\mathrm{f})$, distributed uniformly in the velocity space $(v_\parallel, v_\perp, \varphi)$ so that each particles represents one grid cell. (2) A test particle propagates until it reaches the initial point (t_i, h_i), which is the first point at which the particle leaves the wavefield and never re-encounters it. At this point, the velocity distribution is known. (3) A numerical value of phase space density from the initial distribution is assigned to the particle. (4) The density is mapped to the corresponding grid cell of the final, perturbed distribution. Reprinted from Hanzelka et al. (2021).

correction which is often omitted in the implementation of the Boris algorithm (Zenitani and Umeda, 2018). The whole process is summarized by the following list of equations ($m_\mathrm{e} = 1$, $e = 1$, $c = 1$):

$$\boldsymbol{r}_{i+3/2} = \boldsymbol{r}_{i+1/2} + \Delta t \boldsymbol{v}_{i+1}\,, \tag{5.6}$$

$$\boldsymbol{v}_{i+1} = \frac{\boldsymbol{u}_{i+1}}{\gamma_{i+1}}\,, \tag{5.7}$$

$$\gamma_{i+1} = \sqrt{1 + |\boldsymbol{u}_{i+1}|^2}\,, \tag{5.8}$$

$$\boldsymbol{u}_{i+1} = \boldsymbol{u}_+ + \boldsymbol{\varepsilon}\,, \tag{5.9}$$

$$\boldsymbol{u}_+ = \boldsymbol{u}_- + \boldsymbol{u}' \times \boldsymbol{s}\,, \tag{5.10}$$

$$\boldsymbol{s} = \frac{2\boldsymbol{\tau}}{1 + |\boldsymbol{\tau}|^2}\,, \tag{5.11}$$

$$\boldsymbol{u}' = \boldsymbol{u}_- + \boldsymbol{u}_- \times \boldsymbol{\tau}\,, \tag{5.12}$$

$$\boldsymbol{\tau} = \tan\left(\frac{-\Delta t}{2\gamma'}|\boldsymbol{B}_{i+1/2}|\right)\frac{\boldsymbol{B}_{i+1/2}}{|\boldsymbol{B}_{i+1/2}|}\,, \tag{5.13}$$

$$\gamma' = \left(\frac{1}{2}\left(\gamma_-^2 - |\boldsymbol{\beta}|^2 + \sqrt{(\gamma_-^2 - |\boldsymbol{\beta}|^2) + 4(|\boldsymbol{\beta}|^2 + (\boldsymbol{\beta}\cdot\boldsymbol{u}_-)^2)}\right)\right)\,, \tag{5.14}$$

$$\gamma_- = \sqrt{1 + |\boldsymbol{u}_-|^2}\,, \tag{5.15}$$

$$\boldsymbol{\beta} = \frac{-\Delta t}{2}\boldsymbol{B}_{i+1/2}\,, \tag{5.16}$$

$$\boldsymbol{u}_- = \boldsymbol{u}_i + \boldsymbol{\varepsilon}\,, \tag{5.17}$$

$$\boldsymbol{\varepsilon} = \frac{-\Delta t}{2}\boldsymbol{E}_{i+1/2}\,, \tag{5.18}$$

$$\boldsymbol{u_i} = \gamma_i \boldsymbol{v_i} \,. \tag{5.19}$$

The x and y components of the position vector are discarded as they are not needed for further analysis.

The parameters of the initial hot electron distribution are kept consistent with the wave model, see Section 4.3; this choice of input parameters results in a high equatorial temperature anisotropy $A_0 = 3.8$. Because particles in the relevant energy range are only weakly relativistic, we choose a uniform sampling in the velocity space $(v_\parallel, v_\perp, \varphi)$. For the study of irregularities in the velocity space, we sample velocities in the range $v_\parallel \in (-0.5c, 0.0c)$ and $v_\perp \in (0.0c, 1.0c)$ with 256×256 points, and phases $\varphi \in [0, 2\pi)$ with 64 points ($v > c$ particles are removed). The evolution of phase space holes is mapped with 1024 points in the parallel velocity and 512 points in the gyrophase, with perpendicular velocity being fixed. In this simulation, the range of $v_\parallel$ depends on the resonance width. For additional comments on the grid choice and related uncertainties, see Hanzelka et al. (2021), Section 2.2.

5.3 Interaction with a single subpacket

With the simulation setup described above, we investigated the evolution of the equatorial hot electron distribution during interaction with the first subpacket of the model wavefield. Following the particle trajectory analysis in Figures 2.5 and 2.9, we expect that the positive chirp rate will lead to the formation of a teardrop-shaped electron hole centred at the resonance velocity associated with the plane wave. Plot of $f(\zeta, v_\parallel, v_\perp = 0.4c)$ in Figure 5.2a confirms the theoretical predictions, but the density in the hole is far from uniform. Furthermore, a significant density increase is observed at higher parallel velocities $|v_\parallel|$ and higher values of the ζ angle. Nevertheless, the integrated distribution in the inset plot shows favourable nongyrotropy for the production of negative resonant current. During later stages of the subpacket evolution, the width of the resonance island decreases, and the phase distribution starts to homogenize, as shown in Figure 5.2c. At $t = 1760\,\Omega_\mathrm{e}^{-1}$, when the first subpacket transitions into the second one, the integrated parallel velocity distribution shows a step-like feature associated with the remnant of the electron hole, representing thus a connection between the NGTO and the BWO theory (Sections 3.2 and 3.3).

While the nonlinear growth theory assumes that the distribution in perpendicular velocities can be well approximated by a δ-function (Equation 3.20), the effect of $v_\perp$ on the resonance velocity is not entirely negligible. Figure 5.3 shows that although the peak change in density appears near $v_\perp = V_{\perp 0}$, the perturbations due to nonlinear interactions are significant from $v_\perp = 0$ up to $v_\perp = 0.7c$. The perturbation consists of two stripes of increased and decreased phase space density. The density increase is related to scattering from high to low pitch angles associated with loss of energy and appears at larger parallel velocities, close to the resonance velocity curve defined by the starting frequency of the subpacket. The density decrease is related to the transport of trapped particles from low to high pitch angles and their acceleration and appears at smaller parallel velocities, close to the resonance velocity curve defined by the final frequency of the subpacket. Furthermore, we observe that the density decrease disappears at low pitch angles, which is a consequence of the anomalous resonance (see Figure 2.6 for visual explanation).

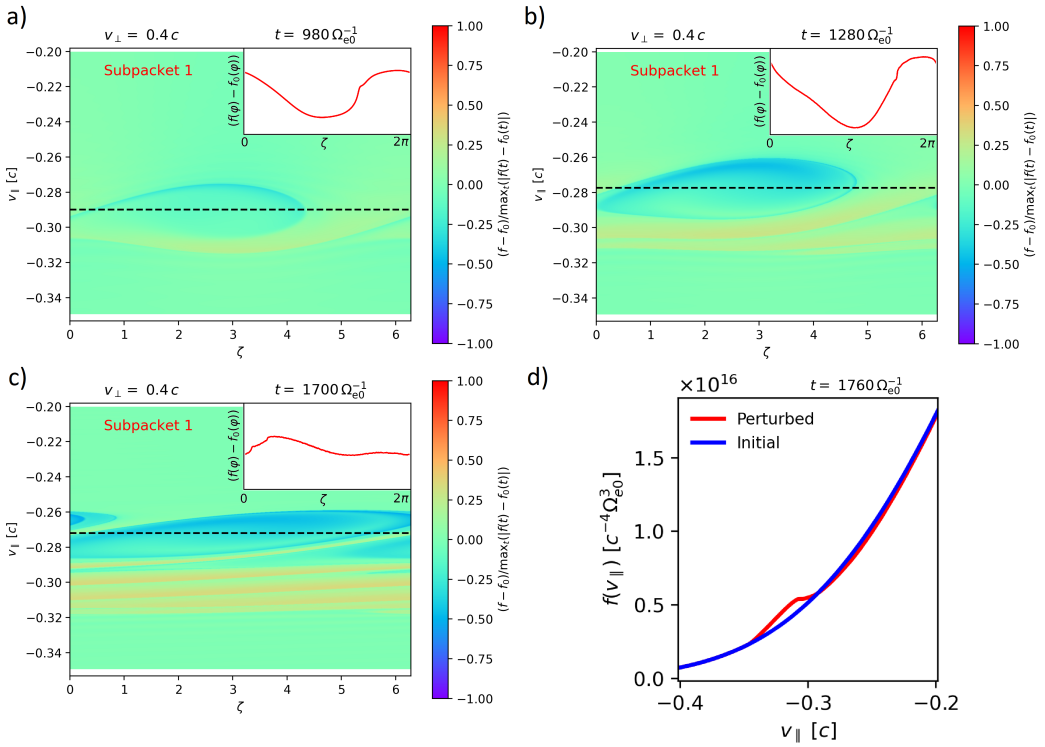

Figure 5.2: a) Equatorial phase space density near the peak of the first subpacket. A 512×1024 grid was used in the $(\zeta, v_\parallel)$ space, with only a single value of $v_\perp$. The inset plot shows the shape of the distribution integrated over parallel velocities. The black dashed line represents the resonance velocity. b) Same as a), but at a later stage of the evolution. c) Final state of the $f(\zeta, v_\parallel, v_\perp = 0.4c)$ distribution before triggering of the second subpacket. d) Integrated $f_(v_\parallel)$ distribution in normalized units, showing the step-like feature formed by the first subpacket. Note that this distribution was obtained from integration over perpendicular velocities and phases based on the simulation with 3D velocity space sampling, $(\zeta, v_\parallel, v_\perp) \sim 64 \times 256 \times 256$. Adapted from Hanzelka et al. (2021).

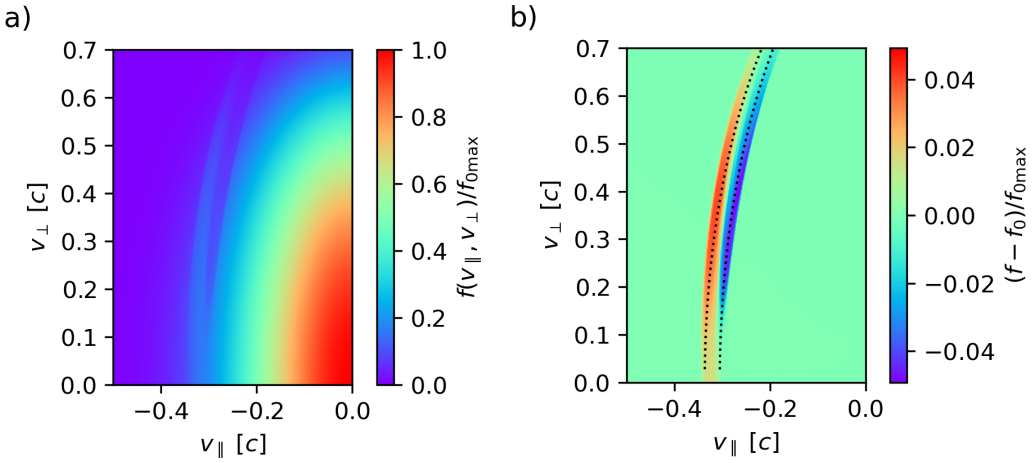

Figure 5.3: a) Perturbed velocity distribution after interaction with the first subpacket, $(t, h) = (1760\,\Omega_e^{-1}, 0)$. b) Difference between the final and initial distribution. Adapted from Hanzelka et al. (2021).

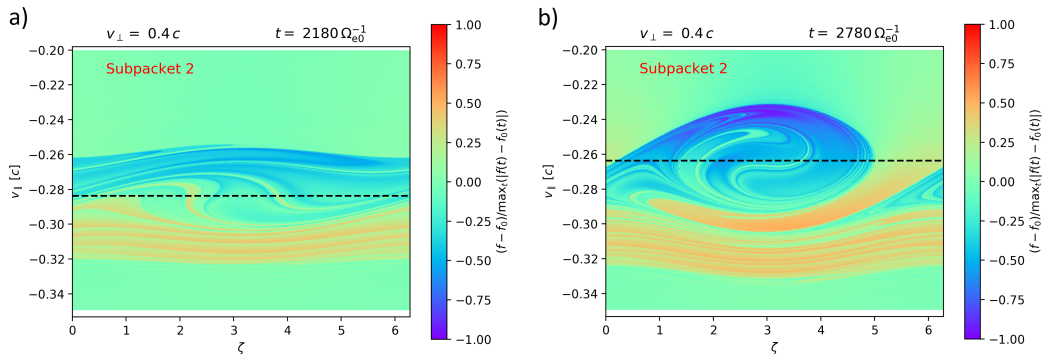

Figure 5.4: Evolution of equatorial phase space density showing the formation of electron hole associated with the second subpacket. The snapshot in panel a) is taken during the growth phase, while panel b) corresponds to the peak of the subpacket. Adapted from Hanzelka et al. (2021).

5.4 Interaction with a full chorus element

5.4.1 Transition between subpackets

The second subpacket interacts with the previously perturbed distribution and starts entrapping particles from the low-density stripe depicted in 5.3. In our model, the slight drops in frequency between packets increase the resonance velocity, and therefore, part of the scattered particles from the high-density region also becomes trapped, as we can see in the initial stage of electron hole formation in Figure 5.4a. Without the repeated detrapping and phase mixing caused by amplitude modulations, a massive depletion would form at resonance velocities corresponding to the wave frequencies towards the end of the chorus element; however, such large perturbations have not been observed (cf. Section 5.5). Figure 5.4b shows the electron hole that formed near the peak of the second subpacket and reveals that the fine density structures within the resonance island gradually fall below the resolution of the grid, resulting in a more homogeneous appearance.

Let us now show that the chosen resolution is close to the limit of applicability of statistical plasma theory. Integration of an averaged phase space density over a single grid cell (choosing $\Delta v_\perp = c/256$ as in the large scale simulation) reveals that this velocity-space cell contains $3 \cdot 10^{-4}$ particles per cubic meter. Let us define 10^6 as the minimal number of particles necessary for statistical treatment. Assuming that the phase space structure does not change much over one hundredth of a wavelength, we conclude that the wavefield should remain nearly constant in a field-line cross section of radius $\sim 10^3$ m. Hanzelka and Santolík (2019) proposed that density filamentations with characteristic radial dimensions of 10^4 m should commonly occur in the inner magnetosphere, influencing the distribution of chorus wave amplitude. Therefore, we can conclude that increasing the resolution will not reveal any additional features of the velocity distribution since the concept of phase space density stops being meaningful for smaller grid cells.

In Section 5.3, we associated the decrease in phase space density with an increase in energy and phase angle. In Figure 5.5, we show the changes in particle kinetic energy E_k and equatorial pitch angle α_eq in the resonance region of the second subpacket. We observe that the scattering of untrapped particles affects the unperturbed portion of the distribution and leads to moderate changes in pitch angle (decrease by less than 15°). On the other hand, the trapped particles come from the previously perturbed region and experience a successive increase in pitch angle up to 20° and more. This

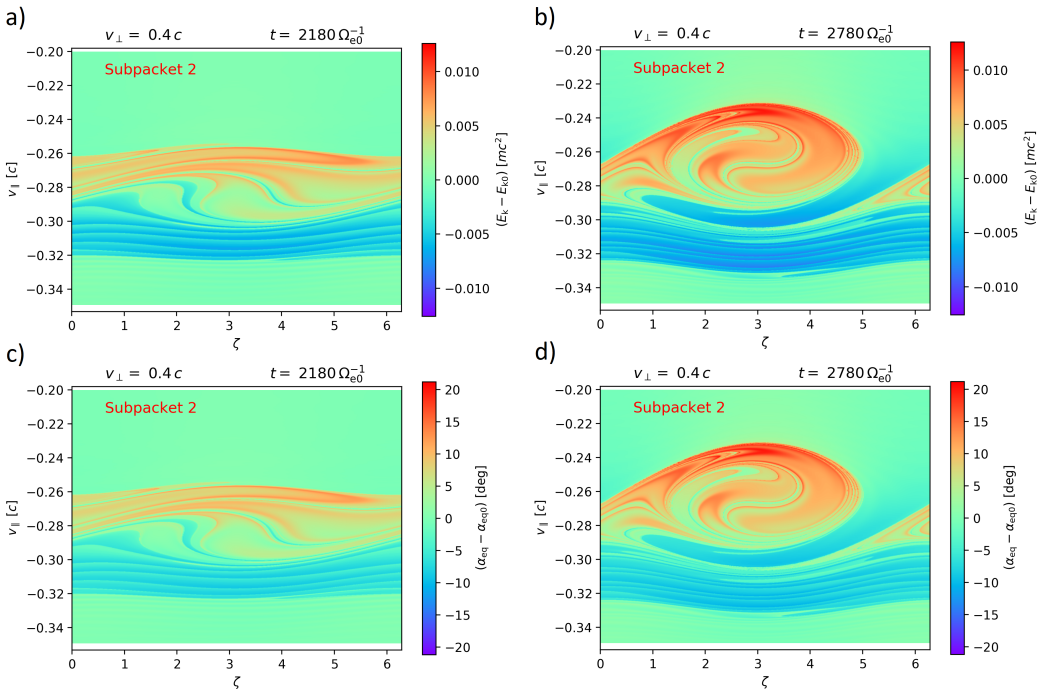

Figure 5.5: Changes of particle kinetic energy and equatorial pitch angle in electron holes from Figure 5.4. Adapted from Hanzelka et al. (2021).

nonlocal transport poses difficulty for a mathematical formulation of the nonlinear response function (Artemyev et al., 2021). For trajectory examples exhibiting successive trapping, see Section 5.4.3. For animations showing the evolution of the electron hole depicted in Figures 5.4 and 5.5, see digital attachments Vid1, Vid2 and Vid3.

5.4.2 Perturbed velocity distribution

Using the backwards-in-time simulation method, we sampled the equatorial distribution at amplitude minima of the chorus element at $h = 0$. An animation showing the evolution of the phase space density can be found in the digital attachment Vid4. The final state after the decay of the last subpacket is presented in Figure 5.6. The stripe structure is still visible but becomes distorted towards smaller parallel velocities associated with the high-frequency end of the element. Electrons that interacted with the low-frequency end at higher latitudes arrive at the equator with increased parallel velocities resulting from the conservation of the first adiabatic invariant. This causes straightening of the stripes, making them visible in the reduced distribution in Figure 5.6d. The most prominent feature of the perturbed distribution is the low-density stripe stretched approximately along the resonance velocity curve of the last subpacket. The complete evolution of the equatorial distribution reveals that this density depletion is always present at the leading edge of the propagating perturbation, supported by the successive trapping of resonant electrons.

The nonlinear resonant interaction with a rising-tone chorus element results in a decrease in PSD at high pitch angles and an increase in density in the low pitch angles region. The hot electron distribution thus experiences a reduction of anisotropy, and consequently, the growth of new triggering waves through the linear anisotropy-driven instability diminishes. The PSD gradients formed by the perturbation stripes are also unstable, but our simulation cannot capture their decay. We assume that the energy stored in these instabilities transfers into the weaker part of the power spectrum observed to the right of the element in Figure 4.8a. These diminishing parts of

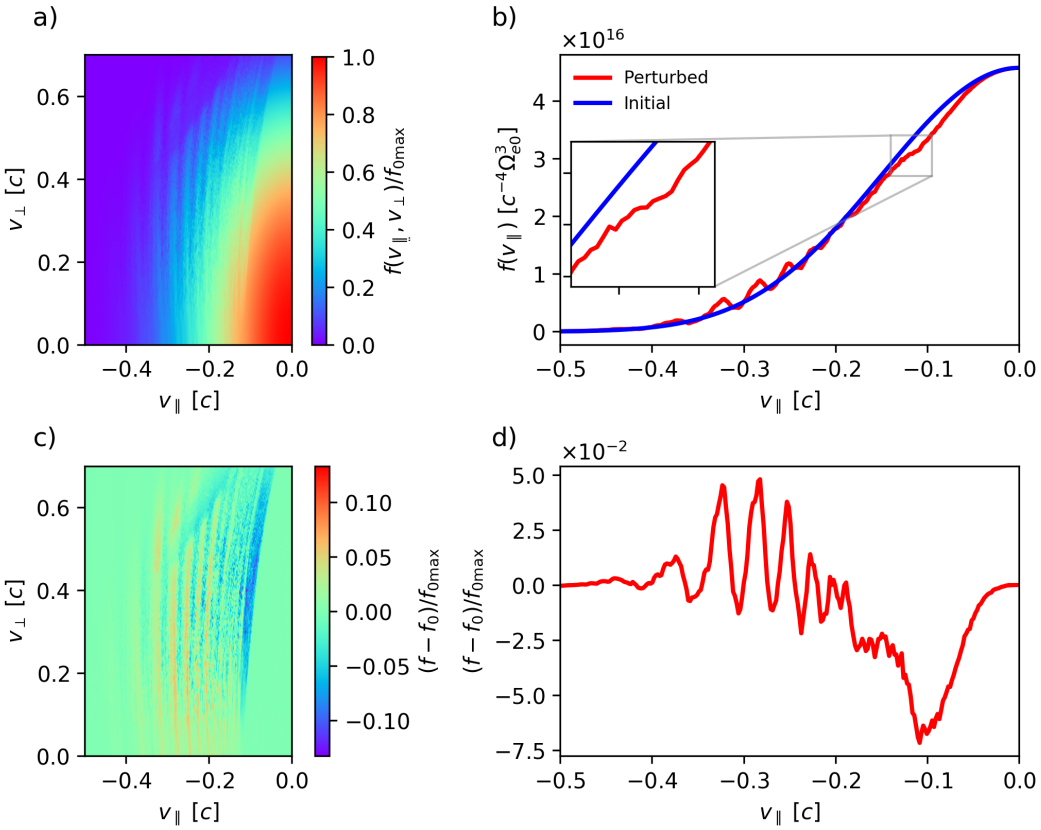

Figure 5.6: a) Perturbed hot electron velocity distribution at $h = 0$ after interaction with the whole chorus element. b) Integrated 1D distribution $f(v_\parallel)$ with the inset plot showing the lack of any apparent plateau or step. c) Difference between the initial and perturbed 2D distribution. d) Difference between initial and perturbed 1D distribution. Prominent peaks between $-0.35c$ and $-0.2c$ are due to the straightening of density elevations (panel c) caused by the adiabatic motion of electrons in the dipole magnetic field. Reprinted from Hanzelka et al. (2021).

the spectrum are also observed in BWO-based simulation (Demekhov, 2017) and PIC simulations (Nogi and Omura, 2022), and may sometimes appear as short falling tones driven by the electron hills formed from the scattered particles.

The $f(v_\parallel)$ distribution in Figure 5.6b shows that there is no clear step in phase space density that could serve as the source of energy for wave growth within the BWO theory. However, we must remember that this theory was developed for non-relativistic velocities (see Section 3.3.2) and that a relativistic extension should be concerned with a step function in the direction perpendicular to the resonance velocity curve (Trakhtengerts, 1995).

5.4.3 Particle trajectories in a symmetric wavefield

The vertical stripe structure of PSD elevations in Figure 5.6c is disrupted by an oblique stripe of density depletion at higher perpendicular velocities. This is an effect of the symmetric chorus wavefield caused by particles that first experienced trapping and acceleration by the element propagating to negative h, reached their mirror point at $h > 0$ and then returned to the equator. Some particles can also experience a second, scattering interaction with the element propagating to positive h. However, such cases are rare and can appear only in chorus elements with sufficiently long duration. In Figure 5.7, we show a trajectory example with multiple interactions, crossing the equa-

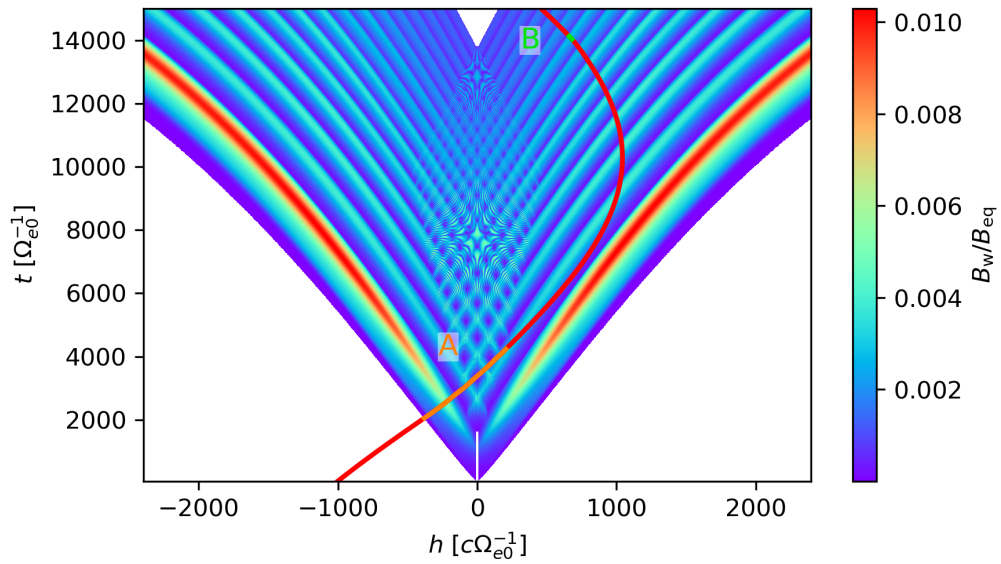

Figure 5.7: Time-space trajectory (world line) of an electron experiencing multiple nonlinear resonant interactions, with wave amplitude of the chorus model in the background. The orange line segment *A* shows where the electron was trapped and experienced an increase in pitch angle, shifting the mirroring point closer to the equator. The short, green line segment B locates the resonant scattering event. The amplitude pattern in regions with overlapping chorus elements results from the perfect symmetry of the wave phase and is not important for the wave-particle interactions. Reprinted from Hanzelka et al. (2021).

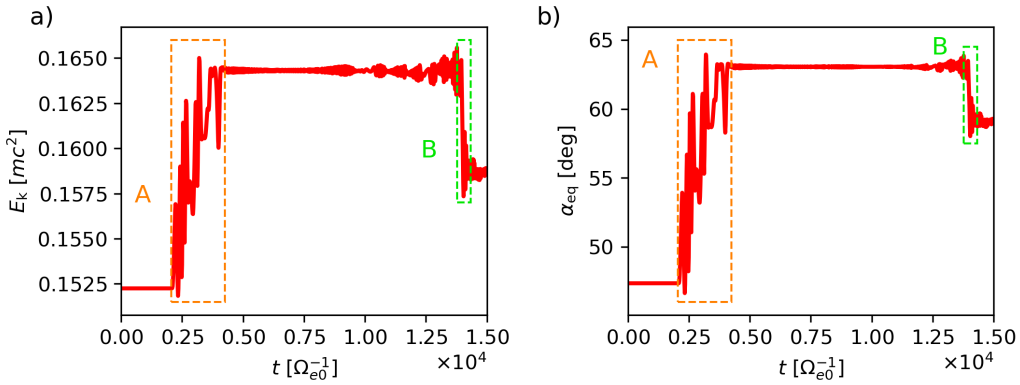

Figure 5.8: a) Evolution of the kinetic energy along the electron trajectory from Figure 5.7. The orange and green rectangles highlight the trapping and scattering events, respectively. b) Evolution of the equatorial pitch angle, same format as the previous panel. Reprinted from Hanzelka et al. (2021).

tor about 60 ms after the end of the last subpacket. In a model with an asymmetric growth rate, one of the elements could be triggered later, increasing the occurrence of such trajectories.

Changes in kinetic energy and equatorial pitch angle along the particle trajectory from Figure 5.7 are plotted in 5.8. As already inferred from the study of electron holes in the previous section, successive trapping happens over larger regions of space and time and must be treated as nonlocal, while the scattering of untrapped particles happens on time scales shorter than subpacket duration and can be thus viewed as local. We also further confirm that successive trapping causes larger changes in pitch angle than the local scattering.

Between times $0.75 \cdot 10^4\,\Omega_{e0}^{-1}$ and $1.35 \cdot 10^4\,\Omega_{e0}^{-1}$, we may notice oscillations in kinetic energy caused by the chorus element propagating in the direction of $\boldsymbol{B}_0$. This effect, the so-called nonresonant scattering, is experienced by particles whose trajectories are significantly modified by the presence of the resonance island without passing through the first-order cyclotron resonance ($\mathrm{d}\zeta/\mathrm{d}t$ does not change sign). It is best described as a stochastic process, leading to random jumps in energy and pitch angle between subpackets. However, unlike the (E_k, α)-diffusion in quasilinear theory, the nonresonant scattering depends on the gradient of the amplitude envelope of the whistler wave packet. The theory of electron interaction with EMIC waves as presented by Chen et al. (2016) can be applied here, with suitable modifications required by the whistler wave mode. These stochastic effects are small compared to the nonlinear resonant interaction and will be ignored in further discussion.

5.5 Measurability analysis of perturbations to electron distribution

Simulation results presented above reveal that the response of a hot electron population to rising-tone chorus elements with subpacket structure is associated with the emergence of a unique perturbation structure in the $f(v_\parallel, v_\perp)$ distribution. And although these perturbations appear to be very distinct, they have never been observed by spacecraft instruments, chiefly due to their short duration.

We assume the number N of particles measured in each velocity space bin to be Poisson distributed with a relative standard deviation $1/\sqrt{N}$. A one-sigma level of significance thus requires

$$N_\mathrm{req} = \left(\frac{\max(F, F_0)}{F - F_0}\right)^2 = \left(\frac{\max(f, f_0)}{f - f_0}\right)^2 \tag{5.20}$$

particles per bin, where $F = f(\boldsymbol{v})v^4$ is the particle flux and the subscript 0 represents the initial state (for a more accurate treatment of the confidence intervals at low values of N, see Section 2.3 in Hanzelka et al. (2021)). Therefore, we must now focus on relative PSD or fluxes, instead of the absolute values. The number of detected particles per bin per time T is

$$\frac{N}{T} = FG(v) \tag{5.21}$$

with $G(v)$ standing for the geometric factor of the detector. The quantity F/N_req can be used as a replacement for the N/N_req ratio until we specify the parameters of the instrument.

The relative change in electron PSD after interaction with the first subpacket is plotted in Figure 5.9a, showing that the perturbation gets more prominent towards larger perpendicular velocities. It remains significant up to pitch angles close to 90° where the character of the perturbation changes due to relativistic turning acceleration (not shown). Particle fluxes are strongest at high pitch angles in the perpendicular velocity range from $0.4c$ to $0.7c$ (Figure 5.9b), but the relative perturbations weaken towards higher wave frequencies due to detrapping. As a result, the highest F/N_req ratios can be found near resonance velocity curves corresponding to the centre of the element. Figures 5.9c and 5.9d show plots of these ratios for Packet 1 and Packet 5. As stated earlier, the combination of test-particle simulations with a plane wave model does not properly capture the evolution of the stripe structure after the nonlinear interaction, so we must limit our analysis to the active region (the most recently formed PSD depletion). Therefore, we should look into the approximate energy range from 70 keV

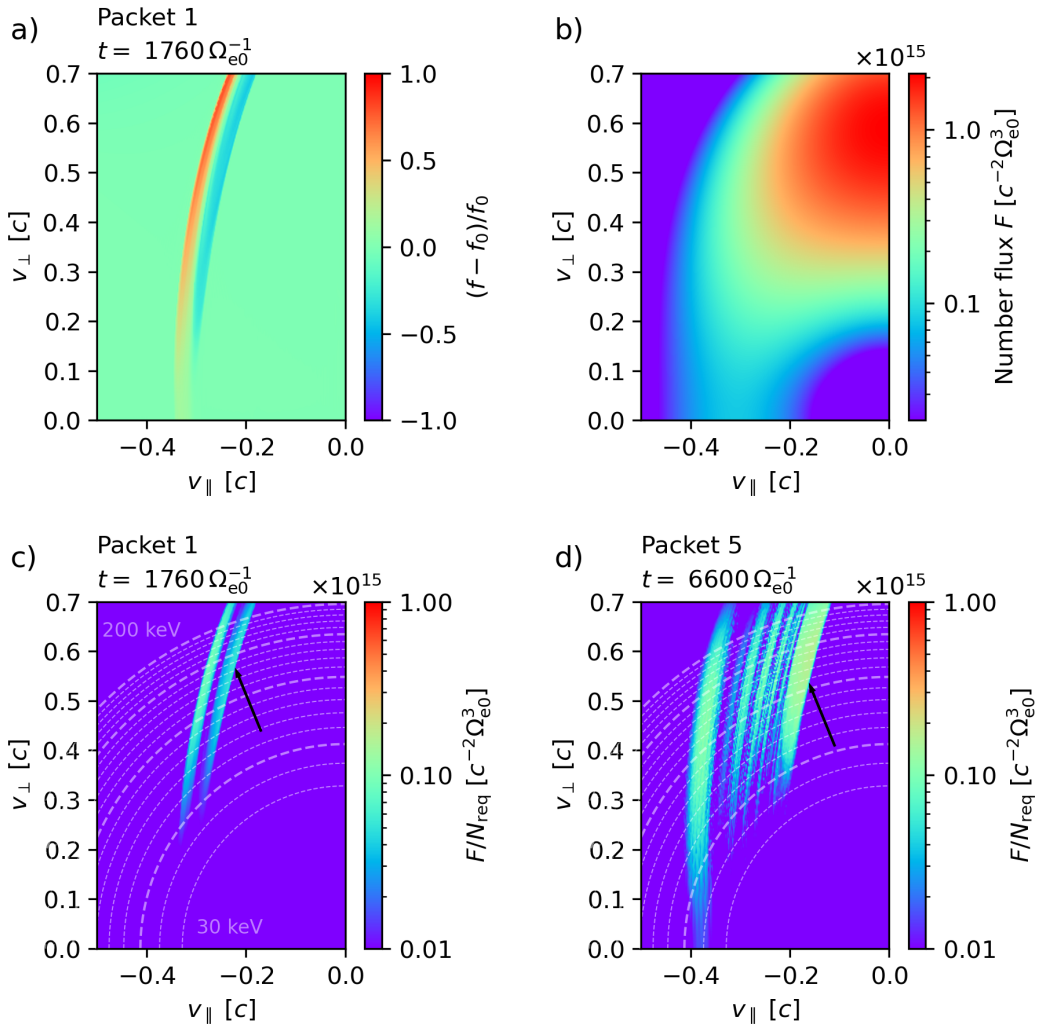

Figure 5.9: a) Relative change in equatorial phase space density after the interaction with the first subpacket of the model chorus element. b) Equatorial Number flux of electrons at $t = 0$. c) F/N_{req} ratio for the single-packet pertrubation. Energy contours increase by 10 keV per step, with thick lines denoting multiples of 50 keV. d) F/N_{req} ratio after the fifth subpacket. The black arrow points at the PSD depletion associated with the electromagnetic electron hole. Reprinted from Hanzelka et al. (2021).

to 200 keV and sample it with a pitch-angle binning that can resolve the width of the perturbation stripe.

In Hanzelka et al. (2021) we reviewed four electrostatic particle detectors from instrument suites of currently or recently active spacecraft and assessed their ability to detect the signs of nonlinear wave-particle interaction in the hot electron distribution. These four were: FPI (MMS, Pollock et al. (2016)), HOPE (Van Allen Probes, Funsten et al. (2013)), PEACE (Cluster, Johnstone et al. (1997)), and MEP-e (Arase, Kasahara et al. (2018)). It was found that MEP-e offers data from energy levels that overlap with the required energy range, but its angular resolution and geometric factor are too low to resolve the PSD depletion and to show that the perturbation is significant. PEACE can achieve a high angular resolution of 3.75° in a special single-anode mode and has the highest geometric factor, but was not designed for measurements of energies above 30 keV and thus cannot detect electrons coming from the high-flux regions. In general, the size of energy bins and the accumulation time per energy level are sufficient across all available instruments, and the deficiencies come from pitch-angle resolution.

To reproduce the data type provided by a particle detector, we ran our simulation from 16 evenly spaced time points, covering a 15.6 ms time interval from the beginning to the end of the fifth subpacket, measured at $h = 0$. The duration of the packet happens to closely match the accumulation time of MEP-e. The logarithmic energy levels were also based on MEP-e, and each level was further divided into 16 logarithmic cells. The pitch angles were sampled uniformly by 256 points from 180° to 90°. After averaging over time and individual energy levels, we tried grouping the pitch angles into bins from 3° to 12° to see which provides the most significant results. In the highest energy bin, $E_\mathrm{k} \in (73.1, 87.5)\,\mathrm{keV}$, the lowest value of the $N_\mathrm{req}/N_\mathrm{exp}$ ratio fluctuated between 1 and 2 for angular bins ranging from 3° to 6°, and was higher than 2 otherwise. The number of expected particles in the PSD depletion was less than 5 for the MEP-e geometric factor $G(E_\mathrm{k}) = 0.7 \cdot 10^{-8}\,\mathrm{m^2\,sr}$ per $\Delta\alpha = 22.5°$, confirming that the detector could not accumulate enough particles at increased pitch angle resolutions.

In further investigation, we assumed a hypothetical instrument with an angular bin size of 4.5°, and also increased the geometric factor to $G(E_\mathrm{k}) = 1.4 \cdot 10^{-8}\,\mathrm{m^2\,sr}$, which is comparable to the PEACE instrument with $G(E_\mathrm{k}) = 6.0 \cdot 10^{-8}\,\mathrm{m^2\,sr}$ per $\Delta\alpha = 15°$. Figures 5.10a-c summarize our results by showing the PSD difference $f - f_0$, the expected particle count N_exp, the required particle count N_req, and the ratio $N_\mathrm{req}/N_\mathrm{exp}$. We can expect to capture about 50 particles per bin in the depletion region, which is more than we need to achieve a one-sigma significant measurement. Since $N_\mathrm{req}/N_\mathrm{exp}$ is smaller than 1/4 at the deepest point of the perturbation, we can even reach the two-sigma level. It should be noted that the significance is based on comparison with an ideal unperturbed state, but we can always estimate this state by extrapolation from the neighbouring pitch angle bins where the nonlinear interaction has not yet taken place.

In Figures 5.10d-f, we show simultaneous measurements at four different energy levels with a hypothetical extension up to 125 keV. The stripe of decreased PSD is well resolved, and the particle counts reach values from 50 to 100 across all pitch-angle–energy bins where the depletion was detected. $N_\mathrm{req}/N_\mathrm{exp}$ drops down below 0.1 at the highest energy level, confirming that the traces of nonlinear interaction could be detected by a dedicated instrument with a high angular resolution.

5.6 Scattering into loss cone and atmospheric precipitation

5.6.1 Introduction and simulation setup

Whistler mode waves are known to contribute to acceleration and precipitation of radiation belt electrons in a wide range of energies, starting at around 10 keV and going up to units of MeV. The theory of cyclotron interaction and the simulation results in Section 5.4 dictate that acceleration of relativistic electrons can happen only at large pitch angles. However, particles with high values of the equatorial pitch angle are trapped in the dipole magnetic field and need to be strongly scattered to reach the bounce loss cone defined by pitch angle (Porazik et al., 2014)

$$\alpha_\mathrm{loss} = \frac{\pi}{2} \pm \left(\frac{\pi}{2} - \arcsin\left(\frac{B_\mathrm{eq}}{B_\mathrm{m}}\right)\right) \tag{5.22}$$

(neglecting higher-order corrections to the magnetic moment, radial diffusion, and azimuthal drift), where B_m is the magnetic field strength at the point where electrons stop being able to mirror because of collisions with dense atmospheric layers. As demonstrated by Kubota and Omura (2018), the energetic electron population must interact

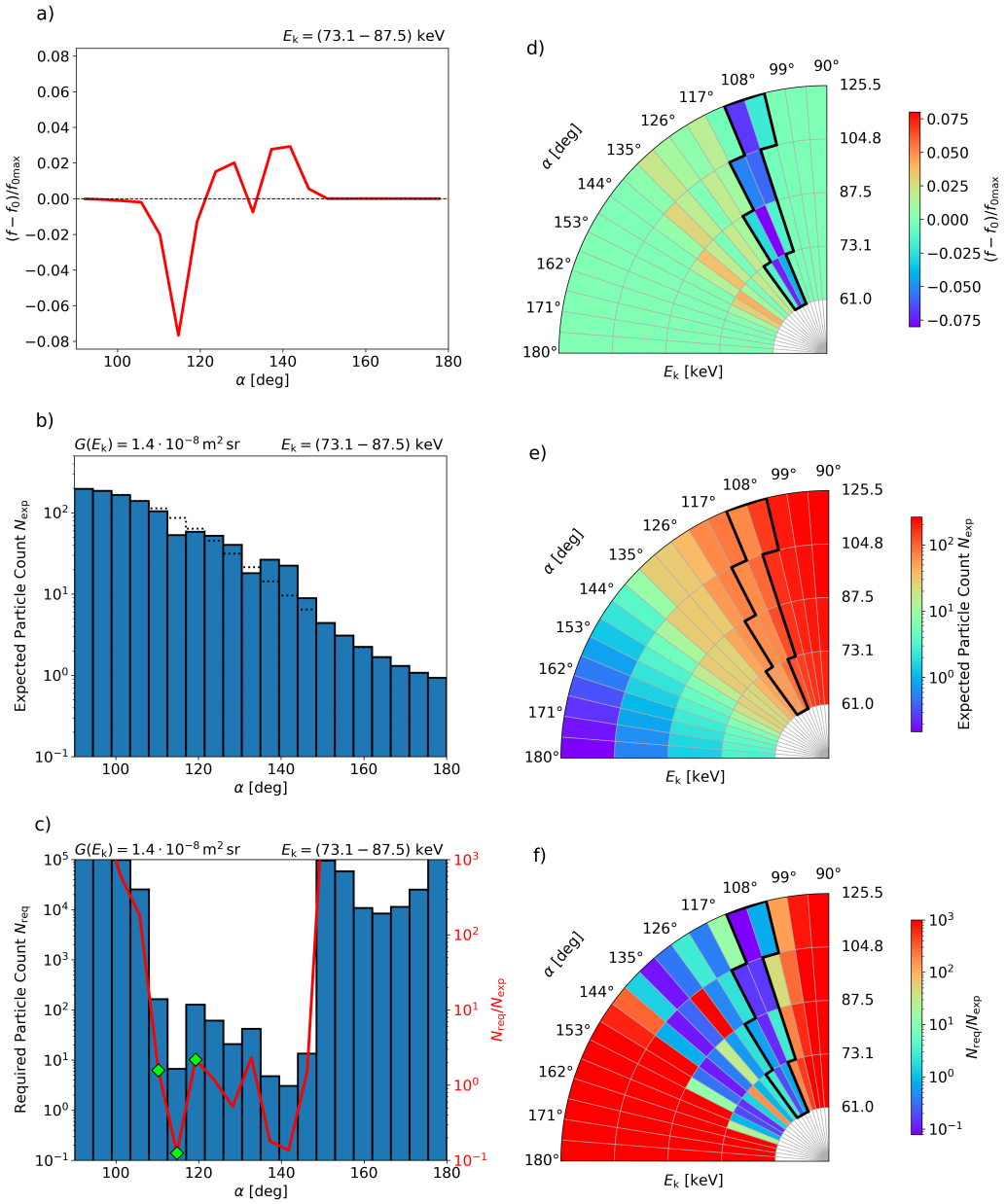

Figure 5.10: a) A normalized difference of the initial and perturbed pitch-angle distribution at a single energy level corresponding to the upper limit of the MEP-e energy range. b) Expected particle count based on the enhanced geometric factor $G(E_k) = 1.4 \cdot 10^{-8}\,\mathrm{m}^2\,\mathrm{sr}$. Blue bars represent the perturbed distribution, and the dotted outlines stand for the initial distribution. c) The required particle count plotted with blue bars, with a red line overlay representing the N_{req}/N_{exp} ratio. The green diamonds highlight the pitch angle bins that cover the density depletion. d-f) Similar to a-c, but for four different energy levels. Note that each level is assumed to be sampled at the same time, and the polar plots thus do not represent a detector sweeping over multiple energy levels. The black outline helps visually identify the PSD depletion associated with an electromagnetic electron hole. Adapted from Hanzelka et al. (2021).

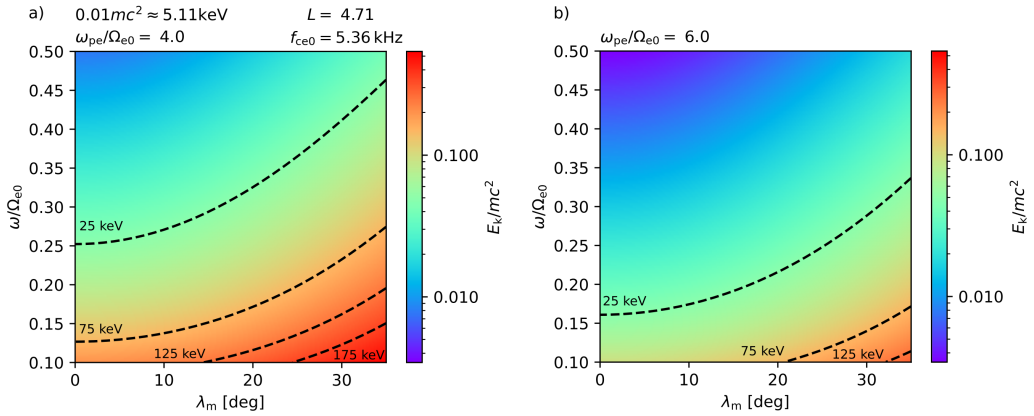

Figure 5.11: Minimum resonant energy for cyclotron interaction over a range of frequencies and latitudes along magnetic field line $L = 4.71$. Panel a) represents a low density environment with $\omega_{pe}/\Omega_{e0} = 4.0$, b) shows a higher density case with $\omega_{pe}/\Omega_{e0} = 6.0$.

with 10^2 to 10^3 chorus elements to cause significant precipitating fluxes at energies $E_k > 1\,\mathrm{MeV}$, which amounts to time periods in the order of 10^2 to 10^3 seconds. On the other hand, relativistic electron bursts (duration $t < 1\,\mathrm{s}$) have been observed in association with chorus wave activity (Breneman et al., 2017), but it is unclear how would the $n = -1$ cyclotron resonance quickly accelerate and subsequently scatter the electrons on such a short time scale.

The test particle method used in this chapter allows for detailed studies of precipitating fluxes caused by a single parallel-propagating element and can thus predict only subrelativistic ultra-fast precipitation events where the scattered electrons were already near the loss cone. This restriction imposes an upper energy limit given by the first order cyclotron resonance condition at $\alpha \approx 0°$. In Figure 5.11, we plot the minimum resonant energies against wave frequency and magnetic latitude for two values of ω_{pe}. Because the occurrence of parallel chorus emissions quickly drops above approximately 35° of latitude (Santolík et al., 2014b), and the wave frequency rarely ventures below $0.15\Omega_{e0}$ (Teng et al., 2017), we can estimate that the maximum energy of electrons scattered to the loss cone directly by the nonlinear resonance to be about 200 keV. The precise value depends on the width of the resonance region and the definition of the boundary between resonant and nonresonant interaction. For comparison, the IDP particle detector onboard the low-orbit DEMETER spacecraft measured electrons with energies 70 keV and higher (Sauvaud et al., 2006). The ELFIN CubeSat mission provides electron fluxes of precipitating electrons with energies starting at 50 keV (Angelopoulos et al., 2020). Estimates from Figure 5.11 suggest that if we want to observe the bursts of precipitating electrons with detectors available on recent spacecraft missions, we should focus on cases where the chorus elements start at very low frequencies and where the cold plasma density is low.

Considering the energy range constraints, we decided to model the chorus wavefield after an element observed by the Van Allen Probe A spacecraft on 01 March 2013 from 14:52:08.45 to 14:52:08.61. This element starts at $\omega = 0.17\Omega_{e0}$, and its observation correlates with the spacecraft's passage through a low-density region with $\omega_{pe} = 4.1\Omega_{e0}$. Using the observed amplitudes and frequencies as presented in Figures 5.12a-c, we constructed a model of B_w and ω shown in Figures 5.12d-e. The input parameters for the model were the following: $\omega_0 = 0.17\,\Omega_{e0}$, $\omega_f = 0.44\,\Omega_{e0}$, $B_{surf} = 2.0 \cdot 10^{-5}\,\mathrm{T}$, $Q = 0.75$, $\tau = 0.5$, $\omega_{pe} = 4.1\,\Omega_{e0}$, $\omega_{phe} = 0.375\,\Omega_{e0}$, $V_{\perp 0} = 0.45\,c$, $U_{t,\parallel 0} = 0.20\,c$, $L = 4.71$. The advection equations are solved up to $h = 2200\,c\Omega_{e0}^{-1}$, which translates to $\lambda_m \approx 37°$.

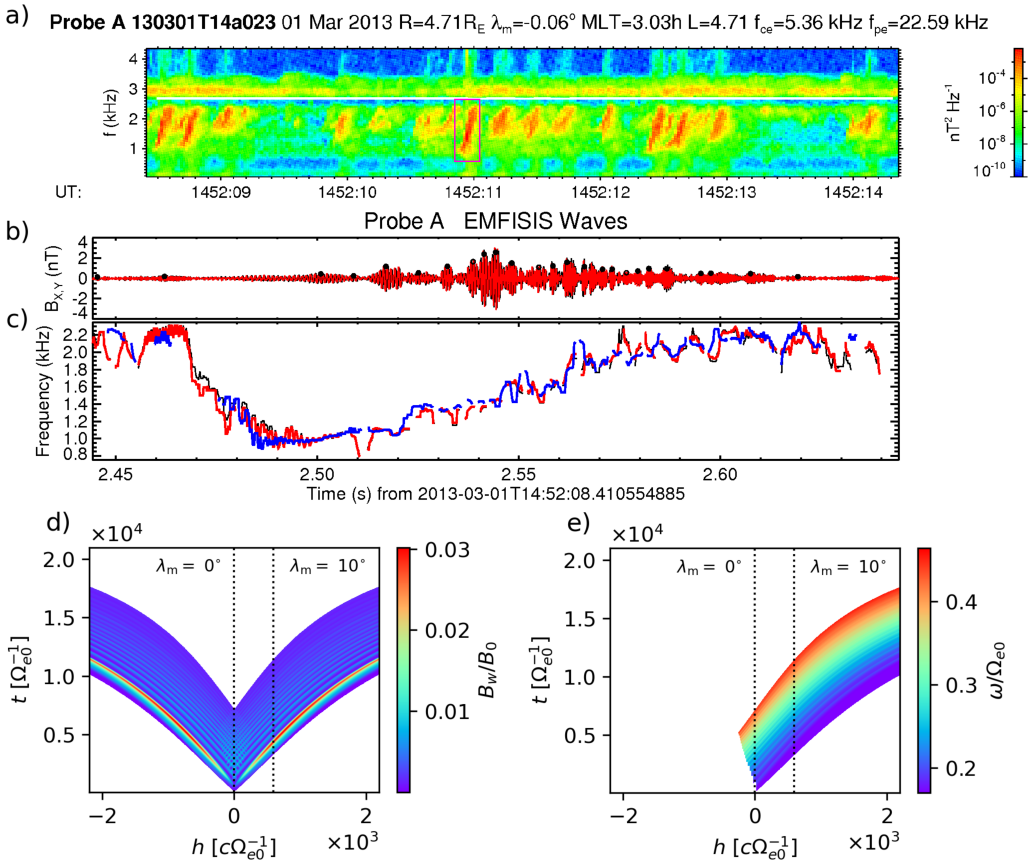

Figure 5.12: Van Allen Probe measurements (a-c) used as a reference for an NGTO-based chorus wave model (d-e). Formatting is similar to Figures 4.6 and 4.8.

In order to capture the full extent of the precipitating fluxes, the backwards-in-time test-particle simulation must be started at h left of the source of the last subpacket. We set $h_\mathrm{f} = -268\,c\Omega_{\mathrm{e}0}^{-1}$ and shift the starting point in time from $t_\mathrm{f} = 500\Omega_{\mathrm{e}0}^{-1}$ to $t_\mathrm{f} = 21000\Omega_{\mathrm{e}0}^{-1}$ with steps of $500\Omega_{\mathrm{e}0}^{-1}$. Due to this large number of different starting points, we reduce the sampling of the $(v_\parallel, v_\perp, \varphi)$ space to a $128 \times 128 \times 64$ grid, with the range of $v_\parallel$ extending from $0.0c$ up to $-0.6c$ and φ covering the full angle. The perpendicular velocity range is limited to $v_\perp < 0.06$, which is sufficient to cover the loss cone at h_f. The initial bi-Maxwellian distribution from Equation 3.11 is modified by setting

$$f(u_\parallel, u_\perp, h) = 0 \quad \text{for} \quad \alpha < \alpha_\mathrm{loss}\,, \tag{5.23}$$

i.e., the loss cone is assumed to be empty, corresponding to a state without any wave activity. The time step was decreased to $0.02\Omega_{\mathrm{e}0}^{-1}$ to ensure tolerable errors in the Boris algorithm over the whole range of latitudes.

5.6.2 Phase space density perturbations at low pitch angles

We start our investigation by looking at snapshots from the evolution of the phase space density distribution in the $(v_\parallel, v_\perp)$ space, presented in Figure 5.13. We notice that the loss cone region near the resonance velocity is immediately filled, nearly homogeneously across $v_\perp$. This behaviour can be explained by the wide range of electron perpendicular velocity oscillations plotted in green in Figure 2.6a. Significant perturbations of PSD along α_loss are also detected at parallel velocities up to $-0.15\,c$, much smaller than $V_\mathrm{R}/c \approx -0.35$. This effect comes from the ζ-dependence of resonance velocity at

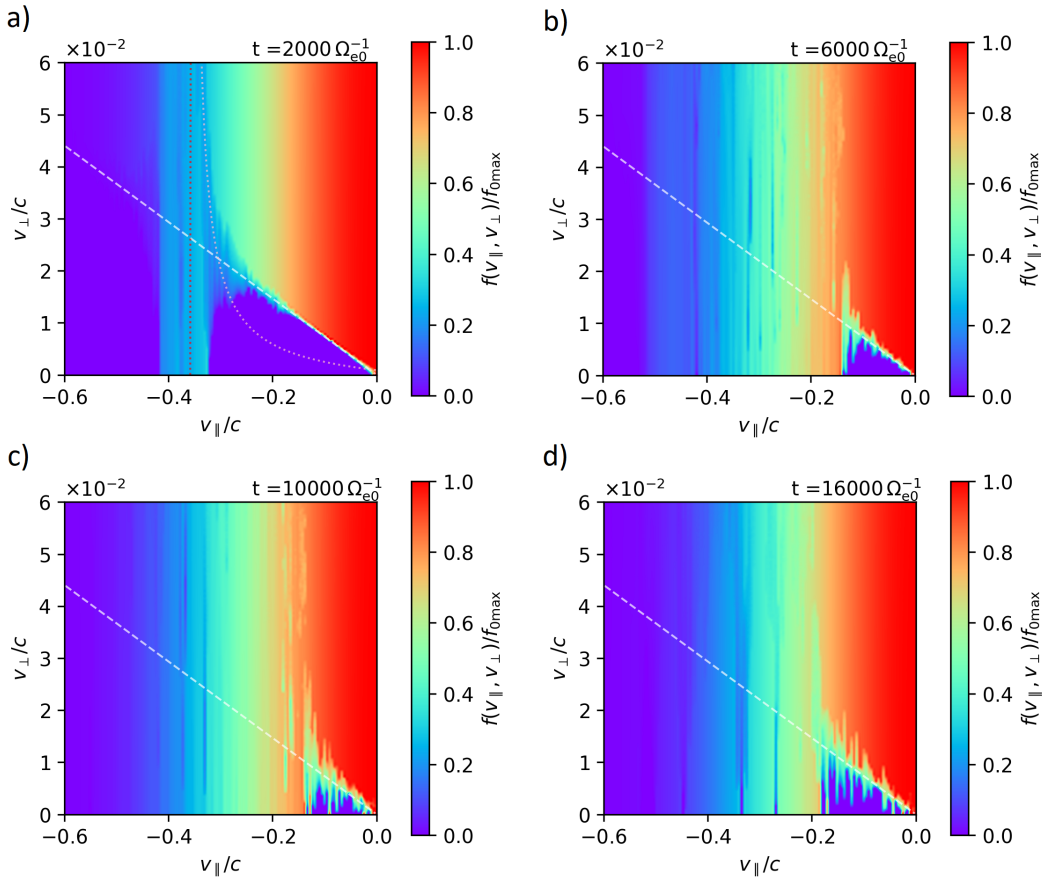

Figure 5.13: Evolution of the hot electron distribution $f(v_\parallel, v_\perp, h = -268\, c\Omega_{e0}^{-1})$ at low perpendicular velocities due to interaction with the chorus element from Figure 5.12. The dashed white line determines the boundary of the local loss cone. The dark red dotted curve in panel a) represents the resonance velocity for $\omega/\Omega_{e0} = 0.2$ (mean frequency of the second subpacket), and the pink dotted curve stands for a ζ-dependent resonance velocity $V_R^{\zeta=\pi}$.

low $v_\perp$. In Figure 5.13a, resonance velocity curves $V_R^{\pi/2}$ and V_R^{π} (analogous to resonance momentum curves from Equation 2.33) are plotted for $\omega/\Omega_{e0} = 0.2$, $\Omega_w/\Omega_{e0} = 7.5 \cdot 10^{-3}$. As we move forward in time, we start seeing particles that have interacted with the high-frequency end of the chorus element, causing scattering at low energies (Fig. 5.13b,c). Towards the end of the simulation (Fig. 5.13d), resonant particles arrive from higher latitudes where the relative frequencies and amplitudes of the subpackets become small, resulting in weaker scattering at higher energies. There are no significant PSD decreases outside the loss cone; as expected from the results presented in Figure 5.3b, the depletion stripe disappears below $v_\perp/c = 0.1$. The full time evolution is available as an animation in the digital attachment Vid5.

To quantify the filling of the loss cone, we first carry out the coordinate transform $(v_\parallel, v_\perp) \to (E_k, \alpha)$, yielding (with $m_e = 1$, $c = 1$)

$$f(v_\parallel, v_\perp) v_\perp \mathrm{d}v_\parallel \mathrm{d}v_\perp = f(E_k, \alpha) \left(1 - \frac{1}{(1+E_k)^2}\right) \frac{1}{\sqrt{(1+E_k)^6 - (1+E_k)^4}} \mathrm{d}E_k \sin\alpha \,\mathrm{d}\alpha$$
$$\overset{E_k \ll 1}{\approx} f(E_k, \alpha) \sqrt{2E_k} \mathrm{d}E_k \sin\alpha \,\mathrm{d}\alpha\,. \tag{5.24}$$

As a second step, we integrate over pitch angles from α_{loss} to π to obtain the distribution of loss-cone electrons over energies. Figure 5.14 compares these energy distributions

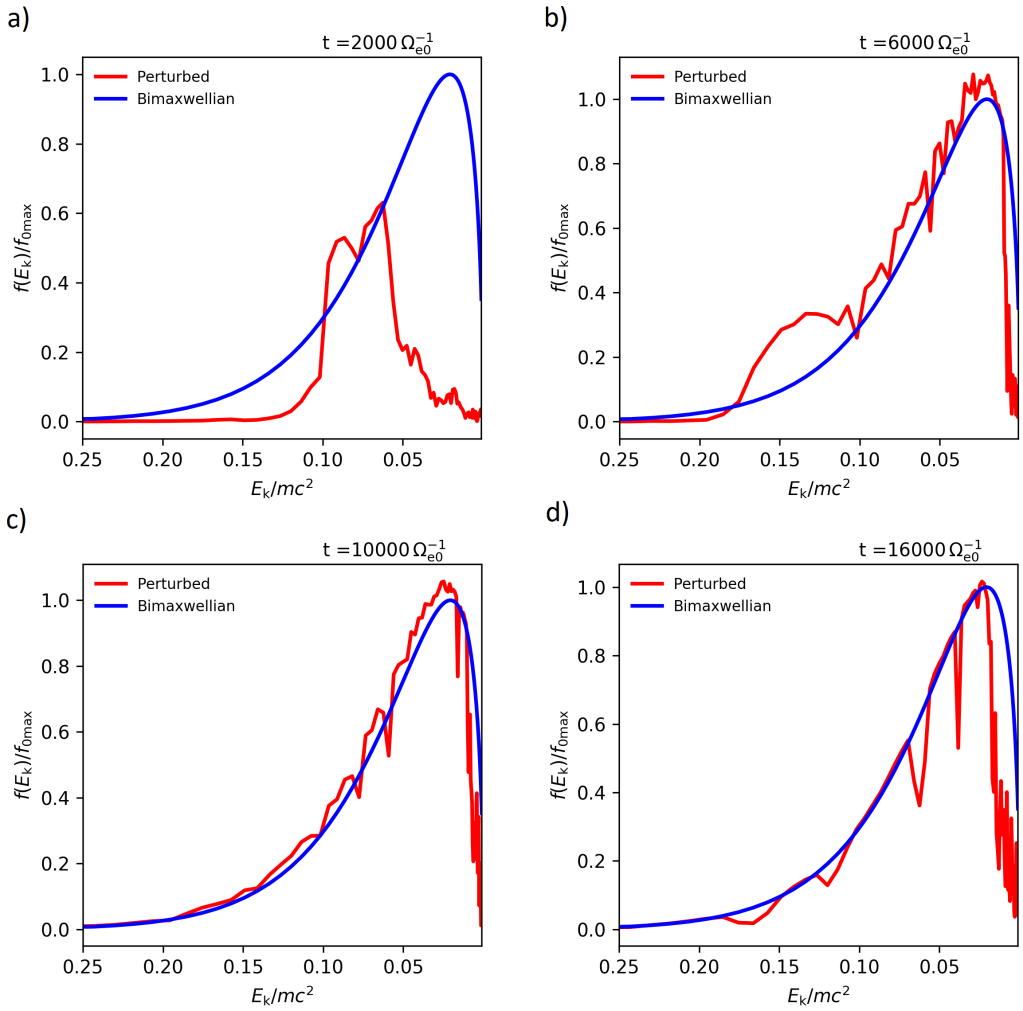

Figure 5.14: Evolution of the energy distribution of loss-cone electrons, plotted at the same time points as the velocity distributions in Figure 5.13. Red lines represent the loss cone content obtained from simulation; the blue line shows a bi-Maxwellian distribution with a full loss cone. At energies below $0.01mc^2 \approx 5\,\mathrm{keV}$, the noise in the perturbed distribution is a low grid resolution effect, further amplified by the $(v_\parallel, v_\perp) \rightarrow (E_\mathrm{k}, \alpha)$ rebinning. Animated evolution of the 1D distribution is available in the digital attachment Vid6.

to bi-Maxwellian distributions with a full loss cone. Scattering induced by the first subpacket causes a major overfilling at resonant energies, reaching more than a double of the bi-Maxwellian PSD. This could be seen as a side effect of the overestimation of B_w in the first subpacket. However, perturbations plotted in Figures 5.14b-c show that the lower amplitude, higher frequency portion of the chorus element also causes overfilling, although only fractional. At the late stage of the evolution, where the relative amplitude of subpackets falls below $10^{-3}B_0$, the PSD in loss-cone matches the bi-Maxwellian. This corresponds to the strong diffusion limit from the quasilinear theory (Kennel and Petschek, 1966). The test particle simulation thus suggests that nonlinear scattering of electrons due to cyclotron resonance with parallel-propagating chorus waves can break the strong diffusion limit when the wave amplitudes are $> 10^{-3}B_0$.

5.6.3 Precipitating fluxes

Resonant electrons which have fallen into the loss cone due to nonlinear scattering can be assumed to propagate down to atmospheric altitudes as prescribed by the adiabatic

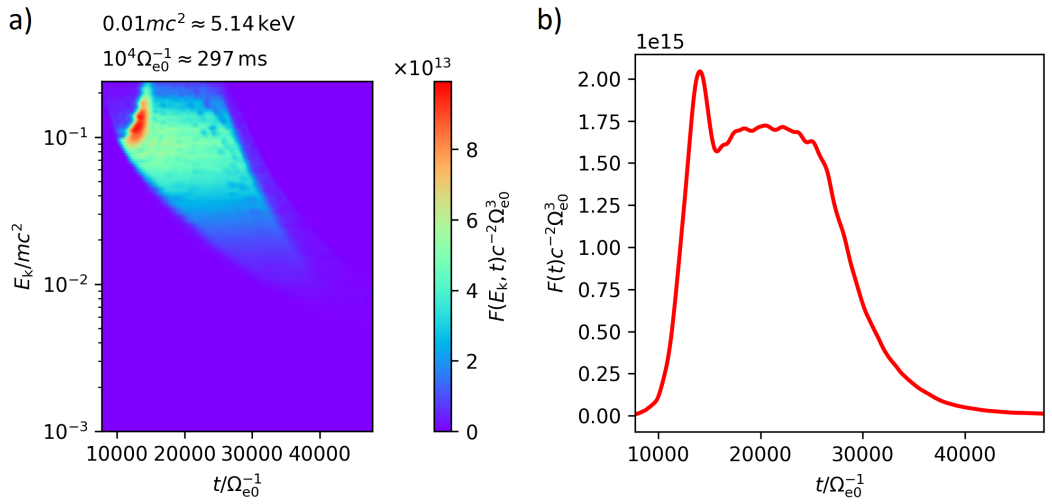

Figure 5.15: a) Number flux across energies as observed at the footprint of field line $L = 4.71$ along which the chorus element propagates. $t = 0$ corresponds to the start of the chorus element. b) Integrated number flux from the first panel.

motion in a magnetic dipole field. For simplicity, we track the particles (representative of each velocity bin) exactly to the surface of the Earth, although the path of precipitating electrons typically ends in the lower ionospheric layers (60 km to 150 km) due to electron-ion recombination (Hargreaves, 1992). We define the omnidirectional flux differential as

$$\mathrm{d}F(E_\mathrm{k}, \alpha, t) \overset{E_\mathrm{k} \ll 1}{\approx} 2f(E_\mathrm{k}, \alpha, t) E_\mathrm{k} \sin\alpha \,\mathrm{d}\alpha \,\mathrm{d}E_\mathrm{k} \,. \tag{5.25}$$

Our goal is to compute the evolution of number flux throughout the precipitation event. This is done in three steps:

1. $f(v_\parallel, v_\perp, t_\mathrm{f})$ obtained across the 42 time points are interpolated on a finer temporal grid with 1000 points and then transformed/rebinned to $f(E_\mathrm{k}, \alpha, t_\mathrm{f})$. The energy grid has 128 logarithmically spaced points from $10^{-3} m_\mathrm{e}c^2$ to $10^0 m_\mathrm{e}c^2$, and the pitch angle grid has 128 linearly spaced points within the loss cone.

2. (E_k, α) bins and the associated PSD are mapped to the ground, and the time of flight of individual particles representing each bin is numerically integrated. PSD values are interpolated to the energy-angle grid from the previous point and then interpolated to a new 1000-point time grid ranging from $8 \cdot 10^3 \Omega_{e0}^{-1}$ to $4 \cdot 10^4 \Omega_{e0}^{-1}$ (approximate interval between the arrival of the first and the last precipitating electron). $f(E_\mathrm{k}, \alpha, t)$ is thus obtained.

3. Equation 5.25 is integrated over pitch angles to get the evolution of the energy flux differential over time and then integrated over energies to get the number flux $F(t)$.

Figure 5.15a shows that strong flux first appears near the energy level of 50 keV, corresponding to the resonance velocity of the first subpacket. The energy range then widens, reaching up to about 150 keV and extending down below 10 keV. The low energy precipitating electrons have small parallel velocities and arrive up to one second after the initiation of the chorus element. In Figure 5.15b, we present the integrated number flux, which confirms the effects of the very strong first subpacket, while the remaining fine structure of chorus does not translate to any clear structure in the precipitating flux.

5.7 Discussion and conclusion

In summary, our research presented in Hanzelka et al. (2021) has shown that nonlinear interaction of rising-tone chorus elements with electrons results in the formation of a characteristic stripe structure in the velocity distribution, and this structure could be detected with an electrostatic particle detector with an angular resolution of about 6° or better, which is currently not available in spacecraft instrument suites. A conclusive measurement of a phase space density depletion along resonance velocity curves could be considered as a direct confirmation of the electromagnetic electron hole on a subpacket timescale. We must add that Mozer et al. (2018) have used particle data from the Magnetospheric Multiscale mission to create a superposition of velocity distributions with appropriate resonance velocity shifts, achieving a statistically significant measurement of an electron hole structure associated with bipolar pulses. This statistical method is unfortunately not so useful in chorus studies due to the variations of perturbation stripes across the phase space.

The need for high angular resolution is rather unique since most experiments are concerned with the overall shape of the $f(v_\parallel, v_\perp)$ distribution or the $f(E_\mathrm{k}, \alpha)$ distribution and do not specifically focus on the resonance region. The cyclotron resonant electrons are expected to have the highest fluxes at pitch angles between approximately 60° and 120°, with energies going above approximately 100 keV. It would be possible to shift the simulated fluxes to lower energies by using a different initial velocity distribution, but as we discussed in Chapter 4, the range of $U_{\mathrm{t}\perp}$ that can lead to strong nonlinear wave growth is limited. Given the energy range and benevolent requirements on energy bin size, semiconductor detectors might be more suitable for the task, taking MagEIS from the Van Allen Probes as an example (Blake et al., 2013). Unfortunately, we are not aware of a semiconductor electron detector programmed to store data in sufficiently small time steps, and the design issues with the angular resolution are ubiquitous. We conclude that the investigation of nonlinear cyclotron interaction on subpacket timescale requires a dedicated spacecraft mission with a detector design based on the results from Section 5.5, accompanied by a search coil for measurements of magnetic field fluctuations induced by chorus.

The numerical study of electron precipitation is in qualitative agreement with the self-consistent PIC simulations of Hikishima et al. (2010), who observed similar bursts of energetic electrons in association with intense parallel-propagating chorus elements. However, in their simulation, the energies of precipitating fluxes were mostly below 50 keV due to a higher initial frequency of chorus, and partially also because of the limited latitudinal range of the simulation box. In the recent test-particle simulations of Chen et al. (2021), a simplified model of ducted and unducted chorus emissions was developed based on wave advection equations (ducted) and ray approximation (unducted), and the microburst precipitation was found to reach energies around 300 keV. Nevertheless, spacecraft observations reported by Breneman et al. (2017) show relativistic microbursts associated with chorus extending to energies near 1 MeV. According to simulations and theory presented in this thesis, such high energies can be achieved only by scattering electrons with very high initial equatorial pitch angles that have been previously accelerated, possibly by some other mechanism, e.g., the relativistic turning acceleration (Omura et al., 2007).

Another interesting result of the electron loss study is the overfilling of the loss cone due to cyclotron resonance. Zhang et al. (2022) observed loss cone overfilling (breaking of the strong diffusion limit) on the low-orbit ELFIN spacecraft and explained it by nonlinear Landau resonance with oblique chorus waves. Because Landau-resonant electrons oscillate in $v_\parallel$ but not in $v_\perp$ (at least in the nonrelativistic limit, cf. Section 2.1), the transport happens nearly perpendicular to PSD contours at low pitch

angles, enabling the exchange of a phase space volume from the nearly empty loss cone with a highly populated volume just above the loss cone boundary. On the other hand, cyclotron-resonant electrons at low pitch angles oscillate mainly in $v_\perp$ and are thus unlikely to cause overfilling. We ascribe our observations partly to the very high model chorus amplitudes that extend the range of oscillations and cause non-negligible changes in parallel electron velocity and partly to the high temperature anisotropy of the initial hot electron distribution. Loss cone overfilling due to nonlinear cyclotron resonance is thus expected to be a very rare event in the outer radiation belt.

Another application of the simulated number fluxes can be found in the research of pulsating auroras. These types of auroras are associated with electron precipitation by discrete chorus elements (Miyoshi et al., 2020), and polar station measurements of auroral intensity have revealed peaks correlated with strong, well-defined subpackets (Ozaki et al., 2018). These observations fully agree with the number flux profile in Figure 5.15, which starts with a prominent peak corresponding with the first, strong subpacket, and then transitions to minor, hardly discernible modulations associated with the weaker packets.

The backtracing test-particle method is very efficient for studying PSD perturbations caused by nonlinear interaction, providing high-resolution snapshots from the evolution of the hot electron distribution. However, taking a longer sequence of snapshots proves very costly because the simulation needs to be repeated for each point. An analogous issue would appear if we tried to study the changes in the distribution along h. The advantage of being able to resolve fine structures is mitigated by the unknown fluctuations, which should be added to the initial smooth distribution to achieve more realistic results. The *a posteriori* choice of initial distribution can save a lot of processing time, yet it cannot be applied when the wave model already prescribes a distribution. For future research, we suggest either using multipoint spacecraft measurements and simulating the interaction in a region limited by the data or running a test-particle simulation through wavefield obtained from self-consistent simulations. Such numerical experiments would be useful to obtain reliable reference values for the design of particle detectors on future radiation belt missions.

Conclusion and future outlook

Nonlinearities in magnetospheric wave-particle interactions are a fascinating topic with a rich history of experimental and theoretical studies. Our contribution to the subject focused on modelling of chorus elements and numerical investigation of electron scattering and precipitation. Despite the obvious inclination towards fundamental theory and simulations, all the presented work was done with spacecraft observations in mind, discussing also the design of future experiments.

We used the nonlinear growth theory of Omura et al. to construct a semi-empirical model of parallel-propagating, rising-tone chorus element in the lower frequency band. Inspired by high-resolution observations from Van Allen Probes, we introduced a triggering scheme with a moving source that produces elements with a fine subpacket structure and irregular growth in frequency. The complicated relations between output and input parameters were analyzed visually by marginal correlation plots. The amplitudes and the chirp rates were in a good agreement with experimental case studies. We also discussed the interpretation of subpackets as a superposition of multiple plane waves, showing possibilities for further research on this topic.

The one-dimensional wavefield model was used to investigate perturbation to hot electron distribution through test particle methods. Reconstructions of phase space density from back-traced energetic electrons revealed elevation and depression aligned to resonance velocity curves of individual subpackets. Step like features in the reduced distribution confirmed the relation between backward-wave-oscillator theory and the nonlinear growth theory. We identified the region of phase space with the most prominent density decrease and compared the change in electron flux to the resolution of various particle analyzers on currently and recently operating spacecraft. We showed that observation of nonlinear PSD perturbations on a millisecond scale should be possible with a dedicated instrument, but an improvement in angular resolution is needed. Such observation would provide direct confirmation of the nonlinear effects of chorus subpackets on energetic electrons.

The same test-particle method and numerical wave model were used to predict the precipitation of energetic electrons due to one-hop interaction with a single chorus element. We demonstrated that significant fluxes appear across energies up to about 150 keV, and prominent subpacket features are still apparent in the integrated flux, which may influence pulsations of aurorae. Moreover, we discovered that loss cone overfilling (breaking of strong diffusion limit by nonlinear interaction) could be caused by cyclotron resonance when the packet amplitude exceeds approximately 1 % of the ambient magnetic field. However, we concluded that cyclotron resonance is much less likely to cause overfilling than Landau resonance.

Despite the simulation efforts presented here and in the large volume of recent literature on chorus, not all features of chorus-electron interaction have been satisfactorily explained. The exact origin of chirp is still debated, and there is currently no efficient way to handle the frequency changes within the hamiltonian formalism. Furthermore, the source of obliquity and the overall significance of parallel field components in the growth mechanism requires further investigation, possibly numerical, as self-consistent 2D simulations are slowly becoming feasible (Ke et al., 2017). Additionally, the non-diffusive aspects of long-term electron interactions with chorus elements have not yet been thoroughly investigated (Allanson et al., 2021), and thus precise models of chorus elements may be needed for simulation of radiation belt dynamics on larger scales.

We believe that the future goal of microscopic chorus growth theories should be to incorporate finite frequency band aspects of the elements, along with the inclusion of

irregularities of the cold plasma background and their effects on amplitude modulations and obliquity. On more macroscopic scales, we should aim to derive effective nonlinear transport coefficients (diffusive and advective), which could be entered on the input of Fokker-Planck simulations. In all these endeavours, observational results must be closely followed and compared to the theory, and conversely, the analytic computations should motivate the design of future wave and particle instruments. On the side of data analysis, neural networks could help build data sets of chorus elements detected from burst mode measurements, following the successful applications on atmospheric tweeks and lightning whistlers (Maslej-Krešňáková et al., 2021; Harid et al., 2021).

All findings and discoveries made in studies of Earth's magnetospheric chorus can be later adapted to the discrete EMIC emissions and to magnetospheres of outer planets, contributing to our continuous efforts towards a better understanding of magnetospheric dynamics.

Bibliography

Agapitov, O. V., Mourenas, D., Artemyev, A. V., Mozer, F. S., et al. Synthetic Empirical Chorus Wave Model From Combined Van Allen Probes and Cluster Statistics. *J. Geophys. Res. Space Physics*, 123(1):297–314, January 2018. doi: 10.1002/2017JA024843.

Albert, J. M., Artemyev, A. V., Li, W., Gan, L., and Ma, Q. Models of Resonant Wave-Particle Interactions. *J. Geophys. Res. Space Physics*, 126(6):e29216, June 2021. doi: 10.1029/2021JA029216.

Albert, J. M. Cyclotron resonance in an inhomogeneous magnetic field. *Phys. Fluids B: Plasma Phys.*, 5(8):2744–2750, August 1993. doi: 10.1063/1.860715.

Albert, J. M., Tao, X., and Bortnik, J. *Aspects of Nonlinear Wave-Particle Interactions*, pages 255–264. American Geophysical Union (AGU), 2012. ISBN 9781118704752. doi: 10.1029/2012GM001324.

Allanson, O., Watt, C. E. J., Allison, H. J., and Ratcliffe, H. Electron Diffusion and Advection During Nonlinear Interactions With Whistler Mode Waves. *J. Geophys. Res. Space Physics*, 126(5):e28793, May 2021. doi: 10.1029/2020JA028793.

Allen, R. C., Zhang, J. C., Kistler, L. M., Spence, H. E., et al. A statistical study of EMIC waves observed by Cluster: 1. Wave properties. *J. Geophys. Res. Space Physics*, 120(7):5574–5592, July 2015. doi: 10.1002/2015JA021333.

Al'tshul', L. M. and Karpman, V. I. Theory of Nonlinear Oscillations in a Collisionless Plasma. *Sov. J. Exp. Theor. Phys.*, 22:361, February 1966.

Angelopoulos, V., Tsai, E., Bingley, L., Shaffer, C., et al. The ELFIN Mission. *Space Sci. Rev.*, 216(5):103, July 2020. doi: 10.1007/s11214-020-00721-7.

Artemyev, A. V., Neishtadt, A. I., Vainchtein, D. L., Vasiliev, A. A., et al. Trapping (capture) into resonance and scattering on resonance: Summary of results for space plasma systems. *Commun. Nonlinear Sci. Numer. Simulat.*, 65:111–160, December 2018. doi: 10.1016/j.cnsns.2018.05.004.

Artemyev, A. V., Neishtadt, A. I., Vasiliev, A. A., Zhang, X.-J., et al. Long-term dynamics driven by resonant wave-particle interactions: from Hamiltonian resonance theory to phase space mapping. *J. Plasma Phys.*, 87(2):835870201, March 2021. doi: 10.1017/S0022377821000246.

Baker, D. N., Erickson, P. J., Fennell, J. F., Foster, J. C., et al. Space Weather Effects in the Earth's Radiation Belts. *Space Sci. Rev.*, 214(1):17, February 2018. doi: 10.1007/s11214-017-0452-7.

Baumjohann, W. and et al. *Basic Space Plasma Physics (Revised Edition)*. Imperial College Press, 2012. doi: 10.1142/9781848168961.

Bell, T. F., Inan, U. S., Haque, N., and Pickett, J. S. Source regions of banded chorus. *Geophys. Res. Lett.*, 36:L11101, June 2009. doi: 10.1029/2009GL037629.

Bellan, P. M. Pitch angle scattering of an energetic magnetized particle by a circularly polarized electromagnetic wave. *Phys. Plasmas*, 20(4):042117, April 2013. doi: 10.1063/1.4801055.

Bernstein, I. B. Geometric optics in space- and time-varying plasmas. *Physics of Fluids*, 18:320–324, March 1975. doi: 10.1063/1.861140.

Blake, J. B., Carranza, P. A., Claudepierre, S. G., Clemmons, J. H., et al. The Magnetic Electron Ion Spectrometer (MagEIS) Instruments Aboard the Radiation Belt Storm Probes (RBSP) Spacecraft. *Space Sci. Rev.*, 179(1-4):383–421, November 2013. doi: 10.1007/s11214-013-9991-8.

Bortnik, J., Li, W., Thorne, R. M., Angelopoulos, V., et al. An Observation Linking the Origin of Plasmaspheric Hiss to Discrete Chorus Emissions. *Science*, 324:775, May 2009. doi: 10.1126/science.1171273.

Breneman, A. W., Crew, A., Sample, J., Klumpar, D., et al. Observations Directly Linking Relativistic Electron Microbursts to Whistler Mode Chorus: Van Allen Probes and FIREBIRD II. *Geophys. Res. Lett.*, 44:11,265–11,272, November 2017. doi: 10.1002/2017GL075001.

Budden, K. G. *The Propagation of Radio Waves: The Theory of Radio Waves of Low Power in the Ionosphere and Magnetosphere*. Cambridge University Press, 1985. ISBN 9780521369527.

Bud'ko, N. I., Karpman, V. I., and Pokhotelov, O. A. Nonlinear theory of the monochromatic circularly polarized VLF and ULF waves in the magnetosphere. *Cosmic Electrodynamics*, 3:147–164, January 1972.

Bunch, N. L., Spasojevic, M., and Shprits, Y. Y. Off-equatorial chorus occurrence and wave amplitude distributions as observed by the Polar Plasma Wave Instrument. *J. Geophys. Res. Space Physics*, 117(A4):A04205, April 2012. doi: 10.1029/2011JA017228.

Chen, L. and Zonca, F. Physics of Alfvén waves and energetic particles in burning plasmas. *Rev. Mod. Phys.*, 88(1):015008, January 2016. doi: 10.1103/RevModPhys.88.015008.

Chen, L., Thorne, R. M., Bortnik, J., and Zhang, X.-J. Nonresonant interactions of electromagnetic ion cyclotron waves with relativistic electrons. *J. Geophys. Res. Space Physics*, 121(10):9913–9925, October 2016. doi: 10.1002/2016JA022813.

Chen, L., Santolík, O., Hajoš, M., Zheng, L., et al. Source of the low-altitude hiss in the ionosphere. *Geophys. Res. Lett.*, 44(5):2060–2069, March 2017. doi: 10.1002/2016GL072181.

Chen, L., Zhang, X.-J., Artemyev, A., Zheng, L., et al. Electron microbursts induced by nonducted chorus waves. *Front. Astron. Space Sci.*, 8:163, October 2021. doi: 10.3389/fspas.2021.745927.

Cornilleau-Wehrlin, N., Chauveau, P., Louis, S., Meyer, A., et al. The Cluster Spatio-Temporal Analysis of Field Fluctuations (STAFF) Experiment. *Space Sci. Rev.*, 79:107–136, January 1997. doi: 10.1023/A:1004979209565.

Crabtree, C., Tejero, E., Ganguli, G., Hospodarsky, G. B., and Kletzing, C. A. Bayesian spectral analysis of chorus subelements from the van allen probes. *J. Geophys. Res. Space Physics*, 122(6):6088–6106, 2017. doi: 10.1002/2016JA023547.

Dawson, J. On Landau Damping. *Physics of Fluids*, 4(7):869–874, July 1961. doi: 10.1063/1.1706419.

de Soria-Santacruz, M., Spasojevic, M., and Chen, L. EMIC waves growth and guiding in the presence of cold plasma density irregularities. *Geophys. Res. Lett.*, 40(10): 1940–1944, May 2013. doi: 10.1002/grl.50484.

Demekhov, A. G. Generation of VLF emissions with the increasing and decreasing frequency in the magnetosperic cyclotron maser in the backward wave oscillator regime. *Radiophys. and Quantum Electron.*, 53(11):609–622, April 2011. doi: 10.1007/s11141-011-9256-x.

Demekhov, A. G. Relationship Between the Parameters of the Linear and Nonlinear Wave Generation Stages in a Magnetospheric Cyclotron Maser in the Backward-Wave Oscillator Regime. *Radiophys. and Quantum Electron.*, 59(10):773–781, March 2017. doi: 10.1007/s11141-017-9746-6.

Demekhov, A. G. and Trakhtengerts , V. Y. Dynamics of the magnetospheric cyclotron ELF/VLF maser in the backward-wave-oscillator regime. II. The influence of the magnetic-field inhomogeneity. *Radiophys. and Quantum Electron.*, 51(11):880–889, November 2008. doi: 10.1007/s11141-009-9093-3.

Demekhov, A. G. and Trakhtengerts, V. Y. Dynamics of the Magnetospheric Cyclotron ELF/VLF Maser in the Backward-Wave-Oscillator Regime. I. Basic Equations and Results in the Case of a Uniform Magnetic Field. *Radiophys. and Quantum Electron.*, 48(9):639–649, September 2005. doi: 10.1007/s11141-005-0109-3.

Demekhov, A. G., Taubenschuss, U., and Santolík, O. Simulation of VLF chorus emissions in the magnetosphere and comparison with THEMIS spacecraft data. *J. Geophys. Res. Space Physics*, 122(1):166–184, January 2017. doi: 10.1002/2016JA023057.

Demekhov, A. G., Taubenschuss, U., Hanzelka, M., and Santolík, O. Frequency Dependence of Very Low Frequency Chorus Poynting Flux in the Source Region: THEMIS Observations and a Model. *Geophys. Res. Lett.*, 47(6):e86958, March 2020. doi: 10.1029/2019GL086958.

Denavit, J. and Sudan, R. N. Whistler sideband instability. *Phys. Fluids*, 18(5):575–584, May 1975. doi: 10.1063/1.861173.

Foster, J. C., Erickson, P. J., Omura, Y., Baker, D. N., et al. Van Allen Probes observations of prompt MeV radiation belt electron acceleration in nonlinear interactions with VLF chorus. *J. Geophys. Res. Space Physics*, 122(1):324–339, January 2017. doi: 10.1002/2016JA023429.

Foster, J. C., Erickson, P. J., and Omura, Y. Subpacket structure in strong VLF chorus rising tones: characteristics and consequences for relativistic electron acceleration. *Earth Planets Space*, 73(1):140, December 2021. doi: 10.1186/s40623-021-01467-4.

Fu, X., Gary, S. P., Reeves, G. D., Winske, D., and Woodroffe, J. R. Generation of Highly Oblique Lower Band Chorus Via Nonlinear Three-Wave Resonance. *Geophys. Res. Lett.*, 44(19):9532–9538, October 2017. doi: 10.1002/2017GL074411.

Funsten, H. O., Skoug, R. M., Guthrie, A. A., MacDonald, E. A., et al. Helium, Oxygen, Proton, and Electron (HOPE) Mass Spectrometer for the Radiation Belt Storm Probes Mission. *Space Sci. Rev.*, 179(1-4):423–484, November 2013. doi: 10.1007/s11214-013-9968-7.

Gao, X., Li, W., Thorne, R. M., Bortnik, J., et al. Statistical results describing the bandwidth and coherence coefficient of whistler mode waves using THEMIS waveform data. *J. Geophys. Res. Space Physics*, 119(11):8992–9003, November 2014. doi: 10.1002/2014JA020158.

Gao, X., Chen, L., Li, W., Lu, Q., and Wang, S. Statistical Results of the Power Gap Between Lower-Band and Upper-Band Chorus Waves. *Geophys. Res. Lett.*, 46(8): 4098–4105, April 2019. doi: 10.1029/2019GL082140.

Gendrin, R. Le guidage des whistlers par le champ magnetique. *Planet. Space Sci.*, 5 (4):274,IN1,279–278,IN2,282, August 1961. doi: 10.1016/0032-0633(61)90096-4.

Gołkowski, M. and Gibby, A. R. On the conditions for nonlinear growth in magnetospheric chorus and triggered emissions. *Phys. Plasmas*, 24(9):092904, September 2017. doi: 10.1063/1.4986225.

Grison, B., Santolík, O., Cornilleau-Wehrlin, N., Masson, A., et al. EMIC triggered chorus emissions in Cluster data. *J. Geophys. Res. Space Physics*, 118(3):1159–1169, March 2013. doi: 10.1002/jgra.50178.

Grison, B., Hanzelka, M., Breuillard, H., Darrouzet, F., et al. Plasmaspheric Plumes and EMIC Rising Tone Emissions. *J. Geophys. Res. Space Physics*, 123(11):9443–9452, November 2018. doi: 10.1029/2018JA025796.

Grison, B., Santolík, O., Lukačevič, J., and Usanova, M. E. Occurrence of EMIC Waves in the Magnetosphere According to Their Distance to the Magnetopause. *Geophys. Res. Lett.*, 48(3):e90921, February 2021. doi: 10.1029/2020GL090921.

Gurnett, D. A. and Bhattacharjee, A. *Introduction to Plasma Physics: With Space, Laboratory and Astrophysical Applications*. Cambridge University Press, 2017. ISBN 9781316849026.

Gurnett, D. A. and O'Brien, B. J. High-Latitude Geophysical Studies with Satellite Injun 3, 5, Very Low Frequency Electromagnetic Radiation. *J. Geophys. Res.*, 69(1): 65–89, January 1964. doi: 10.1029/JZ069i001p00065.

Gustafsson, G., Bostrom, R., Holback, B., Holmgren, G., et al. The Electric Field and Wave Experiment for the Cluster Mission. *Space Sci. Rev.*, 79:137–156, January 1997. doi: 10.1023/A:1004975108657.

Hanzelka, M., Santolík, O., Hajoš, M., Němec, F., and Parrot, M. Observation of ionospherically reflected quasiperiodic emissions by the DEMETER spacecraft. *Geophys. Res. Lett.*, 44:8721–8729, September 2017. doi: 10.1002/2017GL074883.

Hanzelka, M., Santolík, O., Omura, Y., and Kolmašová, I. Measurability of the Nonlinear Response of Electron Distribution Function to Chorus Emissions in the Earth's Radiation Belt. *J. Geophys. Res. Space Physics*, 126(9):e29624, September 2021. doi: 10.1029/2021JA029624.

Hanzelka, M. and Santolík, O. Effects of Ducting on Whistler Mode Chorus or Exohiss in the Outer Radiation Belt. *Geophys. Res. Lett.*, 46(11):5735–5745, June 2019. doi: 10.1029/2019GL083115.

Hanzelka, M., Santolík, O., Omura, Y., Kolmašová, I., and Kletzing, C. A. A Model of the Subpacket Structure of Rising Tone Chorus Emissions. *J. Geophys. Res. Space Physics*, 125(8):e28094, August 2020. doi: 10.1029/2020JA028094.

Hargreaves, J. K. *The Solar-Terrestrial Environment: An Introduction to Geospace – the Science of the Terrestrial Upper Atmosphere, Ionosphere, and Magnetosphere.* Cambridge Atmospheric and Space Science Series. Cambridge University Press, 1992. ISBN 9780521427371.

Harid, V., Liu, C., Pang, Y., Alvina, A. J., et al. Automated Large-Scale Extraction of Whistlers Using Mask-Scoring Regional Convolutional Neural Network. *Geophys. Res. Lett.*, 48(15):e93819, August 2021. doi: 10.1029/2021GL093819.

Helliwell, R. A. A theory of discrete VLF emissions from the magnetosphere. *J. Geophys. Res.*, 72(19):4773–4790, October 1967. doi: 10.1029/JZ072i019p04773.

Helliwell, R. A., Katsufrakis, J., Trimpi, M., and Brice, N. Artificially Stimulated Very Low Frequency Radiation from the Ionosphere. *J. Geophys. Res.*, 69(11):2391–2394, June 1964. doi: 10.1029/JZ069i011p02391.

Higuera, A. V. and Cary, J. R. Structure-preserving second-order integration of relativistic charged particle trajectories in electromagnetic fields. *Phys. Plasmas*, 24(5): 052104, May 2017. doi: 10.1063/1.4979989.

Hikishima, M., Omura, Y., and Summers, D. Microburst precipitation of energetic electrons associated with chorus wave generation. *Geophys. Res. Lett.*, 37(7):L07103, April 2010. doi: 10.1029/2010GL042678.

Horne, R. B. Path-integrated growth of electrostatic waves – The generation of terrestrial myriametric radiation. *J. Geophys. Res.*, 94:8895–8909, July 1989. doi: 10.1029/JA094iA07p08895.

Hospodarsky, G. B. Spaced-based search coil magnetometers. *J. Geophys. Res. Space Physics*, 121(12):12,068–12,079, December 2016. doi: 10.1002/2016JA022565.

Hospodarsky, G. B., Kurth, W. S., Kletzing, C. A., Bounds, S. R., et al. *Plasma Wave Measurements from the Van Allen Probes*, chapter 10, pages 127–143. American Geophysical Union (AGU), 2016. ISBN 9781119066880.

Hsieh, Y.-K. and Omura, Y. Nonlinear Damping of Oblique Whistler Mode Waves Via Landau Resonance. *J. Geophys. Res. Space Physics*, 123(9):7462–7472, September 2018. doi: 10.1029/2018JA025848.

Ichimaru, S. *Statistical Plasma Physics: Basic Principles (1st ed.)*. CRC Press, 2004. ISBN 978-0813341781.

Johnstone, A. D., Alsop, C., Burge, S., Carter, P. J., et al. Peace: a Plasma Electron and Current Experiment. *Space Sci. Rev.*, 79:351–398, January 1997. doi: 10.1023/A:1004938001388.

Juhász, L., Omura, Y., Lichtenberger, J., and Friedel, R. H. Evaluation of Plasma Properties From Chorus Waves Observed at the Generation Region. *J. Geophys. Res. Space Physics*, 124(6):4125–4136, June 2019. doi: 10.1029/2018JA026337.

Karpman, V. I. Nonlinear Effects in the ELF Waves Propagating along the Magnetic Field in the Magnetosphere. *Space Sci. Rev.*, 16(3):361–388, September 1974. doi: 10.1007/BF00171564.

Karpman, V. I., Istomin, I. N., and Shkliar, D. R. Effects of Nonlinear Interaction of Monochromatic Waves with Resonant Particles in the Inhomogeneous Plasma. *Phys. Scr.*, 11(5):278–284, May 1975. doi: 10.1088/0031-8949/11/5/008.

Kasahara, S., Yokota, S., Mitani, T., Asamura, K., et al. Medium-energy particle experiments—electron analyzer (MEP-e) for the exploration of energization and radiation in geospace (ERG) mission. *Earth Planets Space*, 70(1):69, May 2018. doi: 10.1186/s40623-018-0847-z.

Katoh, Y. A simulation study of the propagation of whistler-mode chorus in the Earth's inner magnetosphere. *Earth Planets Space*, 66:6, December 2014. doi: 10.1186/1880-5981-66-6.

Ke, Y., Gao, X., Lu, Q., Wang, X., and Wang, S. Generation of rising-tone chorus in a two-dimensional mirror field by using the general curvilinear PIC code. *J. Geophys. Res. Space Physics*, 122(8):8154–8165, August 2017. doi: 10.1002/2017JA024178.

Kennel, C. F. and Petschek, H. E. Limit on Stably Trapped Particle Fluxes. *J. Geophys. Res.*, 71:1–28, January 1966.

Kletzing, C. A., Kurth, W. S., Acuna, M., MacDowall, R. J., et al. The Electric and Magnetic Field Instrument Suite and Integrated Science (EMFISIS) on RBSP. *Space Sci. Rev.*, 179(1-4):127–181, November 2013. doi: 10.1007/s11214-013-9993-6.

Kubota, Y. and Omura, Y. Nonlinear Dynamics of Radiation Belt Electrons Interacting With Chorus Emissions Localized in Longitude. *J. Geophys. Res. Space Physics*, 123 (6):4835–4857, June 2018. doi: 10.1029/2017JA025050.

Kurita, S., Katoh, Y., Omura, Y., Angelopoulos, V., et al. THEMIS observation of chorus elements without a gap at half the gyrofrequency. *J. Geophys. Res. Space Physics*, 117:A11223, November 2012. doi: 10.1029/2012JA018076.

Kurth, W. S., De Pascuale, S., Faden, J. B., Kletzing, C. A., et al. Electron densities inferred from plasma wave spectra obtained by the Waves instrument on Van Allen Probes. *J. Geophys. Res. Space Physics*, 120:904–914, February 2015. doi: 10.1002/2014JA020857.

Kuzichev, I. V., Soto-Chavez, A. R., Park, J., Gerrard, A., and Spitkovsky, A. Magnetospheric chorus wave simulation with the TRISTAN-MP PIC code. *Phys. Plasmas*, 26(7):072901, July 2019. doi: 10.1063/1.5096537.

Lampton, M. Daytime observations of energetic auroral-zone electrons. *J. Geophys. Res.*, 72(23):5817–5823, December 1967. doi: 10.1029/JZ072i023p05817.

Landau, L. D. On the vibrations of electron plasma. *Journal of Physics*, 10(1):25–34, 1946.

Lee, J. H. and Angelopoulos, V. On the presence and properties of cold ions near Earth's equatorial magnetosphere. *J. Geophys. Res. Space Physics*, 119(3):1749–1770, March 2014. doi: 10.1002/2013JA019305.

Leisner, J. S., Russell, C. T., Dougherty, M. K., Blanco-Cano, X., et al. Ion cyclotron waves in Saturn's E ring: Initial Cassini observations. *Geophys. Res. Lett.*, 33(11): L11101, June 2006. doi: 10.1029/2005GL024875.

Li, J., Bortnik, J., An, X., Li, W., et al. Origin of two-band chorus in the radiation belt of Earth. *Nat. Commun.*, 10:4672, October 2019. doi: 10.1038/s41467-019-12561-3.

Li, W., Thorne, R. M., Angelopoulos, V., Bortnik, J., et al. Global distribution of whistler-mode chorus waves observed on the THEMIS spacecraft. *Geophys. Res. Lett.*, 36(9):L09104, May 2009. doi: 10.1029/2009GL037595.

Li, W., Thorne, R. M., Bortnik, J., Shprits, Y. Y., et al. Typical properties of rising and falling tone chorus waves. *Geophys. Res. Lett.*, 38(14):L14103, July 2011. doi: 10.1029/2011GL047925.

Liu, X. and Chen, L. Instability in a relativistic magnetized plasma. *Phys. Plasmas*, 26(4):042902, April 2019. doi: 10.1063/1.5089749.

Lorentzen, K. R., Blake, J. B., Inan, U. S., and Bortnik, J. Observations of relativistic electron microbursts in association with VLF chorus. *J. Geophys. Res.*, 106(A4): 6017–6028, April 2001. doi: 10.1029/2000JA003018.

Macúšová, E., Santolík, O., DécréAu, P., Demekhov, A. G., et al. Observations of the relationship between frequency sweep rates of chorus wave packets and plasma density. *J. Geophys. Res. Space Physics*, 115(A12):A12257, December 2010. doi: 10.1029/2010JA015468.

Maslej-Krešňáková, V., Kundrát, A., Mackovjak, Å. i., Butka, P., et al. Automatic Detection of Atmospherics and Tweek Atmospherics in Radio Spectrograms Based on a Deep Learning Approach. *Earth Space Sci.*, 8(11):e02007, November 2021. doi: 10.1029/2021EA002007.

Maxworth, A. S. and Gołkowski, M. Magnetospheric whistler mode ray tracing in a warm background plasma with finite electron and ion temperature. *J. Geophys. Res. Space Physics*, 122:7323–7335, July 2017. doi: 10.1002/2016JA023546.

Miyoshi, Y., Saito, S., Kurita, S., Asamura, K., et al. Relativistic Electron Microbursts as High-Energy Tail of Pulsating Aurora Electrons. *Geophys. Res. Lett.*, 47(21): e90360, November 2020. doi: 10.1029/2020GL090360.

Mourenas, D., Artemyev, A. V., Agapitov, O. V., Krasnoselskikh, V., and Mozer, F. S. Very oblique whistler generation by low-energy electron streams. *J. Geophys. Res. Space Physics*, 120(5):3665–3683, May 2015. doi: 10.1002/2015JA021135.

Mozer, F. S., Agapitov, O. V., Giles, B., and Vasko, I. Direct Observation of Electron Distributions inside Millisecond Duration Electron Holes. *Phys. Rev. Lett.*, 121(13): 135102, September 2018. doi: 10.1103/PhysRevLett.121.135102.

Nakamura, S., Omura, Y., and Summers, D. Fine Structure of Whistler Mode Hiss in Plasmaspheric Plumes Observed by the Van Allen Probes. *J. Geophys. Res. Space Physics*, 123(11):9055–9064, November 2018. doi: 10.1029/2018JA025803.

Nakamura, S., Omura, Y., Shoji, M., Nosé, M., et al. Subpacket structures in EMIC rising tone emissions observed by the THEMIS probes. *J. Geophys. Res. Space Physics*, 120(9):7318–7330, September 2015. doi: 10.1002/2014JA020764.

Nogi, T. and Omura, Y. Nonlinear Signatures of VLF-Triggered Emissions: A Simulation Study. *J. Geophys. Res. Space Physics*, 127(1):e29826, January 2022. doi: 10.1029/2021JA029826.

Nunn, D. A theory of VLF emissions. *Planet. Space Sci.*, 19(9):1141–1167, September 1971. doi: 10.1016/0032-0633(71)90110-3.

Nunn, D. A self-consistent theory of triggered VLF emissions. *Planet. Space Sci.*, 22 (3):349–378, March 1974. doi: 10.1016/0032-0633(74)90070-1.

Nunn, D. A nonlinear theory of sideband stability in ducted whistler mode waves. *Planet. Space Sci.*, 34(5):429–451, May 1986. doi: 10.1016/0032-0633(86)90032-2.

Nunn, D., Zhang, X. J., Mourenas, D., and Artemyev, A. V. Generation of Realistic Short Chorus Wave Packets. *Geophys. Res. Lett.*, 48(7):e92178, April 2021. doi: 10.1029/2020GL092178.

Ojha, B., Omura, Y., Singh, S., and Lakhina, G. S. Multipoint Analysis of Source Regions of EMIC Waves and Rapid Growth of Subpackets. *J. Geophys. Res. Space Physics*, 126(11):e29514, November 2021. doi: 10.1029/2021JA029514.

Omura, Y., Matsumoto, H., Nunn, D., and Rycroft, M. J. A review of observational, theoretical and numerical studies of VLF triggered emissions. *J. Atm. Ter. Phys.*, 53:351–368, May 1991. doi: 10.1016/0021-9169(91)90031-2.

Omura, Y., Katoh, Y., and Summers, D. Theory and simulation of the generation of whistler-mode chorus. *J. Geophys. Res. Space Physics*, 113:A04223, April 2008. doi: 10.1029/2007JA012622.

Omura, Y. Nonlinear wave growth theory of whistler-mode chorus and hiss emissions in the magnetosphere. *Earth Planets Space*, 73(1):95, April 2021. doi: 10.1186/s40623-021-01380-w.

Omura, Y. and Nunn, D. Triggering process of whistler mode chorus emissions in the magnetosphere. *J. Geophys. Res. Space Physics*, 116(A5):A05205, May 2011. doi: 10.1029/2010JA016280.

Omura, Y., Furuya, N., and Summers, D. Relativistic turning acceleration of resonant electrons by coherent whistler mode waves in a dipole magnetic field. *J. Geophys. Res. Space Physics*, 112(A6):A06236, June 2007. doi: 10.1029/2006JA012243.

Omura, Y., Hikishima, M., Katoh, Y., Summers, D., and Yagitani, S. Nonlinear mechanisms of lower-band and upper-band VLF chorus emissions in the magnetosphere. *J. Geophys. Res. Space Physics*, 114(A7):A07217, July 2009. doi: 10.1029/2009JA014206.

Omura, Y., Pickett, J., Grison, B., Santolik, O., et al. Theory and observation of electromagnetic ion cyclotron triggered emissions in the magnetosphere. *J. Geophys. Res. Space Physics*, 115(A7):A07234, July 2010. doi: 10.1029/2010JA015300.

Omura, Y., Nunn, D., and Summers, D. *Generation Processes of Whistler Mode Chorus Emissions: Current Status of Nonlinear Wave Growth Theory*, pages 243–254. American Geophysical Union (AGU), 2013. ISBN 9781118704752. doi: 10.1029/2012GM001347.

Omura, Y., Nakamura, S., Kletzing, C. A., Summers, D., and Hikishima, M. Nonlinear wave growth theory of coherent hiss emissions in the plasmasphere. *J. Geophys. Res. Space Physics*, 120(9):7642–7657, September 2015. doi: 10.1002/2015JA021520.

Omura, Y., Hsieh, Y.-K., Foster, J. C., Erickson, P. J., et al. Cyclotron Acceleration of Relativistic Electrons Through Landau Resonance With Obliquely Propagating Whistler-Mode Chorus Emissions. *J. Geophys. Res. Space Physics*, 124(4):2795–2810, April 2019. doi: 10.1029/2018JA026374.

O'Neil, T. Collisionless Damping of Nonlinear Plasma Oscillations. *Phys. Fluids*, 8 (12):2255–2262, December 1965. doi: 10.1063/1.1761193.

Orfanidis, S. *Electromagnetic Waves and Antennas*. Sophocles J. Orfanidis, 2016. URL `https://www.ece.rutgers.edu/~orfanidi/ewa/`.

Ossakow, S. L., Ott, E., and Haber, I. Nonlinear Evolution of Whistler Instabilities. *Phys. Fluids*, 15(12):2314–2326, December 1972. doi: 10.1063/1.1693875.

Ozaki, M., Shiokawa, K., Miyoshi, Y., Hosokawa, K., et al. Microscopic Observations of Pulsating Aurora Associated With Chorus Element Structures: Coordinated Arase Satellite-PWING Observations. *Geophys. Res. Lett.*, 45(22):12,125–12,134, November 2018. doi: 10.1029/2018GL079812.

Palmadesso, P. and Schmidt, G. Collisionless Damping of a Large Amplitude Whistler Wave. *Phys. Fluids*, 14(7):1411–1418, July 1971. doi: 10.1063/1.1693622.

Pedersen, A., Cornilleau-Wehrlin, N., de La Porte, B., Roux, A., et al. The Wave Experiment Consortium (WEC). *Space Sci. Rev.*, 79:93–106, January 1997. doi: 10.1023/A:1004927225495.

Pickett, J. S., Grison, B., Omura, Y., Engebretson, M. J., et al. Cluster observations of EMIC triggered emissions in association with Pc1 waves near Earth's plasmapause. *Geophys. Res. Lett.*, 37(9):L09104, May 2010. doi: 10.1029/2010GL042648.

Píša, D., Souček, J., Santolík, O., Hanzelka, M., et al. First-year ion-acoustic wave observations in the solar wind by the RPW/TDS instrument on board Solar Orbiter. *Astron. Astrophys.*, 656:A14, December 2021. doi: 10.1051/0004-6361/202140928.

Pollock, C., Moore, T., Jacques, A., Burch, J., et al. Fast Plasma Investigation for Magnetospheric Multiscale. *Space Sci. Rev.*, 199(1-4):331–406, March 2016. doi: 10.1007/s11214-016-0245-4.

Porazik, P., Johnson, J. R., Kaganovich, I., and Sanchez, E. Modification of the loss cone for energetic particles. *Geophys. Res. Lett.*, 41(22):8107–8113, November 2014. doi: 10.1002/2014GL061869.

Press, W. H., Teukolsky, S. A., Vetterling, W. T., and Flannery, B. P. *Numerical Recipes in C (2nd Ed.): The Art of Scientific Computing*. Cambridge University Press, New York, NY, USA, 1992. ISBN 0-521-43108-5.

Rönnmark, K. Computation of the dielectric tensor of a Maxwellian plasma. *Plasma Physics*, 25:699–701, June 1983. doi: 10.1088/0032-1028/25/6/007.

Roytershteyn, V. and Delzanno, G. L. Nonlinear coupling of whistler waves to oblique electrostatic turbulence enabled by cold plasma. *Phys. Plasmas*, 28(4):042903, April 2021. doi: 10.1063/5.0041838.

Russell, C. T., Luhmann, J. G., and Strangeway, R. J. *Space Physics: An Introduction*. Cambridge University Press, 2016. ISBN 9781107098824.

Saikin, A. A., Zhang, J. C., Allen, R. C., Smith, C. W., et al. The occurrence and wave properties of H^+-, He^+-, and O^+-band EMIC waves observed by the Van Allen Probes. *J. Geophys. Res. Space Physics*, 120(9):7477–7492, September 2015. doi: 10.1002/2015JA021358.

Santolík, O. and Chum, J. The Origin of Plasmaspheric Hiss. *Science*, 324:729–730, March 2009. doi: 10.1126/science.1172878.

Santolík, O., Gurnett, D. A., Pickett, J. S., Parrot, M., and Cornilleau-Wehrlin, N. Spatio-temporal structure of storm-time chorus. *J. Geophys. Res. Space Physics*, 108:1278, July 2003a. doi: 10.1029/2002JA009791.

Santolík, O., Parrot, M., and Lefeuvre, F. Singular value decomposition methods for wave propagation analysis. *Rad. Sci.*, 38:1010, February 2003b. doi: 10.1029/2000RS002523.

Santolík, O., Gurnett, D., and Pickett, J. Multipoint investigation of the source region of storm-time chorus. *Ann. Geophys.*, 22:2555–2563, July 2004. doi: 10.5194/angeo-22-2555-2004.

Santolík, O., Gurnett, D. A., Pickett, J. S., Parrot, M., and Cornilleau-Wehrlin, N. A microscopic and nanoscopic view of storm-time chorus on 31 March 2001. *Geophys. Res. Lett.*, 31(2):L02801, January 2004. doi: 10.1029/2003GL018757.

Santolík, O., Pickett, J. S., Gurnett, D. A., Menietti, J. D., et al. Survey of Poynting flux of whistler mode chorus in the outer zone. *J. Geophys. Res. Space Physics*, 115: A00F13, July 2010. doi: 10.1029/2009JA014925.

Santolík, O., Kletzing, C. A., Kurth, W. S., Hospodarsky, G. B., and Bounds, S. R. Fine structure of large-amplitude chorus wave packets. *Geophys. Res. Lett.*, 41:293–299, January 2014a. doi: 10.1002/2013GL058889.

Santolík, O., Macúšová, E., Kolmašová, I., Cornilleau-Wehrlin, N., and Conchy, Y. Propagation of lower-band whistler-mode waves in the outer Van Allen belt: Systematic analysis of 11 years of multi-component data from the Cluster spacecraft. *Geophys. Res. Lett.*, 41:2729–2737, April 2014b. doi: 10.1002/2014GL059815.

Santolik, O., Kolmasova, I., Kurth, W. S., Hospodarsky, G. B., et al. Whistler-mode waves with large amplitudes in the radiation belt region: new results from the Van Allen Probes. In *EGU General Assembly Conference Abstracts*, EGU General Assembly Conference Abstracts, page 8683, April 2015.

Sauvaud, J. A., Moreau, T., Maggiolo, R., Treilhou, J. P., et al. High-energy electron detection onboard DEMETER: The IDP spectrometer, description and first results on the inner belt. *Planet. Space Sci.*, 54(5):502–511, April 2006. doi: 10.1016/j.pss.2005.10.019.

Sazhin, S. S. Landau damping of low frequency whistler-mode waves. *Ann. Geophys.*, 9:690–695, October 1991.

Sazhin, S. *Whistler-mode Waves in a Hot Plasma*. Cambridge University Press, Cambridge, 1993. ISBN 9780521401654.

Schunk, R. W. and Nagy, A. F. *Ionospheres*. Cambridge University Press, November 2004. ISBN 9780521607704.

Schwinger, J. On the Green's Functions of Quantized Fields. I. *Proc. Natl. Acad. Sci.*, 37(7):452–455, July 1951. doi: 10.1073/pnas.37.7.452.

Shklyar, D. R. and Prokhorenko, S. A. Reflection from the ionosphere and exit to the ground of whistler wave packets: A dynamical model. *J. Atmos. Sol.-Terr. Phys.*, 201:105222, May 2020. doi: 10.1016/j.jastp.2020.105222.

Shoji, M., Miyoshi, Y., Kistler, L. M., Asamura, K., et al. Discovery of proton hill in the phase space during interactions between ions and electromagnetic ion cyclotron waves. *Sci. Rep.*, 11:13480, January 2021. doi: 10.1038/s41598-021-92541-0.

Soto-Chavez, A. R., Wang, G., Bhattacharjee, A., Fu, G. Y., and Smith, H. M. A model for falling-tone chorus. *Geophys. Res. Lett.*, 41(6):1838–1845, March 2014. doi: 10.1002/2014GL059320.

Stix, T. *Waves in Plasmas*. American Institute of Physics, Melville NY, 1992. ISBN 9780883188583.

Streltsov, A. V., Woodroffe, J., Gekelman, W., and Pribyl, P. Modeling the propagation of whistler-mode waves in the presence of field-aligned density irregularities. *Phys. Plasmas*, 19(5):052104, May 2012. doi: 10.1063/1.4719710.

Stubbe, P. and Sukhorukov, A. I. On the physics of Landau damping. *Phys. Plasmas*, 6(8):2976–2988, August 1999. doi: 10.1063/1.873584.

Suchy, K. Real hamilton equations of geometric optics for media with moderate absorption. *Rad. Sci.*, 16(06):1179–1182, November 1981. ISSN 1944-799X. doi: 10.1029/RS016i006p01179.

Sudan, R. N. and Ott, E. Theory of triggered VLF emissions. *J. Geophys. Res.*, 76 (19):4463–4476, July 1971. doi: 10.1029/JA076i019p04463.

Sugiyama, H., Singh, S., Omura, Y., Shoji, M., et al. Electromagnetic ion cyclotron waves in the Earth's magnetosphere with a kappa-Maxwellian particle distribution. *J. Geophys. Res. Space Physics*, 120:8426–8439, October 2015. doi: 10.1002/2015JA021346.

Summers, D. and Thorne, R. M. Relativistic electron pitch-angle scattering by electromagnetic ion cyclotron waves during geomagnetic storms. *J. Geophys. Res. Space Physics*, 108(A4):1143, April 2003. doi: 10.1029/2002JA009489.

Summers, D., Thorne, R. M., and Xiao, F. Relativistic theory of wave-particle resonant diffusion with application to electron acceleration in the magnetosphere. *J. Geophys. Res.*, 103(A9):20487–20500, September 1998. doi: 10.1029/98JA01740.

Summers, D., Omura, Y., Miyashita, Y., and Lee, D.-H. Nonlinear spatiotemporal evolution of whistler mode chorus waves in Earth's inner magnetosphere. *J. Geophys. Res. Space Physics*, 117(A9):A09206, September 2012. doi: 10.1029/2012JA017842.

Swanson, D. G. *Plasma Waves, 2nd Edition*. Series in Plasma Physics. Taylor & Francis, 2003. ISBN 9780750309271.

Tao, X., Zonca, F., and Chen, L. Identify the nonlinear wave-particle interaction regime in rising tone chorus generation. *Geophys. Res. Lett.*, 44(8):3441–3446, April 2017. doi: 10.1002/2017GL072624.

Tao, X., Zonca, F., Chen, L., and Wu, Y. Theoretical and numerical studies of chorus waves: A review. *Sci. China Earth Sci.*, 63(1):78–92, January 2020. doi: 10.1007/s11430-019-9384-6.

Tao, X., Zonca, F., and Chen, L. A "Trap-Release-Amplify" Model of Chorus Waves. *J. Geophys. Res. Space Physics*, 126(9):e29585, September 2021. doi: 10.1029/2021JA029585.

Taubenschuss, U. and Santolík, O. Wave Polarization analyzed by Singular Value Decomposition of the Spectral Matrix in the Presence of Noise. *Surveys Geophys.*, 40:39–69, August 2018. doi: https://doi.org/10.1007/s10712-018-9496-9.

Taubenschuss, U., Khotyaintsev, Y. V., Santolík, O., Vaivads, A., et al. Wave normal angles of whistler mode chorus rising and falling tones. *J. Geophys. Res. Space Physics*, 119(12):9567–9578, December 2014. doi: 10.1002/2014JA020575.

Teng, S., Tao, X., Xie, Y., Zonca, F., et al. Analysis of the Duration of Rising Tone Chorus Elements. *Geophys. Res. Lett.*, 44(24):12,074–12,082, December 2017. doi: 10.1002/2017GL075824.

Teng, S., Tao, X., and Li, W. Typical Characteristics of Whistler Mode Waves Categorized by Their Spectral Properties Using Van Allen Probes Observations. *Geophys. Res. Lett.*, 46(7):3607–3614, April 2019. doi: 10.1029/2019GL082161.

Trakhtengerts, V. Y. Magnetosphere cyclotron maser: Backward wave oscillator generation regime. *J. Geophys. Res.*, 100(A9):17205–17210, September 1995. doi: 10.1029/95JA00843.

Trakhtengerts, V. Y. A generation mechanism for chorus emission. *Ann. Geophys.*, 17: 95–100, January 1999. doi: 10.1007/s00585-999-0095-4.

Trakhtengerts, V. Y. and Rycroft, M. J. *Whistler and Alfvén Mode Cyclotron Masers in Space*. Cambridge University Press, Cambridge, 2008. ISBN 9780521871983.

Trakhtengerts, V. Y., Rycroft, M. J., and Demekhov, A. G. Interrelation of noise-like and discrete ELF/VLF emissions generated by cyclotron interactions. *J. Geophys. Res.*, 101(A6):13293–13302, June 1996. doi: 10.1029/95JA03515.

Trakhtengerts, V. Y., Demekhov, A. G., Hobara, Y., and Hayakawa, M. Phase-bunching effects in triggered vlf emissions: Antenna effect. *J. Geophys. Res. Space Physics*, 108(A4), 2003. doi: 10.1029/2002JA009415.

Tsurutani, B. T., Chen, R., Gao, X., Lu, Q., et al. Lower-Band "Monochromatic" Chorus Riser Subelement/Wave Packet Observations. *J. Geophys. Res. Space Physics*, 125(10):e28090, October 2020. doi: 10.1029/2020JA028090.

van Allen, J. A., Ludwig, G. H., Ray, E. C., and McIlwain, C. E. Observation of high intensity radiation by satellites 1958 alpha and gamma. *Journal of Jet Propulsion*, 28(9):588–592, 1958. doi: 10.2514/8.7396.

Vomvoridis, J. L. and Denavit, J. Test particle correlation by a whistler wave in a nonuniform magnetic field. *Phys. Fluids*, 22(2):367–377, February 1979. doi: 10.1063/1.862589.

Vomvoridis, J. L., Crystal, T. L., and Denavit, J. Theory and computer simulations of magnetospheric very low frequency emissions. *J. Geophys. Res.*, 87(A3):1473–1490, March 1982. doi: 10.1029/JA087iA03p01473.

Wu, Y., Tao, X., Zonca, F., Chen, L., and Wang, S. Controlling the Chirping of Chorus Waves via Magnetic Field Inhomogeneity. *Geophys. Res. Lett.*, 47(10):e87791, May 2020. doi: 10.1029/2020GL087791.

Wygant, J. R., Bonnell, J. W., Goetz, K., Ergun, R. E., et al. The Electric Field and Waves Instruments on the Radiation Belt Storm Probes Mission. *Space Sci. Rev.*, 179(1-4):183–220, November 2013. doi: 10.1007/s11214-013-0013-7.

Xiao, F., Thorne, R. M., and Summers, D. Instability of electromagnetic R-mode waves in a relativistic plasma. *Phys. Plasmas*, 5(7):2489–2497, July 1998. doi: 10.1063/1.872932.

Yoon, Y. D. and Bellan, P. M. Nondiffusive Pitch-Angle Scattering of a Distribution of Energetic Particles by Coherent Whistler Waves. *J. Geophys. Res. Space Physics*, 125(6):e27796, June 2020. doi: 10.1029/2020JA027796.

Zenitani, S. and Umeda, T. On the Boris solver in particle-in-cell simulation. *Phys. Plasmas*, 25(11):112110, November 2018. doi: 10.1063/1.5051077.

Zhang, X. J., Mourenas, D., Artemyev, A. V., Angelopoulos, V., et al. Rapid Frequency Variations Within Intense Chorus Wave Packets. *Geophys. Res. Lett.*, 47(15):e88853, August 2020. doi: 10.1029/2020GL088853.

Zhang, X. J., Artemyev, A., Angelopoulos, V., Tsai, E., et al. Superfast precipitation of energetic electrons in the radiation belts of the Earth. *Nat. Commun.*, 13, March 2022. doi: 10.1038/s41467-022-29291-8.

Zonca, F., Tao, X., and Chen, L. A Theoretical Framework of Chorus Wave Excitation. *J. Geophys. Res. Space Physics*, 127(2):e2021JA029760, January 2022. doi: 10.1029/2021JA029760.

List of Abbreviations

BWO	Backward Wave Oscillator
CFL	Courant-Friedrichs-Lewy (condition)
DEMETER	Detection of Electro-Magnetic Emissions Transmitted from Earthquake Regions (spacecraft)
ELFIN	Electron Losses and Fields Investigation (spacecraft)
EMFISIS	Electric and Magnetic Field Instrument Suite and Integrated Science (RBSP instrument)
EMIC	ElectroMagnetic Ion Cyclotron (waves)
FPI	Fast Plasma Investigation (MMS instrument)
HOPE	Helium, Oxygen, Proton and Electron (mass spectrometer on RBSP)
IDP	Instrument de Détection de Particules (DEMETER instrument)
KUPDAP	Kyoto University Plasma Dispersion Analysis Package
MagEIS	Magnetic Electron Ion Spectrometer (RBSP instrument)
MEP-e	Medium-Energy Particle experiments – electrons (Arase spacecraft instrument)
MMS	Magnetospheric MultiScale (spacecraft mission)
NGTO	Nonlinear Growth Theory of Omura et al.
PDE	Partial Differential Equation
PEACE	Plasma Electron And Current Experiment (Cluster spacecraft instrument)
PIC	Particle-In-Cell (simulation method)
PSD	Phase space density
RBSP	Radiation Belt Storm Probes (former name of the Van Allen Probes)
RMS	Root Mean Square
STAFF	Spatio-Temporal Analysis of Field Fluctuations (Cluster spacecraft instrument)
STFT	Short-Time Fourier Transform
SVD	Singular Value Decomposition
TARA	TrAp Release Amplify (model)
THEMIS	Time History of Events and Macroscale Interactions during Substorms (spacecraft)
WHAMP	Waves in Homogeneous Anisotropic Magnetized Plasma (software)

List of Symbols

The table below lists every mathematical symbol used in the thesis along with its brief definition. Some symbols may have multiple meanings, depending on the context. To avoid any confusion, the equation where the symbol first appears is recorded in the right column. Particle index s can stand for electrons 'e', protons 'p', or unspecified ions 'i'.

In Sections 2.2 and 2.3, we use the normalized units with $c = 1$, $e = 1$, $m_\mathrm{e} = 1$. In Chapters 3 and 4, the speed of light c is written explicitly, but the charge and mass are normalized. In the rest of the text, all physical constants are explicit, unless stated otherwise in front of individual equations.

The symbols are ordered alphabetically, with English letters first and Greek symbols second.

Symbol	Definition	Equation
A	(relativistic) pitch angle anisotropy	1.97
A_0	equatorial pitch angle anisotropy	3.18
$\boldsymbol{A}$	magnetic vector potential	2.55
A_m	critical value of anisotropy	1.100
a	coefficient in the parabolic approximation of magnetic field strength	3.35
$\boldsymbol{B}$	magnetic field vector	1.1
$\boldsymbol{B}_0$,B_0	ambient (zero-order) magnetic field	1.35
B_m	magnetic field strength at the mirror point of bounce motion	5.22
B_surf	equatorial magentic field strength at the surface of the Earth	4.4
$\boldsymbol{B}_\mathrm{w}$,$B_\mathrm{w}$	wave magnetic field	2.11
$\tilde{B}_\mathrm{w}$	wave magnetic field in complex form	3.1
C_m	constant of particle motion in a whistler wave	2.62
C_s	thermal speed of particle species s	1.13
c	speed of light *in vacuo*	1.9
D	Stix crossover coefficient	1.53
$\mathcal{D}$	dispersion tensor	1.23
$\bar{D}$	determinant of dispersion tensor (dispersion relation)	1.25
$\bar{D}_\mathrm{i}$	imaginary part of the dispersion relation	1.49
$\bar{D}_\mathrm{r}$	real part of the dispersion relation	1.48
$\bar{D}_\mathrm{w}$	whistler mode dispersion relation	3.49
$\mathrm{d}F$	omnidirectional flux differential	5.25
$\boldsymbol{E}$	electric field vector	1.1
E_B	ellipticity of magnetic field	1.104
E_k	kinetic energy	2.9
$\boldsymbol{E}_\mathrm{w}$,$E_\mathrm{w}$	wave electric field	2.4
$\tilde{E}_\mathrm{w}$	wave electric field in complex form	3.1
e	elementary charge	1.1
$\hat{\boldsymbol{e}}_\parallel$	unit vector parallel to the magnetic field	1.44
F	particle number flux	5.20
F_B	planarity of magnetic field	1.105
F_h	phase space distribution of hot electrons, normalized to unity	1.96

Symbol	Definition	Equation
F_s	phase space distribution normalized to unity, particle species s	1.44
f_{eq}	equatorial hot electron distribution	3.9
f_{h}	phase space distribution of hot electrons	1.96
f_s	single-particle phase space distribution of particle species s	1.1
	first-order perturbation of PSD	1.35
f_{s0}	zero-order perturbation of PSD	1.35
f_δ	reduced distribution appearing in the NGTO	3.19
g_0	reduced unperturbed hot electron distribution	3.24
g_{tr}	reduced distribution of trapped electrons	3.24
G	constant replacing g_{tr} in the waterbag model of trapped electrons	3.24
$G(v)$,$G(E_{\mathrm{k}})$	geometric factor of particle instruments in dependence on velocity or energy	5.21
$\mathcal{H}$	Hamiltonian of a charged particle in an electromagnetic field	2.55
$\mathcal{H}_0$	Hamiltonian of a charged particle's adiabatic motion	2.62
$\mathcal{H}_1$	perturbation to the adiabatic Hamiltonian	2.61
h	distance measured along a field line	2.39
h_0	initial position of the point-like source of a chorus element	3.32
h_{f}	starting position of particle motion	5.3
h_i	starting position of the i-th subpacket	4.2
h_{i}	initial position of particle motion	5.3
h_{step}	spatial dimension of a numerical grid cell	4.4
I	normalized first adiabatic invariant multiplied by the wave frequency	2.60
I_R	invariant I evaluated at resonance	2.65
$\boldsymbol{I}$	unit matrix	1.16
$\boldsymbol{J}$	induced current density	1.7
J_0	ζ-independent factor appearing in formulation of the resonant current J_{B} and J_{E}	3.27
J_{B}	resonant current component parallel to the wave magnetic field	3.5
$J_{\mathrm{B,max}}$	$-J_{\mathrm{B}}/J_0$ evaluated at S_{max}	3.27
$\tilde{J}_{\mathrm{c}}$	cold plasma current density in complex form	3.4
J_{E}	resonant current component parallel to the wave electric field	3.5
$J_{\mathrm{E,max}}$	$-J_{\mathrm{E}}/J_0$ evaluated at S_{max}	3.27
$\boldsymbol{J}_{\mathrm{ext}}$	external current density	1.7
J_{norm}	current density normalization	4.4
$\boldsymbol{J}_{\mathrm{R}}$	resonant current density	3.4
$\tilde{J}_{\mathrm{R}}$	resonant current density in complex form	3.4
$\boldsymbol{J}_{\mathrm{tot}}$	total current density	1.5
J_n	Bessel function of the first kind of order n	1.44
K	normalization constant appearing in f_δ	3.19
k	wavenumber	1.14
$k_\perp$	wavenumber component perpendicular to magnetic field	1.43
$k_\parallel$	wavenumber component parallel to magnetic field	1.42
$\boldsymbol{k}$	wave vector	1.14

Symbol	Definition	Equation
$\boldsymbol{k}_0$	mean wave vector of a Gaussian pulse	1.28
k_B	Boltzmann constant	1.11
L	Stix left-hand coefficient	1.56
	(L-shell) equatorial standoff distance of a field line in units of planetary radii	1.83
$\mathcal{M}$	square root of electron to proton mass ratio	1.64
M_{ij}	spectral matrix	1.104
m_s	rest mass of particle species s	1.8
N	number of particles	5.20
$N_{\mathrm{D}s}$	number of particles per Debye sphere	1.10
N_exp	expected number of particles detected by a particle analyzer	5.21
N_req	number of particles required for a significant measurement	5.20
N_S	number of subpackets in a single chorus element	4.9
n	order of resonance (integer)	1.46
n_eq	equatorial hot electron density	3.9
n_he	hot electron number density	1.96
n_s	number density of particle species s	1.10
P	Stix longitudinal coefficient	1.54
p	complex frequency in Laplace transform	1.85
$p_\parallel$	momentum-like variable in the Hamiltonian formulation of cyclotron resonance	2.61
Q	depth of depletion in the trapping region	3.24
$\boldsymbol{r}_\mathrm{L}$,$r_\mathrm{L}$	Larmor radius	2.39
R	Stix right-hand coefficient	1.55
$\mathcal{R}$	fraction of resonant electrons	1.96
R_yx	axis ratio of (k_x, x) oscillations of ducted rays	1.81
$\boldsymbol{r}$	position vector	1.1
$\boldsymbol{r}$	position vector	1.1
S	Stix hybrid coefficient	1.52
	eikonal function	1.67
	inhomogeneity factor	2.43
S_max	point at which $-J_\mathrm{E}/J_0$ maximizes	3.27
$\boldsymbol{S}$	Poynting vector	1.30
s	index of particle species	1.1
$\boldsymbol{s}$	normalization of rotation variable in the Boris algorithm	5.11
s_duct	sign of density change in a field-aligned duct	1.80
s_J	suppression factor for the resonant current	4.8
s_n	substitution in the inhomogeneity factor S, linked with the density gradient	2.45
s_Ω	substitution in the inhomogeneity factor S, linked with the magnetic field gradient	2.46
s_ω	substitution in the inhomogeneity factor S, linked with the frequency drift	3.30
$\boldsymbol{T}$	flux of acoustic energy	1.30
$\boldsymbol{T_n}$	tensor appearing in the hot plasma dispersion relation	1.44
T_N	duration of J_R formation and saturation	3.42
T_tr	nonlinear trapping period	2.9
t	time coordinate	1.1
t_end	time at which the i-th subpacket ends	4.3

Symbol	Definition	Equation
t_f	time at the final point of particle motion	5.3
t_gr	time of particle arrival to the ground	5.25
t_i	starting time of the i-th subpacket	4.3
t_i	time at the initial point of particle motion	5.3
t_max	time at which the i-th subpacket saturates	4.3
t_step	time step in wave simulations	4.4
$\boldsymbol{U}$	canonical momentum of a charged particle in an electromagnetic field	2.55
$U_\perp$,$U_{\perp 0}$	first perpendicular moment, "0" stands for equatorial value	3.19
U_R	relativistic resonance momentum (usually cyclotron)	2.18
U_R^ζ	modified relativistic resonance momentum	2.33
$U_{\mathrm{t}\perp}$	perpendicular thermal momentum	2.38
$U_{\mathrm{t}\perp 0}$	perpendicular thermal momentum at the equator	3.9
$U_{\mathrm{t}\parallel}$	parallel thermal momentum	2.38
$U_{\mathrm{t}\parallel 0}$	parallel thermal momentum at the equator	3.9
$\boldsymbol{u}$,u	relativistic particle momentum vector	1.1
$u_\perp$	relativistic momentum perpendicular to magnetic field	1.38
$u_{\perp 0}$	initial relativistic momentum perpendicular to magnetic field	1.38
$u_\parallel$	relativistic momentum parallel to magnetic field	3.11
$u_{\parallel 0}$	$u_\parallel$-intercept of the resonance momentum curve	1.38
	initial relativistic momentum perpendicular to magnetic field	3.11
$\boldsymbol{V}_\mathrm{g}$,$V_\mathrm{g}$	group velocity	1.29
$\boldsymbol{V}_\mathrm{p}$,$V_\mathrm{p}$	phase velocity	1.27
V_R	resonance velocity (usually cyclotron)	2.19
$V_{\mathrm{R}0}$	resonance velocity ($n = 0$)	2.2
$V_{\mathrm{R}1}$	resonance velocity ($n = \pm 1$)	2.3
$v_{\boldsymbol{E}\times\boldsymbol{B}}$	$\boldsymbol{E} \times \boldsymbol{B}$ drift velocity magnitude	5.6
$\boldsymbol{v}_s$	velocity vector of particle species s	1.1
$v_\perp$	velocity perpendicular to magnetic field	2.3
$v_\parallel$	velocity parallel to magnetic field	2.3
W	energy density	1.33
	factor combining the effects of magnetic field nonuniformity and temperature anisotropy	3.16
	phase shift in the chorus excitation theory of Zonca et al.	3.49
w	characteristic width of a density duct	1.80
w_i	i-th singular value	1.104
x	x-component of the position vector	1.80
Z_s	signed charge of particle species s in units of the elementary charge	1.1
z	z-component of the position vector	2.4
α	pitch angle of a charged particle in magnetic field	5.22
α_eq	equatorial pitch angle	5.22
α_loss	loss cone pitch angle	5.22
α_s	substitution in resonance condition	1.42
$\boldsymbol{\beta}$	magnetic field substitution in the Boris algorithm	5.16
β_s	argument is Bessel functions in hot plasma dispersion relation	1.43

Symbol	Definition	Equation
Γ	growth rate in the chorus excitation theory of Zonca et al.	3.49
Γ_{N}	convective nonlinear growth rate	3.33
γ'	averaged Lorentz factor in the Boris algorithm	5.14
γ_-	Lorentz factor of intermediate momentum in the Boris algorithm	5.15
γ_s	Lorentz factor of particle species s	1.9
γ_{BWO}	sideband growth rate appearing in applications of the BWO theory	3.45
γ_{L}	linear growth rate (imaginary part of frequency)	1.49
$\gamma_{\mathrm{L}0}$,$\gamma_{\mathrm{L}1}$	approximate linear growth rates associated with the $n = 0$ and $n = \pm 1$ resonance	1.93
γ_{NL}	nonlinear growth rate	2.8
γ_{R}	Lorentz factor of resonant particles	1.96
ΔT	duration of a single chorus element	4.9
Δt	time step in particle simulations	5.6
$\Delta\alpha$	angular resolution of particle detectors	5.21
$\Delta\omega$	frequency difference between two overlapping waves	4.5
δ	Dirac delta distribution	1.50
δ_ω	normalized frequency difference	4.9
δt_i	time interval between the saturation point and the end point of the i-th subpacket	4.2
$\delta\omega$	wave frequency perturbation	3.8
$\boldsymbol{\varepsilon}$	dielectric tensor	1.16
	electric field substitution in the Boris algorithm	5.9
ε_0	vacuum permittivity	1.2
ζ	phase difference defined for $n = \pm 1$ resonance	2.13
ζ_0,ζ_1,ζ_2	characteristic points at the inhomogeneous trapping region boundary	2.48
ζ_n	phase difference defined for the n-th cyclotron resonance	2.13
η	phase difference defined for $n = 0$ resonance	2.6
θ_{G}	Gendrin angle	1.61
θ_{k}	wave normal angle $\angle(\boldsymbol{k}, \boldsymbol{B}_0)$	1.51
θ_{S}	polar angle of the Poynting vector $\angle(\boldsymbol{k}, \boldsymbol{B}_0)$	1.61
$\lambda_{\mathrm{D}s}$	Debye length of particle species s	1.10
λ_{drift}	upstream drift of a chorus element source in latitude	4.9
λ_{m}	magnetic latitude	4.4
μ,$\boldsymbol{\mu}$	refractive index (vector form)	1.26
μ_0	vacuum permeability	1.5
ν	resonance mismatch defined for $n = \pm 1$ resonance	2.6
ρ	charge density	1.2
$\boldsymbol{\sigma}$	conductivity tensor	1.15
$\sigma_\perp$	perpendicular thermal speed of a bi-Maxwellian electron distribution	1.92
$\sigma_\parallel$	parallel thermal speed of a bi-Maxwellian electron distribution	1.92
τ	ratio of the times T_{N} and T_{tr}	3.42
$\boldsymbol{\tau}$	rotation variable in the Boris algorithm	5.13
Φ	electrostatic potential	1.85
φ	azimuthal coordinate (particle phase)	1.38

Symbol	Definition	Equation
ψ_{B}	phase of wave magnetic field	2.11
ψ_{E}	phase of wave electric field	3.2
Ω_{e0}	unsigned equatorial electron cyclotron frequency	2.41
Ω_{HO}	frequency of harmonic oscillations of a ducted ray	1.82
Ω_{opt}	optimum amplitude in the NGTO	3.43
Ω_s	unsigned cyclotron frequency of particle species s	1.41
Ω_{thr}	threshold amplitude in the NGTO	3.40
Ω_{w}	normalized wave amplitude $B_{\mathrm{w}}e/m_{\mathrm{e}}$	2.14
$\tilde{\Omega}_{\mathrm{w}}$	normalized wave amplitude $B_{\mathrm{w}}e/(m_{\mathrm{e}}\Omega_{\mathrm{e0}})$	2.16
ω	wave frequency	1.14
$\tilde{\omega}$	wave frequency normalized to Ω_{e0}	2.19
ω_{f}	terminal frequency of a chorus element	4.4
ω_i	initial frequency of the i-th subpacket	4.4
ω_{lh}	lower hybrid frequency	1.52
$\omega_{\mathrm{p}s}$	plasma frequency of particle species s	1.2
ω_{pe}	electron plasma frequency normalized to Ω_{e0}	2.19
ω_{phe}	plasma frequency of hot electrons	3.38
ω_{tr}	nonlinear trapping frequency	2.7
ω_{uh}	upper hybrid frequency	1.52

List of Publications

Publications appended to the thesis

A.1 Hanzelka, M., Santolík, O., Omura, Y., Kolmašová, I., and Kletzing, C. A. A Model of the Subpacket Structure of Rising Tone Chorus Emissions. *J. Geophys. Res. Space Physics*, 125(8):e28094, August 2020. doi: 10.1029/2020JA028094.

A.2 Hanzelka, M., Santolík, O., Omura, Y., and Kolmašová, I. Measurability of the Nonlinear Response of Electron Distribution Function to Chorus Emissions in the Earth's Radiation Belt. *J. Geophys. Res. Space Physics*, 126(9):e29624, September 2021. doi: 10.1029/2021JA029624.

Other publications

- Píša, D., Souček, J., Santolík, O., Hanzelka, M. et al. First-year ion-acoustic wave observations in the solar wind by the RPW/TDS instrument on board Solar Orbiter. *Astronomy & Astrophysics*, 656(A14), December 2021. doi: 10.1051/0004-6361/202140928

- Demekhov, A. G., Taubenschuss, U., Hanzelka, M., and Santolík, O. Frequency dependence of very low frequency chorus Poynting flux in the source region: THEMIS observations and a model. *Geophys. Res. Lett.*, 47(6):e86958, March 2020. doi: 10.1029/2019GL086958.

- Hanzelka, M., and Santolík, O. Effects of ducting on whistler mode chorus or exohiss in the outer radiation belt. *Geophys. Res. Lett.*, 46(11):5735–5745, June 2019. doi: 10.1029/2019GL083115.

- Grison, B., Hanzelka, M., Breuillard, H., Darrouzet, F. et al. Plasmaspheric plumes and EMIC rising tone emissions. *J. Geophys. Res. Space Physics*, 123(11):9443-9452, November 2018. doi: 10.1002/2015JA022264.

- Hanzelka, M., Santolík, O., Hajos, M., Němec, F, Parrot, M. Observation of ionospherically reflected quasiperiodic emissions by the DEMETER spacecraft. *Geophys. Res. Lett.*, 44(17):8721-8729, September 2017. doi: 10.1002/2017GL074883.

- Chen, L., Santolík, O., Hajos, M., Zheng, L., Zhima, Z., Heelis, R., Hanzelka, M. et al. Source of the low-altitude hiss in the ionosphere. *Geophys. Res. Lett.*, 44(5):2060-2069, March 2017. doi: 10.1002/2016GL072181.

- Martinez-Calderon, C., Shiokawa, K., Miyoshi, Y., Keika, K., Ozaki, M., Schofield, I., Connors, M., Kletzing, C., Hanzelka, M et al. ELF/VLF wave propagation at subauroral latitudes: Conjugate observation between the ground and Van Allen Probes A. *J. Geophys. Res. Space Physics*, 121(6):5384-5393, June 2016. doi: 10.1002/2015JA022264

A. Attachments

A.1 Comment on the corrections to nonlinear growth theory presented by Omura 2021

In the nonlinear growth theory of chorus emissions developed by Omura et al., the electrons which contribute to the resonant current reach weakly relativistic velocities. In Omura et al., 2009, it is argued that the electron distribution should be initially bi-Maxwellian in relativistic momenta, but the power of Lorentz factor in the formula for resonant current is not consistent with this choice. Omura 2021 presented the consistent formula expressed in relativistic momenta. Below we provide additional discussion on the non-relativistic and weakly relativistic electron distributions and their treatment within the nonlinear growth theory.

* * *

We have two velocity distributions defined as

$$f(v_\parallel, v_\perp, \varphi) = \frac{1}{(2\pi)^{3/2} V_{\mathrm{t}\perp}^2 V_{\mathrm{t}\parallel}} \exp\left(\frac{-v_\parallel^2}{2V_{\mathrm{t}\parallel}^2}\right) \exp\left(\frac{-v_\perp^2}{2V_{\mathrm{t}\perp}^2}\right) \tag{A.1}$$

and

$$g(u_\parallel, u_\perp, \varphi) = \frac{1}{(2\pi)^{3/2} U_{\mathrm{t}\perp}^2 U_{\mathrm{t}\parallel}} \exp\left(\frac{-u_\parallel^2}{2U_{\mathrm{t}\parallel}^2}\right) \exp\left(\frac{-u_\perp^2}{2U_{\mathrm{t}\perp}^2}\right) , \tag{A.2}$$

where $u = \gamma v$. These distributions are normalized by two different integrals,

$$\int_{-\infty}^{\infty} f(\mathbf{v})\, \mathrm{d}^3 v = 1 \tag{A.3}$$

and

$$\int_{-\infty}^{\infty} f(\mathbf{u})\, \mathrm{d}^3 u = 1\,. \tag{A.4}$$

In the integration over classical velocities, we allow for superluminal velocities, because the distribution function is assumed to have negligible magnitude at these velocities.

If we wanted to integrate the distribution g over a certain volume of the classical velocity space (to obtain the particle density which appears in the definition of current density), we would have to carry out the change of coordinates

$$g(u_\parallel, u_\perp, \varphi)\mathrm{d}^3 u \to g(v_\parallel, v_\perp, \varphi)\mathrm{d}^3 v\,. \tag{A.5}$$

In the cylindrical coordinates, we have

$$\mathrm{d}^3 u = \mathrm{d}u_\parallel u_\perp \mathrm{d}u_\perp \mathrm{d}\varphi\,, \tag{A.6}$$

and by calculating the derivatives, we get

$$\mathrm{d}u_\parallel = (1 + v_\perp^2)\gamma^3 \mathrm{d}v_\parallel\,, \tag{A.7}$$

$$u_\perp \mathrm{d}u_\perp = (1 + v_\parallel^2)\gamma^4 v_\perp \mathrm{d}v_\perp\,. \tag{A.8}$$

The normalization factor becomes

$$\frac{1}{(2\pi)^{3/2}\gamma^3 V_{\mathrm{t}\perp}^2 V_{\mathrm{t}\parallel}}\,, \tag{A.9}$$

and if we combine all the expressions together, we get

$$g(v_\parallel, v_\perp, \varphi)\mathrm{d}^3 v = \frac{1}{(2\pi)^{3/2} V_{\mathrm{t}\perp}^2 V_{\mathrm{t}\parallel}} (1+v_\parallel^2)(1+v_\perp^2)\gamma^4 \exp\left(\frac{-v_\parallel^2}{2V_{\mathrm{t}\parallel}^2}\right) \exp\left(\frac{-v_\perp^2}{2V_{\mathrm{t}\perp}^2}\right) \mathrm{d}v_\parallel \mathrm{d}v_\perp v_\perp \mathrm{d}\varphi\,. \tag{A.10}$$

Now we can see that the two distributions f and g are different, because

$$\frac{g}{f} = (1 + v_\parallel^2)(1 + v_\perp^2)\gamma^4 \,. \tag{A.11}$$

The distribution g is well normalized, because we are not integrating the classical velocities up to infinity as with f, but we limit them to a ball with a radius of the speed of light. The factor g/f compensates for these bounds imposed on the integration region.

In the calculation of resonant current within the nonlinear growth theory (source at $h = 0$), the situation is slightly different. In the construction of the resonant potential, it is assumed that all the particles have a constant parallel velocity V_R and a constant perpendicular velocity $V_{\perp 0}$. Accordingly, we assume that the γ-factor in the integration of the resonant phase space region can be replaced by a constant $\gamma_\mathrm{R} = (1 - V_\mathrm{R}^2 - V_{\perp 0}^2)^{-1/2}$. Therefore, the velocity transformation is simply

$$\mathrm{d}^3 u = \gamma_\mathrm{R}^3 \mathrm{d}^3 v \,, \tag{A.12}$$

and this factor of γ_R^3 is exactly compensated by the normalization factor,

$$\frac{1}{(2\pi)^{3/2} U_{\mathrm{t}\perp}^2 U_{\mathrm{t}\parallel}} \to \frac{1}{\gamma_\mathrm{R}^3} \frac{1}{(2\pi)^{3/2} V_{\mathrm{t}\perp}^2 V_{\mathrm{t}\parallel}} \,. \tag{A.13}$$

Therefore, if we exchange f for g in the calculation of the resonant current, the quantity J_0 will remain exactly the same. In Omura et al. 2008, between equations 46 and 47, we have

$$J_0 = 2^{3/2} e \frac{\omega_\mathrm{tr}}{k} V_{\perp 0}^2 Q F \,, \tag{A.14}$$

with

$$F \sim \frac{1}{V_{\perp 0} V_{\mathrm{t}\parallel}} \,. \tag{A.15}$$

If we wish to replace F by

$$G \sim \frac{1}{U_{\perp 0} U_{\mathrm{t}\parallel}} \tag{A.16}$$

instead, we will get and extra factor of γ_R^2, and after writing ω_tr out as

$$\chi k^{1/2} V_{\perp 0}^{1/2} \Omega_\mathrm{w}^{1/2} \gamma_\mathrm{R}^{-1/2} \,, \tag{A.17}$$

we get

$$\begin{aligned} J_0 &= (2e)^{3/2} (m_\mathrm{e} k \gamma_\mathrm{R})^{-1/2} (1 - V_\mathrm{p}^2/c^2)^{1/2} V_{\perp 0}^{1/2} V_{\perp 0}^2 \gamma_\mathrm{R}^2 Q G B_\mathrm{w}^{1/2} \\ &= (2e)^{3/2} (m_\mathrm{e} k)^{-1/2} \gamma_\mathrm{R}^{-1} (1 - V_\mathrm{p}^2/c^2)^{1/2} U_{\perp 0}^{5/2} Q G B_\mathrm{w}^{1/2} \,, \end{aligned} \tag{A.18}$$

which is exactly the same formula as in the Equation 3.27.

If we wish to recover the corrections to Γ_N and Ω_thr in Omura et al. 2009 and to Ω_opt in Omura et al. 2011, we simply observe that

$$\Gamma_\mathrm{N} \sim J_\mathrm{E} \sim J_0 \Rightarrow \text{ correction } \gamma^2 \,, \tag{A.19}$$

$$\Omega_\mathrm{thr} \sim \Gamma_\mathrm{N}^{-2} \Rightarrow \text{ correction } \gamma^{-4} \,, \tag{A.20}$$

and

$$\Omega_\mathrm{opt} \sim \delta\omega \sim J_\mathrm{B} \sim J_0 \Rightarrow \text{ correction } \gamma^2 \,. \tag{A.21}$$

A.2 Hanzelka et al. [2020]

Hanzelka, M., Santolík, O., Omura, Y., Kolmašová, I., and Kletzing, C. A. A Model of the Subpacket Structure of Rising Tone Chorus Emissions. *J. Geophys. Res. Space Physics*, 125(8):e28094, August 2020. doi: 10.1029/2020JA028094.

A.3 Hanzelka et al. [2021]

Hanzelka, M., Santolík, O., Omura, Y., and Kolmašová, I. Measurability of the Nonlinear Response of Electron Distribution Function to Chorus Emissions in the Earth's Radiation Belt. *J. Geophys. Res. Space Physics*, 126(9):e29624, September 2021. doi: 10.1029/2021JA029624.